2018

THE INTERACTION OF IGNITION AND IN-CYLINDER FLOW ON FLAME KERNEL DEVELOPMENT AND ITS IMPACTS ON COMBUSTION IN AN OPTICALLY ACCESSIBLE DIRECT INJECTION ENGINE

Yanyu Wang
Michigan Technological University, yanyuw@mtu.edu

THE INTERACTION OF IGNITION AND IN-CYLINDER FLOW ON FLAME KERNEL DEVELOPMENT AND ITS IMPACTS ON COMBUSTION IN AN OPTICALLY ACCESSIBLE DIRECT INJECTION ENGINE

By

Yanyu Wang

A DISSERTATION

Submitted in partial fulfillment of the requirements for the degree of

DOCTOR OF PHILOSOPHY

In Mechanical Engineering – Engineering Mechanics

MICHIGAN TECHNOLOGICAL UNIVERSITY

2018

This dissertation has been approved in partial fulfillment of the requirements for the Degree of DOCTOR OF PHILOSOPHY in Mechanical Engineering – Engineering Mechanics.

Department of Mechanical Engineering – Engineering Mechanics

Dissertation Advisor:	*Jeffrey D. Naber*
Committee Member:	*Mahdi Shahbakhti*
Committee Member:	*Seong-Young Lee*
Committee Member:	*Duane Bucheger*
Department Chair:	*William W. Predebon*

Table of Contents

List of figures

List of tables

Preface

This dissertation contains three published papers related to the progress of the research by the author. These papers are re-published in this dissertation with permission granted from the original publisher – SAE International.

Chapter 7 was originally published as a SAE technical paper with SAE number 2017-01-0672 titled *"An Experimental Study on the Interaction between Flow and Spark Plug Orientation on Ignition Energy and Duration for Different Electrode Designs"* in 2017 SAE world congress.

Chapter 8 was originally published as a journal article titled *"Investigation of Impacts of Spark Plug Orientation on Early Flame Development and Combustion in a DI Optical Engine"* in SAE International Journal of Engines in 2017.

Chapter 9 is a paper titled *"Investigation of Flow Conditions and Tumble near the Spark Plug in a DI Optical Engine at Ignition"*. It has been approved for publication for 2018 SAE world congress.

Each of the above papers is re-published in this dissertation to its entirety content-wise. However the format has been modified to fit the overall format of this dissertation, and the cited resources are extracted from each paper and all cited references are listed in the reference section in chapter 11.

I am the first author of all above mentioned publications, and I am also the main person who has conducted the experiment and processed the data. All the work including this dissertation is done under guidance and supervision of Dr. Jeffrey Naber.

Acknowledgements

I give my sincere gratitude to my advisor Dr. Jeffrey Naber, who has been guiding and supporting my research with great patience and admirable knowledge from the first day of my participation in the advanced power systems research team. I also give my most sincere thanks to my other committee members Dr. Mahdi Shahbakhti, Dr. Seong-Young Lee and Dr. Duane Bucheger for their guidance and help on my research.

Thanks also go to my friends at APS Labs, Jiongxun Zhang, Paul Dice, Joel Duncan, Owen Martilla, Carl Jolma, Jesse Hill, Xin Wang and Zhuyong Yang. The research could not have gone as smoothly without their help and support.

I would like to acknowledge Ford Motor Company for their sponsorship of the research and guidance. Thanks specifically go to Garlan Huberts, Mike Czekala and Qiuping Qu from Ford Motor Company. They provided great amount of valuable suggestions and recommendations to this research.

I would also like to acknowledge Mahle Powertrain for providing the optical engine and I especially thank Mike Bunce and Eric Smith for giving us guidance on instrumenting the optical engine.

List of abbreviations

AIT	after ignition timing
AKI	anti-knock index
ATDC	after top dead center
BD	breakdown
BMEP	brake mean effective pressure
BSFC	brake specific fuel consumption
BTDC	before top dead center
CA	crank angle
CA50	crank angle position where 50% of fuel is burned
CA0010	crank angle duration from ignition to 10% of fuel is burned
CA1090	crank angle duration from 10% to 90% of fuel is burned
CAFE	corporate average fuel economy
COV	coefficient of variation
DAQ	data acquisition system
DI	direct-injection
DI-SI	direct-injection spark-ignition
DOE	Department of Energy
ECU	engine control unit

EGR	exhaust gas recirculation
EGT	exhaust gas temperature
EMOP	exhaust maximum opening position
EPA	Environmental Protection Agency
EST	electronic spark timing
EVC	exhaust valve closing
EVO	exhaust valve opening
E70	gasoline blended with 70% of ethanol in volume
fps	frames per second
GDI	gasoline direct injection
GHG	greenhouse gas
IMEP	gross indicated mean effective pressure
IMOP	intake maximum opening position
IVC	intake valve closing
IVO	intake valve opening
LDV	light-duty vehicle
MAP	manifold absolute pressure
MFB	mass fraction burned
NHTSA	National Highway Traffic Safety Administration

NMEP	net mean effective pressure
msAIT	milliseconds after ignition
PFI	port fuel injection
PIV	particle imaging velocimetry
PLIF	planar laser-induced fluorescence
PWM	pulse width modulation
RPM	revolutions per minute
SA	spark advance
SI	spark-ignition (or spark-ignited)
SP	spark plug
STD	standard deviation
TDC	top dead center
TP	tumble plank
TWC	three-way catalyst
VVT	variable valve timing
2D-PDF	2-dimensional probability distribution function
1D-PDF	1-dimensional probability distribution function

Abstract

A significant challenge facing spark-ignited (SI) engines to achieve higher efficiency via highly diluted combustion is the quickly increased combustion instability as the dilution level increases. The flow motion variation has been identified as a dominant factor that introduces combustion variability at highly diluted conditions. However, the detailed mechanism of how the variation in flow motion impacts the flame kernel development and introduces combustion instability is only partially understood. This research investigated the impacts of the in-cylinder flow on variability of the ignition and early flame kernel development in a single cylinder direct-injection spark-ignition (DI-SI) optically accessible engine and accessory test benches. Firstly, different types of spark plug electrode designs were studied on a spark plug flow fixture bench. The results showed that the impacts of incoming flow on the ignition output vary as the incoming flow direction is changed. The ignition energy drops and discharge duration prolongs as the incoming flow is blocked by any part of the electrodes. Secondly, the flow motion near the spark plug region was investigated in an optical engine through high-speed imaging of the spark discharge arc stretching and flow field measurement via particle imaging velocimetry. It was observed that at motored conditions there is a consistent trend that the flow can change direction from the bulk motion as the piston approaches the top dead center (TDC). The transition of flow direction near the spark plug is a source of variability in initial flame kernel convection and propagation. It was found that by increasing the tumble motion, the transition window can be retarded later in the cycle. Lastly, the impacts of the unstable in-cylinder flow motion on the flame kernel initiation and development was studied at both diluted and stoichiometric conditions. The 2D and 1D probability distribution functions of the flame kernel indicated that the reversed flow direction near the spark plug at ignition timing results in smaller and less stretched flame kernels, which are a source of combustion variability. As the tumble level is increased, the window where the transition of flow direction occurs near the spark plug also changes. This research indicates that, at the studied loads and speeds, higher tumble level helps maintain a consistent flow motion near the spark plug at the ignition timing, which results in faster growing flame kernels.

1 Introduction

1.1 Background

1.1.1 Energy Scene in the U.S. Transportation Sector

According to the annual energy outlook report [1] released by the Department of Energy (DOE), the transportation sector energy consumption is 28.1 quadrillion BTU in 2015, which accounts for more than 70% of petroleum consumption in the United States. The energy consumed through motor gasoline is about 17 quadrillion BTU, and 16 of which is consumed by light-duty vehicles (LDV). The projection made by DOE indicates that LDV energy consumption will drop to 11.8 quadrillion BTU in 2040 due to the higher corporate average fuel economy (CAFE) standards.

Though the general trend in automotive industry is electrification, according to the another report [2] released by Environmental Protection Agency (EPA), vehicles powered purely by gasoline engines currently make over 95% of the market, where vehicles powered by other means, including diesel, hybrid, electric and etc. only make less than 5% of the market. The projection made by DOE [1] calculates that in 2040, 61% of all new LDV sales will have alternative power plants; however, many will still have gasoline engines as part of the power source (e.g., hybrid vehicles). Though the sale of new LDVs with alternative power sources increases substantially in 2040, the gasoline engine only powered LDVs still make 39% of the market, which is far from negligible.

As outlined, internal combustion engines fueled with gasoline will remain the main power plants for light duty vehicles for the foreseeable future in the United States. With tightening emissions and fuel economy regulations, intensive research on improving engine efficiency and reducing emissions is of great urgency.

1.1.2 LDV Emissions and Fuel Economy Regulations in US

Since the emissions from vehicles were found to be the source of smog and air pollution in Los Angeles in the mid of 20th century, the California government and the US federal government have been increasingly tightening the regulations on vehicle toxic emissions. With the concerns of global warming due to greenhouse gas effects, regulations on fuel economy of vehicle fleet have also been more demanding than ever before.

The EPA Tier 2 standards regulated NOx emissions to be not higher than 70 mg/mi fleet average for 120,000mi/10yrs period, with 8 bins to specifically regulate NOx, NMOG, CO, PM and HCHO emissions. Similarly, California LEV II standards required the fleet average NMOG to not exceed 35 mg/mi for passenger cars and 43 mg/mi for heavier light-duty trucks in 2010 [3]. The EPA Tier 2 and California LEV II have completed phased in today.

Starting from 2017, the LDV emissions are becoming more stringent through the EPA Tier 3 and California LEV III standards (LEV III started phasing in in 2015). These standards are designed in coordination with each other. Both standards require fleet average NMOG+NOx emissions combined to not exceed 30 mg/mi by 2025. Tier 3 reduces particular matter (PM) emissions to 3 mg/mi while LEV III continues to tighten it down to 1mg/mi across the fleet [4]. Both EPA Tier 3 and California LEV III regulations require 100% phase-in by 2025.

The CAFE standard by National Highway Traffic Safety Administration (NHTSA) sets a combined fleet-wide fuel economy of 40.3-41.0 mpg for model year 2017 – 2021, while the harmonized Green House Gas standards by EPA require 163 g/mi CO2 emissions, equivalent to 54.5 mpg calculated using CAFE method for passenger cars in model year 2025 [5, 6].

In summary, the emission regulations are getting ever more stringent. This is beneficial to the living environment and human health; however, this does pose a great challenge to automobile manufacturers. Multiple technologies have been under intensive study with the

end goal of reducing engine emissions and improving engine efficiency. The research documented in this dissertation aimed to provide further insights into the causes of combustion instability under diluted combustion conditions, which are a promising way to achieve higher SI engine efficiency.

1.1.3 Brief Review of Advanced Technologies for Efficiency Improvement and Emissions Reduction

1.1.3.1 Engine Downsizing

One of the major trends of modern SI engines is downsizing [7-11]. Through downsizing, the originally low and medium load points are moved towards higher loads. The throttle opens wider and thus reduces the pumping losses. To compensate the loss of peak torque and power due to the smaller displacement of the engine, boosting the intake charge, either through turbochargers or superchargers, is required for the downsized engines to retain performance to a comparative level with their larger size counterparts. Further, since the downsized engines are usually boosted, it has higher propensity of knock at high loads due to the increased specific power, thus gasoline direct injection (DI) technology is commonly utilized due to the charge cooling effect of the direct injected fuel. Besides the reduced pumping losses, downsized engines also have the advantages of high power density, faster catalyst light-off and potentially lower friction losses.

1.1.3.2 Gasoline Direct Injection

Gasoline direct injection (GDI) has been widely used in production SI engines [7, 11-13]. The fuel is directly injected into the cylinder; no liquid puddle is formed on the back of the intake valves nor on the intake port wall. The injection pressure ranges from about 4 MPa at low and part loads to above 20 MPa at high loads/ high speeds. The high injection pressure facilitates the atomization of fuel; however, since the fuel is directly injected into the cylinder, it is a challenge to achieve the same level of homogeneous mixing as its port fuel injection (PFI) counterparts. The major benefit of GDI is the charge cooling. As the

fuel is injected, atomized and vaporized in the cylinder, it cools down the intake charge so the tendency of knock decreases. Commonly with GDI technology implemented, the compression ratio can be increased due to the reduced knock sensitivity benefited from direct-injection (DI) charge cooling.

1.1.3.3 Variable Valve Timing and Lift

Modern SI engines have adopted the capability of real-time adjustment of the intake camshaft phasing or both intake and exhaust camshaft phasing to improve performance and increase efficiency [12-14]. Optimization of the cam phasing can reduce the pumping losses, change the amount of internal exhaust residual [15] and to speed up the light off the three-way catalyst during cold start [16]. As a result, the engine efficiency increases and the NOx emissions can be reduced. Variable valve timing (VVT) is also a key technology to reduce the low speed turbo lag on modern turbocharged engines [7, 11, 17].

1.1.3.4 Diluted Combustion (Lean or EGR)

As discussed above, both downsizing and VVT improve the engine efficiency partially through reducing the pumping losses of the engine. Another method of de-throttling the engine is diluting the intake charge, either by increasing the air/fuel ratio (lean combustion) or by exhaust gas recirculation (EGR). By increasing the air/fuel ratio, or displacing part of the fresh air, the throttle needs to be opened wider so the intake manifold pressure increases, leading to reduction of pumping losses. Additionally, by introducing dilution with lean charge or EGR, the heat capacity of the charge increases, and the combustion temperature decreases, leading to lower heat losses and lower tendency of knock [18-21]. Multiple advanced combustion systems are under intensive research based on diluted combustion [21-26].

1.1.3.5 NOx Reduction

The SI engines that power light-duty vehicles in the US are most commonly operating at homogenously stoichiometric conditions. The three-way catalyst converter is a highly

efficient emission reduction device at stoichiometric conditions and is widely used as the main aftertreatment system on LDVs. With stoichiometric combustion, the oxidization of CO and HCs and reduction of NOx simultaneously occur in the three-way catalyst converter forming CO2, H2O and N2 [16]. As the air/fuel ratio deviates from stoichiometric to lean, although the raw NOx production decreases due to the lower combustion temperature, this amount of NOx cannot be further reduced by the three-way catalyst since CO and HCs would react with the excessive oxygen that is present in the exhaust, preventing the reduction of NOx.

1.1.3.6 PM Reduction

As GDI technology becomes widely adopted, the emissions of particular matter (PM) need extra effort to be reduced. As discussed above, since the fuel is directly injected in the cylinder, it has less time to be fully atomized, vaporized and mixed with the intake charge. Because of the high injection pressure, the fuel jet could also impinge on the piston forming a pool if injection timing is early. The large droplets from the poor atomization and the fuel pool on the piston result higher amount of PM compared with PFI engines. Under the stringent PM emission standards set by Tier 3 and LEV III, gasoline particle filters might become necessary [27-29].

1.1.4 Major Challenges on the Path of Improving SI Engine Efficiency

For lean combustion in SI engines, one challenge is that the three-way catalyst (TWC) would stop functioning if the combustion deviates from stoichiometric ratio. For lean combustion where the excessive oxygen is present in the emissions, HCs and CO would oxide with O2 instead of being a reducing agent for NOx. This issue can be resolved by diluting the charge by EGR instead of excessive air. However, the biggest challenge facing both lean combustion and EGR is that combustion stability rapidly decreases as the dilution level increases, eventually to a point where the engine is no longer drivable [30]. The combustion instability limits the thermal efficiency gains that can be obtained through dilution.

1.2 Research Motivation

To enable further thermal efficiency improvement of SI engines through de-throttling by either lean combustion or EGR, the combustion has to be stabilized under highly diluted conditions. It is crucial that the sources of cycle by cycle combustion variability should be identified and the mechanism of how these sources influence the combustion process should be understood.

The variability of the flow motion in the cylinder has been identified as one major cause of combustion variability [31, 32]. The interaction between the flow motion and the ignition discharge changes the ignition output and characteristics of the resulting initial flame kernel, and the initial flame kernel is a dominant factor that influences later stages of combustion [25, 33, 34]. However, the understanding of the relationship between the variations in flow motion and variability of flame kernel development and combustion is still incomplete.

To further the understanding of the causes of combustion instability, with the capability offered by a single cylinder DI-SI optically accessible engine, this research investigated the interaction between the flow motion and spark ignition discharge arc, quantified the flow motion near the spark plug region at ignition timing which is commonly set for both stoichiometric and diluted conditions, and investigated how the variations in flow motion near the spark plug influences the flame kernel initiation and propagation at both stoichiometric and diluted conditions.

1.3 Goals and Objectives

This research aimed to further the understanding of how the variations in flow motion introduces variability to combustion for DI-SI engines, by investigating the in-cylinder flow motion at different loads/speeds, and its interaction with the spark ignition discharge arc and resulting flame kernels. To reach this goal, the following objectives were set.

1.3.1 Test Platform Instruments Objectives

- Instrument the test platform for the single cylinder DI-SI optically accessible engine to fully functional level in synchronization with other data acquisition (DAQ) systems including combustion analyzer, high-speed camera, particle imaging velocimetry (PIV) laser/camera system, and ignition DAQ system.
- Instrument high-speed camera system in coordination with the optical engine operation to acquire high-speed images of the ignition arc and flame kernels.
- Instrument PIV laser/camera system to quantitatively measure flow field inside the cylinder.
- Instrument high-speed-sampling-rate NI-PXI data acquisition system to capture the secondary ignition voltage and current.
- Instrument prototype engine controller to fulfill research requirements, including skip-firing of the engine, driving multiple ignition coil/discharge, enabling multiple injection events, synchronizing with the high-speed camera, PIV system, and ignition measurement system.

1.3.2 Data Processing Codes Objectives

Universal Matlab codes were developed as follows to post-process the data from each DAQ system:

- Data processing for in-cylinder pressure transducer data to obtain mass fraction burned (MFB) results. The custom combustion analysis code is needed as the optical engine is skip-fired.
- Image processing to obtain ignition arc and flame kernel metrics including centroids, projected area, and probability distribution.
- Calculating ignition metrics including breakdown voltage, secondary ignition energy, discharge duration and number of re-strikes.
- False trigger detection to recognize the useless data recorded by false triggers caused by the electrical noise in the test cell.

- Processing for test data synchronization and organization. In the meantime, videos are generated comprising the high-speed images and other synchronized data of interest. This serves the purpose of visual communication of the findings with our research partner.

Besides the universal codes, individual Matlab codes were designed for each set of tests to fulfill the respective analysis requirements of different sets of data.

1.3.3 Experiment and Analysis Objectives

- Study the interaction between flow and spark plug orientation on ignition energy and ignition discharge duration for different electrode designs at different orientations between the flow direction and the spark plug axis in a spark plug flow fixture.
- Investigate the impacts of spark plug orientation on early flame development and combustion in the optical engine.
- Investigate the flow motion near the spark plug at different levels of tumble motion and engine speeds.
- Statistically analyze the variability of the flow motion near the spark plug and its resulting impacts on the early flame kernel development.

1.3.4 Research Milestones

To achieve the goals of this research, the following milestones have been successfully met. Each milestone will be fully explained in the following sections of this dissertation. Before conducting the experiments, related studies found in literature were reviewed in-depth, which will be discussed in chapter 2. Concurrently with literature review, the instrumentation of the engine and accessory data acquisition systems were in progress and eventually completed. The detailed description of the engine test platform and experimental setup will be introduced in chapter 3. The remaining research milestones are marked by three publications, and they will be re-published to their entirety in chapters 7 to 9 respectively in this dissertation with approval of the original publishers. Chapter 10

summarizes the whole study and highlights the new knowledge that is brought to light through the investigations.

2 Literature Review

Combustion instability under lean conditions has been under intensive research by both automotive industry and academia. In-depth review of the studies reported in the literature was conducted to gain an understanding of current status of this topic, which will be discussed in this chapter.

Through imaging study of the flame kernels in a 3-valve optical engine with a side-located spark plug, Bates [35] concluded that the large size of the very early flame kernel is related to the faster burn rate throughout the early stages of combustion, and these large initial flame kernels appear before any significant mass faction burned. The states of early flame kernels influenced by the local flow including shape, size and location cause variations in later stages of combustion through controlling the later flame geometries. He also concluded that the degree of the flame kernel conforming to the shape of cylinder causes variations in combustion in that it determines how far the flame front needs to travel to complete the combustion. At lean conditions, it was found that one significant cause of combustion variability is that part-burn cycles are usually followed by a strong-burn cycle due to the remaining unburned fuel in the cylinder. For his study with the side-located spark plug, the impacts from the interaction between the flow and the flame kernel are amplified since the flame front needs to travel a longer distance to complete the combustion.

The influence of the flow velocity near the spark plug on early flame development was investigated by Johansson using laser Doppler velocimetry in an optical engine fueled with natural gas [31, 36]. It was concluded that the flow motion is the main cause of cycle by cycle variations in combustion, and both high frequency and low frequency components of flow velocity have impacts on the early combustion. There is a high correlation between flow velocity frequency range of 4 – 7 kHz near the spark plug and ignition delay (ignition to 0.5% fuel burned), where the correlation coefficient is above 0.7. This frequency range corresponds to 0.5 – 1.5 mm eddy size under Taylor's hypothesis. He also determined that the influence of the flow motion on the early combustion stays constant as the equivalence ratio is changed. The follow-up study [37] by the same author discovered that variations in

turbulence can explain 50% of flame growth fluctuation if there is no great fluctuation in fuel and residual gas fraction. As the fluctuation in air/fuel ratio increases, 65% of the flame growth rate fluctuations can be explained by local equivalence ratio variations. They also found that the correlation coefficient between mixture homogeneity and early stage of combustion is low under well-mixed conditions, but it increases above 80% as the inhomogeneity increases, and the correlation peaks at 4.5 mm radius range from the spark plug electrode tip. The same study showed that there is a consistent average correlation of 70% between turbulence and the 0.5% heat release, and correlation of 50% between mean flow motion and 0.5% heat release.

Pischinger and Heywood from MIT [34] investigated the effects of heat losses to the spark plug electrodes on flame kernel development and on combustion. They discovered that the heat losses to the spark-plug electrodes and variations in ignition energy can contribute significantly to cycle-by-cycle variations in flame kernel development, especially at lean ignition limit. Initial flame kernels that convect away from spark-plug electrodes tend to grow faster than the ones that center at the electrodes, due to the lower heat losses to the electrodes when the flame kernels move away. They identified the flow to be the dominant factor that causes variations in initial flame kernel growth. By comparing a standard spark plug and a thin-electrode spark plug, they found that the thin-electrode spark plug results in larger flame kernels in average due to its smaller contact area between the electrodes and the flame kernel, leading to lower heat losses to the electrodes; and because of the faster burning flame, the MBT is retarded with the thin-electrode spark plug and the cycle by cycle variations in combustion are reduced. The standard spark plug has a higher probability of producing slowly growing flame kernels. They also showed that the thin-electrode spark plug has a tendency to operate in arc mode, and the combustion is sensitive to the spark plug orientation at lean limit.

Ayala and Heywood [30] investigated the underlying mechanism that governs the increasing variability in combustion at lean conditions. The study indicated the increase in combustion variability is caused by the initial variability in the eddy burning time at lean conditions. They found the variability in the initial eddy burning time is largely responsible

for the variations in 0-10% burn duration (CA0010). The eddy burning time is inversely dependent on the laminar flame speed and positively dependent on the turbulence microscale. The laminar flame speed decreases as the mixture gets lean, leading to increase in the variability of the initial eddy burning time. The variability will be further amplified throughout the entire combustion process due to different physical states the flame kernel experiences as it grows starting from the initial variations in eddy burning time. This integral effect causes larger variations in later combustion stages. That is to say, the slowly burning cycles will continue to burn slowly since the pressure and temperature rise will be slow, and the faster burning cycles will continue to burn faster. By increasing the turbulence, the microscale decreases, such that the initial eddy burning time will also decrease. The reduced variability in initial eddy burning time will reduce the variability of the entire combustion process. They also identified the critical value of CA0010 to be 40°CA, beyond which the variation of CA0010 rapidly increases causing rapid increase in variability of 10-90% burn duration CA1090 and net mean effective pressure (NMEP).

Aleiferis et al. [33] discovered in an optical engine modified from a Honda VTEC SI engine with stratified charge that the early stage of combustion from 0-40°CA window plays a significant role in determining the later stages of combustion and eventually the gross indicated mean effective pressure (IMEP) of the cycle. That is to say: the quality of the cycle is determined within a very short time after ignition. Their conclusion was supported by high correlation between the characteristics of the early flame kernel and combustion metrics that reflect later stages of combustion including IMEP and 50% mass fraction burned (CA50). They also investigated the effects of different spark plug orientations on combustion and found the crossflow orientation results in the lowest coefficient of variation (COV) of IMEP.

Further work by Aleiferis et al. [38] in a lean-burn stratified-charge spark-ignition optical engine investigated the correlation between the early flame development to 0-5% mass fraction burned (CA0005). A strong correlation was observed between 5% mass fraction burned (CA05) and IMEP, indicating the early flame kernel is the dominant factor that determines the later stages of combustion at lean conditions, in agreement with results from

other studies. It was found that a high convection velocity is preferred up to 30°CA after ignition on the tumble plane; however on the swirl plane, high convection velocity is only preferred to 10°CA and after that a slower convection velocity is preferred. The authors' results did not show strong correlation between the wrinkling of the early flame kernel with CA05.

Zhao et al. [32] studied the potential causes of the cyclic variability of combustion in a PFI SI engine through large-eddy simulation with the G-equation combustion model. It was shown by numerically de-coupling the effects from flow and equivalence ratio distribution at the relevant operating conditions, that the fluctuation in the flow motion at the time of ignition is the dominant factor that causes cyclic variations in combustion rather than the local inhomogeneity of the mixture. They also found that flame volume shape tends to be flatter and more symmetric with respect to the ignition axis for cycles of high peak pressure.

Sjoberg et al. [39] from Sandia National Labs investigated the impacts of in-cylinder flow motion on stratified and well-mixed combustion in DI-SI engines. They observed that for the well-mixed combustion, the apparent heat release rate profiles are essentially unchanging with respect to crank angle as the engine speed changes. It has been firmly established and proved that the well-mixed combustion is governed by turbulence which increases linearly with the engine speed, and higher tumble increases flame speed and thus decreases the cycle by cycle variations of the combustion. However, as for stratified combustion, the apparent heat release rate profiles are unchanging with respect to time. The authors proposed the hypotheses that combustion of stratified charge is mainly controlled by the mixing rate and turbulence generated by the fuel injection, and the disturbance from the variations of the intake charge flow to the fuel jet is the primary cause of the increased cycle by cycle variations in combustion observed at higher engine speeds, since it influences the mixing, ignition and combustion. He also observed that for fuel blended with 70% ethanol (E70) with stratified charge, the most stable combustion occurs with spark timing coinciding with the injection timing, and COV of IMEP increases as the engine speed is increased for the stratified mode, but not for the well-mixed mode.

Looking at the results altogether from [30, 39, 40], one can reason that since for well-mixed charge, the combustion speed is governed by turbulence which increases with engine speed, so the combustion variability does not increase significantly for the well-mixed mode. However, the stratified mode combustion is less governed by turbulence, but more by the mixing of the late injected fuel plume. The increased engine speed would introduce higher variations in the flow motion resulting in increased variability of the interaction between the intake flow and the injected fuel which could lead to higher cyclic combustion variability.

Peterson et al. [41] characterized the spark energy dependence on equivalence ratio and flow motion characteristics near the spark plug, including velocity and shear rate vorticity, in a spray-guided DI-SI optical engine. They determined that there is a moderate correlation between spark energy and equivalence ratio. The spark energy drops at $\phi > 2.3$ where soot deposit occurs on the spark plug. By injecting air instead of fuel, they studied the influence of air motion on spark energy. They found the increase in shear rate leads to a linear increase in spark energy; however, the correlation between vorticity and spark energy is low.

Further work by Peterson et al. [42, 43] studied the ignition and flame development in a spray-guided DI-SI optical engine, in order to understand the causes of partial burn and misfired cycles in stratified mode through PIV, planar laser-induced fluorescence (PLIF) and combustion luminosity with nitrogen dilution. Their study showed as dilution increases, the flame kernel size decreases and spatial flame probability decreases, which is expected since dilution slows down the flame speed. With 0 – 18% dilution, misfires and partial-burn cycles tend to occur in the low spark energy range, though all cycles exhibit spark energy high enough to ignite the mixture. For the same dilution level, misfires and partial-burn cycles also tend to happen in low velocity range and slightly lean range. They also observed that for well-burn cycles, early flame kernel keeps in contact with the past flammable fuel cloud and chases it into the piston bowl and quickly consumes it. For the partial-burn cycles, the initial flame kernel separates from the flammable mixture cloud for a period of time and gets surrounded by lean mixture, and then comes back in contact with

the flammable mixture cloud again, resulting in only part of fuel being burned. The early flame kernel separated from the flammable cloud eventually extinguishes for the misfired cycles. The probability distribution function (PDF) analysis showed that the well-burn cycles have similar early flame kernel at different dilution levels, and the difference enlarges in the later stage of combustion. The flame kernel is consistently convecting to the piston bowl where large portion of the fuel plume is burned for well-burn cycles. The PDF of partial-burn cycles show smaller early flame kernels compared with well-burn cycles, yet they are also similar at different dilution levels; however, they do not convect to the piston bowl where the flammable fuel plume is located until the late stage of compression stroke. For the misfired cycles, the flame kernel is still formed, but quickly extinguishes.

3 Test Platform Setup

The test platform of the single cylinder optically accessible engine is located at the Advanced Power System Labs (APS Labs) at Michigan Technological University. The optical engine is mounted on a movable engine cart with interfaces for the sensors and actuators to attach to accessory systems. The main accessory systems include the high speed camera system, the PIV laser/camera system and other DAQ systems. This section will detail the description and documentation of the optical engine test platform.

3.1 Single Cylinder Optically Accessible Engine

The optical engine (Figure 3-1) is modified from a 2.0 liter 4-cylinder Ford Ecoboost engine by Mahle Powertrain. The specifications of the optical engine are summarized in Table 3-1. Cylinder 2 is the working cylinder and other cylinders are deactivated. The cylinder head is separated from the engine block and elevated to accommodate the Bowditch piston extension on the original number 2 piston. On top of the Bowditch piston extension is threaded a flat-top aluminum piston with a 58 mm diameter Sapphire (single-crystal aluminum oxide Al2O3) window insert. Cylinder 1, 3, and 4 are deactivated, namely the cam lobes for these cylinders are ground off; however the original pistons in these cylinders are kept which move freely while the optical engine runs. Between the upper surface of the engine block and the elevated cylinder head is featured a deck which is able to move up and down guided by four poles driven by a manually operated hydraulic system. This deck will be referred to as the clamping deck. On top of the clamping deck at the position aligned with the working cylinder is installed the aluminum liner holder. The liner holder can be considered as the lower section of the entire liner of the optical engine, where the upper liner is the optical liner which is made of quartz (Fused Silica). The optical liner is secured against the cylinder head during engine operation by the liner holder, which is pushed by the clamping deck via 350 psi hydraulic pressure. This configuration allows convenient removal of the optical liner for maintenance between tests, simply by releasing the hydraulic pressure.

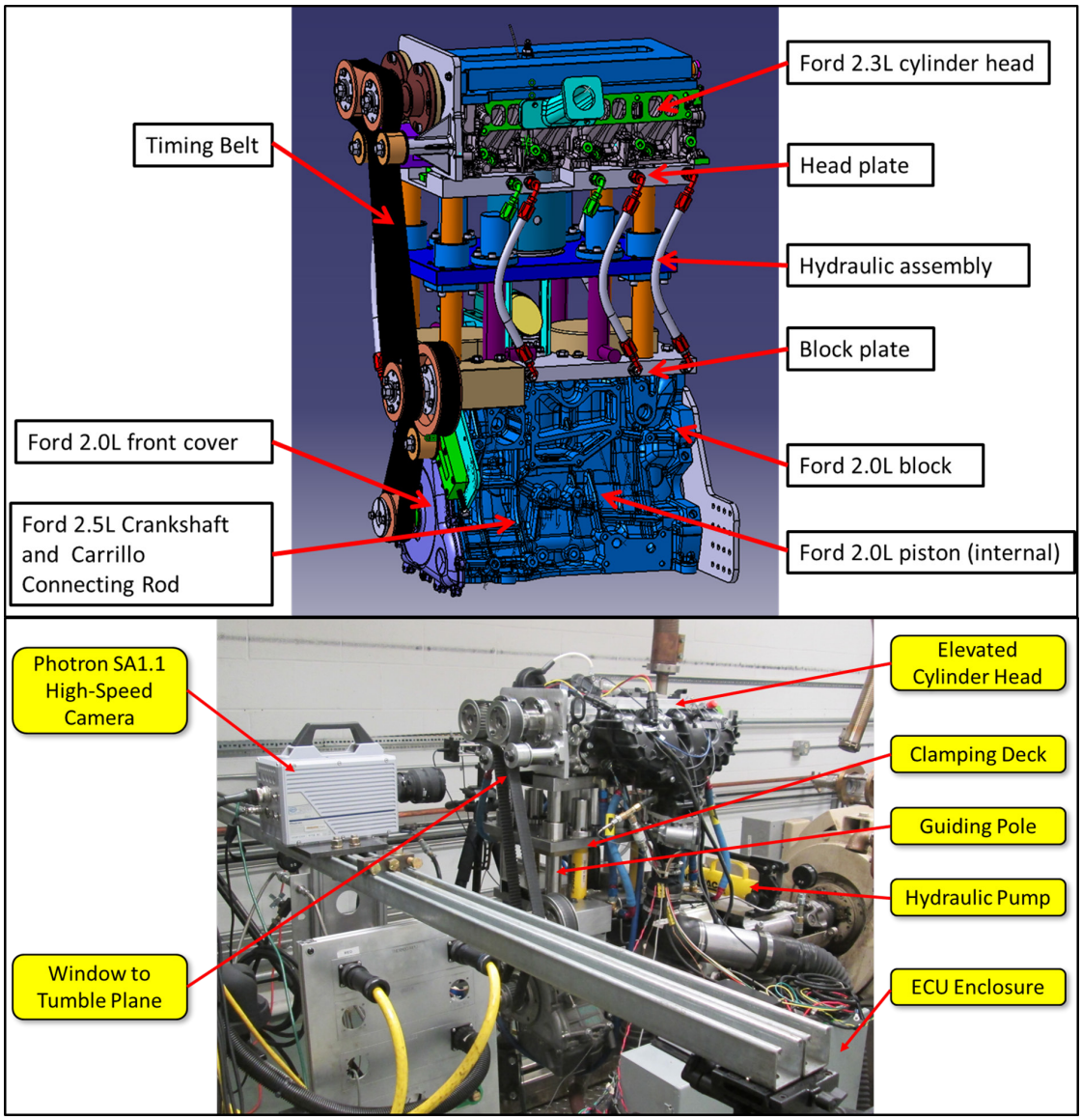

Figure 3-1: MTU – Mahle optical engine. Upper: 3D schematic of the optical engine (Source: Mahle Powertrain). Lower: optical engine in the test cell.

Table 3-1: Optical engine specifications.

Optical Cylinder Displacement (Liter)	0.6
Bore (mm)	87.5
Stroke (mm)	100
Compression Ratio	10.01 : 1
Fuel	AKI 87
Injection Pressure	4.5 MPa
Injector	Bosch multi-hole GDI injector
Injection Events	Single or multiple injection capability
Ignition	Smart/dumb, single/multiple coil capability
Piston	flat top piston with sapphire insert
Intake	Ford 2L Ecoboost intake manifold
Exhaust	custom exhaust pipe

The top curvature of the optical liner (Figure 3-2) matches the pentroof shape of the cylinder head. Two types of gasket material have been verified to offer satisfactory sealing. The first material is the graphite gasket of 1/16'' thickness with stainless steel insert. It has sufficient flexibility to conform to the top curvature of the optical liner. The second material is a type of exhaust gasket material with stainless insert. It also provides satisfactory sealing, and since its surface is non-conductive, it is advantageous in that ion probes can be used with it for ion sensing tests. Details of both types of materials are provided in Table 12-2 in the appendix 12.3.

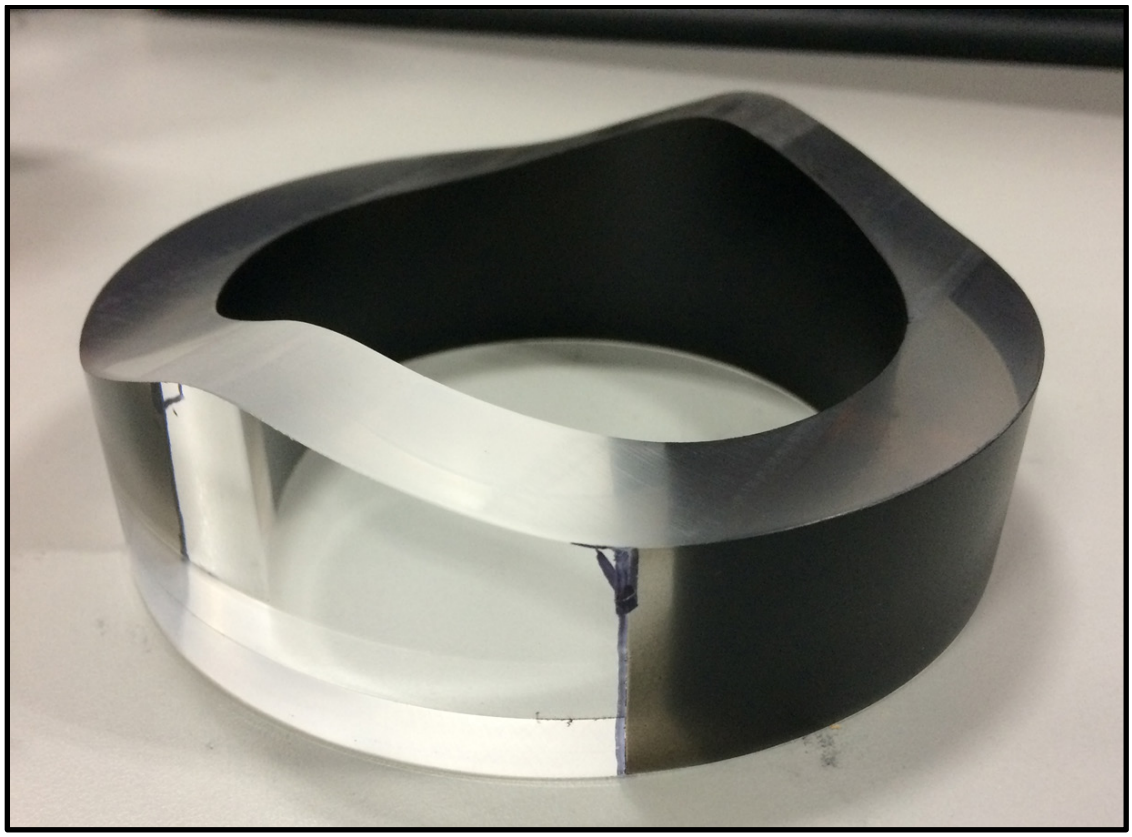

Figure 3-2: Optical liner (quartz).

The gasket is cut to the desired shape by water jet. The shape of the finished gasket is slightly oval rather than circle. The schematic of the gasket is attached in Figure 12-10 in the appendix 12.4. The gasket is glued onto the top of the optical liner (Figure 3-3) by 3M Super 77 multipurpose adhesive, and should be immediately placed into the optical engine and held by 350 psi hydraulic pressure for at least 30 minutes to secure the sealing. Once the gasket is verified to be applied successfully on the optical liner, it will serve for a good long time if proper handling is followed. More detailed description of the procedures of cleaning, painting the optical liner and applying the gasket and aligning the optical liner with the cylinder head during installation is provided in the appendix 12.5.

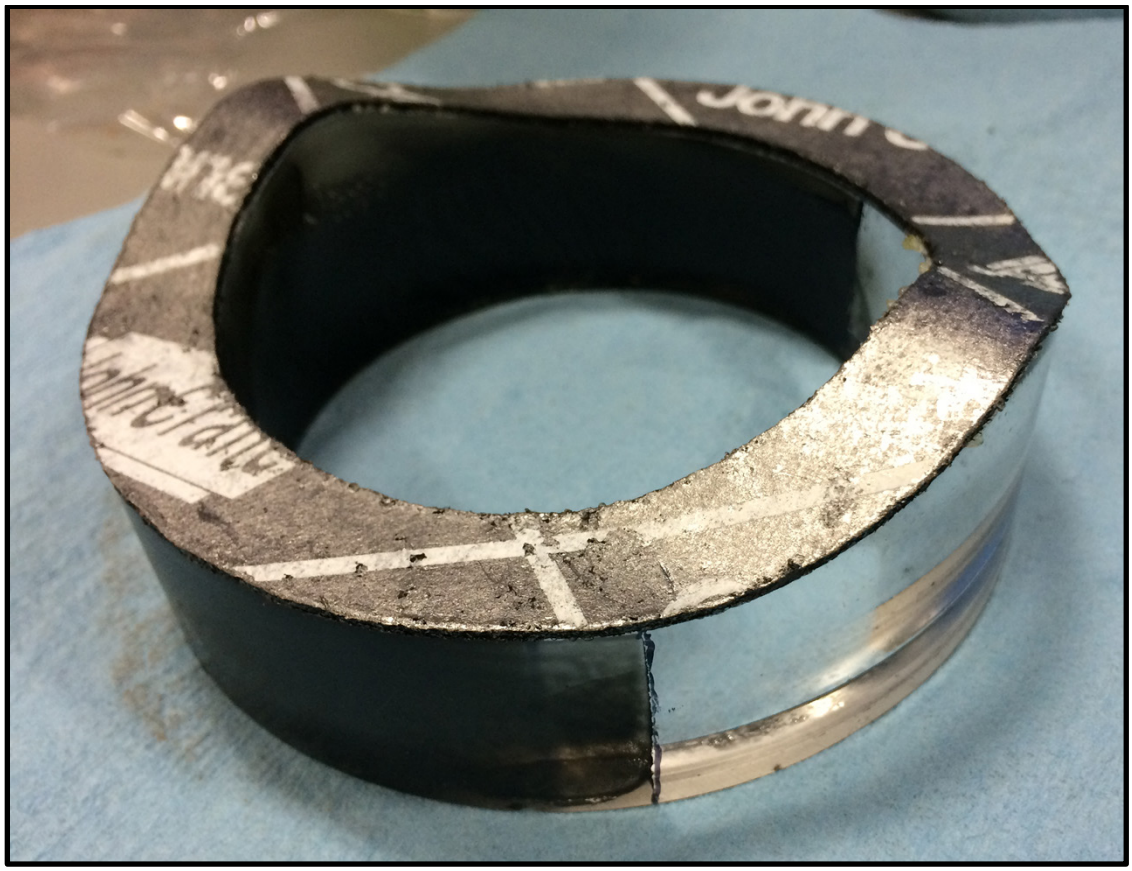

Figure 3-3: Optical liner with gasket glued on top.

The optical piston features an aluminum piston frame which is thread on top of the Bowditch extension. The Sapphire piston window is secured in the center of the aluminum piston frame as can be seen in Figure 3-4. More detailed documentation of the optical piston assembly can be found in the appendix 12.2.

Figure 3-4: The optical piston and Sapphire insert.

The characteristics of the optical liner and piston materials are summarized in Table 3-2.

Table 3-2: Properties of optical window insert and optical liner. (Source: Mahle Powertrain)

Piston Window	
Material	Sapphire
Transmission Wavelength	150 to 6000nm
Density at 20C	3.98 g/cm^3
Hardness (Mohs)	9
Tensile Strength	275 to 400 MPa
Compression Strength (ultimate)	2.0 GPa
Coeff. Of Thermal Expansion	8.4e-6/K
Melting Point	2040°C
Liner Upper Window	
Material	Fused Silica
Transmission Wavelength	250 to 1700 nm
Density	2.648 g/cm^3
Hardness (Mohs)	5.5-6.5
Tensile Strength	48.3 MPa
Compression Strength	>1.1 MPa
Coefficient of Thermal Expansion	0.54e-6/K
Melting Point	1665°C

3.1.1 Camshaft

As stated above, the cam lobes on both intake and exhaust camshafts are ground off for cylinder 1, 3 and 4, and only the working cylinder retains the breathing capability. The cam phasers are also removed and replaced by fixed cams and driven by a timing belt instead of a chain (Figure 3-1). The cam timing can be adjusted manually and precisely. The procedure of cam position adjustment is given in the appendix 12.6. The current cam positions are provided in Table 3-3, and corresponding cam profiles are illustrated in Figure 3-5. The overlap is relatively large because the combustion variability is intentionally

increased by increasing the overlap to facilitate the investigation of the causes of combustion variability with high amount of residuals.

Table 3-3: Optical engine cam positions (intake cam advanced by 30°CA from default).

	Crank Position
IVO (°BTDC)	19
IVC (°ABDC)	37
IMOP (°ATDC)	99.5
EVO (°BBDC)	36
EVC (°ATDC)	8
EMOP (°BTDC)	104
Overlap (°CA)	27

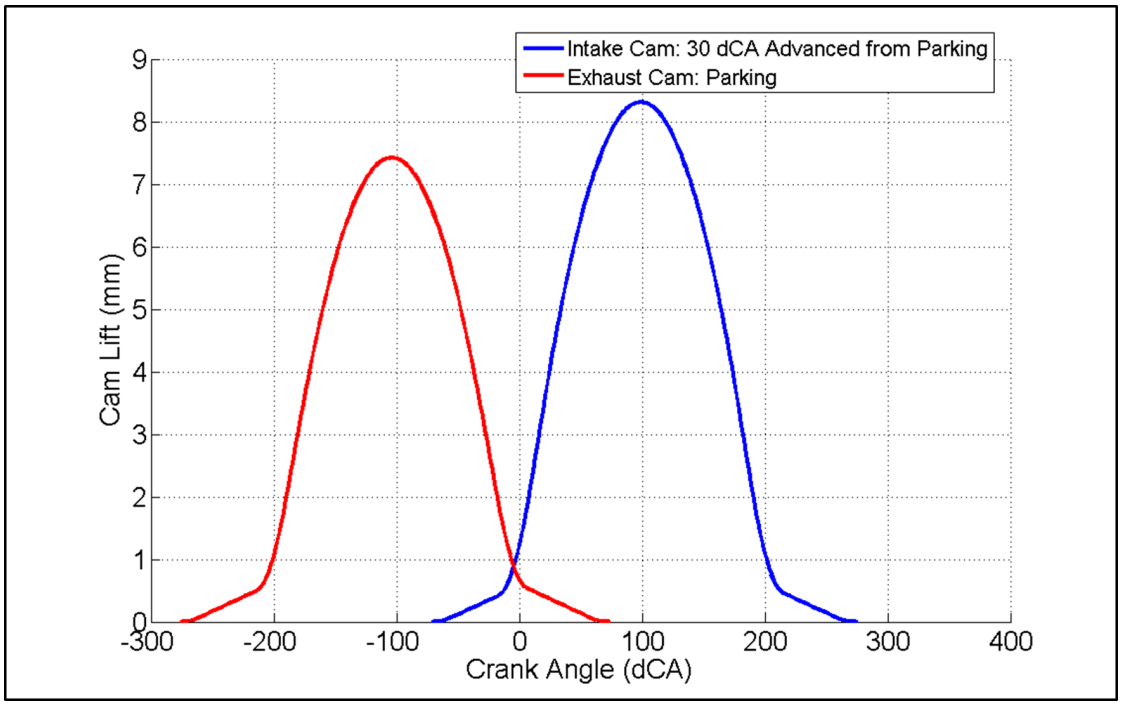

Figure 3-5: Optical engine cam profile (intake cam advanced by 30°CA from parking).

3.1.2 Lubricating and Cooling System

As the cylinder head is elevated and separated from the engine block, the conventional way of lubricating and cooling cannot be used on the optical engine, and thus the original

coolant pump has been removed. Instead, engine oil is used as both lubricating and cooling medium. The oil is pumped by an external oil pump out of the oil sump and heated by a 4 kW oil heater; the heated oil is sent to the cylinder head and cylinder block in both original oil channels and cooling channels to provide lubricating and cooling. The original internal oil pump feeds the oil to the camshaft journals to lubricate the camshafts. The schematic of the oil path is shown in Figure 3-6.

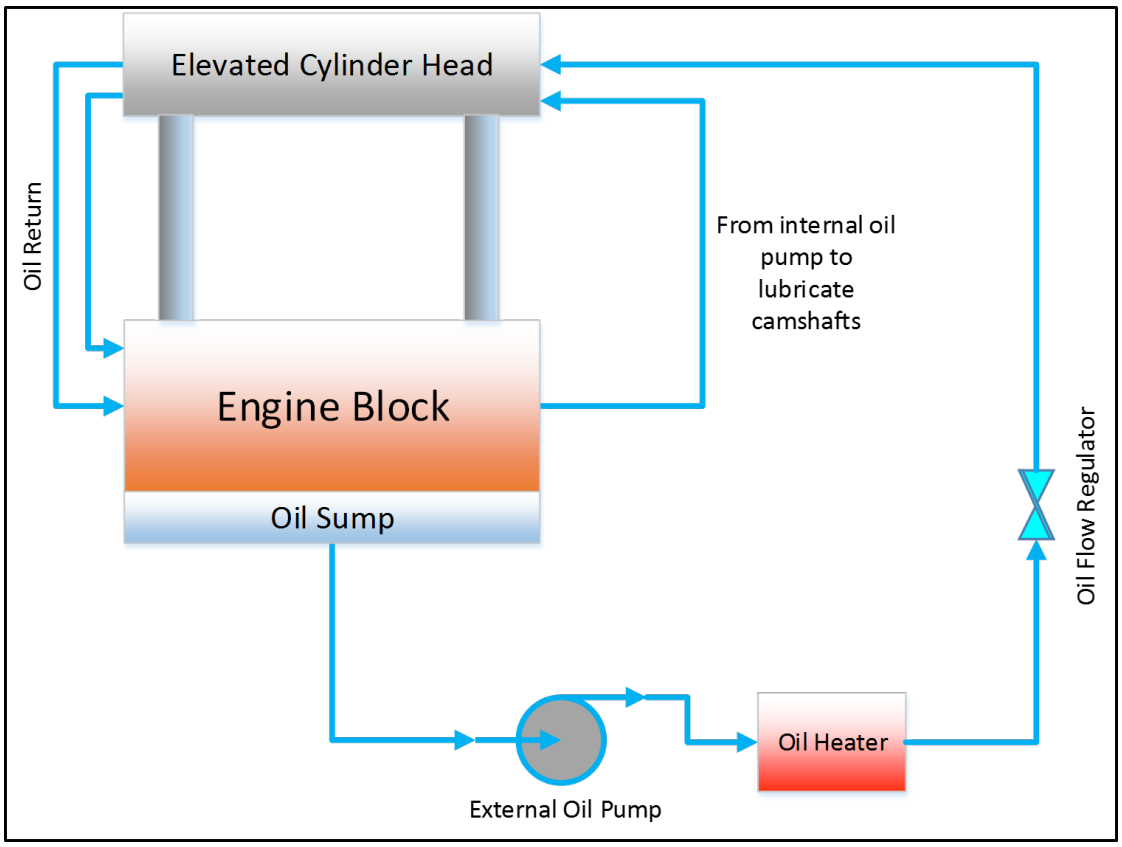

Figure 3-6: Schematic of oil flow path.

3.1.3 Encoder

The optical engine is operated with a 62 – 2 tooth crank position wheel and a hall-effect sensor sending crank position signal based on which the engine control unit (ECU) functions. The ECU is capable of interpolating the crank angle signal to 1/12th degree for higher precision control. For high-speed in-cylinder pressure measurement and analysis,

the crank position is measure by a 0.5° resolution optical encoder, based on which the combustion analyzer ACAP samples data. The TDC of the optical engine is found using a TDC probe with an aluminum piston fabricated into the identical shape as the optical piston.

3.1.4 In-cylinder Pressure Sensor

The in-cylinder pressure is measured by a PCB115A (SN: 700) piezoelectric pressure transducer coupled with a flame arrestor to reduce the thermal shock. A mounting port is fabricated in to the cylinder head between one of the intake valves and one of the exhaust values approximately 32 mm away from the spark-plug axis. The charge signal from the piezoelectric pressure transducer is amplified and converted to voltage signal by an ACAP charge amplifier and recorded by ACAP. The specifications of the in-cylinder pressure transducer can be found in the appendix 12.7.

3.1.5 Ignition System

The ignition system is composed of ignition coils, the spark plug and electronic spark timing (EST) signals. The configuration varies depending on whether smart or dumb coils are being used.

For smart ignition coils, the EST signal from the ECU is sent to the coil directly (Figure 3-7).

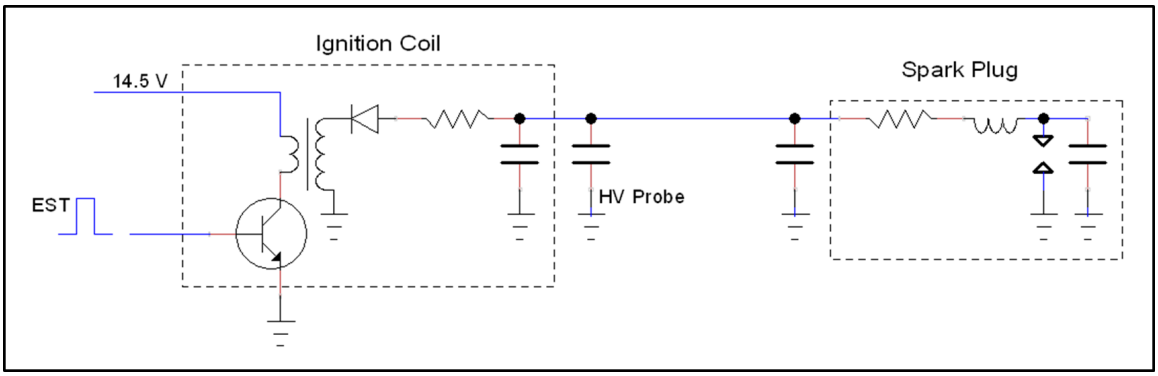

Figure 3-7: Wiring schematic of the smart ignition coil.

Dumb ignition coils are used for all tests conducted in this research. The dumb coils are fabricated with access to the low side of the secondary circuit, which allows measurement of the secondary discharge energy. The dumb coils are driven by an external ignition driver. The wiring schematic is shown in Figure 3-8.

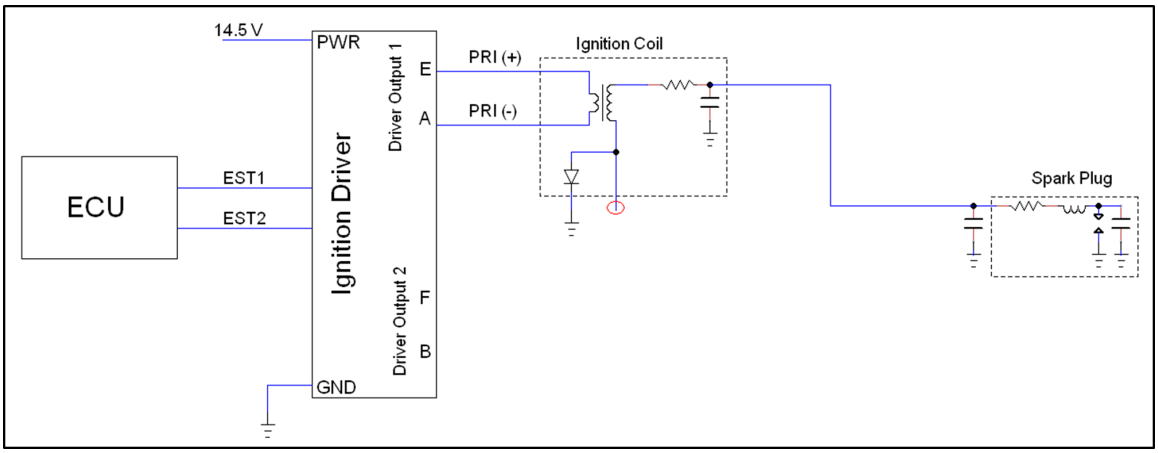

Figure 3-8: Wiring schematic of single dumb ignition coil.

Two EST channels are programmed into the engine control unit to enable dual-coil ignition discharge. When the dual-coil ignition system is required, the two coils are connected to the spark plug through a diode pack preventing cross-talking between coils. Figure 3-9 depicts the schematic of the dual-coil ignition system.

The ignition control will be further described in section 3.2.2.

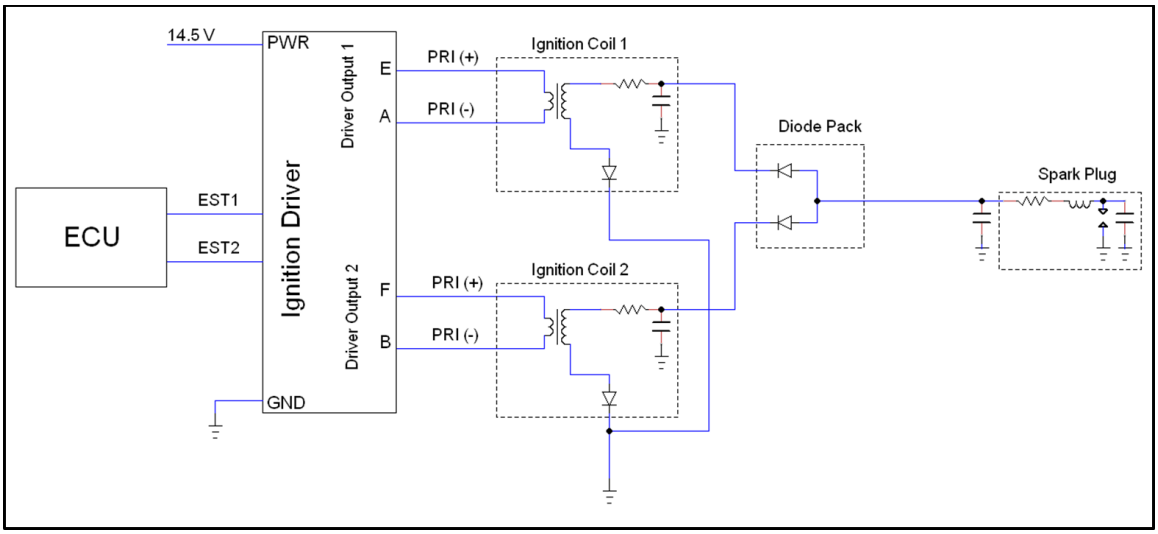

Figure 3-9: Wiring schematic of dual dumb ignition coil.

3.1.6 Fuel Delivery and Injection

The gasoline of anti-knock index (AKI) 87 is stored in a movable fuel cart equipped with a low pressure fuel pump. The low pressure fuel pump pressurizes the fuel to 60 psi and delivers it to an external high pressure fuel pump driven by an electric motor, which then pressurizes the fuel to the required rail pressure ranging from 2 MPa to 10 MPa. The high pressure is controlled by the pulse width modulation (PWM) signal generated from the ECU via the PID control logic using the fuel rail pressure as the feedback. A GDI injector is mounted on the side of the cylinder below and between the intake valves. The low-impedance GDI injector is driven by an external GDI driver in peak and hold current mode. The injection pin is programmed to be capable of dual injections. The triggering of injection will be further discussed in section 3.2.3.

3.2 Engine Control Unit (ECU)

The optical engine is controlled by a 112-pin Mototron prototype engine control unit of model ECM-0554-112-0904-C. The operation of the ECU is synchronized with the 62-2 crank position wheel and the hall-effect sensor. The control strategy of the optical engine is programmed in Simulink with the Motohawk library, and then it is auto-coded and

written into the ECU. The main functionalities of the ECU consist of skip-firing, ignition, injection, and synchronization with other data acquisition systems. Each of these functionalities will be described in detail in this section.

3.2.1 Skip Firing

Skip firing means the optical engine has to be fired intermittently to protect the self-lubricating torlon piston rings. To achieve skip firing, the number of cycles starting from enabling of the ignition and injection has to be known by the ECU. This is realized by a cycle counting function module which is triggered once per cycle as illustrated in Figure 3-10. Pre-determined number of cycles in each firing groups (n_cycle_group), number of fired cycles in each firing group (n_fired_cycle) and number of total cycles (n_cycle_total) are input to the control interface. Once the cycle counting function is enabled, it starts counting cycles and sends out an 'actuator enabler' boolean signal of value 1 (fired mode). When the number of past cycles is greater than the predetermined number of fired cycles in each firing group, the 'actuator enabler' will be set to 0 (motored mode). When the number of past cycles reaches the starting cycle of next firing group, namely, exceeds the number of cycles per group (n_cycle_group), the 'group_cycle_counter' will be reset to 1; at the same time, the 'actuator enabler' will be set to 1 again. When the number of past cycles reaches the predetermined number of total cycles (n_cycle_total), the 'actuator enable' will be set to 0 and the skip-firing operation is completed until next time the cycle counting function is activated in the control interface.

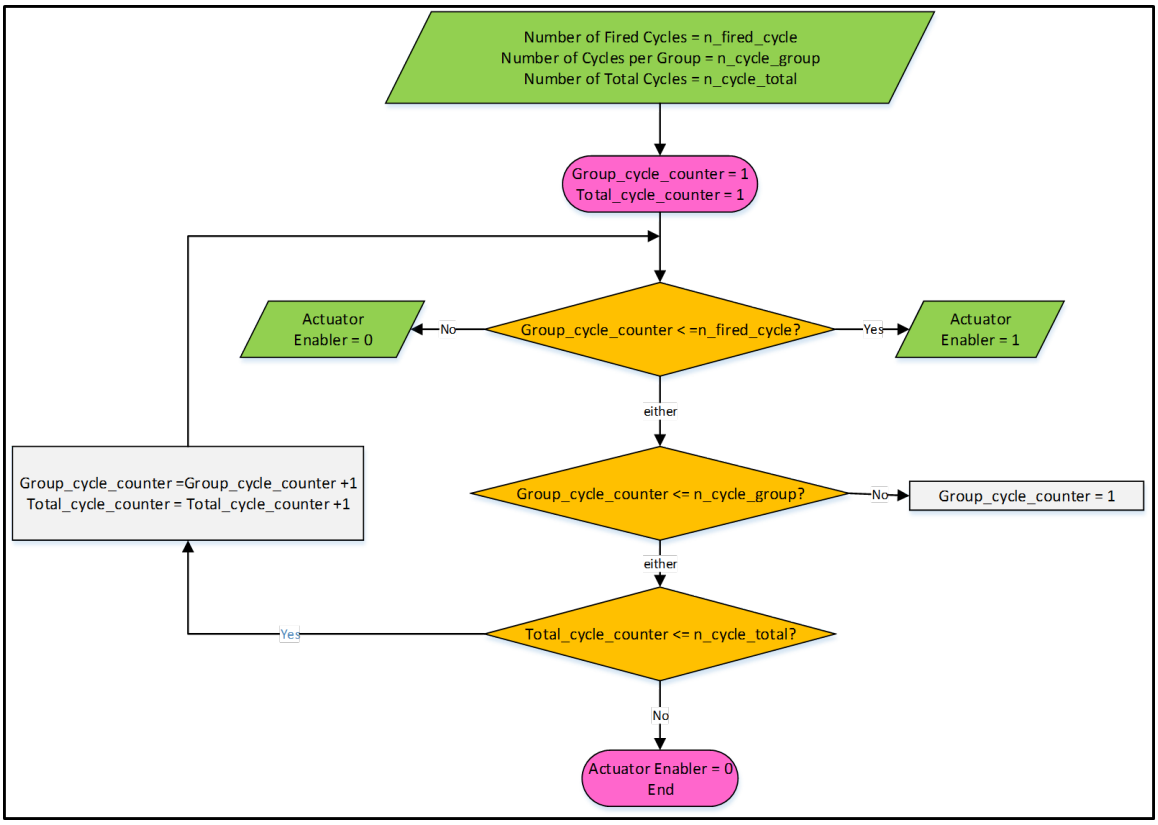

Figure 3-10: Flow chart of skip-fire strategy.

The 'actuator enabler' Boolean signal from the cycle counting function is received by the ignition, injection and other actuator modules. Combined through 'AND' gates with their own 'enabler' signals, the ignition, injection and other actuator modules will be either activated (fired mode) or de-activated (motored mode).

3.2.2 Ignition Driver

Two EST pins are programmed to generate the ignition dwell signals. They will be referred to as EST_1 and EST_2. Each of these two EST signals can be disabled and enabled depending on the engine testing requirements.

The spark timing is controlled at the falling edge of the EST signal, i.e. the breakdown timing (Figure 3-11). The dwell time is calibratable on the control interface and is

converted to crank angle degrees based on the current engine speed. The EST_2 falling edge timing is defined as an offset from the falling edge of the EST_1.

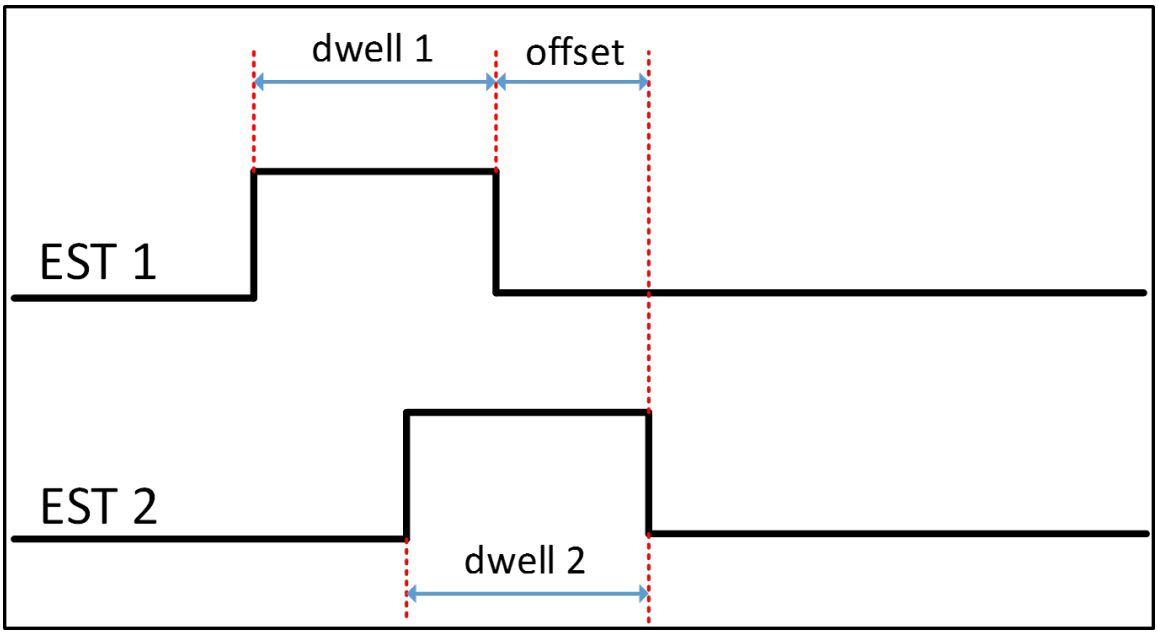

Figure 3-11: Schematic of spark timing control.

3.2.3 Injection Driver

The injection driver in this particular ECU can only drive high-impedance PFI injectors directly. An external GDI driver is required if GDI injectors are to be used. An external Bosch GDI driver (model: ES-HDEV-1) is used to drive the GDI injector on the optical engine. The external driver receives the injection pulse width command from the ECU, and outputs a peak and hold current (approximately 6 A peak and 4 A hold) to the GDI injector solenoid to quickly open the injector pintle with the high current and maintain the opening position of the injector pintle with the lower current. The injection pin from the ECU is programmed to be able to switch between single injection and dual injection modes.

3.2.4 Synchronization Triggers

Multiple data acquisition systems are required to synchronize with the optical engine operation in crank angle positions to obtain meaningful data. The control strategy currently has synchronization triggers for the following DAQ systems.

- High-sampling-rate ignition measurement system (NI-PXI).
- High-speed camera.
- PIV laser/camera system.

The synchronization triggers are programmed through EST pins. The trigger pulse duration is set constant for 1ms, and all the above DAQ systems are triggered at the rising edge of the trigger pulse. The trigger crank angle can be adjusted based on test requirements on the Mototune control interface during testing.

The ignition measurement system and PIV system each utilizes one EST pin for the synchronization trigger signal. For the high speed camera, two EST pins are programmed and wired through a 0-5 V 'OR' gate to realize dual imaging triggers per cycle. This is particularly useful when both the injection event and ignition event need to be imaged.

The AC dynamometer in the test cell generates high current during operation, and it poses electrical noise to all DAQ systems. The electrical noise sometimes can act as false triggers, leading the DAQ systems to record extra data than the amount that is commanded. The false triggers can confuse the synchronization and need to be identified. The identification of false triggers will be discussed in the methodology section for each of the DAQ systems.

3.3 Data Acquisition Systems

3.3.1 Combustion Analyzer

The ACAP system is used for acquiring crank angle based data. The ACAP is operated in synchronization with a BEI 0.5°CA resolution optical encoder (model number: XH20DB-

37-SS-720-ABZC-28V/V-SM18). The signal input to the ACAP is summarized in Table 3-4. The sampled pressure signal is post-processed with custom Matlab codes. The data processing will be discussed in chapter 4.1 in detail.

Table 3-4: Signal input to the combustion analyzer ACAP.

Sensors and Signals	Sensor Make	Model Number	Specifications
Encoder	BEI	XH20DB-37-SS-720-ABZC-28V/V-SM18	0.5°CA resolution
In-cylinder Pressure Transducer	PCB	115A04 SN: 700	0.2036 pC/kPa
Manifold Pressure Sensor	Omega	PX209-030A5V	5.99 psia/v
Lambda Sensor	Bosch Wideband Lambda Sensor		
	Innovate Motorsports Lambda Sensor Controller	LC-1	0 - 5 V for AFR 7.35 - 22.39
Ignition EST			0-5 V TTL signal from ECU

3.3.2 High-Sampling-Rate Ignition Measurement System

A NI-PXI data acquisition system of maximum sampling rate of 10 MHz is instrumented to measure the secondary voltage and current of the ignition. A T-shape high tension lead connects the ignition coil and the spark plug through the diode pack (Figure 3-12). The T-

shape high tension lead provides measurement access to the secondary voltage, which is measured by a Tektronix P6015A high voltage probe. Two current probes (Pearson 6595) are placed on the immediate upstream of the spark plug (high side) and on the ground cable of the secondary circuit of the coils (low side). During ignition discharge, the current measured on the low side accounts for the parasitic capacitance of the secondary coil, and thus it is used to calculate the breakdown and arc energy. The current measured on the high side is used to calculate the glow phase energy.

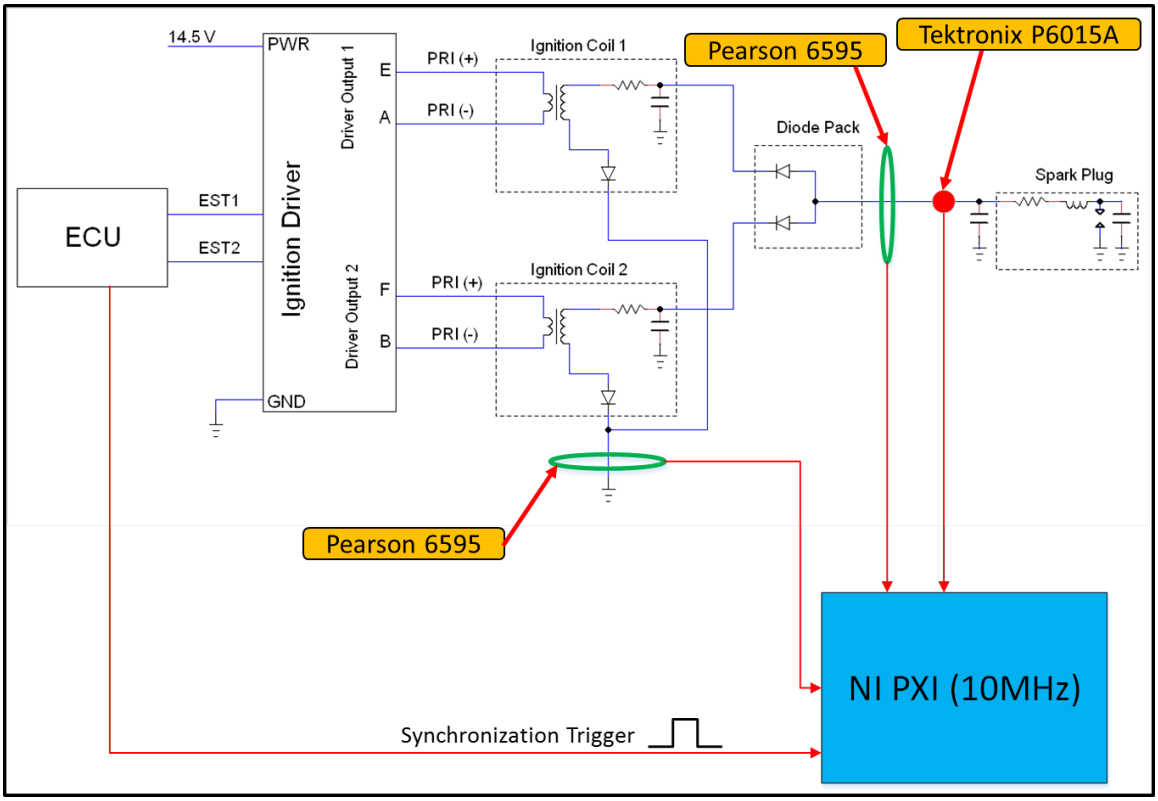

Figure 3-12: Schematic of high-speed sampling rate ignition measurement system.

The PXI system starts sampling the ignition voltage and current at the rising edge of the incoming synchronization trigger signal. The synchronization trigger is sent from an EST pin of the ECU as introduced previously. The timing of the trigger is commonly set at 1ms before the breakdown, i.e. 1 ms before the end of dwell.

3.3.3 High-Speed Camera

The combustion process including the spark arc channel initiation, early flame kernel formation and flame kernel propagation is captured by the Photron SA1.1 high-speed camera. The high-speed camera needs to be placed as close to the firing cylinder as possible to capture enough photons from the combustion chamber and concurrently kept at a safe distance from the moving parts of the engine. A camera bridge is assembled and it straddles across the optical engine cart on the front end of the engine. The high-speed camera is mounted on an x-y translation stage which is bolted in the middle section of the bridge Figure 3-13. The x-y translation stage allows fine-resolution adjustment of the imaging plane. The high-speed camera is positioned in an orientation such that it images the tumble plane through the quartz liner.

The synchronization trigger for the high-speed camera is sent from two EST pins combined by an external 'OR' gate. The trigger can be set as a single trigger or dual triggers on the Mototune interface. The dual triggers enable the high-speed camera to image both the injection event and the combustion event.

3.3.4 PIV Laser/Camera

A Quantel TSI CFR200 Nd:YAG laser PIV (Figure 3-13) system is used for the PIV flow field measurement tests. The specifications of the PIV laser/camera system is summarized in Table 3-5.

Table 3-5: Specifications of the PIV system.

Laser	Nd:YAG
Model Number	CFR 200
Rep Rate (Hz)	15
Wavelength (nm)	532
Pulse Energy (mJ/pulse)	115 × 2
Max Pulse Energy (mJ/pulse)	190 × 2
Laser Pulse Width (ns)	7
Beam Diameter (ms)	6.35

The laser head is calibrated to emit pulses of 532 nm wave length laser with 116 mJ/pulse energy at configurable pulse interval. The laser beam is expanded vertically by a 50 mm cylindrical lens and then focused by a 1000 mm convex lens to form a laser sheet of approximately 1mm width near the spark plug. The laser is reflected through the 45° mirror upwards into the cylinder though the optical piston window. The resolution of the PIV camera is 1600 × 1192 pixels imaging the vicinity of the spark plug through a 200 mm lens. The laser head and accessory optics are set on an optical table (Figure 3-13). During testing, the PIV camera is placed on the x-y translation stage pointing to the tumble plane, and the optical table is placed by the side of the optical engine such that the laser shoots towards the 45° mirror below the optical piston.

Silicone oil of 50 cst. viscosity is atomized by compressed air through a Laskin nozzle particle generator. The silicone seeding is fed into the intake manifold 24 cm upstream of the intake ports such that it has sufficient time to distribute evenly in the intake charge.

The captured image pairs are segregated into 32 × 32 pixel interrogation windows and cross-correlated to obtain the velocity vectors. The velocity field is then validated and the spurious vectors are replaced by the local mean values.

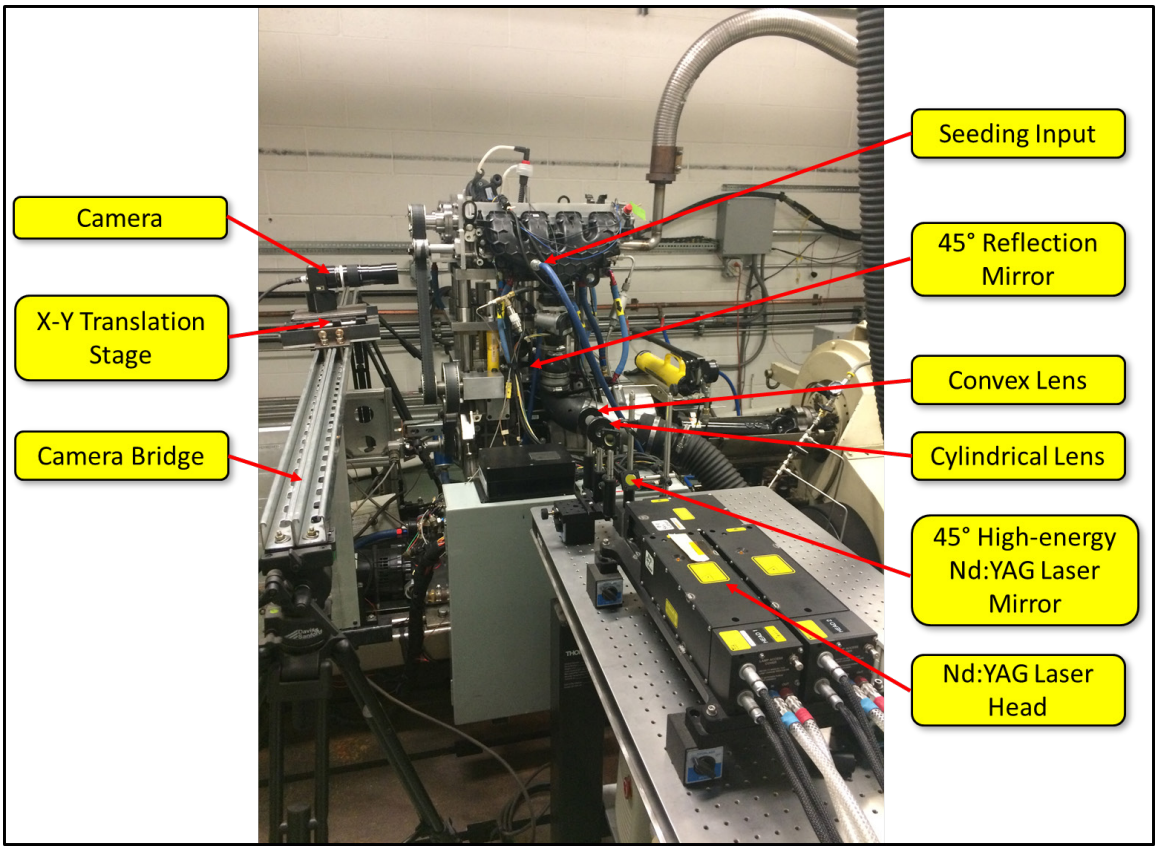

Figure 3-13: Camera bridge and PIV system setup.

4 Methodology

In this section, methods of processing the data collected from each data acquisition system will be discussed. All data analysis is conducted with custom Matlab codes. The discussion will begin with the combustion analysis, followed by calculation of the ignition metrics. The image processing methods for the high-speed camera images and PIV images will be discussed lastly.

4.1 Combustion Analysis

The optical engine differs from the production metal engine from perspectives of cylinder and piston material, intake and exhaust pipe configuration, and etc. Hence general engine performance characteristics (e.g. BSFC, BMEP, EGT, and etc.) are of less interest compared with the metrics describing the in-cylinder conditions; these include the IMEP, MFB, CA50 and etc. Definitions and calculations of these metrics of interest will be provided in this section.

4.1.1 Fired Cycle Identification

As introduced previously, the optical engine is skip-fired for 5 firing groups of 10 fired cycles and 15 motored cycles for the majority of the tests as illustrated in the sample IMEP plot in Figure 4-1. The fired cycles need to be identified and averaged combustion metrics should only be calculated from the fired cycles. Spark EST signals are used to mark the indices of the fired cycles as shown in Figure 4-2. The resulting total number of fired cycles is checked against the pre-determined total number of fired cycles. Any mismatch indicates synchronization errors, which require further false trigger identification before comparing the combustion results with results from other DAQ systems.

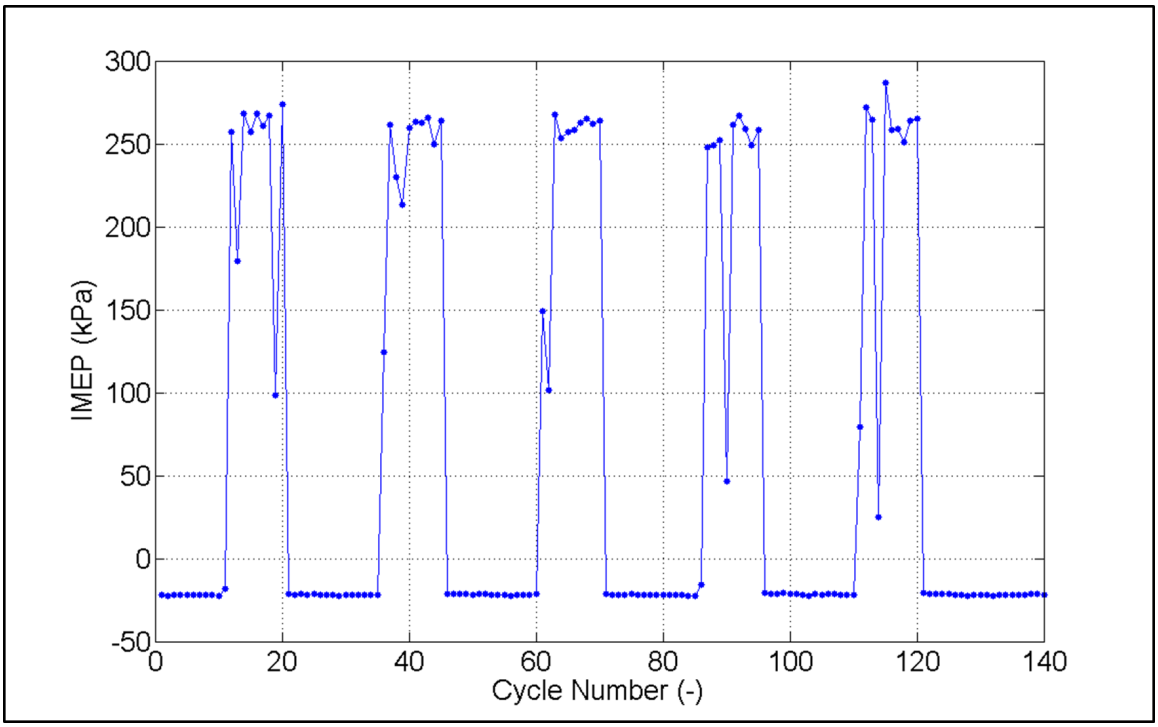

Figure 4-1: Sample IMEP plot for skip-firing strategy (5 firing groups of 10 fired cycles/15 motored cycles).

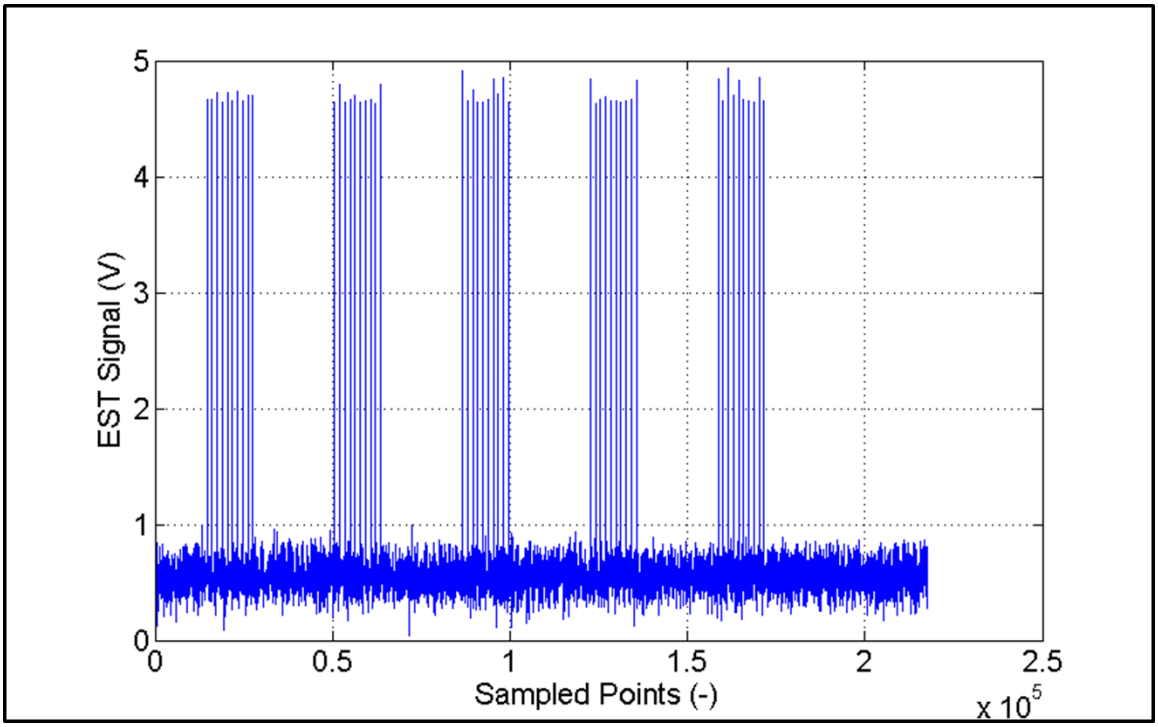

Figure 4-2: EST signal as fired cycle indicators.

4.1.2 Pre-Processing Raw Signals

The in-cylinder pressure signal sampled at 0.5°CA resolution is first filtered by a 3rd order Butterworth filter with 0.1 normalized cut-off frequency, and then interpolated to a finer resolution of 0.1°CA. The original 0.5°CA resolution crank angle signal and instantaneous cylinder volume data are also interpolated into 0.1°CA resolution. The following heat release and mass fraction burned data are calculated from the filtered and interpolated signals.

4.1.3 Gross Indicated Mean Effective Pressure (IMEP)

$$IMEP_{gross} = \frac{\int_{start\ of\ compression}^{end\ of\ expansion} PdV}{V_{displaced}}$$

4-1

To maintain consistency, the gross IMEP will be simply referred to as IMEP in the remainder of this dissertation.

In the above equation 4-1, $P\ and\ V$ represents the in-cylinder pressure and cylinder volume, and $V_{displaced}$ represents displacement volume of the engine.

Due to the differences in engine accessory configurations between the production engine and the optical engine, same BMEP might result from different induced air flow rate and thus different amount of injected fuel. Therefore, IMEP will be analyzed instead since it describes the conditions inside the cylinder.

4.1.4 Heat Release and Mass Fraction Burned (MFB)

The heat release rate is calculated with equation 4-2 based on the 0-D combustion model developed from the conservation of energy.

$$\frac{dQ_{ch}}{d\theta} = \frac{\gamma}{1-\gamma} P \frac{dV}{d\theta} + \frac{1}{\gamma - 1} V \frac{dP}{d\theta}$$

4-2

Where Q_{ch} represents the chemical energy released from the fuel; γ is the specific heat ratio of the fuel/air mixture; P is the in-cylinder pressure and V represents the cylinder volume. Integrating equation 4-2 gives the following equation to obtain the chemical energy release history versus crank angle as in equation 4-3.

$$Q_{ch} = \frac{\gamma}{1-\gamma}\int_{combustion\ window\ start}^{crank\ angle\ untill\ combustion\ window\ end} PdV + \frac{1}{\gamma-1}\int_{combustion\ window\ start}^{crank\ angle\ untill\ combustion\ window\ end} VdP$$

4-3

The above equation (equation 4-3) is integrated over the combustion period starting from the combustion window start point which is set at the spark timing, and ends at combustion window end point which is set at 150°ATDC. This window length is long enough to account for slow burn cycles at conditions as lean as λ = 1.4.

Once the chemical energy release is calculated for each cycle. The energy release trace versus crank angle can be normalized with the total energy release to obtain the mass fraction burned. However, if the combustion is too slow in some cases, the injected fuel might not be combusted completely (partial-burn cycles), and for these cycles, the chemical energy should not be normalized with their respective maximum energy release. The methods to determine partial-burn cycles and to calculate their MFB curves will be discussed as follows.

The cyclic total chemical energy higher than or equal to the 50th percentile cyclic chemical energy release is averaged and 80% of this averaged value is used as the reference total chemical energy release (equation 4-4).

$$Q_{ref} = 0.8 \times \overline{Q_{ch,k}}$$

4-4

Where k is the index of the cycles whose total chemical energy release is greater than or equal to 50th percentile cyclic total chemical energy release value. Cycles whose total chemical energy release is higher than or equal to Q_{ref} are treated as well-burn cycles

(equation 4-5), and their MFB curves are calculated by normalizing the chemical energy release trace with the total chemical energy of each cycle as in equation 4-6.

$$Cycle_{well\_burn} \stackrel{\text{def}}{=} \{cycles | Q_{ch,total} \geq Q_{ref}\} \quad 4\text{-}5$$

$$MFB_{well\_burn} = \frac{Q_{ch,cycle_{well\_burn}}}{Q_{ch,total,cycle_{well\_burn}}} \quad 4\text{-}6$$

Cycles whose total chemical energy release is lower than Q_{ref} are treated as partial burn cycles (equation 4-7), and their MFB curves are calculated by normalizing the chemical energy release trace with $\overline{Q_{ch,k}}$ (equation 4-8).

$$Cycle_{partial\_burn} \stackrel{\text{def}}{=} \{cycles | Q_{ch,total} < Q_{ref}\} \quad 4\text{-}7$$

$$MFB_{partial\_burn} = \frac{Q_{ch,cycle_{partial\_burn}}}{\overline{Q_{ch,k}}} \quad 4\text{-}8$$

A sample cyclic total heat release is shown in Figure 4-3, where the red horizontal line is the reference total heat release. The cycles having total heat release higher than the reference are considered well-burn cycles, and the cycle having total heat release lower than the reference are considered partial-burn cycles.

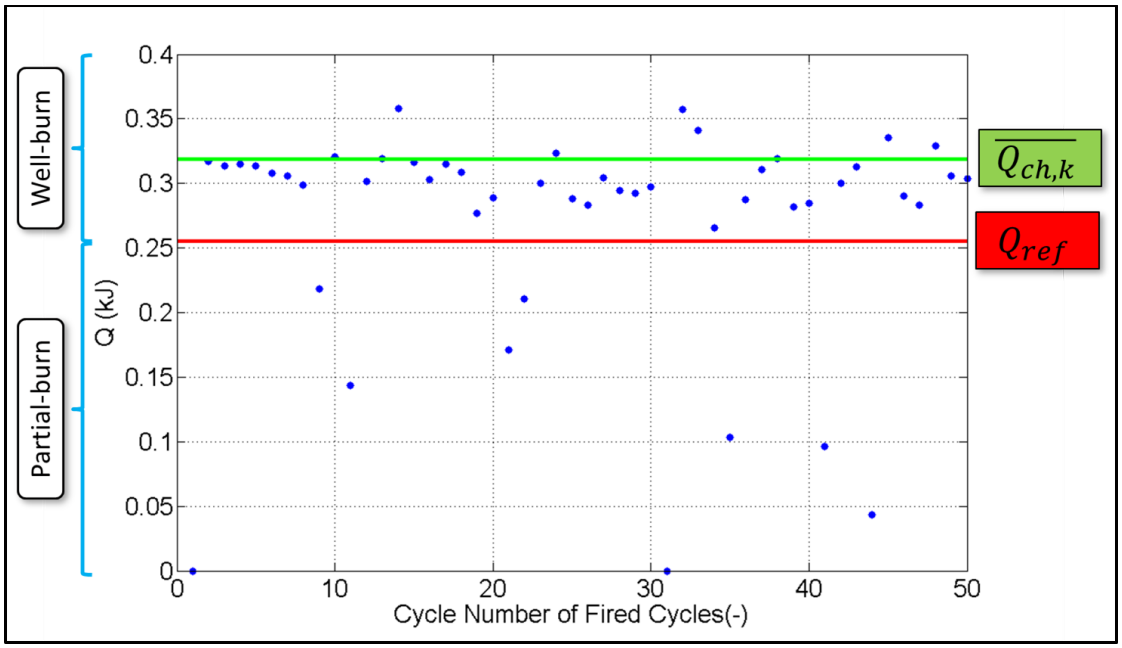

Figure 4-3: Cyclic total heat release for the fired cycles.

A sample figure of MFB traces is shown in Figure 4-4. It is clear that the MFB of partial burn cycles never reach 100%.

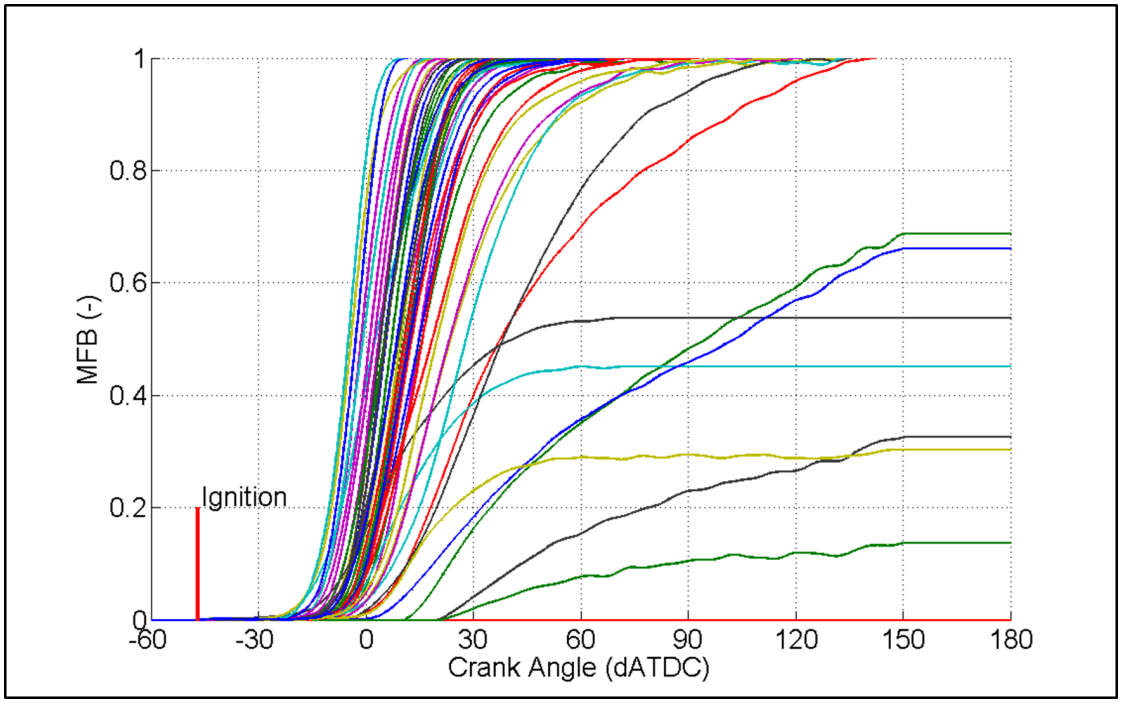

Figure 4-4: Cyclic mass fraction burned curves.

With MFB data obtained by the above calculations, combustion metrics such as ignition delay, CA50 and bulk burn (CA1090) can be conveniently determined from the MFB vs crank angle traces as follows (equation 4-9 through 4-11).

$$CA0010 = CA_{MFB=10\%} - CA_{spark} \quad 4\text{-}9$$

$$CA50 = CA_{MFB=50\%} \quad 4\text{-}10$$

$$CA1090 = CA_{MFB=90\%} - CA_{MFB=10\%} \quad 4\text{-}11$$

4.2 Ignition Metrics

The ignition metrics calculated from the secondary ignition voltage and current include breakdown + arc energy, glow phase energy, and discharge duration. With high in-cylinder flow motion, re-strikes of the discharge may occur when the voltage requirement to form a new discharge channel is lower than the voltage requirement to maintain the existing discharge channel. The number of re-strikes can be estimated from the secondary voltage trace. In this section, the calculation methods for the ignition metrics are discussed.

4.2.1 Synchronization Verification

The sampled ignition data requires synchronization verification before being post-processing. The number of sampled ignition events must match the total number of fired cycles to guarantee synchronization. The verification is done immediately after each set of data is taken, if synchronization error occurs, the test point needs to be repeated.

4.2.2 Zeroing Raw Signal

The ignition measurement is commonly triggered at 1 ms before the breakdown, which covers 10,000 sampled points. For both raw secondary voltage and current signals, the

mean value of the first 8,000 sampled points is subtracted from the entire signal trace for each ignition events (equation 4-12), i.e. zeroing the signals.

$$i_{zeroed} = i_{raw} - \frac{1}{8000}\sum_{k=1}^{8000} i_{raw}[k] \quad \text{4-12}$$

In the above equation, i_{raw} is the raw current signal and i_{zeroed} is the current signal after being zeroed.

4.2.3 Compensation for AC-Coupling Effect and Signal Filtering

As introduced previously, the secondary ignition current is measured by two Pearson 6595 current probes. The bandwidth of this particular probe has a high cut-off frequency of 150 MHz which is suitable for measuring highly dynamic signals. However, the 3 dB roll-off frequency on the lower end of the bandwidth filter of this probe is as high as 100 Hz, resulting in an AC-coupling effect. On the example plot of the secondary current (blue on Figure 4-5), the current gradually drops below zero near the end of the discharge due to this AC coupling of the signal. This is compensated for by the cumulative summation of the current trace weighted by a factor to the current trace (equation 4-13 and 4-14).

$$i_{offset}[k] = \alpha \sum_{k=1}^{N} i_{zeroed}[k] \quad \text{4-13}$$

$$i_{correct} = i_{zeroed} + i_{offset} \quad \text{4-14}$$

In the above equations, $i_{offset}[k]$ is the weighted cumulative summation value at point k to be added to the zeroed current trace; α is the weight coefficient and its value depends on the sampling rate of the DAQ system and i_{zeroed} is the zeroed current trace; $i_{correct}$ is the

corrected current signal. The sample signal after compensation for the AC-coupling effect is shown in red in Figure 4-5.

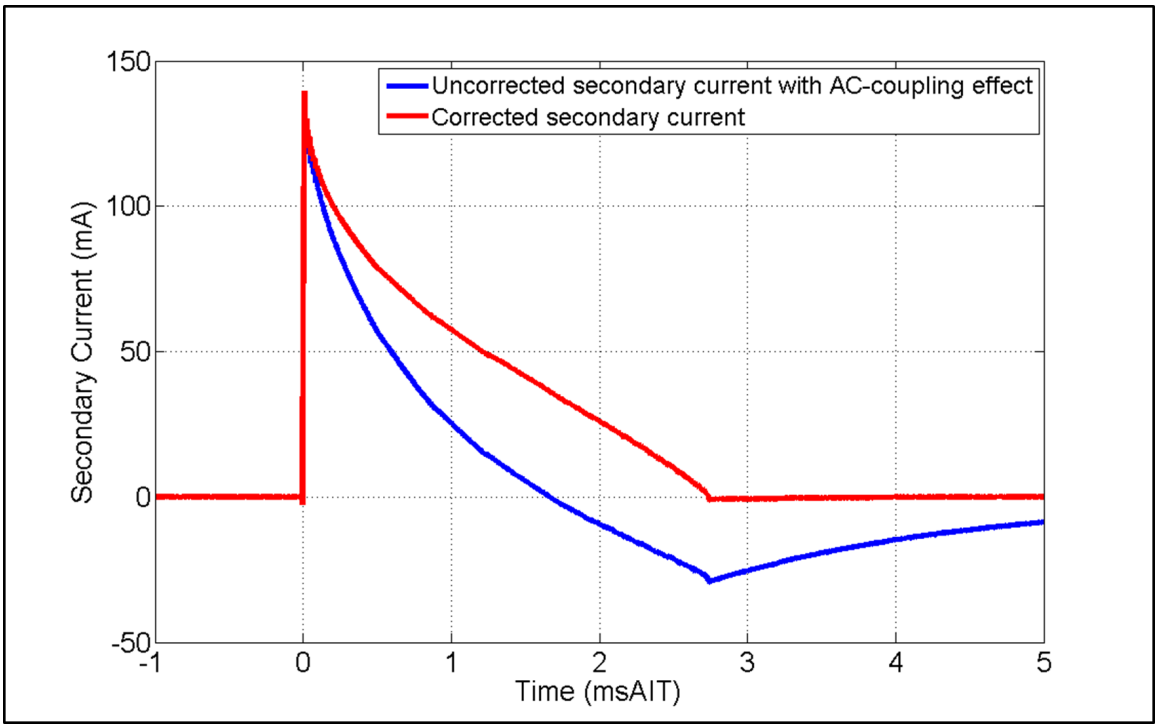

Figure 4-5: uncorrected secondary current with the AC-coupling effect and corrected secondary current.

The corrected signal is then filtered forward and backward with a 4th order Butterworth filter with 0.025 normalized cutoff frequency for glow phase energy calculation.

4.2.4 Breakdown + Arc Energy

At the end of the dwell for the primary coil, the primary circuit breaks open such that the magnetic field formed in the coil collapses and the voltage across the secondary coil rapidly rises to a point that the flux density of the ionized particles between the electrodes increases exponentially to form conductive paths between the electrodes. The exponential increase in current to eventually forming the spark channel is referred to as breakdown, and it only takes a few nanoseconds [44]. The rising voltage in the secondary coil charges the spark plug gap and parasitic capacitance of the secondary circuit from the end point of dwell to

the breakdown, and this period is referred to as pre-breakdown phase. The energy stored in the spark-gap capacitance and secondary circuit parasitic capacitance is assumed to be released in the breakdown phase and the arc phase. It can be calculated with equation 4-15 and 4-16.

$$E_{bd+arc} = \frac{1}{2} C_{sec} V_{bd}^2$$

4-15

$$C_{sec} = \frac{\int_{dwell\_end}^{breakdown\ point} i_{correct} dt}{V_{bd}}$$

4-16

In the above equations, V_{bd} is the breakdown voltage; C_{sec} is the secondary circuit capacitance including the spark plug gap capacitance and the parasitic capacitance; and $i_{correct}$ is the low-side secondary current after compensation for the AC-coupling effect without filtering.

4.2.5 Glow Phase Energy

After the energy stored in the secondary circuit capacitance is released in the breakdown + arc phase, the remaining energy stored in the magnetic field continues to be released in the glow phase. The energy released in the glow phase can be calculated by integrating the secondary voltage multiplied by the secondary current over time subtracting the resistive loss over the internal resistance of the spark plug as in equation 4-17.

$$E_{glow} = \int_{end\ of\ breakdown}^{end\ of\ discharge} v i_{correct\_filt} dt - \int_{end\ of\ breakdown}^{end\ of\ discharge} i_{correct\_filt}^2 R_{sp} dt$$

4-17

In equation 4-17, E_{glow} is the glow phase energy; v is the secondary voltage; $i_{correct\_filt}$ is the filtered secondary current measured on the high side of the secondary circuit with the AC-coupling effect compensated and R_{sp} is the internal resistance of the spark plug. The integration is performed from the end of the breakdown to the end of the discharge.

A sample plot of cyclic ignition gap energy release traces of 20 ignition events is shown in Figure 4-6. The x-axis marks the timing in milliseconds after ignition timing (msAIT). In this particular sample, the average breakdown + arc energy is 1.1 mJ and the average total gap energy is 78.3 mJ.

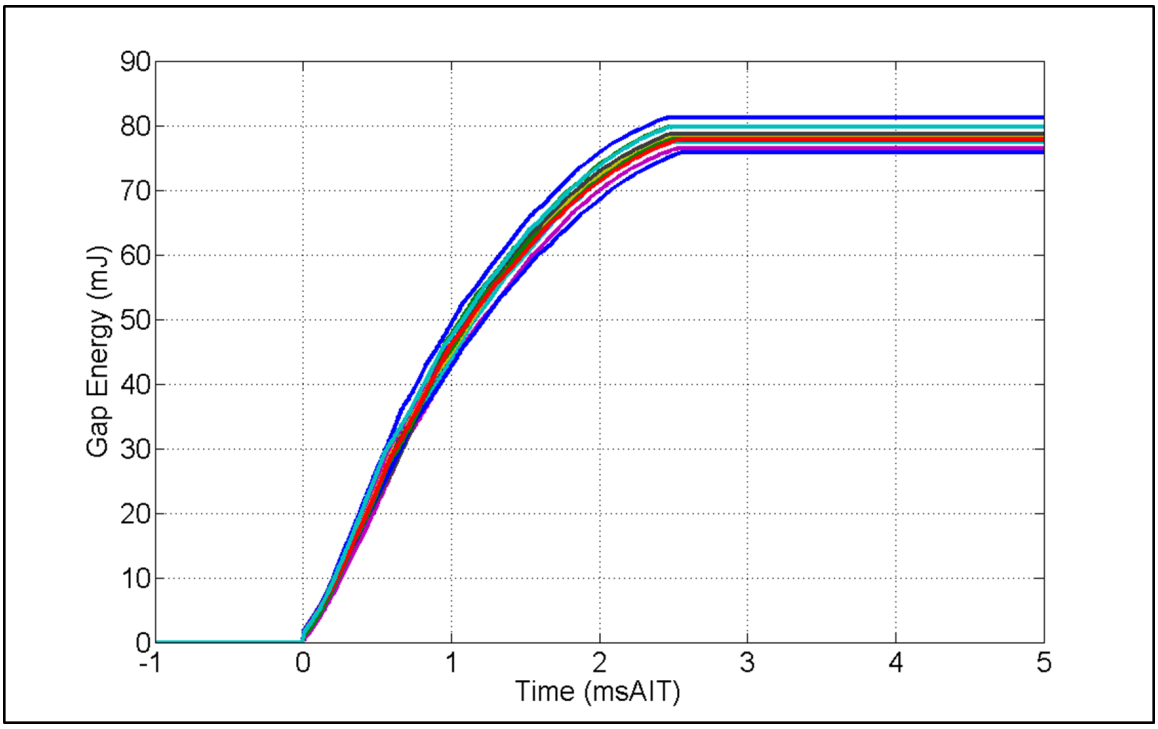

Figure 4-6: Ignition gap energy (1.1 mJ average breakdown + arc energy, 78.3 mJ average total gap energy).

4.3 Image Processing for the High-Speed Camera

The high-speed images captured by the Photron SA1.1 camera are 12-bit grayscale images. The original uint-format images are converted to double precision format for post-processing.

Among all the DAQ systems, the high speed camera is most sensitive to the false triggers. The number of frames recorded per trigger is configurable for the high-speed camera. The method to determine if there is any false trigger registered is simply comparing the total number of recorded frames to the product of the number of frames commanded per trigger

and number of commanded fired cycles. If false triggers exist, a custom Matlab program selects the one frame after spark discharge for all triggered events. The maximum pixel intensity of these frames is analyzed. For real ignition events, due to the higher luminosity of the spark, the maximum pixel value of this particular frame is very high and frequently saturates the camera sensor. However, for false triggers, the maximum value is very low. Next, the indices of real triggered events are marked and passed to the image processing codes so that only the real triggered events go through further analysis.

4.3.1 Flame Kernel Characterization

The high-speed camera is positioned towards the tumble plane, and thus what is captured is the projected flame area. The flame kernel boundary is detected by thresholding the pixel intensity (Figure 4-7). The thresholding value varies based on the test conditions. For instance, when the charge mixture is lean, the combustion luminosity of the flame is low so the thresholding value is set at a low value; when the mixture is stoichiometric or rich, the combustion luminosity of the flame is high, and the thresholding value should also be set high.

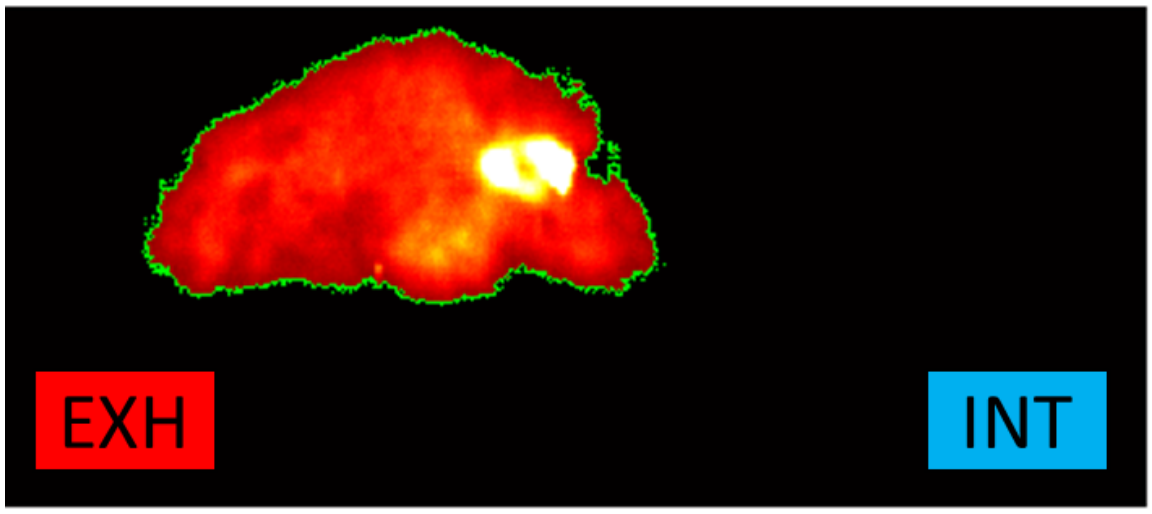

Figure 4-7: Sample flame kernel detection with boundary traced in green and flame false color coded.

After the flame kernel boundary is traced, the image is converted to binary format with the flame kernel area being white and the rest of the image being black (Figure 4-8). The geometric centroid and the projected area of the flame kernel can be conveniently calculated with Matlab regionprops function. The projected flame boundary length can be obtained by counting the number of pixels on the traced boundary. All the flame kernel characteristics are converted from the dimension of pixel to physical dimension by applying the scale factor.

Figure 4-8: The black white image of the detected flame kernel.

4.3.2 Spark Arc Channel Characteristics

The method for calculating the spark arc channel characteristics is the same as calculating for flame kernel characteristics, with the exception that the pixel intensity threshold is increased to a level that only the spark arc channel is selected.

4.3.3 2D Probability Distribution Function (2D-PDF)

The 2D-PDF shows the probability of the flame kernel reaching a certain point in the 2D space captured by the camera (equation 4-18).

$$PDF_{2D,t} = \frac{\sum_{i=1}^{n} I_{t,i} \begin{cases} I_{t,i} = 1, \ I_{t,i} > threshold \\ I_{t,i} = 0, \ I_{t,i} < threshold \end{cases}}{n}$$

4-18

In equation 4-18, I denotes the image intensity matrix; t is the timing of the current processed image in the i'th cycle, either in milliseconds after ignition timing (msAIT) or crank angle degrees after ignition timing (°CA_AIT); i represents which cycle the current processed image is from, and n is the total number of cycles.

The illustration of how 2D-PDF is calculated is shown in Figure 4-9.

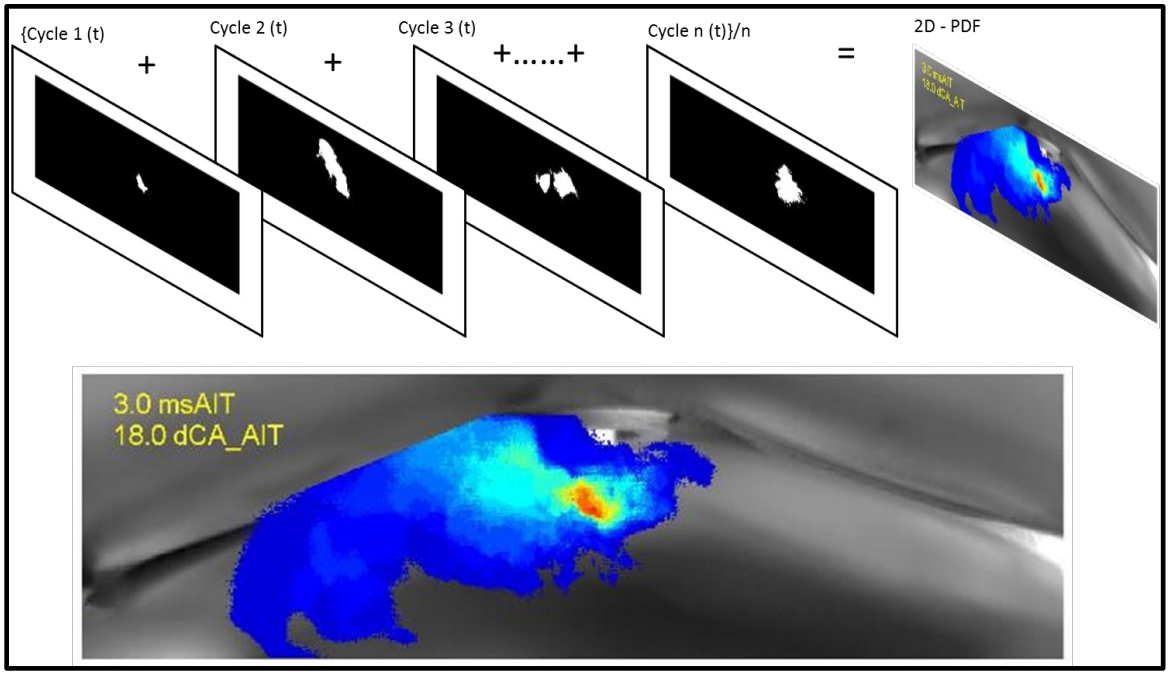

Figure 4-9: Illustration of 2D-PDF.

4.3.4 1D Probability Distribution Function (1D-PDF)

Though the 2D-PDF provides a complete picture of the spatial probability of the flame kernel propagation, it is not straightforward to compare between cases. The 1D-PDF on the other hand serves as a good tool for comparing the probability of the flame kernel propagating to certain locations horizontally or vertically. The 1D-PDF can be considered

as the horizontal or vertical 1D projection of the 2D-PDF. To calculate the 1D-PDF, each line (horizontal or vertical) of pixels is followed and number of flame kernels is counted. The resulting number of flame kernels along each line of pixels is normalized to the total number of cycles to obtain the 1D-PDF. The illustration 1D-PDF can be found in Figure 8-6.

4.4 Image Processing for the PIV system

The production Insight-3G PIV post-processing software is used to calculate the velocity field. The image pairs are first filtered by a 5 × 5 pixel Gaussian filter, and then segregated into 32 × 32 pixel interrogation windows. The interrogation windows from the pair of images are cross-correlated by multiplying their complex conjugates in frequency domain [45]. The peak correlation location is estimated to sub-pixel level with Gaussian estimation.

After the raw velocity field is calculated, the blank points (holes) are filled by the local mean values in 5 × 5 neighborhood. The filled velocity field is validated via median test in the 3 × 3 neighborhood, and the bad vectors are replaced by the secondary peak of the cross-correlation or by the local median value. The result is once again going through the validation process and the remaining bad vectors are replaced by the local median values. Lastly, the velocity field is smoothed by a 3 × 3 Gaussian filter.

5 Main Research Contributions

The biggest challenge facing the application of highly diluted combustion in SI engines is the high combustion instability. The research described in this dissertation furthered the understanding of the causes of the variations in flow motion and its impacts on the ignition, early flame kernel development and the entire combustion process.

The ignition output was discovered to vary as the incoming flow direction is changed with respect to the spark-plug axis [46]. As the flow direction changes, the interaction between the flow and the ground strap(s) of the spark plug changes, this affects how the spark arc channel stretches, and thus leading to varying ignition energy deposit into the spark discharge channel and varying discharge duration. Different spark-plug electrode designs result in different ways of interaction between the incoming flow and the ground strap(s). Hence how the ignition output changes with the flow direction changes is not the same for different designs of electrodes. It can be concluded from the perspective of ignition output that the significance of spark plug indexing angle differs with different types of spark-plug electrode designs.

Next, the influence of flow motion on early flame kernel was investigated in the DI-SI optical engine [47]. Cycle by cycle variations in early flame kernel convection direction was observed at steady-state operating conditions with lean mixture at lambda = 1.4. The high-speed images of the early flame kernels showed that there exists cycles where the initial flame kernel is convecting to the exhaust side of the spark plug which is in agreement with the main tumble motion introduced by the intake air flow. For these cycles, the early flame kernel is more stretched and large. However there also exists cycles where the initial flame kernel is convecting to the intake side of the spark plug which is counter to the main tumble motion. The early flame kernel propagating to the intake side is more centered at the spark-plug electrodes and the projected flame area is smaller. The inconsistency of the early flame kernel convection introduces variability to the early flame size and this in turn results in variations in the entire combustion process.

Furthermore, the causes of the inconsistency of early flame kernel convection were studied by visualizing and quantifying the flow motion near the spark plug at ignition via high-speed imaging of a long-discharge ignition arc channel, flow field measurement using PIV and early flame kernel imaging at stoichiometric condition, with two levels of tumble motion [48]. The results showed that at low tumble, the flow direction near the spark plug points to the exhaust side at early spark timing range (before 50°BTDC), and then it experiences the directional transition stage as the piston approaches TDC in which the flow motion direction varies cycle by cycle near the spark plug. At late spark timing (after 30°BTDC), the flow direction has essentially shifted, pointing to the intake side. At high tumble, the flow motion direction near the spark plug can be better maintained at pointing to the exhaust side. At late spark timing, there are much fewer cycles that have reversed flow motion compared with low tumble cases. The flow motion transition stage occurs at a much later crank angle position with the high tumble. This explains the cause of the inconsistency of early flame kernel convection discussed above at the lean condition (lambda = 1.4), since the spark timing is at 47°BTDC at this particular speed/load at lambda = 1.4.

The research described above indicates that the tumble motion should be improved at lean conditions to help maintain the flow motion direction at pointing to the exhaust side near the spark plug, and thus the early flame kernel can consistently convect to the exhaust side, which lead to more stretched and larger flame kernels. The faster growing flame kernels can then reduce the combustion instability [40].

6 Dissertation Structure

The main content of this dissertation consists of three published papers with the publisher's permission. Each paper describes in detail the studies introduced in the chapter of the main research contributions. The format of the original published papers has been modified to comply with the format of this dissertation. The contents of the papers are re-published in this dissertation without major changes except for the citation numbers. The referenced resources in the original papers are extracted and combined with the resources cited in other sections of this dissertation and a complete list of resources is provided in the chapter of reference list.

Publications included in this dissertation are as follows:

Chapter 7:

Wang, Y., Zhang, J., Dice, P., Wang, X., Shahbakhti, M., Naber, J., Czekala, M., Qu, Q. and Huberts, G., 2017. An Experimental Study on the Interaction between Flow and Spark Plug Orientation on Ignition Energy and Duration for Different Electrode Designs (No. 2017-01-0672). SAE Technical Paper. SAE 2017-01-0672. doi: 10.4271/2017-01-0672.

Chapter 8:

Wang, Y., Zhang, J., Wang, X., Dice, P., Shahbakhti, M., Naber, J., Czekala, M., Qu, Q. and Huberts, G., 2017. Investigation of Impacts of Spark Plug Orientation on Early Flame Development and Combustion in a DI Optical Engine. SAE International Journal of Engines, 10(2017-01-0680). SAE 2017-01-0680. doi: 10.4271/2017-01-0680

Chapter 9:

Wang, Y., Zhang, J., Yang, Z., Wang, X., Dice, P., Shahbakhti, M., Naber, J., Czekala, M., Qu, Q. and Huberts, G., Investigation of Flow Conditions and Tumble near the Spark Plug in a DI Optical Engine at Ignition, SAE 2018-01-0208.

7 Investigation of Interaction between Flow and Spark Plug Orientation on Ignition Output

This paper was published in 2017 SAE world congress. It corresponds to the first stage of research described in the chapter of main research contributions.

In this study, a flow fixture with the capability of adjusting the relative orientation between the incoming flow direction and spark-plug axis was used to investigate how the ignition output varies as the direction of incoming flow is changed. It was discovered that different types of spark-plug electrode designs have different interactions between the ground strap(s) and the incoming flow, resulting in different sensitivity of the spark plug output with respect to the incoming flow direction.

An Experimental Study on the Interaction between Flow and Spark Plug Orientation on Ignition Energy and Duration for Different Electrode Designs

Wang, Y., Zhang, J., Dice, P., Wang, X., Shahbakhti, M., and Naber, J.

Michigan Technological University

Czekala, M., Qu, Q., and Huberts, G.

Ford Motor Company

Michigan Technological University

Department of Mechanical Engineering – Engineering Mechanics

1400 Townsend Drive, Houghton, Michigan, USA 49931

Phone: (906)370-2612

Email: yanyuw@mtu.edu, jnaber@mtu.edu

7.1 Abstract

The effect of flow direction towards the spark plug electrodes on ignition parameters is analyzed using an innovative spark aerodynamics fixture that enables adjustment of the spark plug gap orientation and plug axis tilt angle with respect to the incoming flow. The ignition was supplied by a long discharge high energy 110 mJ coil. The flow was supplied by compressed air and the spark was discharged into the flow at varying positions relative to the flow.

The secondary ignition voltage and current were measured using a high speed (10 MHz) data acquisition system, and the ignition-related metrics were calculated accordingly. Six different electrode designs were tested. These designs feature different positions of the electrode gap with respect to the flow and different shapes of the ground electrodes. The resulting ignition metrics were compared with respect to the spark plug ground strap orientation and plug axis tilt angle about the flow direction.

Analysis of the experimental data indicates that the position of the ground strap with respect to the flow is a primary factor that causes variations in ignition discharge energy and discharge duration. The different types of electrodes are influenced differently as the incoming air flow direction changes with respect to the electrode gap. Double fine wire electrodes produce a wide constant ignition energy and duration window; while side electrode gap has a great variation in gap energy output. The experimental results show that the normalized gap energy increased by 67.7% as the incoming flow changes from 0° index angle to 90° angle.

7.2 Introduction

It is well known that one of the major energy loss in SI engine operation is the throttling loss during low/medium loads [19], where there is great margin for thermal efficiency improvement if the throttling loss is reduced. Engine downsizing and diluted charge have

been under investigation in order to reduce the throttling losses at low to medium loads [9]. In addition, charge dilution also benefits in knock suppression. With the decreased tendency to knock, combustion phasing can be positioned close to MBT point, which improves thermal efficiency of the engine. One of the major barriers to realizing diluted charge combustion is that the combustion becomes unstable as the charge dilution ratio, either by internal or external residual recirculation increases.

The variability of the combustion at diluted condition is believed to be caused by various causes [49, 50]. The study by Nakai et al. shows that the early stage of flame kernel formation is a determining factor of the variability of later combustion phase [25]. Ignition, as the trigger for combustion, plays an important role in early flame kernel development; and therefore variability in ignition event also propagates into the later combustion stages [25].

Although in SI engines, much work has gone into designing the piston and cylinder to control the tumble, the charge flow condition across the spark plug electrodes at the moment of ignition is still variable cycle-by-cycle [37, 47, 51]. Prior studies by Johansson [37] and Zeng et al. [51] demonstrated that the flow velocity in the vicinity of the spark plug varies cycle by cycle both in a homogenously mixed port fuel injection (PFI) SI engine and in a modern stratified injection SI engine. In addition, the study by Dulger et al. [52] investigated the impact of different charge flow velocity across the spark plug on the lean misfire limit, and they found the optimum charge flow velocity lies in the range between 5 to 8 m/s. However, the study by Pischinger et al. [34] showed that the favored charge flow velocity is in the range of 3 to 5 m/s from the perspective of flame kernel formation. Zhang's work [53] in a constant volume combustion chamber also showed the charge flow velocity across the electrode gap can detach the flame kernel from the electrodes too early leading to flame kernel quenching, and multiple spark discharge can facilitate the development of the early flame kernel under high flow velocity.

Further, the ground strap orientation of commonly used J-plug spark plugs, when installed to the specified torque in the cylinder, is determined by the starting point of the thread and

thread length. Once manufactured, there is not much room for further adjustment. Therefore, the questions that need to be answered are: how does the ground strap orientation to the cylinder flow affect the ignition output? Does there exists a certain range of ground strap orientations to the flow in which the ignition can output a stable high gap energy?

Multiple studies have revealed the fact that the orientation of the spark plug affects engine performance in terms of coefficient of variation of indicated mean effective pressure (COVimep) [33, 54]. Usually in engine testing conditions, upstream, downstream and crossflow index orientations are studied; however, a systematic investigation on how ignition output changes as in-cylinder flow direction changes with respect to the spark plug gap is lacking.

This study investigates how the orientation of spark plug electrodes with respect to the charge flow influences the resulting ignition metrics, especially the ignition energy released into the gap and spark discharge duration for different electrode designs. The spark plugs were tested on a newly designed and built bench fixture for adjusting the relative position between the spark plug axis and incoming flow. The details of the structure of the fixture will be discussed in the following section. The spark was released into the ambient flow at a fixed velocity at atmospheric pressure with varying index orientation and tilt angle. The flow velocity was set at 15 m/s for this study as a value representative of a modern high tumble motion engine.

7.3 Experiment Setup

7.3.1 Aerodynamics Fixture

The spark plugs were tested on a custom air flow fixture, which enables adjustment of spark plug axis tilt angle (referred to as tilt angle β) and axis rotation angle (referred to as index angle θ), as shown in Figure 7-1. The tilt angle is defined as the angle between the

incoming flow and the plane normal to the spark plug axis, with the angle between the air flow and spark plug axis smaller than 90° being defined as negative tilt angle, greater than 90° being defined as positive as illustrated in Figure 7-1. The index angle is defined as the angle between the axis of incoming flow and the plane on which the electrodes and ground strap lie. The index angle 0° is defined as when the electrode gap is facing the incoming flow; i.e., the ground strap is NOT shielding the incoming flow from gap, as illustrated in Figure 7-1. The flow is introduced through the tube pointing towards the electrodes; the velocity is controlled by a pressure regulator and calibrated by a hot film velocity probe in place of the spark plug before each test.

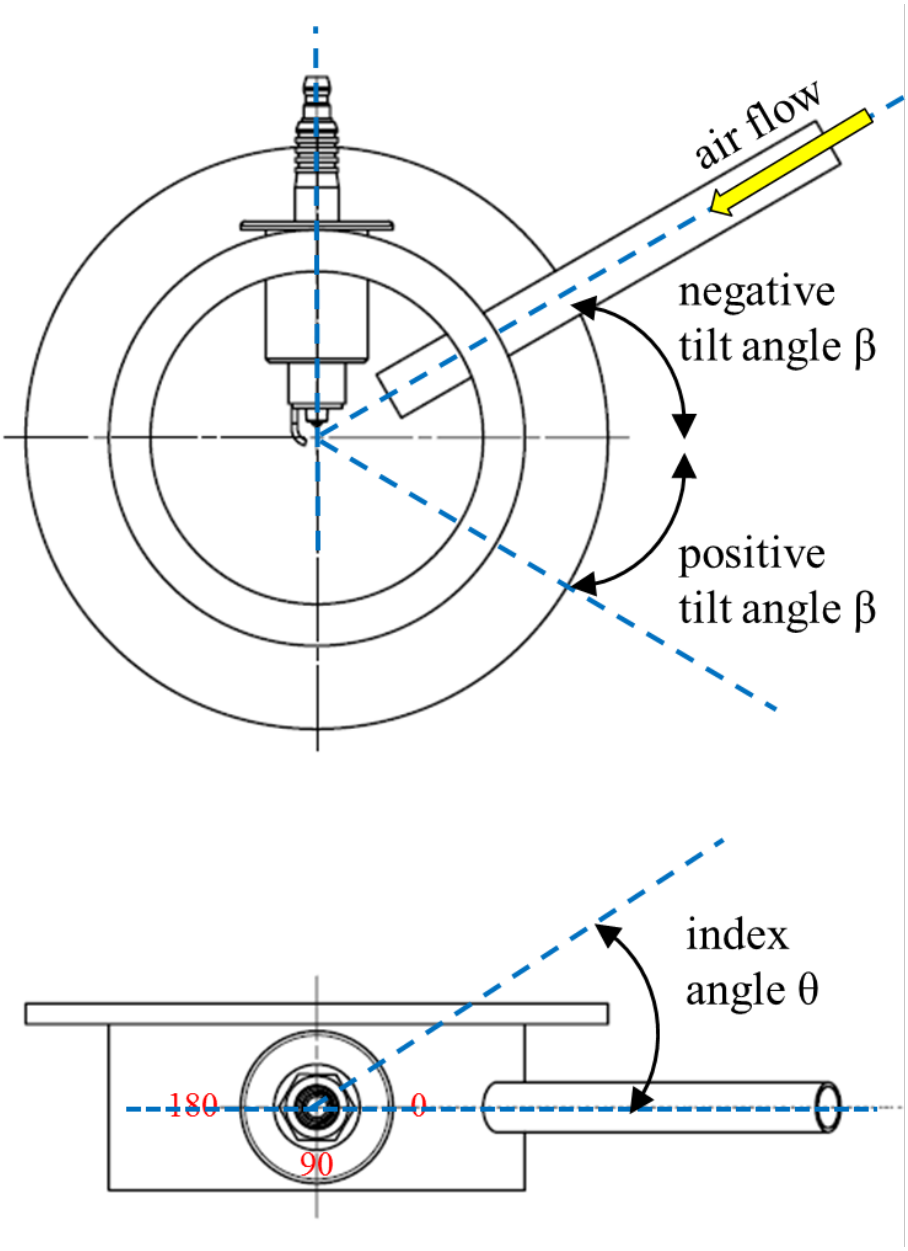

Figure 7-1: Illustration of definition of tilt angle β and index angle θ.

7.3.2 Ignition Data Acquisition

As illustrated in Figure 7-2, the ignition voltage was measured upstream of the spark plug using a Tektronix P6015A high voltage probe, and the ignition current was measured both at low side and high side of the secondary coil using Pearson 6595 current probes. The

current signal from the probe on the low side was used to calculate the breakdown plug arc phase ignition energy; being on the low side accounts for the capacitance inherent to the secondary ignition circuit. The current signal from the probe on the high side was used to calculate the glow phase ignition energy. The Pearson 6595 current probe has a short rise time of 2.5 ns, which is suitable for measuring the current rise during the pre-breakdown capacitance charging period. However, its low cut-off frequency is high at 100 Hz which leads to loss of the DC or low frequency component of the signal. Fortunately, the DC loss can be compensated in the post-processing stage.

The measured voltage and current were recorded by a high-speed (10 MHz) NI-PXI system. Samples of the measured secondary voltage trace and current trace are shown in Figure 7-3 and Figure 7-4. The unit of the time is in milliseconds after ignition timing (msAIT).

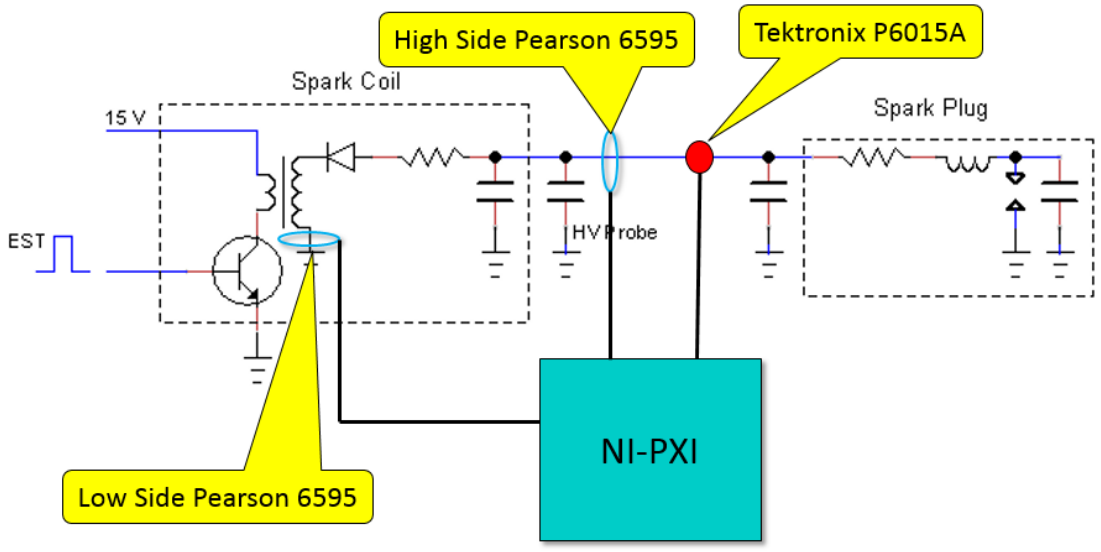

Figure 7-2: Schematic of ignition system and measurement instrumentation.

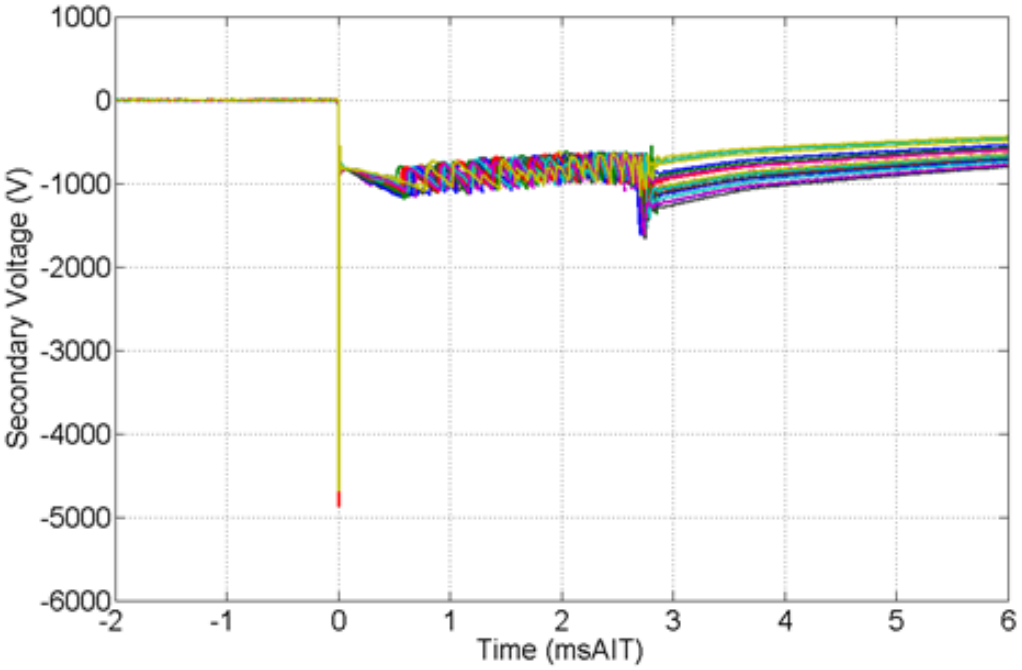

Figure 7-3: Sample secondary voltage traces for 20 ignition events.

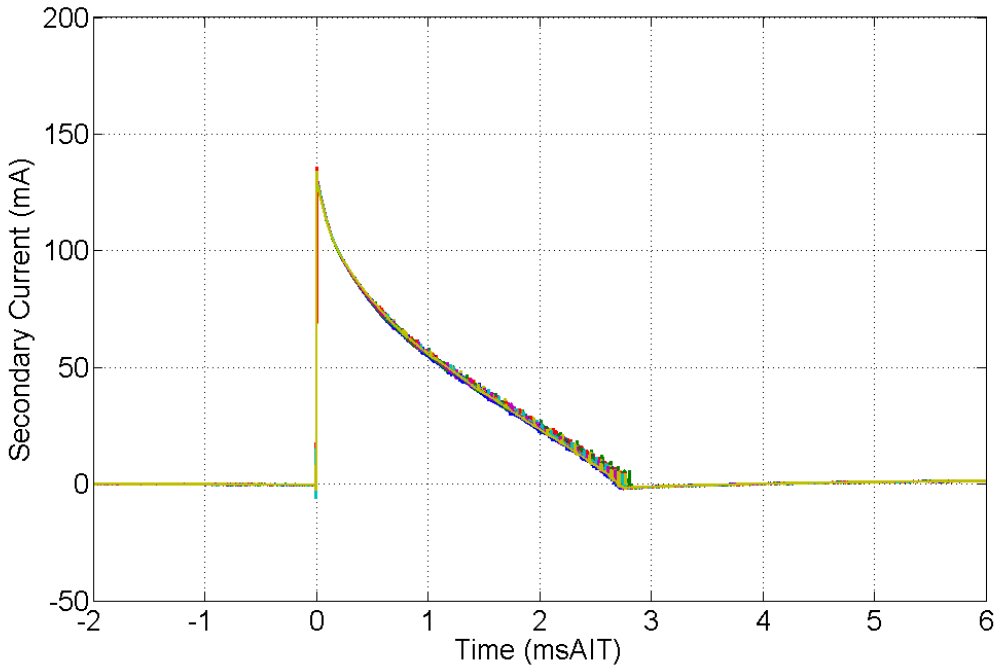

Figure 7-4: Sample secondary current traces for 20 ignition events.

The air flow velocity was set at 5, 10, 15, 20 m/s for the double fine wire spark plug (spark plug A in Figure 7-5) to observe the ignition output dependency on the air flow velocity. The tilt angle was set to -20, 0, 20° and the index angle were from 0° to 180° with finer resolution near 0° and 180°. For each index angle and tilt angle combination, 20 ignition events were executed. The test conditions are summarized in Table 7-1.

Table 7-1: Test conditions

Flow Velocity (m/s)	5,10,15,20
Number of Ignitions per Test Point	20
Tilt Angle β (degs)	-20, 0, 20
Index Angle θ (degs)	0 to 180

The total glow energy was calculated from the obtained secondary voltage and current data from the high side current probe by integrating their product over the discharge duration as in equation 7-1. The resistive loss over the spark plug is defined as the square of secondary current multiplied by the internal resistance of the spark plug, and it is subtracted to obtain the gap glow energy as in equation 7-1. The breakdown plug arc energy is defined as the energy released from the capacitive storage in the secondary ignition circuit; it includes spark plug gap capacitance, coil capacitance, and parasitic capacitance; and it is estimated in one term as in equation 7-2 [55]. The breakdown + arc energy and glow energy are added to obtain the total gap energy in equation 7-3. The results were normalized for better comparison between each test case.

$$E_{glow} = \int_{start}^{end} vidt - \int_{start}^{end} i^2 Rdt \quad 7\text{-}1$$

$$E_{bd+arc} = \frac{1}{2} C V_{bd}^2 \quad 7\text{-}2$$

$$E_{gap} = E_{bd+arc} + E_{glow} \quad 7\text{-}3$$

In equation 7-1 through 7-3, E_{glow} is the energy released between the electrodes; v and i represent the instant secondary voltage and current, and R is the resistance of the spark plug; V_{bd} is the breakdown voltage and C is the capacitance of the secondary circuit.

The discharge duration is defined from the start of breakdown till when the secondary current measured from the high side current probe drops below 10 mA.

The calculated gap energy and discharge duration were averaged over the number of ignition events of each index/tilt angle combination, and then normalized over the highest energy and longest discharge duration respectively for each spark plug in order to remove influence of variation in gap dimension & spark plug resistance between spark plugs. The purpose for this is to focus solely on the comparison of the sensitivity of ground electrode orientation with respect to the incoming flow to the resulting ignition metrics.

7.3.3 Spark Plugs and Their Electrodes

Six spark plugs of electrodes featuring four different orientations of the electrode gap with respect to the spark plug axis were tested in this study. The six spark plugs characterize three different categories of electrodes as can be seen in Figure 7-5 and Figure 7-6. The definition of the angle α between electrodes' axis and spark plug axis is illustrated in Figure 7-7. In Figure 7-5, Spark plug A (SP A) and SP B feature the type of electrodes whose axis is overlaying with the spark plug axis, i.e. α is equal to zero. In addition, SP C, SP D and SP E feature the type of electrodes whose axis is at an angle with the spark plug axis, i.e. α is not equal to zero; and finally, SP F features a ring gap type of electrodes.

The features of the six spark plugs are summarized in Table 7-2 and Figure 7-7. Each spark plug is assigned a letter which will be referred in later sections. Ignition was supplied by a long discharge high energy coil (110 mJ).

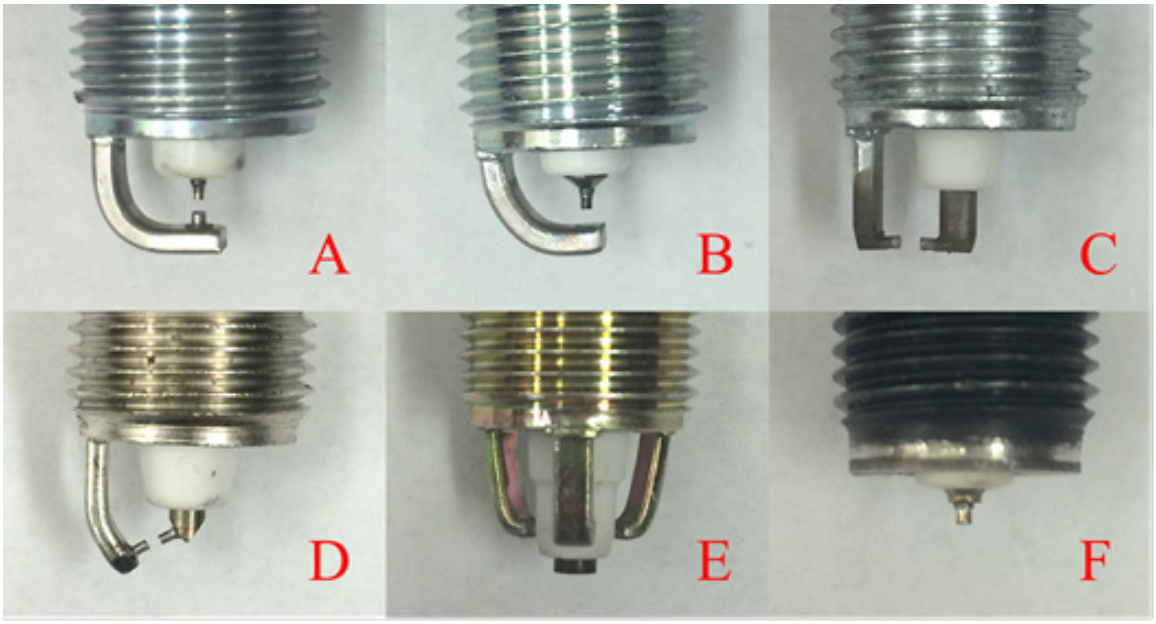

Figure 7-5: A: double fine wire; B: single fine wire; C: horizontal gap; D: angled side gap; E: multiple ground; F: ring gap.

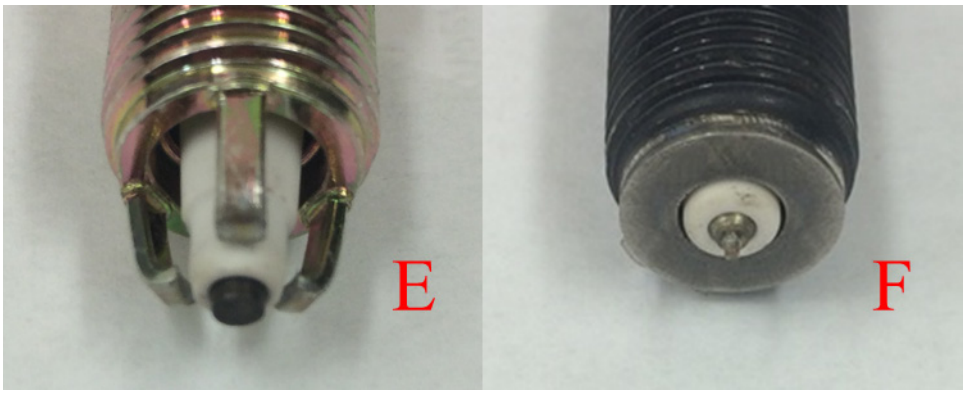

Figure 7-6: Another view of multiple ground (E) and ring gap type (F) spark plugs.

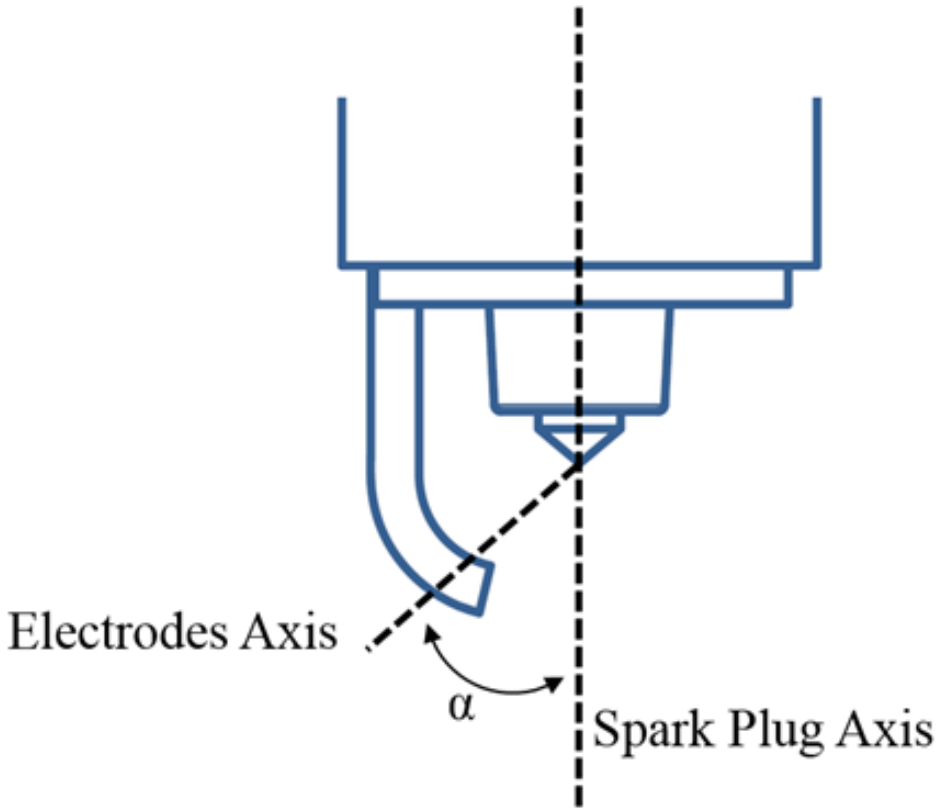

Figure 7-7: Illustration of spark plug axis and electrodes' axis, forming angle α.

Table 7-2: Features of the six studied spark plug electrode designs.

Spark Plug	Electrode Type	Number of Ground Electrode	Electrodes' Axis w.r.t Plug Axis
A	Double Fine Wire	1	parallel
B	Single Fine Wire	1	parallel
C	Horizontal Gap	1	perpendicular
D	Side Gap	1	angled
E	Side Gap × 3	3	angled
F	Ring Gap	0	-

7.4 Results and Discussion

7.4.1 Air Flow Velocity Dependency

Four different air flow velocity settings were tested for the double fine wire spark plug (SP A) to determine the air flow dependency of the ignition output. The results are shown in Figure 7-8. Between 150° to 180° index angle range, the normalized gap energy under 5 m/s air velocity differs from the other three higher air velocity setting by a large margin (13.7% in average compared with 10 m/s setting at 90° index angle). However, at higher velocity settings, the difference becomes much smaller (4% in average between 10 m/s and 15 m/s, and also 4% in average between 15 m/s and 20 m/s at 90° index angle). The cause of the different level of impact from different air flow velocity on the ignition output can be seen in Figure 7-9 in terms of average number of spark re-strikes per ignition event. Air flow at 5 m/s has very low impact on the spark channel stretching, which only leads to about 2 re-strikes per ignition event in average; while higher velocity at 10 m/s, 15 m/s and

20 m/s resulted in more re-strikes due to spark channel being stretched more at higher air velocity.

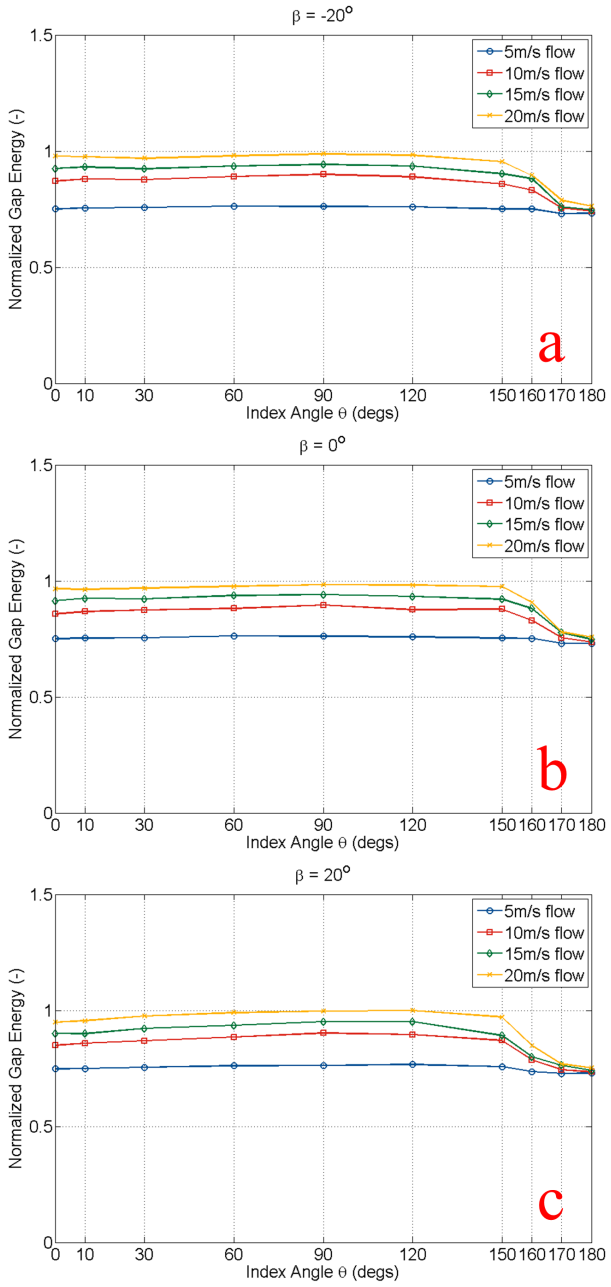

Figure 7-8: Air flow velocity dependency tests of gap energy at -20° tilt angle for spark plug A. (a) β = -20°; (b) β = 0°; (c) β = 20°.

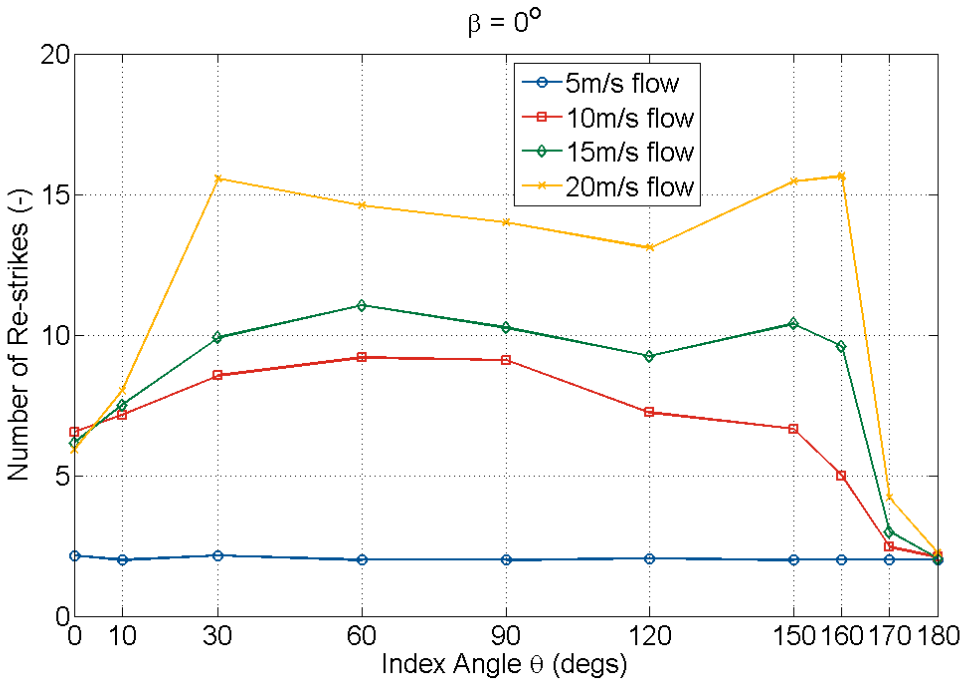

Figure 7-9: Number of re-strikes per ignition event at different air flow velocity at β = 0°;

The tumble motion varies as the piston position changes. Abidin's work [56] revealed that the tumble motion has an increasing and then decreasing trend from the time of intake valve closing (IVC) to TDC, and the tumble ratio could remain above 0.5 until 30° before TDC (BTDC). Johansson's work [31] showed that the flow velocity across the spark plug gap decreases from 10 m/s to around 0 m/s as the piston moves from 40° BTDC to 20° BTDC at 700 rpm. Although charge motion at spark timing and spark plug position is difficult to determine, 15 m/s was chosen for this study as a value representative of a modern high tumble motion engine.

7.4.2 Impact of Flow on Breakdown and Arc Energy

Shown in Figure 7-10 is the breakdown + arc energy of spark plug (SP) A at different index and tilt angles. No apparent trend is observed. This is expected since the breakdown event is mostly influenced by the gas pressure, temperature, mixture composition, according to

Paschen's Law [57]. This indicates that the observed trends in the following sections are mainly due to interactions between the flow and the glow phase of the discharge.

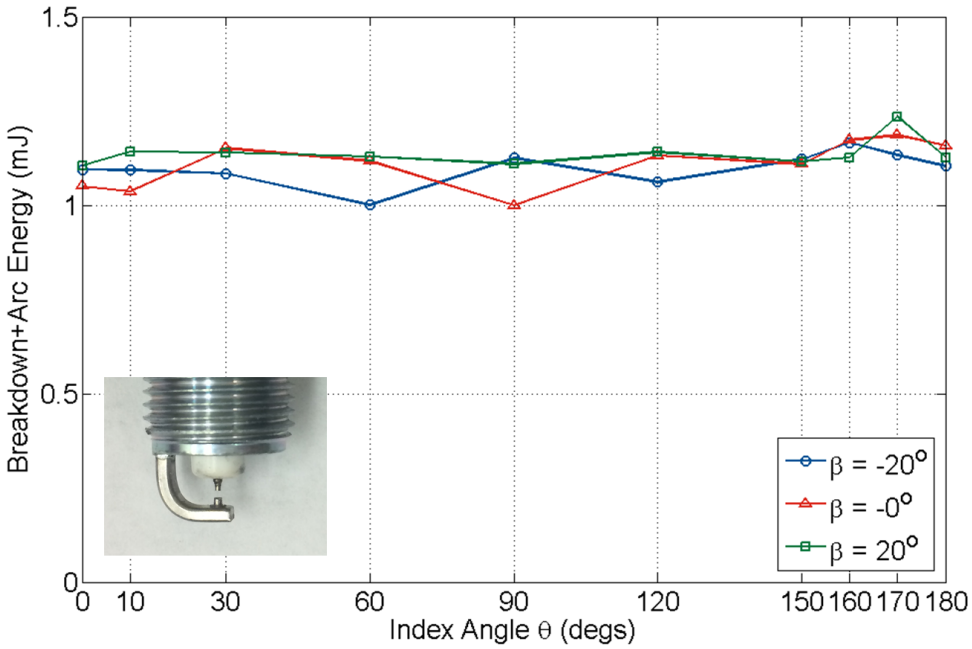

Figure 7-10: Breakdown + arc energy of spark plug A.

7.4.3 Results of Normalized Ignition Metrics

The normalized gap energy and discharge duration of the standard double fine wire denoted SP A are shown in Figure 7-11. Both metrics exhibit a stable output from 0° index up to 150° index; the output energy starts dropping from 150° index to 180° index by 20.8% as the ground strap rotates to the position of shielding the incoming flow from the gap. The duration follows the same trend; it keeps stable till from 150° index to 180° index, it increases by 0.6ms average. The difference in the output metrics between the three studied tilt angles are small from 0° index to 150° index; they diverge starting from 150° index and then converge back at 180° index.

The analysis indicates that, for double fine wire electrodes, the discharge gap energy and duration can be considered constant as long as the incoming flow passes the electrode gap at index angle between 0° to 150°. However, between 150° and 180° index angle, any variation in incoming flow direction could result in different ignition energy and discharge duration output. The same reasoning applies to results of other five types of electrodes.

The normalize gap energy and discharge duration of a standard single fine wire denoted SP B are shown in Figure 7-12. The result of SP A at 0° tilt angle is also shown in dashed line for comparison, and also in figures for the remaining spark plugs. One can easily observe that single fine wire performs worse at stabilizing the ignition output. The trend between 150° index to 180° index is the same as double fine wire: the gap energy dropped by 13.7% while the discharge duration increased by 0.39 ms. However, between 0° index to 150° index, the ignition output is not as stable as double fine wire and the higher energy output occurs at 60° index position for all three tilt angles. This can be attributed to the fact that, during ignition discharge for the single fine wire electrodes, one end of the spark channel is not anchored well as in the case of double fine wire; so it is more prone to the incoming flow disturbance.

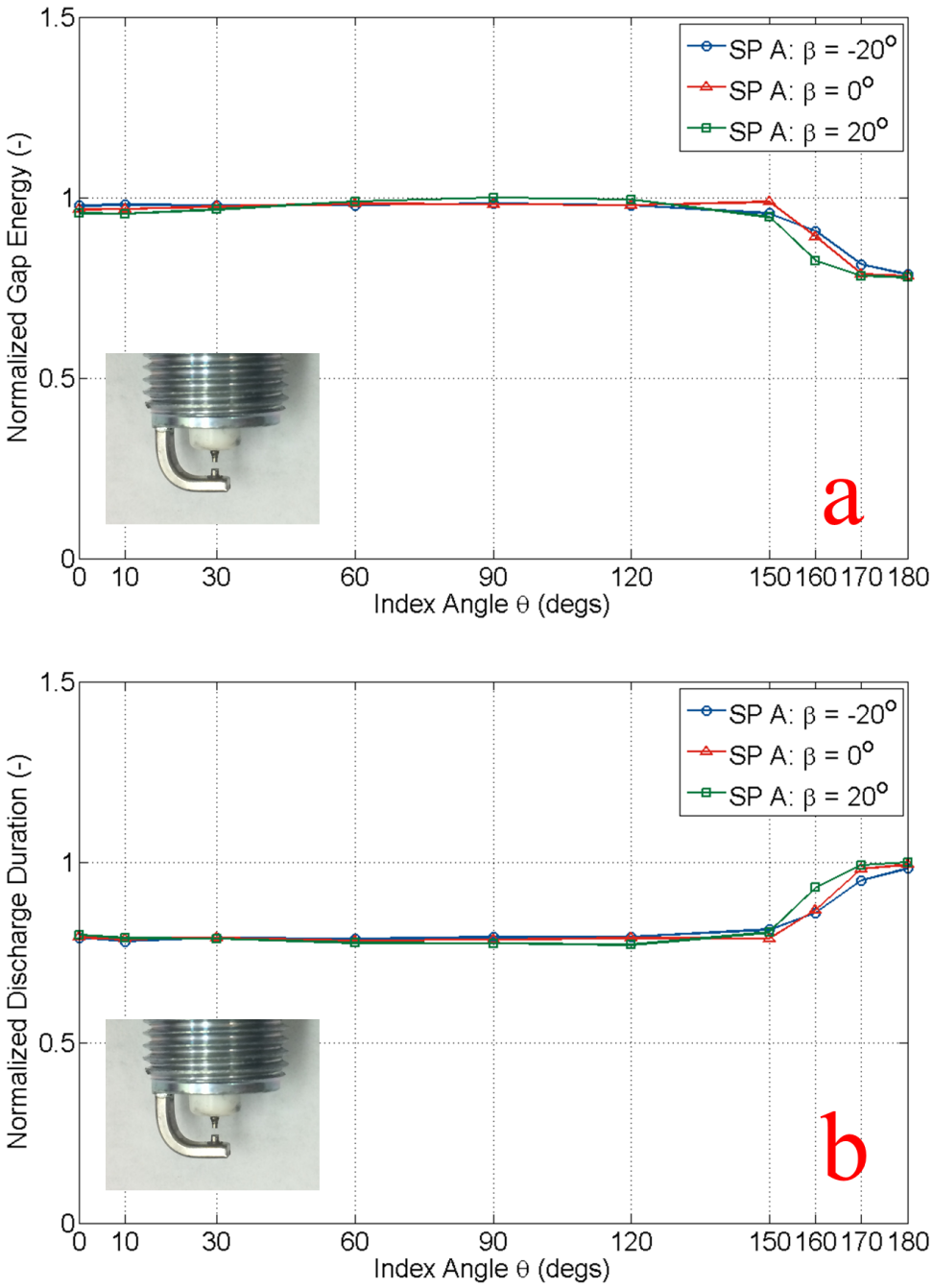

Figure 7-11: Normalized gap energy of SP A. (a) normalized gap energy; (b) normalized discharge duration.

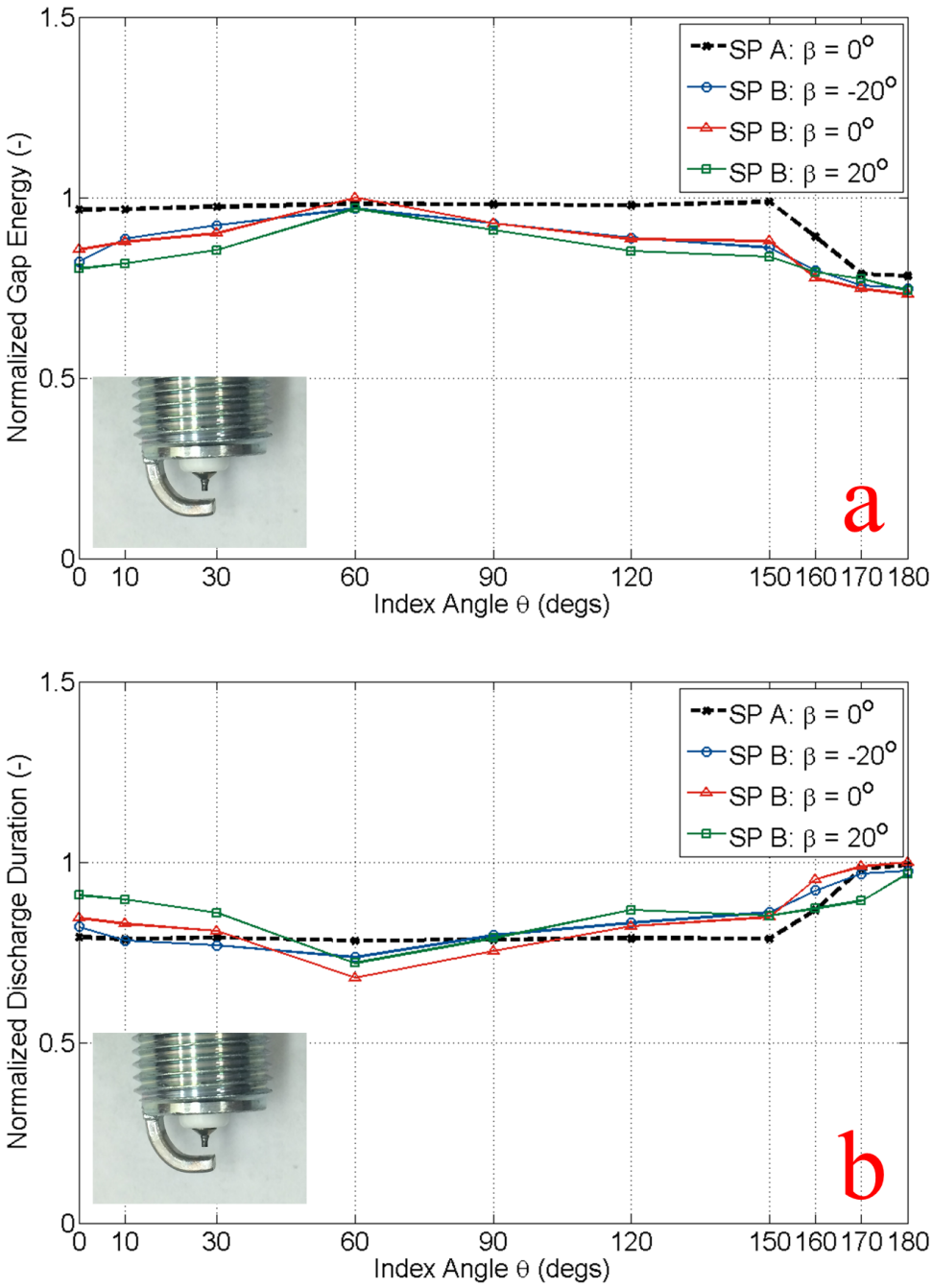

Figure 7-12: Normalized gap energy of SP B with SP A result as reference (dashed line). (a) normalized gap energy; (b) normalized discharge duration.

The above discussed two types of electrodes (Figure 7-11 through Figure 7-12) feature the electrodes' axis being parallel to the spark plug axis (refer to

Table 7-2). The following three types of electrodes to be discussed all feature the unparalleled electrodes' axis with respect to the spark plug axis, i.e. angled ground electrode.

In Figure 7-13, results of a side-gap-electrode spark plug denoted SP C are presented. This type of spark plug features a perpendicular gap with respect to the spark plug axis. The difference between spark plug C and spark plug A is quite noticeable (Figure 7-13), as no constant output zone can be spotted. Each index angle of incoming flow could result in different gap energy output and discharge duration. Further, each tilt angle could also result in variable ignition output, which is especially prominent between 0° index to 120° index, with 20° tilt resulting in highest gap energy output, and -20° tilt giving the lowest gap energy. Correspondingly, 20° tilt results in shortest discharge duration and -20° tilt results in longest discharge duration.

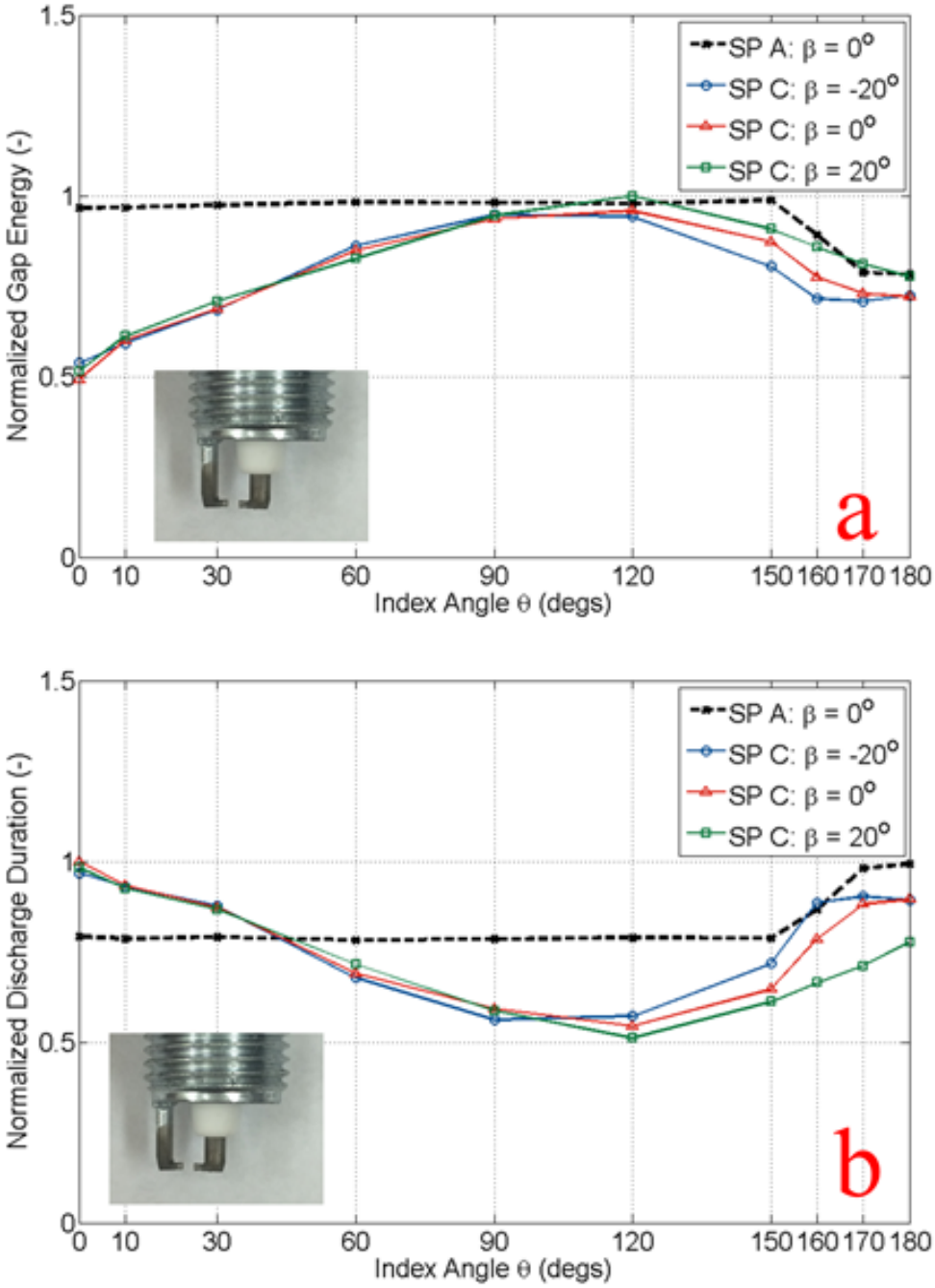

Figure 7-13: Normalized gap energy of SP C. (a) normalized gap energy; (b) normalized discharge duration.

The results presented in Figure 7-14 are also from a side gap spark plug, denoted SP D, but the electrodes' axis is not perpendicular to the spark plug axis. The trend is similar to the

horizontally sided gap SP C shown in Figure 7-13. SP D (Figure 7-14) exhibits a higher variation with respect to the tilt angle, as the three curves are wider spaced than those in Figure 7-13.

A single sided ground electrode does not perform well stabilizing the ignition output as shown in Figure 7-13 and Figure 7-14. Can multiple side ground electrodes help stabilization of ignition output? The answer is positive according to Figure 7-15, which illustrates the result of spark plug E.

Compared with SP C in Figure 7-13, SP E (Figure 7-15) significantly improves the constant ignition output zone. The normalized gap energy remains above 0.8 for all incoming flow index angles. Compared with double fine wire SP A in Figure 7-11, each of SP A and SP E has their advantages. SP A offers lower variations between different tilt angles, while SP E does not have a range where ignition energy significantly drops as in SP A case between 150° index to 180° index.

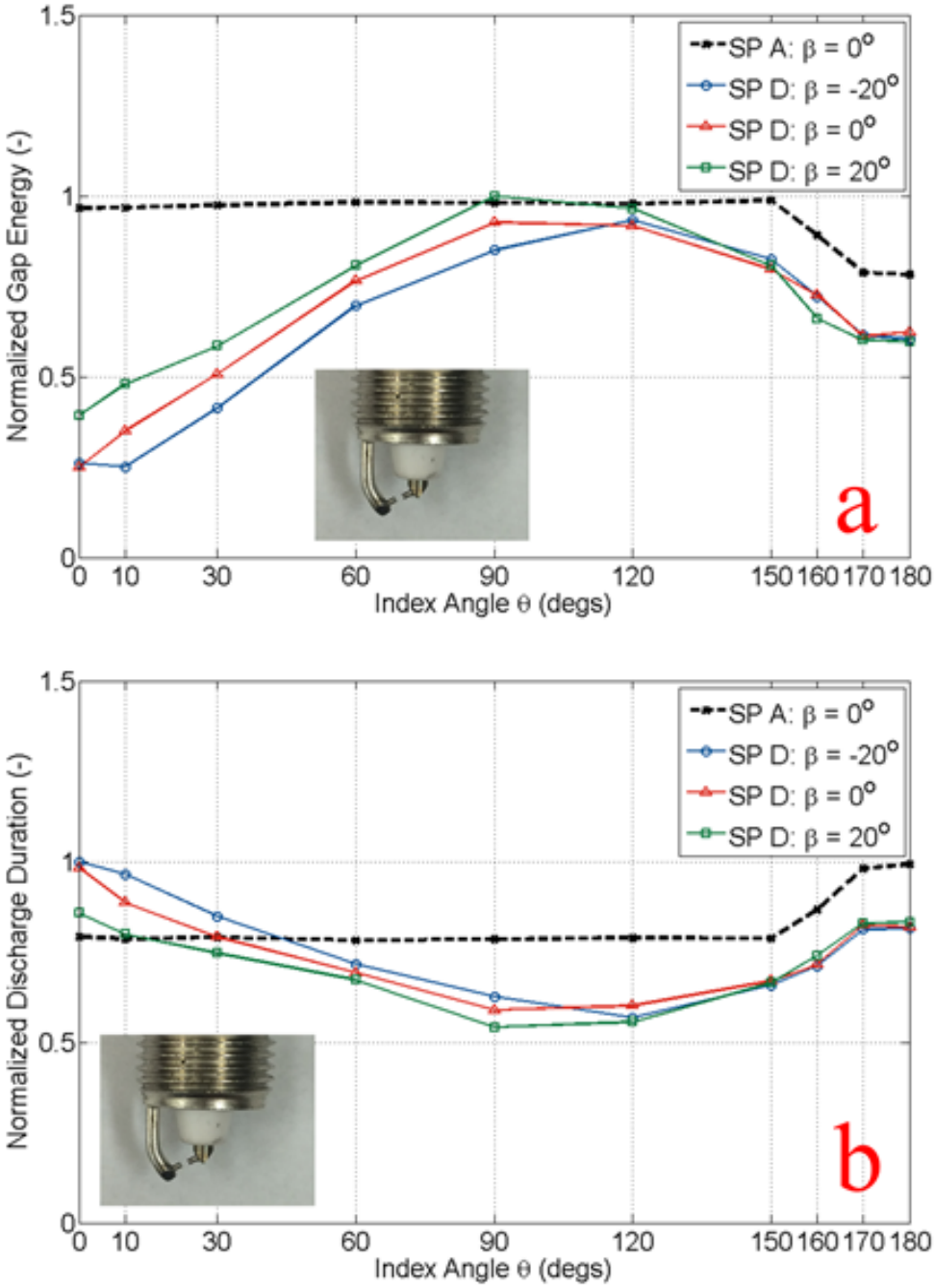

Figure 7-14: Normalized gap energy of SP D. (a) normalized gap energy; (b) normalized discharge duration.

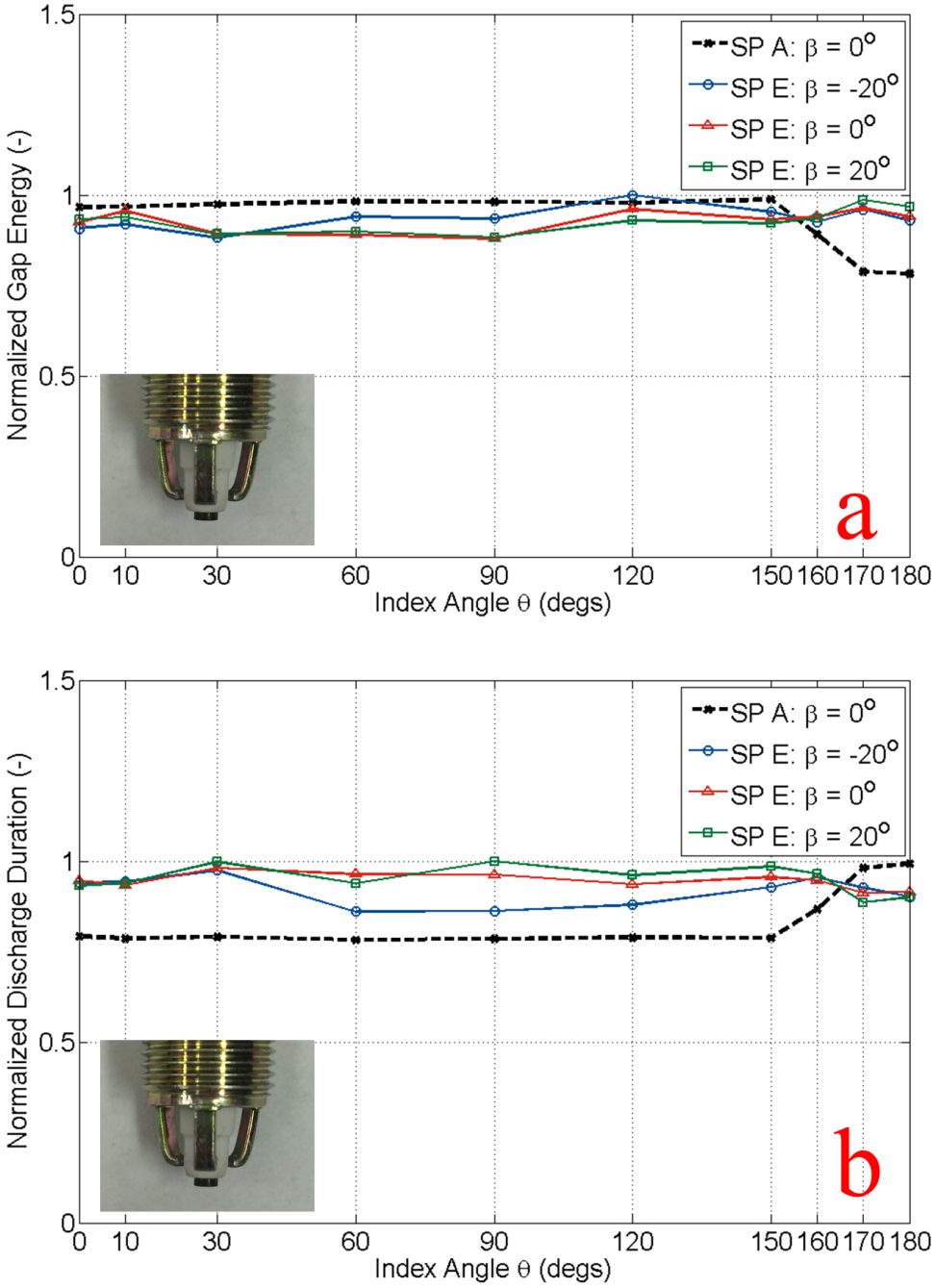

Figure 7-15: Normalized gap energy of SP E. (a) normalized gap energy; (b) normalized discharge duration.

Spark plug F has ring gap type electrodes. The results show that this type of electrode is insensitive to incoming flow variations, as in Figure 7-16. However, this type of electrodes

usually have spark discharge channels close to the insulator or plug ground material, which leads to higher heat loss, resulting in unhealthy flame kernel development.

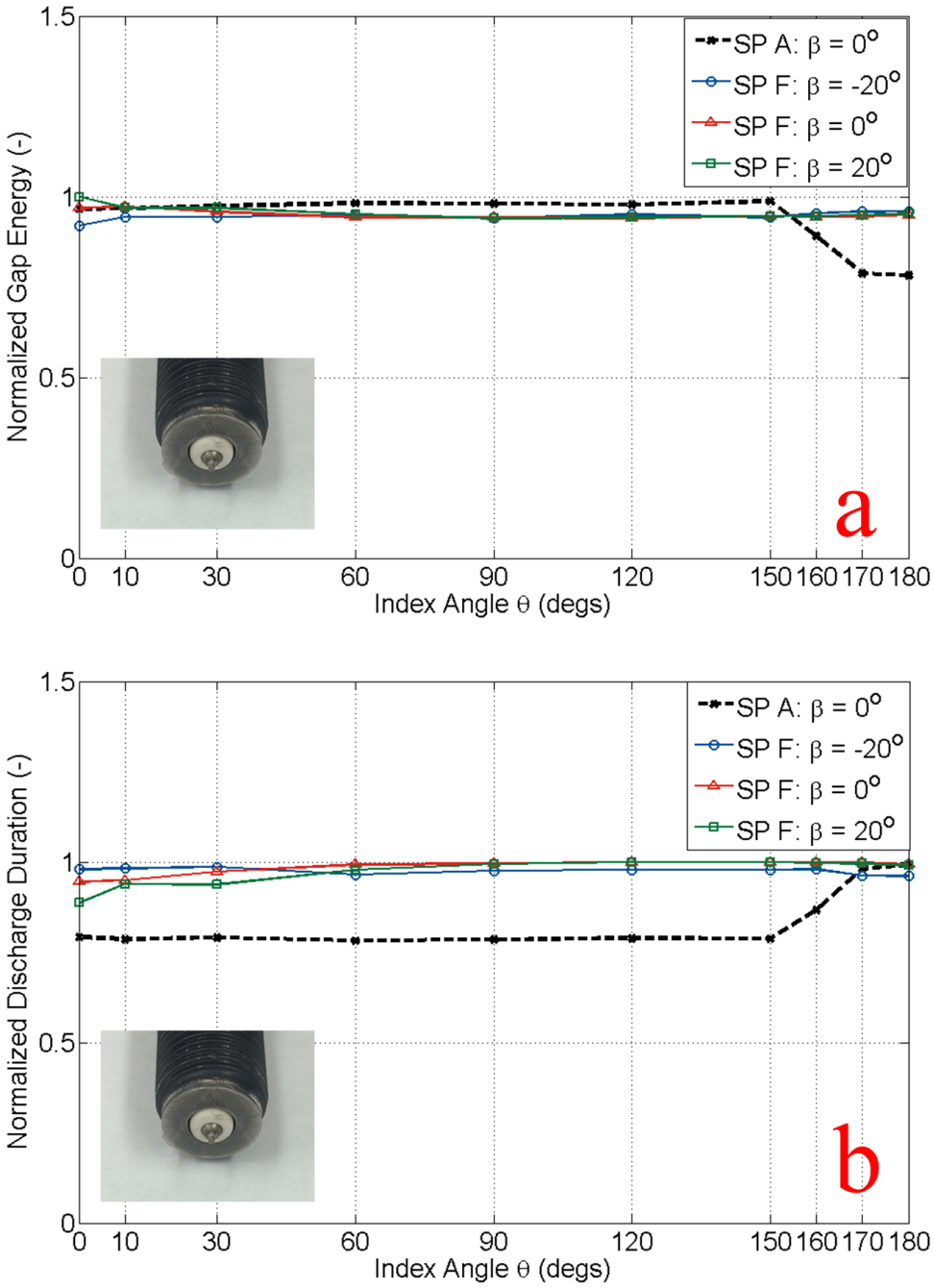

Figure 7-16: Normalized gap energy of SP F. (a) normalized gap energy; (b) normalized discharge duration.

7.4.4 Constant Ignition Output Zone Analysis

The normalized energy at 0° tilt angle over all around index angle is presented in color-coded polar plots Figure 7-17. Normalized energy below 70% is considered undesired zone, and colored with orange – red; normalized energy above 70% is considered constant ignition output zone, and color-coded in green.

It is indicated that the double fine wire (SP A) provides the widest constant ignition output zone range. The two side gap types (SP C D) have the narrowest stable zone.

One needs to use discretion when interpreting the results presented so far. The results only reflect how stable ignition output these different types of electrodes could produce in terms of gap energy and discharge duration. In actual engine operations, many other factors need to be considered, such as heat loss through the flame kernel contacting the spark plug material [34].

7.5 Summary and Conclusions

The effect of air flow direction across the electrode gap with respect to the spark plug on ignition output has been investigated using an air flow fixture which allows both spark plug index angle and tilt angle adjustment with respect to the air flow. The gap energy and discharge duration were calculated from the secondary ignition voltage and current; the results were normalized to the highest value for each spark plug to investigate how well each type of electrodes output constant ignition energy and discharge duration.

- The results show that the double fine wire (SP A) electrodes provide the widest constant ignition output window from 0° to 150° index angle; the gap energy only drops when the ground strap is in the position of shielding the air flow.

- The single sided electrodes (SP C and SP D) lead to a large variation in gap energy and discharge duration as the direction of air flow changes. Multiple sided electrodes alleviate the large variation.

- Though the result of the ring gap shows the widest constant energy window, almost insensitive to the air flow direction, one needs to be careful jumping to conclusion that ring gap would perform the best in actual engine conditions, since the spark channel of this type of electrode attaches closely to the spark plug insulator the ground material, which could lead to high heat loss.

In conclusion, different electrode geometry alters how the ignition output responds to the change of flow direction. When the electrodes' axis is parallel with the spark plug axis as in a standard double fine wire spark plug, a wide index range exists in which the ignition output (gap energy and discharge duration) remains constant as the flow direction changes. When the electrodes' axis is angled, the ignition output becomes sensitive to the flow direction; any change in flow direction could result in different ignition gap energy and discharge duration.

It is important to understand an engine's charge motion at the time of spark, the sensitivity of spark plug electrode geometry to charge motion, and the sensitivity of combustion quality to delivered ignition energy.

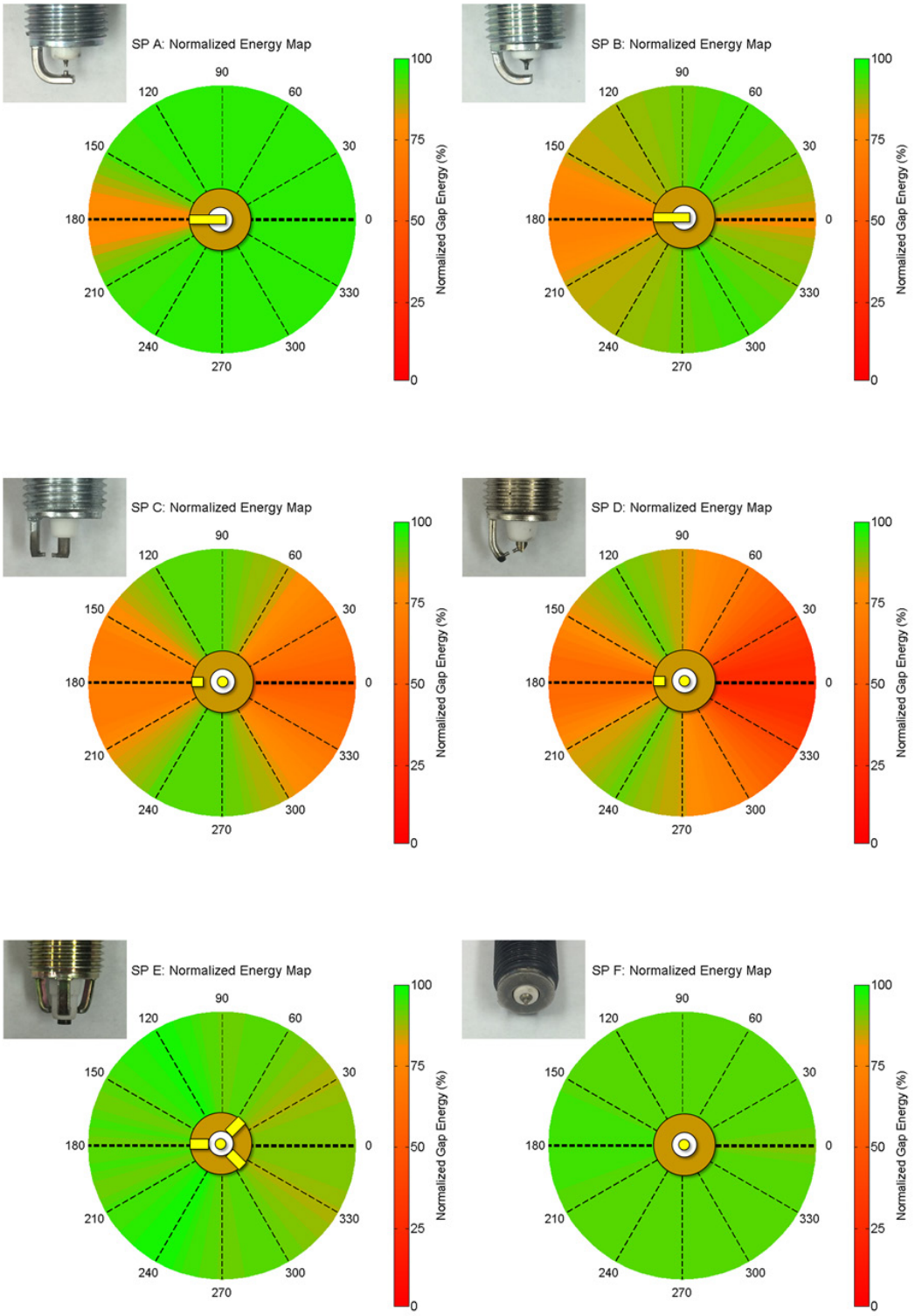

Figure 7-17: Map of normalized energy at 0° tilt angle for all spark plugs studied.

7.6 Acknowledgments

We would like to thank Autolite Spark Plugs, NGK Spark Plugs, Federal-Mogul Powertain and Denso International America for supplying the spark plugs used in this study.

We also give our thanks to Mr. Paul Ostrander of Ford Motor Company for building the spark plug flow fixture used in this work.

Thanks also go to Joel Duncan from Michigan Technological University for his technical support during the course of this project.

7.7 Abbreviations

BD	breakdown
BTDC	before top dead center
COV	coefficient of variation
IMEP	indicated mean effective pressure
IVC	intake valve closing
msAIT	milliseconds after ignition
SP	spark plug
TDC	top dead center

8 Investigation of Cycle by Cycle Variations in Early Flame Kernel Development at Lean Conditions

This paper was also published in 2017 SAE world congress. It corresponds to the second step of research described in the chapter of main research contributions.

In this study, early flame development at lean condition (lambda = 1.4) was high-speed imaged. It was revealed that there exists cycle by cycle variations in early flame kernel convection direction. The early flame kernel convecting to the exhaust side is more stretched and large, and the early flame kernel convecting to the intake side is less stretched, small, and centered at the spark-plug electrodes.

Investigation of Impacts of Spark Plug Orientation on Early Flame Development and Combustion in a DI Optical Engine

Wang, Y., Zhang, J., Wang, X., Dice, P., Shahbakhti, M., and Naber, J.

Michigan Technological University

Czekala, M., Qu, Q., and Huberts, G.

Ford Motor Company

Michigan Technological University

Department of Mechanical Engineering – Engineering Mechanics

1400 Townsend Drive, Houghton, Michigan, USA 49931

Phone: (906)370-2612

Email: yanyuw@mtu.edu, jnaber@mtu.edu

8.1 Abstract

The influence of spark plug orientation on early flame kernel development is investigated in an optically accessible gasoline direct injection homogeneous charged spark ignition engine. This investigation provides visual understanding and statistical characterization of how spark plug orientation impacts the early flame kernel and thus combustion phasing and engine performance.

The projected images of flame kernel were captured through natural flame chemiluminescence with a high-speed camera at 10,000 frames per second, and the ignition secondary discharge voltage and current were measured with a 10 MHz DAQ system. The combustion metrics were determined using measurement from a piezo-electric in-cylinder pressure transducer and real-time engine combustion analyzer.

Three spark plug orientations with two different electrode designs were studied. The captured images of the flame were processed to yield 2D and 1D probability distributions. Charge motion interaction with kernel development was characterized. The data was segregated according to the initial flame kernel convection directions and investigation was conducted to understand how the different spark plug orientations influence the flame kernel propagation cycle-to-cycle.

The results revealed that the two electrode designs produce the same trend for the cycles whose initial flame kernels are convected to the exhaust side of the cylinder: the 90° index orientation (crossflow) produces the largest and fastest growing flame kernels while the 0° index orientation where flame kernel is convected onto the ground strap produces the smallest and slowest growing flame kernels. For the cycles whose initial flame kernels are convected to the intake side, 0° index orientation, however, exhibits slight advantage over the other two index orientations.

8.2 Introduction

Automotive engines are in transition from port fuel injection (PFI) to direct injection (DI) for that DI offers more precise fuel metering, cylinder charge cooling and the potential to achieve lean combustion by stratification. However, in the United States, all direct injection spark ignition (DISI) gasoline engines still operate in stoichiometric homogenous charge conditions with various levels of exhaust gas recirculation (EGR) except during the cold startup period, due to the limitations of the three-way catalyst and high particulate matter produced at stratified conditions. While technologies are being investigated to achieve commercialization of lean and stratified combustion of DI gasoline engines in the United States [58], there is still a need to further optimize the DISI engine in homogenous charge conditions.

One common and widely studied method to reduce gasoline engine NOx emission and to increase thermal efficiency (by de-throttling) is to introduce EGR, either through external EGR or through internal EGR via cam phasing [59]. The residual burned gas increases the charge heat capacity, lowers the peak in-cylinder temperature, thus reducing the production of NOx. As EGR level increases, the combustion stability decreases, eventually to the point that the engine can no longer operate. The physics behind this phenomenon is that as EGR level increases, the combustion becomes increasingly sensitive to the variations in in-cylinder conditions such as charge motion, charge composition, and thus the combustion stability is compromised.

Ignition, as the start and trigger of the combustion process, has been proved to have a dominant role in determining the quality of the entire combustion process. Prior studies [25, 52, 60-62] found that the spark discharge duration has a strong impact on the initial flame kernel size and growth rate, leads to shorter ignition delay and combustion duration and extended lean combustion limit. Nakai's work [25] suggested that 5ms discharge duration could effectively shorten the combustion delay and reduce cycle-by-cycle variations in combustion delay. Chen's work [55] on a production Ford Ecoboost engine and Zhang's work [53] in a constant volume combustion chamber both indicate that, under

high charge flow motion, the timing and scheduling of the energy deposit into the gap could influence the initial flame kernel formation and thus affect the engine performance. The discharge duration and pattern were not the only factors found to impact the variations in combustion metrics [31, 37]. The orientations of the spark plug were found to impact the engine performance as well. Aleiferis et al. [33] found that crossflow orientation produces lowest cycle-by-cycle variation in terms of indicated mean effective pressure (IMEP); they also found the ground strap upstream performs the worst in terms of coefficient of variation of IMEP (COVimep). However, previous study by Anderson and Asik [54] suggested that upstream position performs better than downstream position.

The current work described by this paper tackles this question by investigating how the initial flame kernel is affected by the orientation of the spark plug in a homogenously charged single cylinder optical engine instrumented with a long discharge high energy ignition coil. By varying the spark plug orientations of two different electrode designs, size and location of early flame kernel was investigated.

Though much work has gone into designing the piston, combustion chamber, intake system to control the tumble inside gasoline ignition engines [13], the charge flow condition across the electrodes at the timing of ignition is still variable cycle by cycle. This is observed in this study. Cycles are categorized into two groups based on the initial flame kernel convection direction, either to the exhaust side of the combustion chamber in concurrence to the designed tumble direction or to the intake side counter to the designed tumble direction. Analysis is done for the two groups separately to gain a clear understanding how the relationship between electrode orientation and flow influences the flame kernel development.

In the following sections, the setup of the engine, test-bed, and optical instrumentation is described, followed by the introduction of the calculation methods of 2D and 1D probability distribution. Next, the results are discussed in group of cycles whose initial flame kernels are convected to the exhaust side in concurrence to the designed tumble direction and in group of cycles whose initial flame kernels are convected to the intake side

counter to the designed tumble direction for the two spark plugs respectively. A comparison is then made between the two spark plugs. At last, summary and conclusions are presented.

8.3 Experiment Setup

8.3.1 Optical Engine

The single cylinder optically accessible engine utilized in this research was designed and modified from a Ford four cylinder 2.0 L gasoline direction injection (GDI) engine by Mahle Powertrain (Figure 8-1) [23].The cylinder head is elevated to accommodate the Bowditch piston extension on cylinder number 2, which is the operating cylinder. The bottom of the Bowditch extension is bolted on the original number 2 piston, and on the top of the Bowditch extension is mounted a flat top piston with a 62 mm diameter sapphire (single-crystal aluminum oxide Al2O3) window insert allowing optical access through the piston. The elevated piston is separated from the crankcase and the oil circulation system, so self-lubricating piston rings made from torlon are used. The torlon pistons cannot tolerate high temperature for too long, so skip-firing operation strategy has to be applied during testing. A quartz liner providing optical access to the tumble plane is held against the cylinder head via a hydraulic clamping plate. The hydraulic clamping plate is raised to push the optical liner holder that holds the quartz liner against the cylinder head during engine operation via a hydraulic system; the quartz liner can be conveniently lowered and removed for cleaning and maintenance by releasing the hydraulic system pressure.

The production intake manifold for the original base engine is used to maintain the charge motion. A custom exhaust pipe is used along with the original integrated exhaust manifold. The original exhaust pipe is not used since it was designed to work with the turbocharger system. The optical engine has tumble ratio of about 1 at 2000 rpm. In the current study, the tumble ratio would be lower since the tests were done at 1000 rpm.

During testing, the fuel is pressurized to 4.5 MPa by an external high pressure fuel pump, and delivered to a production Bosch multi-hole GDI injector, which is installed on the edge of the pent-roof cylinder head below the two intake valves. The start of injection (SOI) occurs at 300 crank degrees before top dead center (°BTDC). The injection pressure and SOI were chosen based on the production engine calibration at the same operation conditions. The spark plug is located in the center of the pent-roof cylinder head, and the spark energy is supplied by a high energy coil (110 mJ, 3.2 ms nominal discharge duration). The specifications of the optical engine are summarized in Table 8-1.

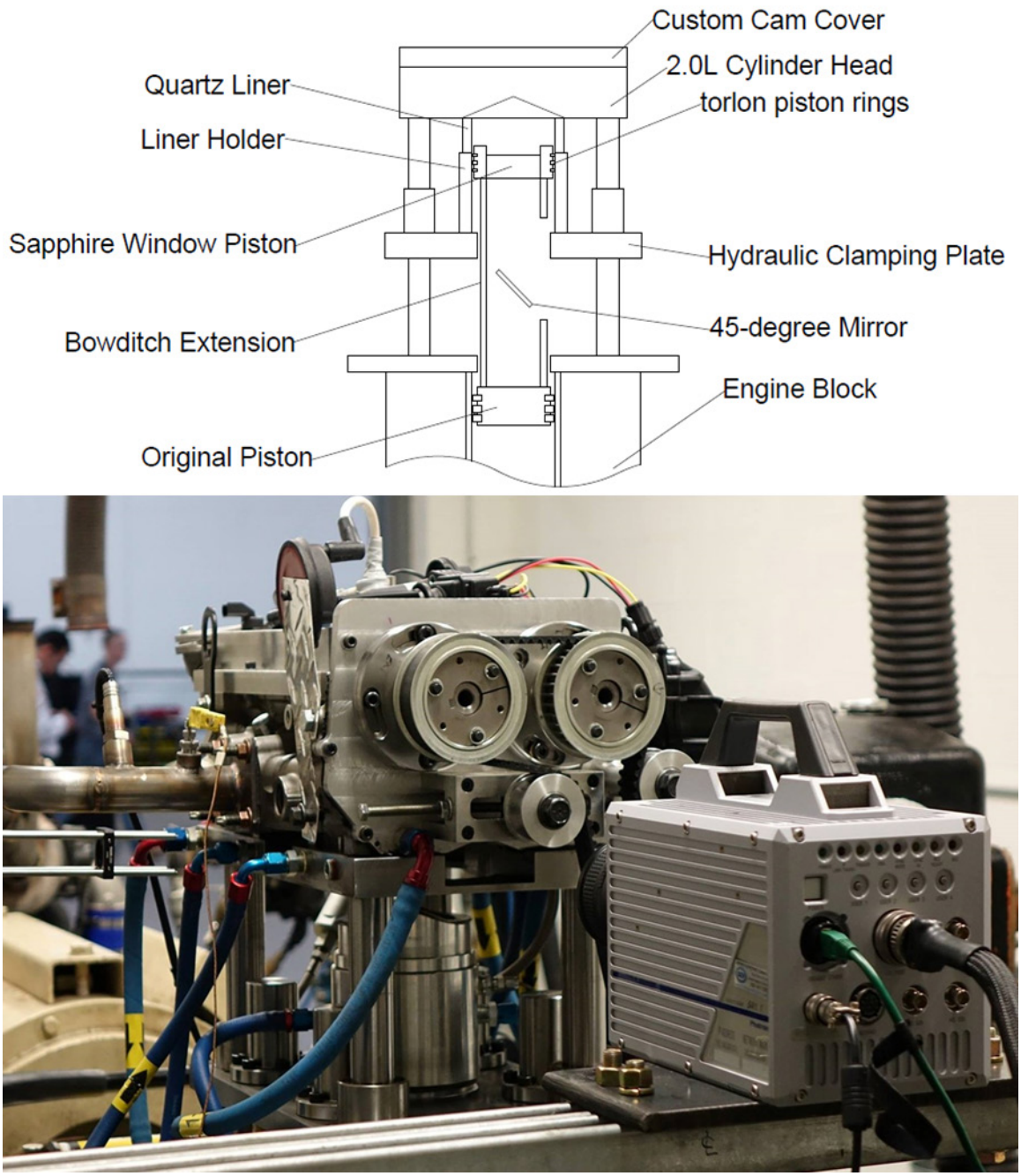

Figure 8-1: Top: schematic of the optical engine; bottom: optical engine with high-speed camera pointing to the tumble plane.

Table 8-1: Specifications of the optical engine.

Optical Cylinder Displacement (Liter)	0.6
Bore (mm)	87.5
Stroke (mm)	100.0
Compression Ratio	10.01 : 1
Fuel	RON 87
Injection Pressure	4.5 MPa
Start of Injection (SOI)	300 BTDC
Injector	Bosch 6-hole GDI injector
Ignition Coil	high energy long discharge coil
Spark Plug	double fine wire and oval-J spark plugs
Piston	flat top piston
Intake	Ford 2L Ecoboost intake manifold
Exhaust	custom exhaust manifold

8.3.2 Spark Plug Electrode Designs

Two spark plug electrode designs were used in this study: the double fine wire and the oval-J plug, as illustrated in Figure 8-2.

The double fine wire spark plug features standard double fine wire electrodes, and the oval-J spark plug also features two fine wire type electrodes; however, the ground electrode lies horizontally instead of vertically.

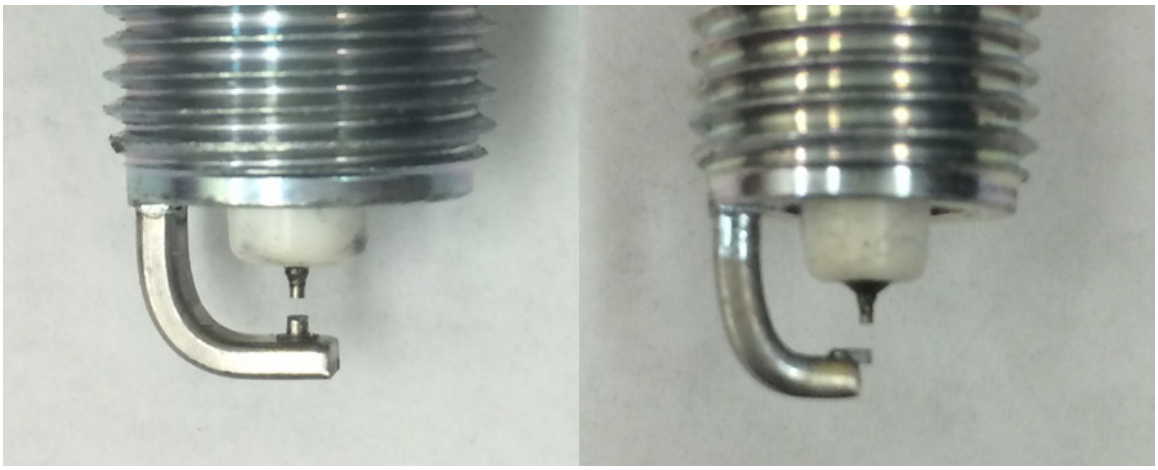

Figure 8-2: Left: double fine wire spark plug; Right: oval-J spark plug.

The specifications of each spark plug are summarized in Table 8-2. Notice for the oval-J spark plug, the exact index angles are 0°, 100° and 170°.

Table 8-2: Specifications of the studied spark plugs.

Spark Plug	Index Orientation (deg)	Gap Size (mm)	Internal Resistance (kΩ)
Double Fine Wire	0	0.65	4.83
	90	0.65	4.04
	180	0.65	4.23
Oval-J	0	0.65	4.21
	100	0.65	4.59
	170	0.65	5.24

8.3.3 Definition of Spark Plug Orientation

Conventionally in literature, the spark plug orientation is termed as crossflow, upstream or downstream. However, this type of definition can be confusing in consideration that the flow direction at the moment of ignition can vary cycle-by-cycle. Therefore, index orientation defined by angle is used and explained as follows.

As shown in Figure 8-3, looking from top of the engine, 0° is defined as spark plug gap facing the intake side; 180° is defined as the spark plug gap facing the exhaust side; while 90° is defined as spark gap facing the front end of the engine where the high-speed camera is located. Negative degrees are defined as the spark gap facing the rear end of the engine where the view of the camera is partially blocked by the ground strap.

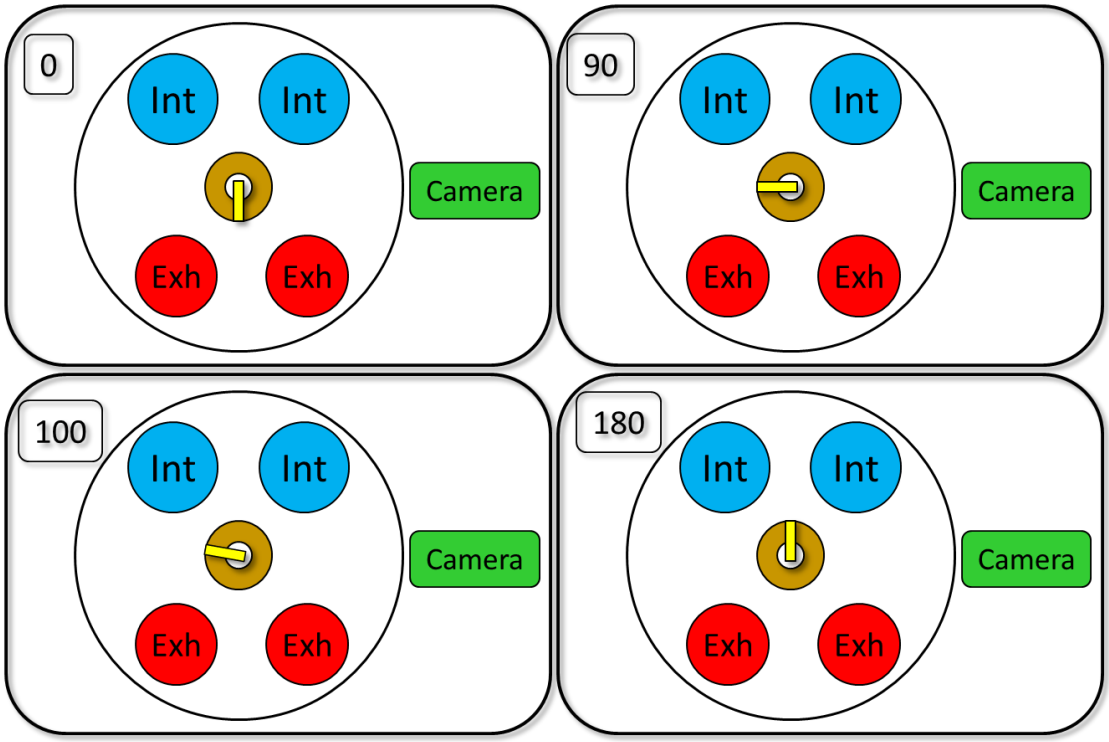

Figure 8-3: Definition of index angle in this study, viewing from top of the engine. "Int" and "Exh" stand for intake side and exhaust side respectively.

8.3.4 High-Speed Camera

The flame images were captured from 3°CA before the end of ignition coil dwell (the end of ignition coil dwell will be referred to as ignition timing in this paper) to 78°CA after ignition with Photron SA1.1 high-speed camera at 10,000 fps frame rate. The camera is positioned on the front end of the engine, pointing to the tumble plane through the quartz liner. The image resolution is 768 × 512 pixels covering a 59mm × 40mm area on the tumble plane. The images presented in this paper are cropped to focus on the spark plug

area; an example of the camera view is shown in Figure 8-4, where on the left is the exhaust side and on the right is the intake side. This study focuses on the flame kernel propagation on the tumble plane.

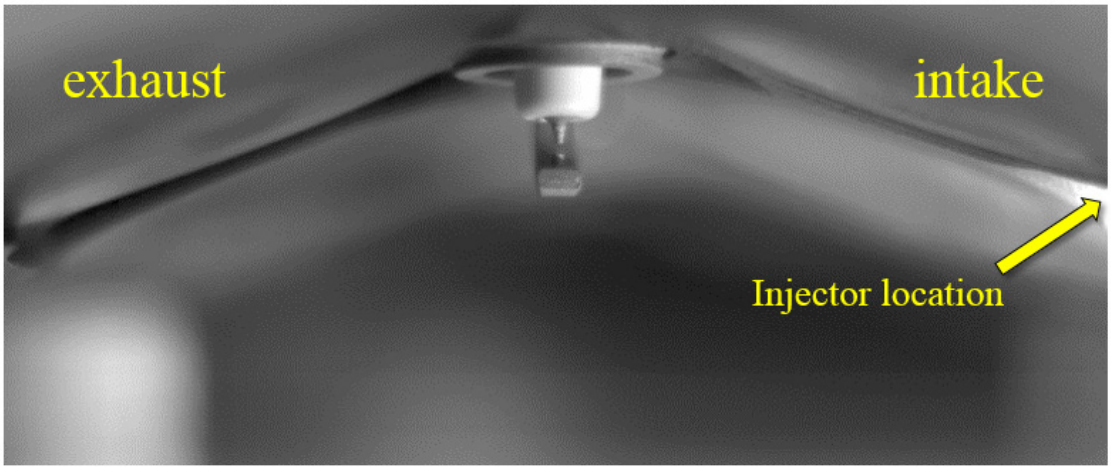

Figure 8-4: High-speed camera view (cropped); injector is located below the intake valves.

Table 8-3: High-speed camera configurations.

Camera Model	Photron SA 1.1
ISO	10,000
Frame Rate (fps)	10,000
Resolution	768 × 512
Lens	Nikon 85 mm + 12 mm Extension
F/stop	1.4
Trigger	3°CA before ignition

8.3.5 Combustion Analysis

In-cylinder pressure was measured by a piezoelectric pressure transducer (PCB 115A04), which is installed through a port drilled between the intake valve and exhaust valve. The

piston position was measured by an optical encoder with 0.5 degree resolution. The data was post-processed in Matlab to obtain the combustion related metrics using the 1D apparent heat release analysis with variable polytropics without heat transfer or crevice volume effects [40].

8.4 Engine Operation

The optical engine was skip-fired for 5 firing groups with each group composed of 15 motored and 10 fired cycles (Figure 8-5). The first five fired cycles of each firing groups were removed from statistical calculations and results, in consideration of the transitional state from the motored cycles to the fired cycles. The fuel was injected at 300°BTDC to achieve a homogeneous mixing at the timing of the initial spark discharge, which occurs at 47°BTDC.

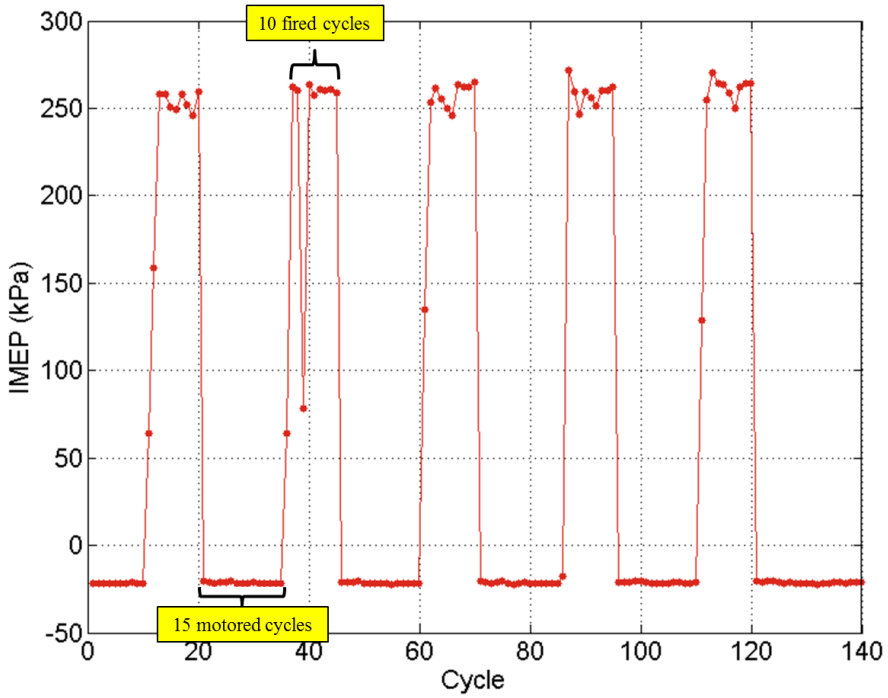

Figure 8-5: Skip-fire strategy: 5 groups of 15 motored cycles and 10 fired cycles.

The tests were conducted at 2.5 bar IMEP at 1000 rpm. Combustion phasing was controlled to an average of 8°ATDC, and the equivalence ratio was controlled near $\lambda = 1.38$, in order to introduce enough variations in combustion between cases. The test matrix is summarized in Table 8-4. Each test point was repeated and results of the two test runs were combined for statistical analysis; this results in 10 firing groups with 5 cycles in each for a total of 50 cycles at each test point. In the first column of Table 8-4, DFW stands for double fine wire electrode design and oval-J stands for oval shape J plug electrode design. Notice for DFW, 0°, 90° and 180° orientation index were used and for oval-J electrode, 0°, 100° and 170° orientation index were used, due to lack of oval-J spark plugs of exact indexing at 90° and 180°. This difference is not expected to be significant based upon flow testing and discharge measurements in other studies [46].

Table 8-4: Test Matrix.

Spark Plug	Spark Plug Orientation (degs)	Target IMEP (bar)	Target Speed (RPM)	Target CA50 (°ATDC)	Target Lambda (-)
DFW	0, 90, 180	2.5	1000	8	1.38
Oval-J	0, 100, 170				

8.5 Data Analysis Methods

8.5.1 Mathematical Tools

The images of the cycle-by-cycle flame kernels were filtered by a 3 × 3 2D-median filter to remove noise and then processed by two equations for better understanding the statistical results. The equations are explained as follows.

8.5.1.1 2D Probability Distribution Function (2D-PDF)

The 2D-PDF shows the probability of the flame kernel reaching a certain point in the 2D space captured by the camera (equation 8-1).

$$PDF_{2D,t} = \frac{\sum_{i=1}^{n} I_{t,i} \begin{Bmatrix} I_{t,i} = 1,\ I_{t,i} > threshold \\ I_{t,i} = 0,\ \ I_{t,i} < threshold \end{Bmatrix}}{n} \quad 8\text{-}1$$

In equation 8-1, I denotes the image intensity matrix; t is the timing of the current processed image in the current cycle, either in milliseconds after ignition timing (msAIT) or crank angle degrees after ignition timing (°CA_AIT); i represents which cycle the current processed image is from, and n is the number of cycles.

The illustration of how 2D-PDF is calculated is shown in Figure 8-6 along with 1D-PDF which will be explained in the following section.

8.5.1.2 1D Probability Distribution Function (1D-PDF)

While 2D-PDF offers a visual image of probability distribution, it is difficult to do a case by case comparison. 1D-PDF serves as a good tool for this purpose. It describes the number of flame kernels along the vertical direction (column) as in Figure 8-6, and the number of flame kernels along the horizontal direction (row). In this study, focus is on 1D-PDF along the vertical direction equation 8-2.

$$PDF_{1D,t,c} = \frac{N_{Flame\ Kernel_{t,c}}}{n} \quad 8\text{-}2$$

In equation 8-2, $N_{Flame\ Kernel}$ is the number of flame kernels, c indicates along the vertical direction.

A simple illustration of 1D-PDF and 2D-PDF is shown in Figure 8-6 using three images at 3 msAIT from three random cycles of the 90° index double fine wire spark testing.

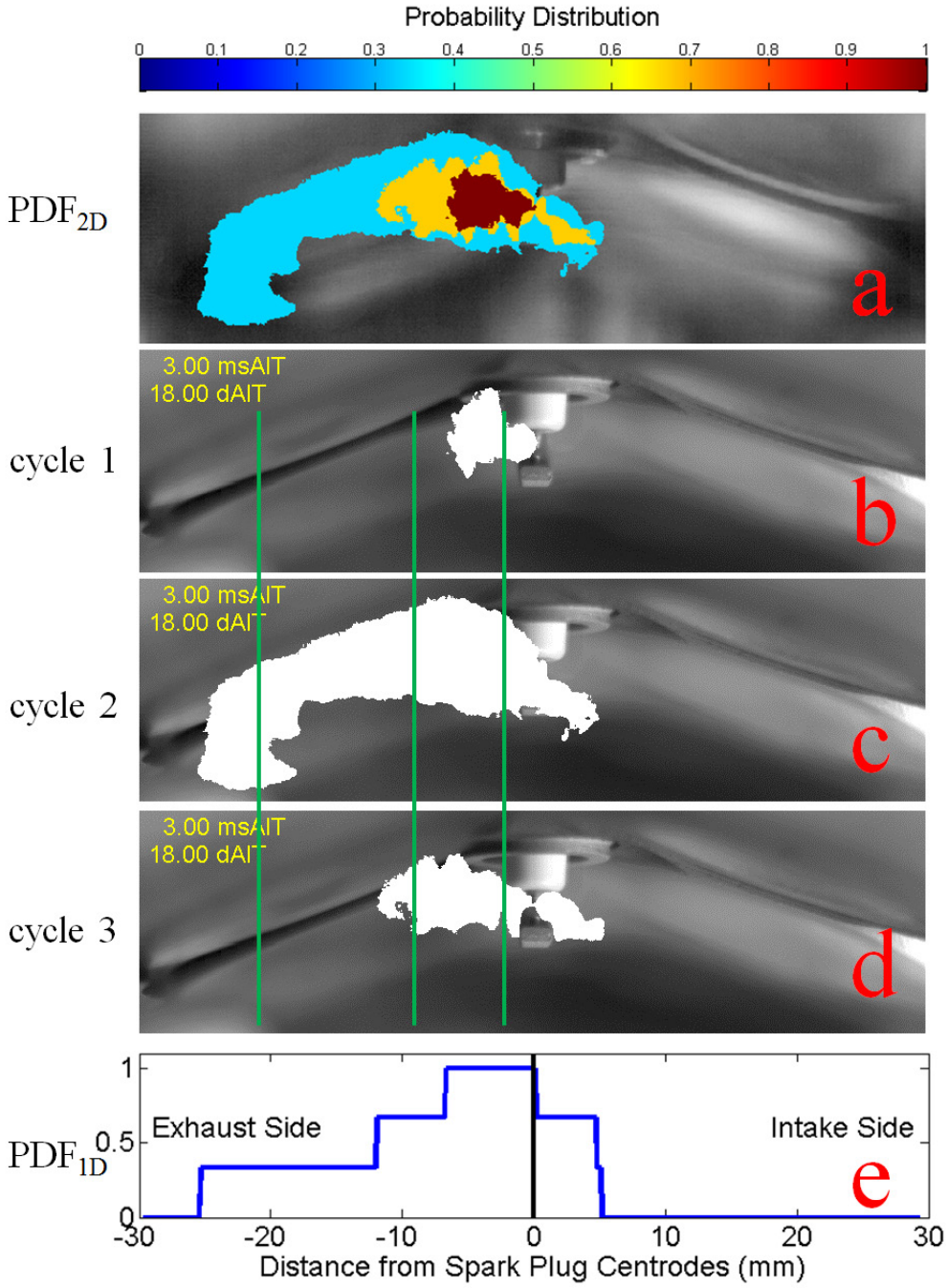

Figure 8-6: Illustration of 2D-PDF and 1D-PDF calculations. (a) 2D-PDF; (b) through (d) flames kernels at 3msAIT from three random cycles; (e) 1D-PDF.

In Figure 8-6, the flame kernels in (b), (c), (d) are added onto each other and normalized over the number of cycles (3 in this illustration) and color-coded to get the 2D-PDF in (a).

The 2D-PDF shows the spatial probability distribution of the flame kernels. To get the 1D-PDF shown in (e), the number of flame kernels are counted along the vertical lines across the three flame kernels in (b), (c) and (d). Three example vertical lines are shown in green. Along the first vertical line, one flame kernel is counted from (c); along the second vertical line, two flame kernels are counted from (c) and (d) , and along the third vertical line, three flame kernels are counted in (b), (c) and (d). The results are then normalized over the number of cycles (3 in this illustration) to get the 1D-PDF in (e).

As can be seen in later sections, comparisons can be conveniently made by overlaying 1D-PDF of different cases.

8.5.2 Categorization of Initial Flame Kernel Convection Direction

The optical engine combustion chamber and intake system were designed to have counterclockwise flow viewing from the front of the engine with exhaust on the left and intake on the right. However, cycle by cycle variations in initial flame convection direction were observed. Therefore, the cycles are categorized based on the initial flame kernel convection direction, either to the exhaust side in concurrence to the designed tumble direction (denoted as group A), to the intake side counter to the designed tumble direction (denoted as group B). The grouping criterion is the flame kernel centroid location relative to the spark plug center at 3msAIT at shown in Figure 8-7. After the categorization, the data analysis methods discussed in the early part of this section are performed on the two groups.

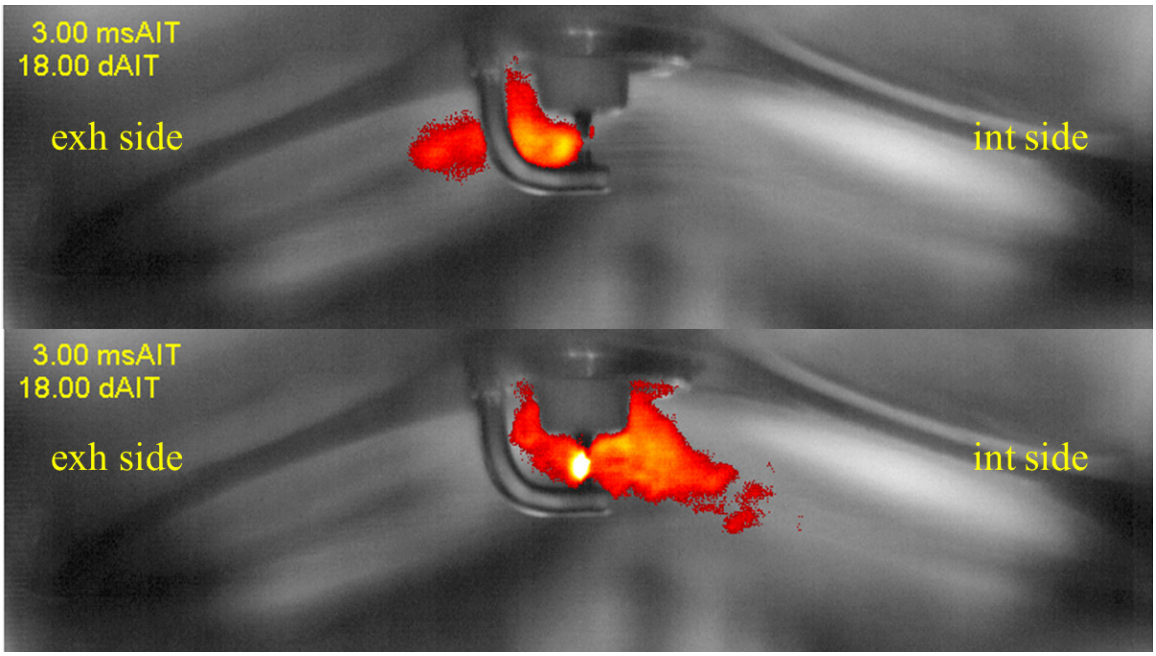

Figure 8-7: Sample initial flame kernel images at 3msAIT; upper: flame kernel convected to exhaust side in concurrence to the designed tumble direction (group A); lower: flame kernel convected to intake side counter to the designed tumble direction (group B).

The ratio of cycles of each group is summarized in Table 8-5. One interesting observation is that as the spark plug index orientation changes from 0° to 180°, the ratio of cycles in group B increases.

Table 8-5: Ratio of cycles of each categorized initial flame kernel convection group

Spark Plug	Gap Orient. (degs)	Ratio of cycles in group A	Ratio of cycles in group B
DFW	0	60%	40%
	90	40%	60%
	180	36%	64%
Oval-J	0	62%	38%
	100	32%	68%
	170	26%	74%

8.6 Results and Discussion

8.6.1 Double Fine Wire Spark Plug

8.6.1.1 Analysis of Group A

The 2D-PDF images of the cycles in group A are presented in Figure 8-8 for the double fine wire spark plug testing. In Figure 8-8, the left column is the 0° spark plug index orientation; in the middle is 90° index and on the right is the 180° index. Observation indicates the 90° index orientation produces the flame kernels that travel fastest into the exhaust side; while for the 0° case, the ground electrode restricts the flame kernel from traveling to the exhaust side. Direct comparison is better made in 1D-PDF plots in Figure 8-9.

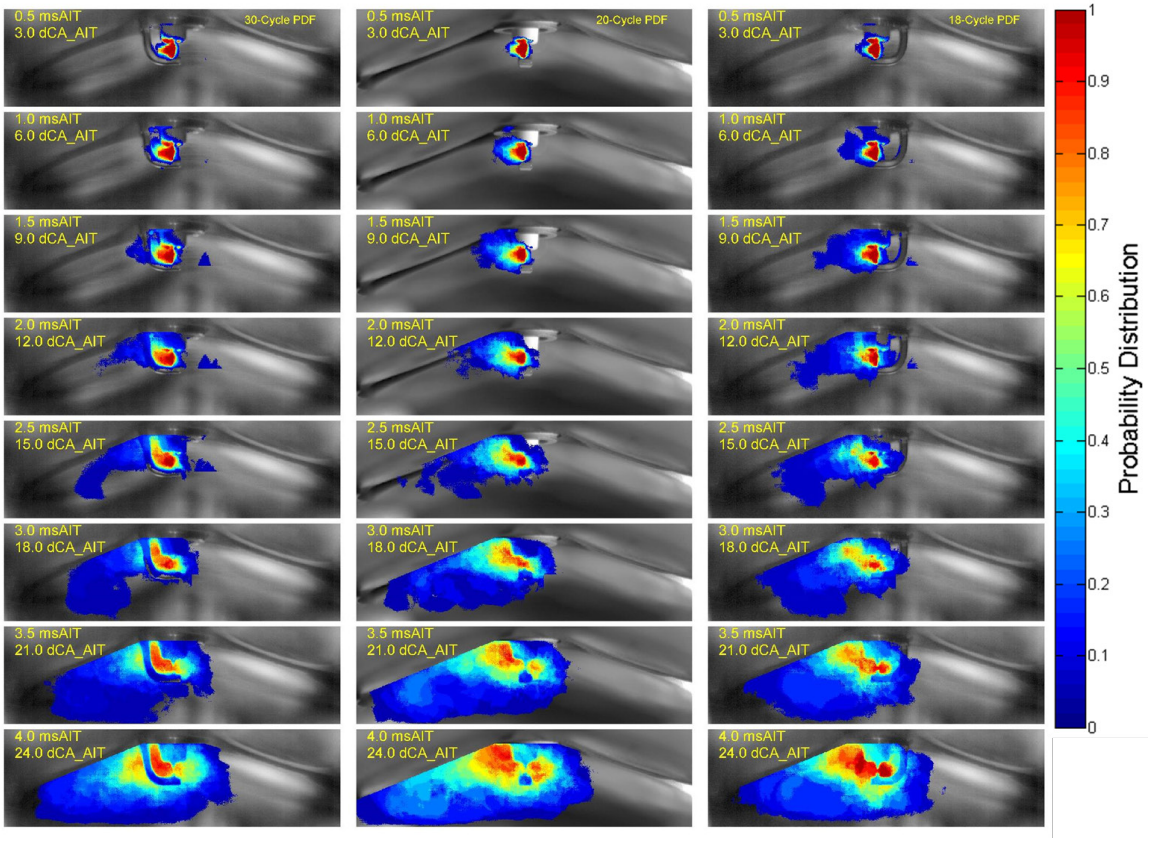

Figure 8-8: 2D-PDF of group A for DFW spark plug. left: 0° index; middle: 90° index; right: 180° index.

The 1D-PDF plots in Figure 8-9 provide a direct comparison between the three studied index orientations. The distance from the exhaust side to the spark plug tip is assigned negative and the distance from the intake side to the spark plug is assigned positive value. It is shown that 90° index orientation has a higher probability that the flame is convected faster to the exhaust (with 50% of cycles whose flame kernels reaching -10 mm at 3 msAIT); while 0° and 180° orientations do not exhibit significant advantages over each other.

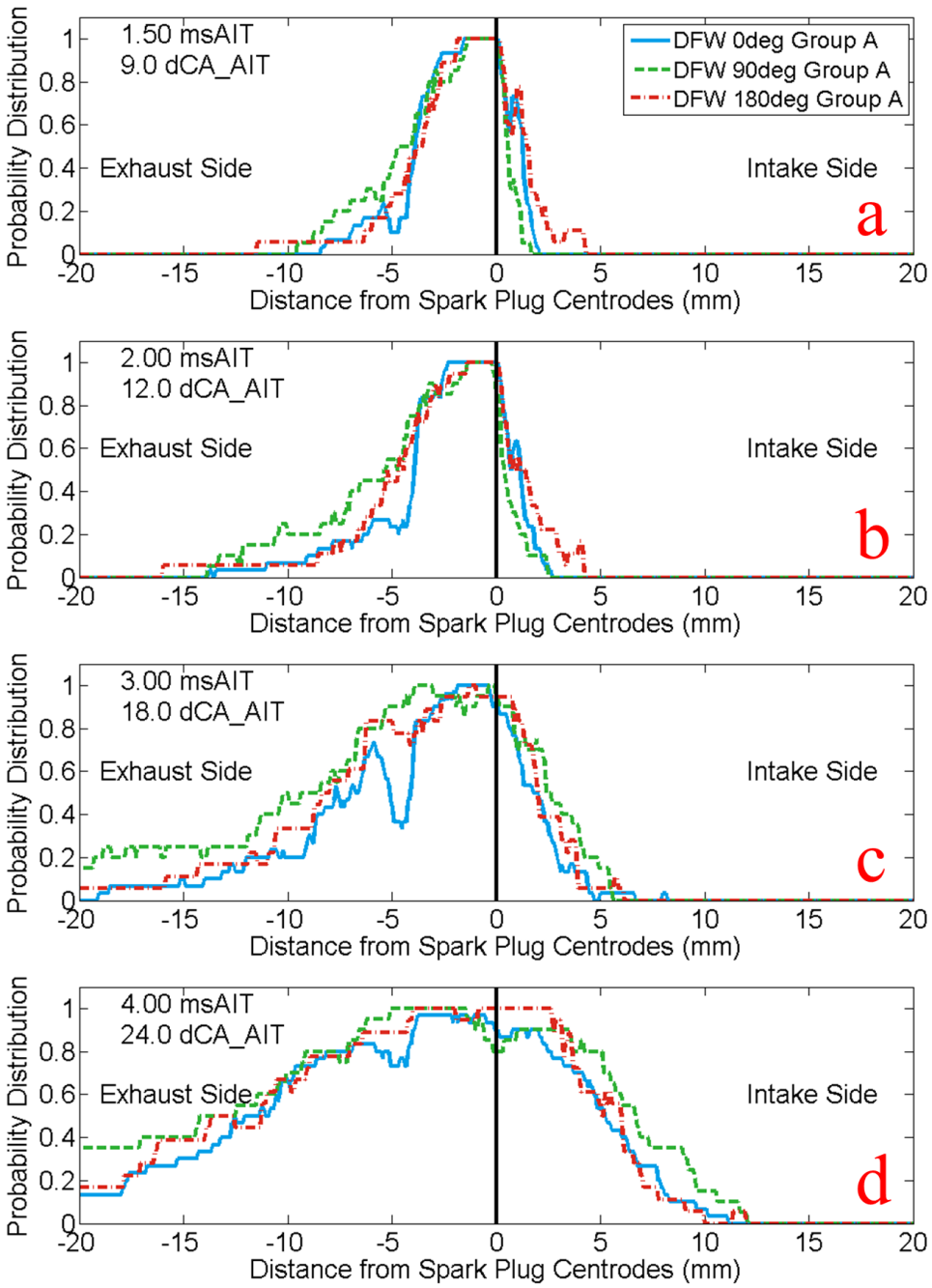

Figure 8-9: 1D-PDF of group A for DFW spark plug. (a) 1.5 msAIT; (b) 2 msAIT; (c) 3 msAIT; (d) 4msAIT.

In Figure 8-10 and Figure 8-11 are the mean mass fraction burned (MFB) and mean in-cylinder pressure of the corresponding cycles. Notice the mean MFB shown in this figure is averaged at each crank angle across the analyzed cycles. They exhibit the same trend as

shown in Figure 8-9, where 90° index orientation results in the fastest MFB with 0° and 180° orientations being close to each other. The 90° index orientation has advantage over the other two index orientations due to that the newly formed flame kernels are more stretched compared with 180° index orientation where the ground strap is shielding the charge flow, and it has less contact area with the ground strap compared to 0° index orientation, which leads to less heat loss. The same trend also applies to observations on the in-cylinder pressure in Figure 8-11.

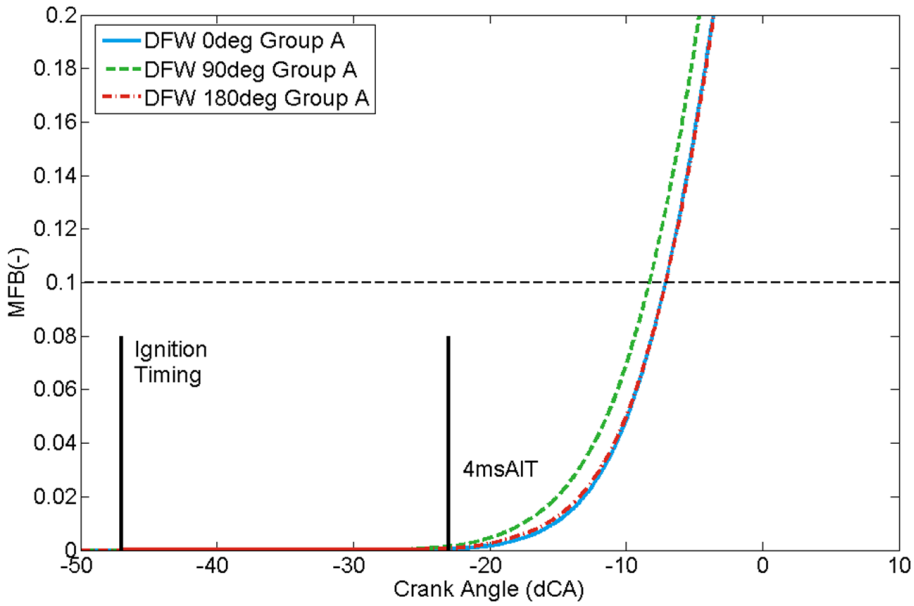

Figure 8-10: Mean MFB for group A for DFW spark plug.

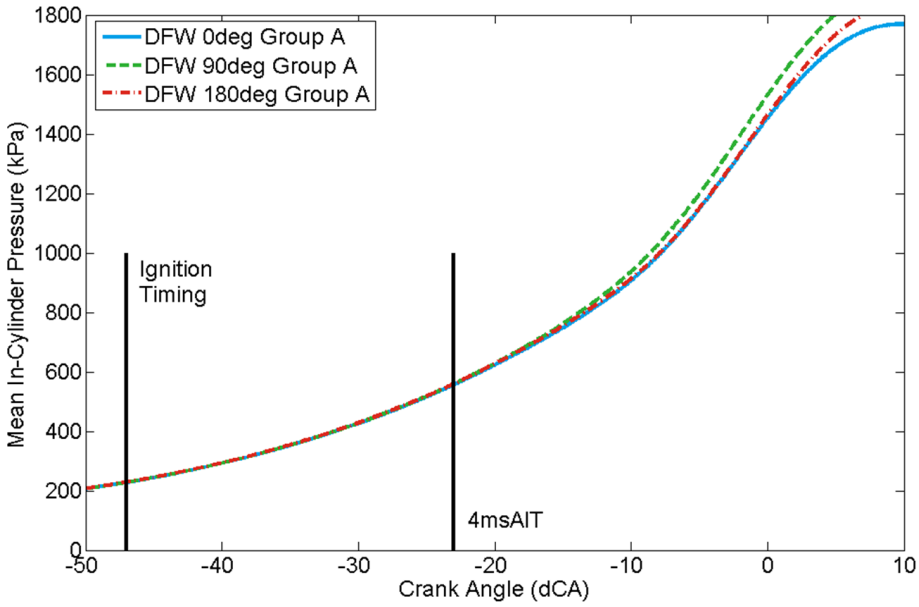

Figure 8-11: Mean in-cylinder pressure for group A for DFW spark plug.

8.6.1.2 Analysis of Group B

Even though this particular engine was designed to have a counterclockwise tumble flow viewing from the front of the engine, the following results indicate that there are cycles whose initial flame kernels are convected to the intake side counter to the designed tumble direction, due to overall low tumble motion.

The 2D-PDF images of group B are presented in Figure 8-12 for the double fine wire spark plug. Visual inspection reveals that, for these cycles, the flame kernels tend to be smaller and more centered on the spark plug and propagate more evenly outwards with less stretching, which indirectly reflected the overall low tumble motion in the cylinder.

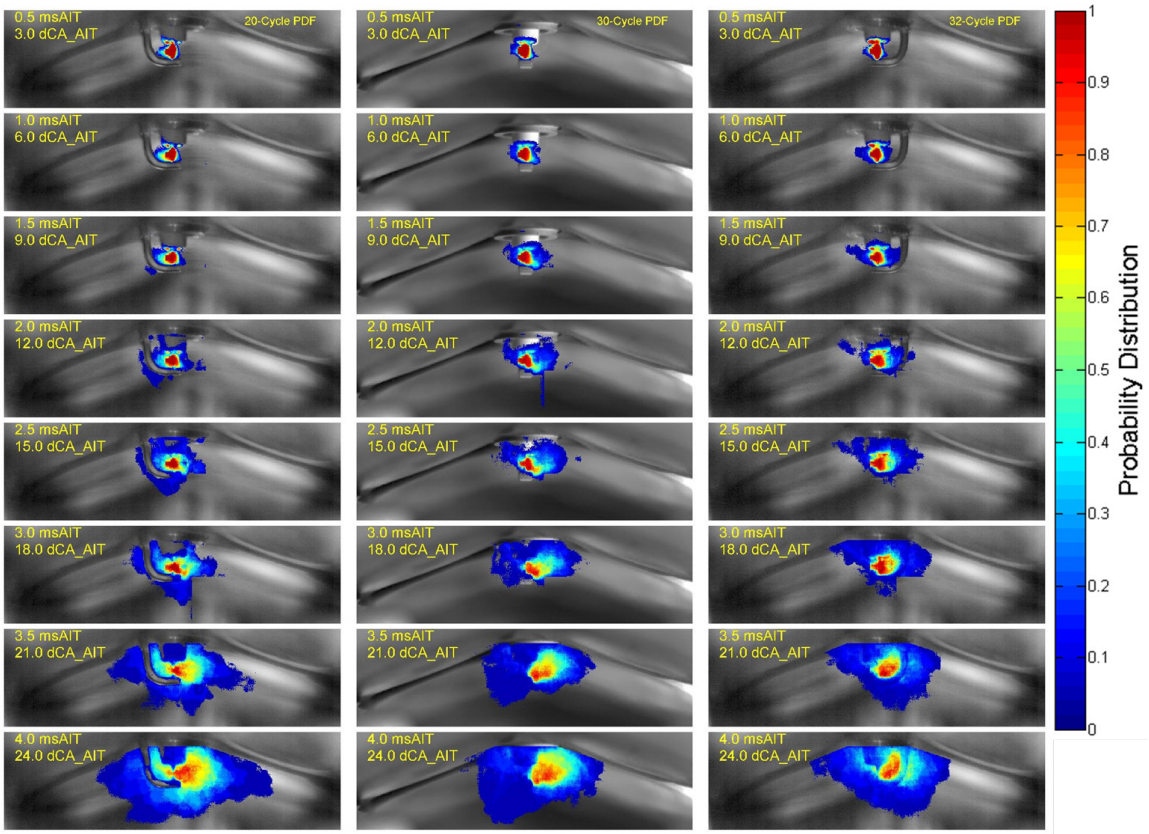

Figure 8-12: 2D-PDF of group B for DFW spark plug. left: 0° index; middle: 90° index; right: 180° index.

The 1D-PDF in Figure 8-13 shows that, especially at 3 msAIT and 4 msAIT, the 90° index orientation results in flame kernels with slightly higher probability to travel faster to the intake side (with 33% of cycles whose flames reaching 10 mm at 4 ms); however, it results in a low probability for the flame to travel to the exhaust side (with only 3% of cycles whose flames reaching -10 mm at 4 msAIT). The 0° index orientation, on the other hand, produces flame kernels with high probability to propagate to the exhaust side. The distinction between the three index orientations is small that none exhibits significant advantages over the other two.

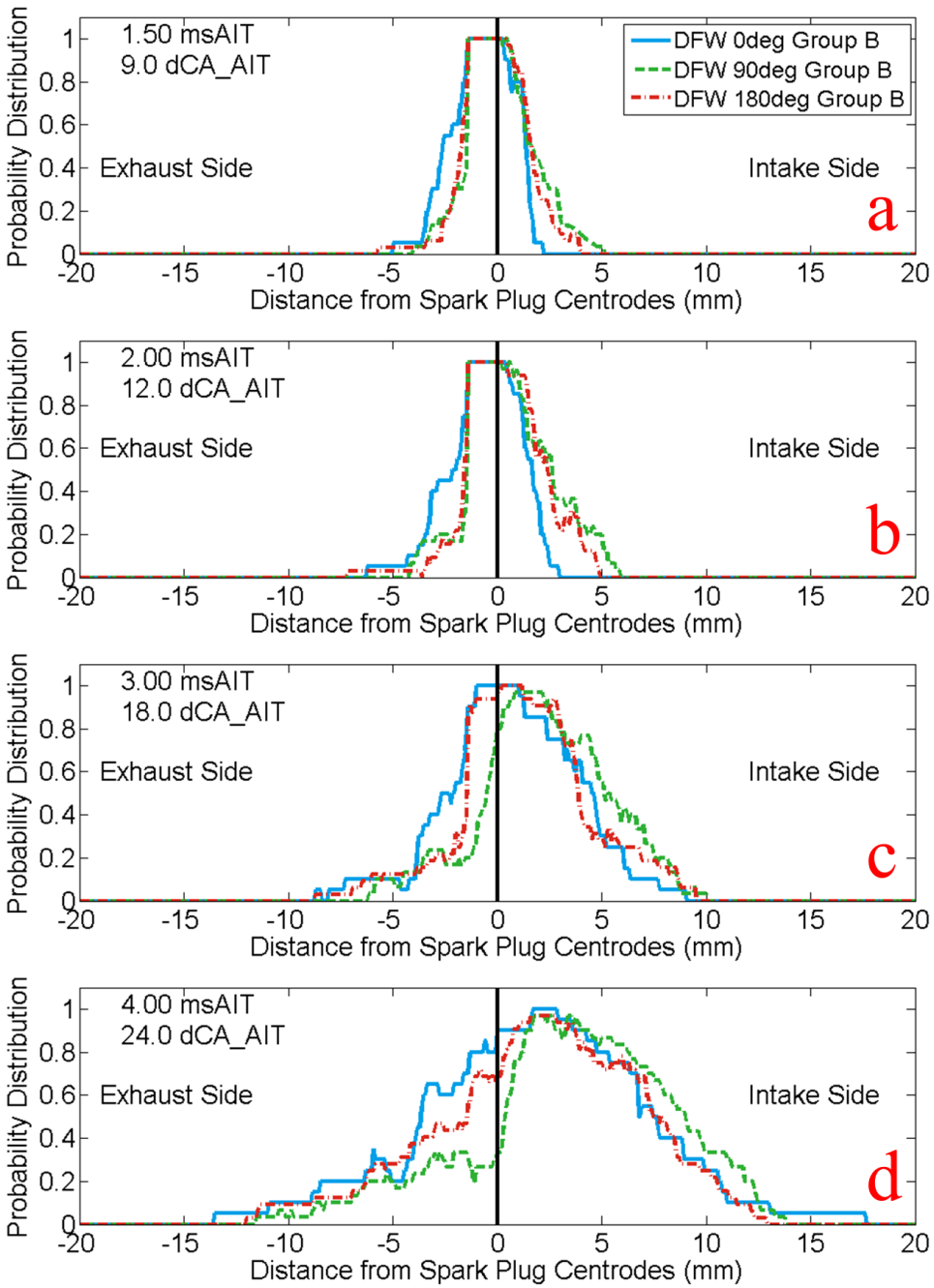

Figure 8-13: 1D-PDF of group B for DFW spark plug. (a) 1.5 msAIT; (b) 2 msAIT; (c) 3 msAIT; (d) 4 msAIT.

The mean MFB profiles and in-cylinder pressure (Figure 8-14 and Figure 8-15), however, demonstrates greater differences between the three index orientations with 0° having the fastest MFB, and 90° and 180° being close to each other.

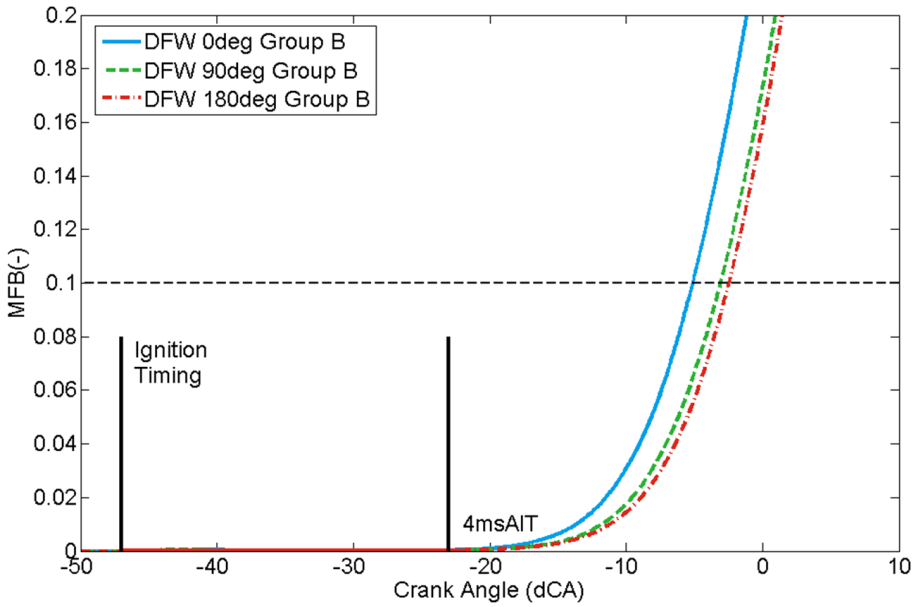

Figure 8-14: Mean MFB for group B for DFW spark plug.

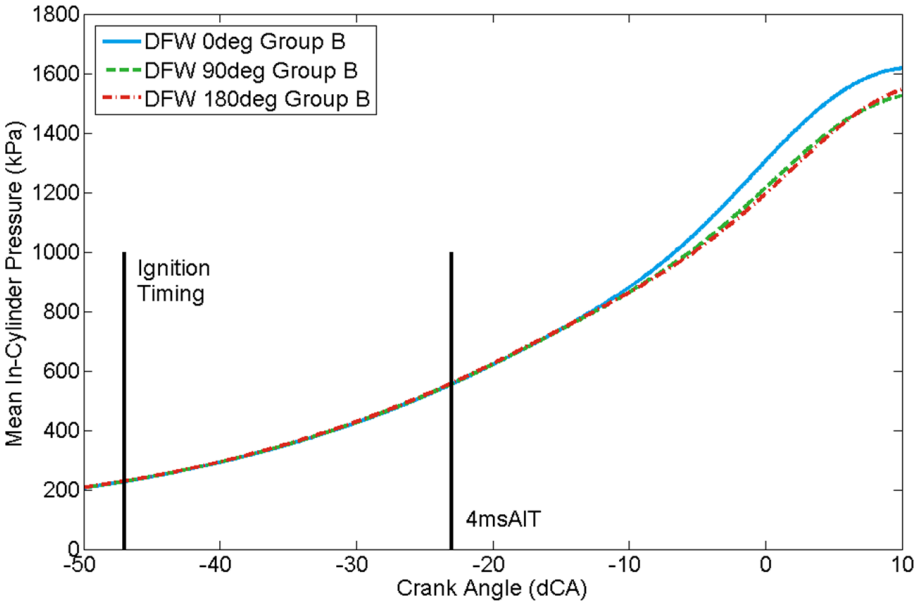

Figure 8-15: Mean in-cylinder pressure for group B for DFW spark plug.

8.6.1.3 Combustion Metrics Analysis

The ignition delay is defined as the duration from the start of ignition to the crank angle of 10% mass faction burned (CA0010), and the combustion duration is defined as the duration from the crank angle of 10% mass fraction burned to 90% mass fraction burned (CA1090). Both CA0010 and CA1090 are averaged for the analyzed 50 cycles and for each categorized group and shown in Table 8-6 and Table 8-7. Notice the averaging here is performed on the calculated metrics (CA0010 and CA1090) across the analyzed cycles, so results might be slightly different than what is shown in the mean MFB plot in Figure 8-10 and Figure 8-14 where the averaging is performed at each crank angle. For group A where initial flame kernels are convected to the exhaust side in concurrence to the designed tumble direction, the 90° index orientation produces the shortest mean ignition delay (40.2°CA) and also the shortest combustion duration (20.5°CA) due to the high probability of the flame kernels propagating to the exhaust side (Figure 8-9) with minimum contact with the spark plug material, thus leading to low heat loss. The 0° index orientation produces the longest ignition delay (41.6°CA) and longest combustion duration (24.1°CA) due to that the initial flame kernels are convected onto the ground strap which can lead to high heat loss.

For group B where initial flame kernels are convected to the intake side counter to the designed tumble direction, the 0° index orientation results in shortest ignition delay (43.8°CA). However, the 180° index orientation results in the shortest combustion duration (25.9°CA). Since there is generally low tumble motion for group B, the impact of the tumble motion on the entire combustion process is uncertain, and the low tumble motion may not be the dominant factor in determining the overall combustion rate; thus the combustion duration may not be well correlated to the ignition delay.

Table 8-6: Ignition delay CA0010 of DFW.

Spark Plug	Gap Orient. (degs)	Overall Mean CA0010 (°CA)	Mean CA0010 for Group A (°CA)	Mean CA0010 for Group B (°CA)
DFW	0	42.5	41.6	43.8
	90	44.1	40.2	46.8
	180	44.3	41.1	46.1

Table 8-7: Combustion duration CA1090 of DFW.

Spark Plug	Gap Orient. (degs)	Overall Mean CA1090 (°CA)	Mean CA1090 for Group A (°CA)	Mean CA1090 for Group B (°CA)
DFW	0	25.3	24.1	27.1
	90	25.4	20.5	28.9
	180	24.2	21.2	25.9

In Figure 8-16, CA1090 is plotted against CA0010 for group A. One can observe that 90° orientation results in better correlation between CA1090 and CA0010, while the other two index orientations result in weak correlation with greater variations in CA1090. The standard deviation (std) of CA1090 for 90° orientation is 2.9°CA and std of CA1090 for 0° and 180° cases are 8.4°CA and 5.1°CA.

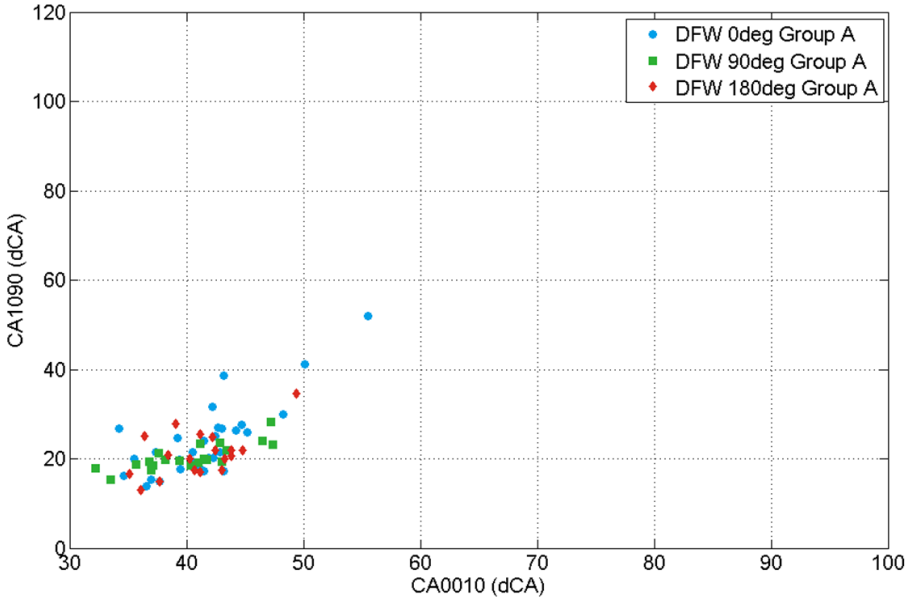

Figure 8-16: CA0190 vs CA0010 of group A for DFW spark plug.

8.6.2 Oval-J Spark Plugs

8.6.2.1 Analysis of Group A

The 2D-PDF images of Group A for the oval-J spark plug are presented in Figure 8-17. The 100° index orientation (center column) shows bigger and more consistent flame kernels than the other two cases. This is further confirmed by the 1D-PDF in Figure 8-18, where 100° index shows higher probability of fastest growing flame kernels both to the exhaust side and the intake side (with 56% of cycles whose flame kernels reaching -10 mm at 4 msAIT), while 0° index orientation results in slowest growing flame kernels (with only 23% of cycles whose flame kernels reaching -10 mm at 4 msAIT).

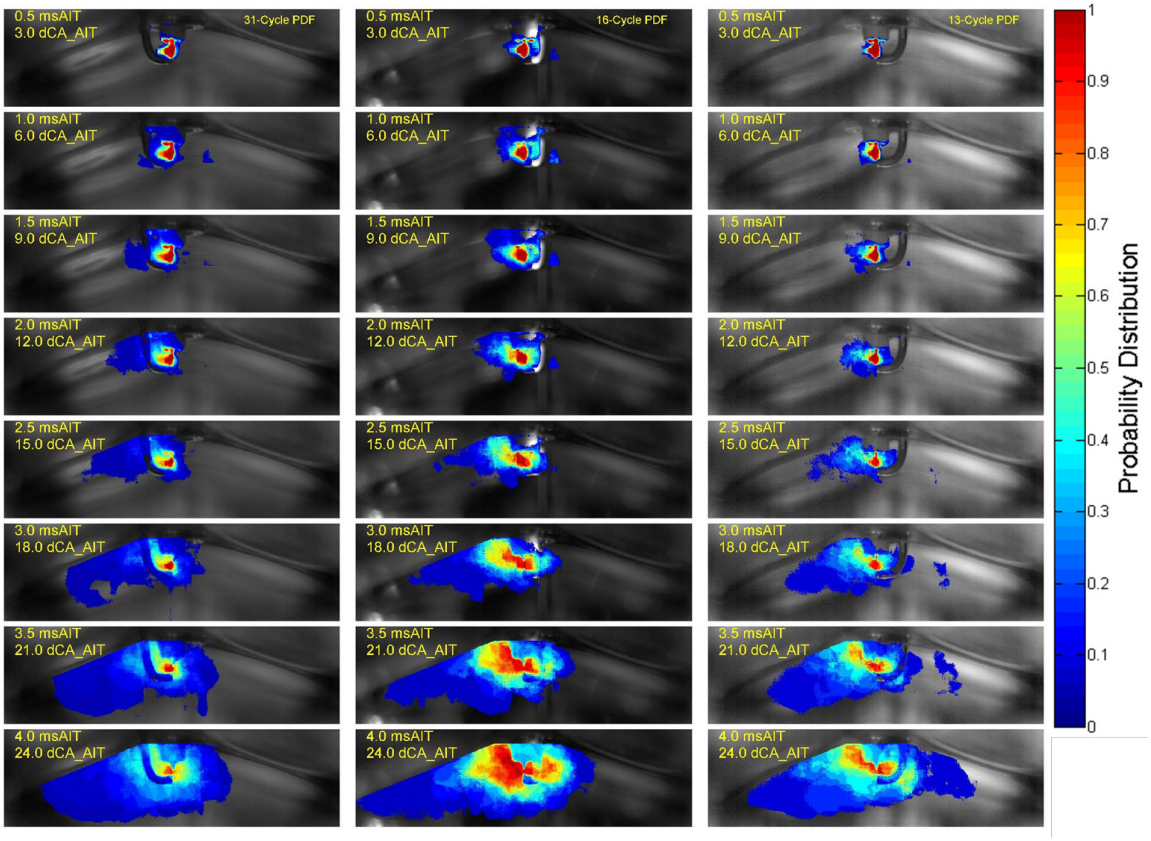

Figure 8-17: 2D-PDF of group A for oval-J spark plug. left: 0° index; middle: 100° index; right: 170° index.

Another interesting finding is that, the oval-J spark plug generally produces smaller flame kernels than the double fine wire at the same timings by comparing Figure 8-8 and Figure 8-17. The comparison will be further described in the following section.

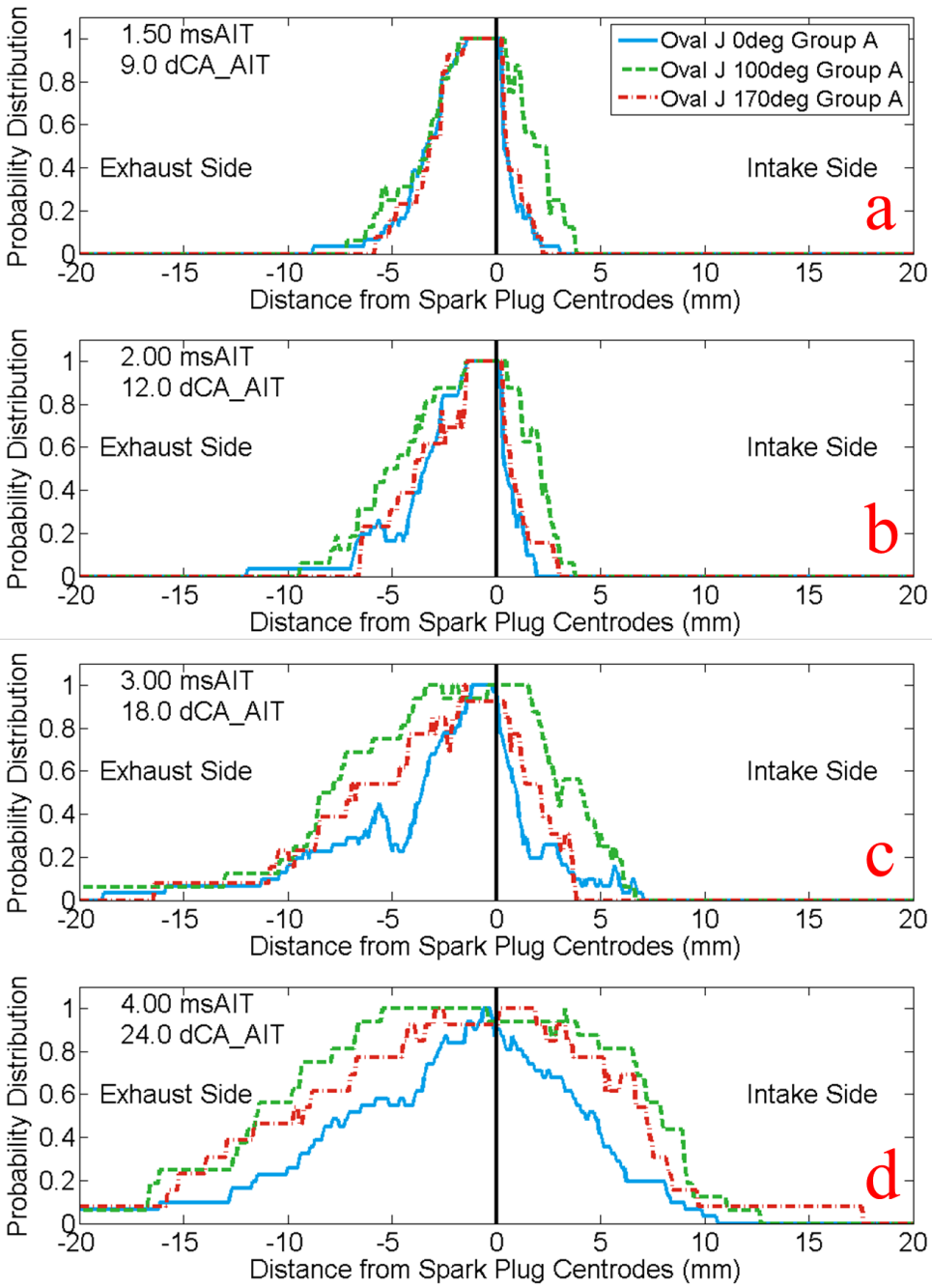

Figure 8-18: 1D-PDF of group A for the oval-J spark plug. (a) 1.5 msAIT; (b) 2 msAIT; (c) 3 msAIT; (d) 4 msAIT.

The MFB curve and in-cylinder pressure show the same trend in Figure 8-19 and Figure 8-20. The 100° results in the fastest burning cycles and fastest rising pressure trace; while

the 0° index orientation results in the slowest burning. This result is consistent with the observation made from the double fine wire case in Figure 8-10 and Figure 8-11.

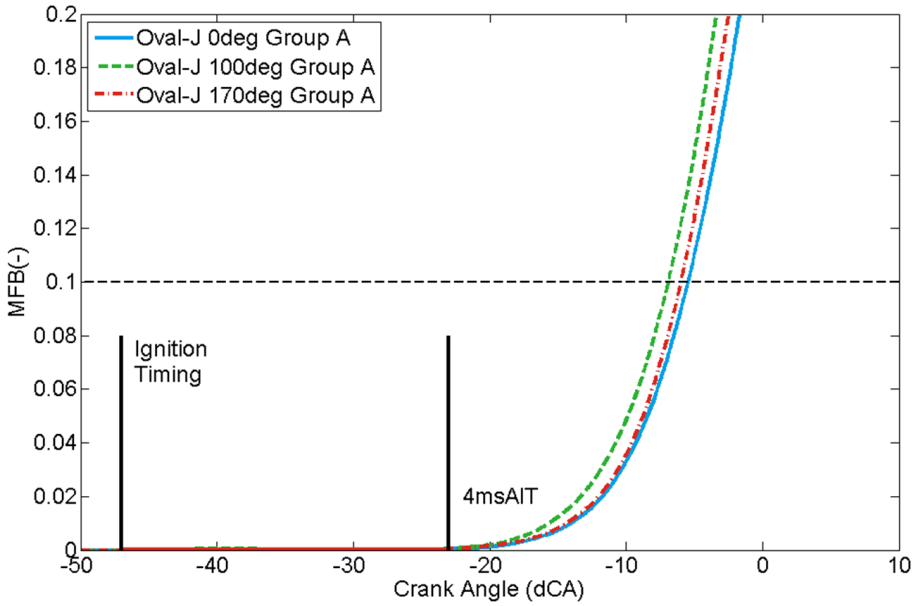

Figure 8-19: Mean MFB for group A for oval-J spark plug.

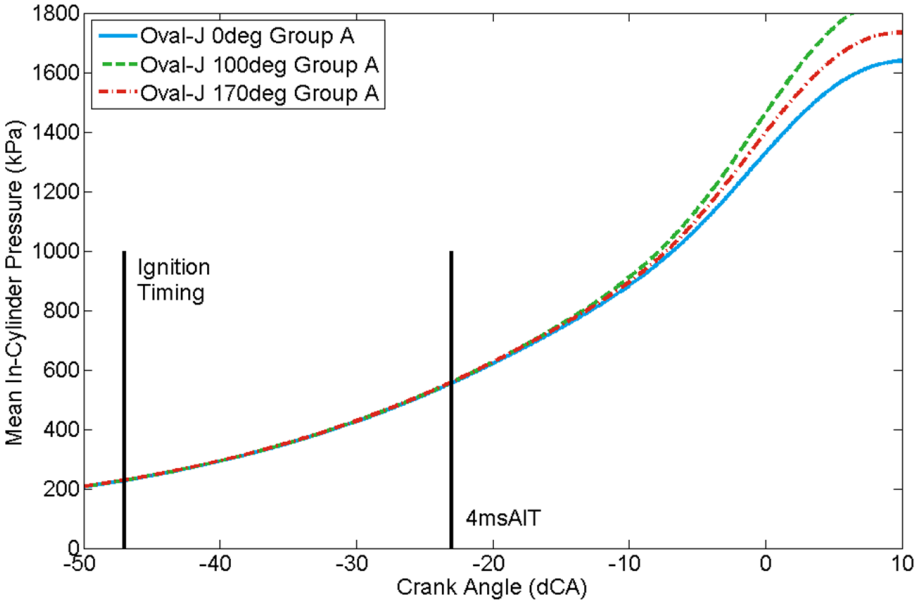

Figure 8-20: Mean in-cylinder pressure for group A for oval-J spark plug.

8.6.2.2 Analysis of Group B

With no exception, the oval-J spark plug testing also saw cycles whose initial flame kernels were convected to the intake side of the cylinder counter to the designed tumble direction. The 2D-PDF results of these cycles are presented in Figure 8-21.

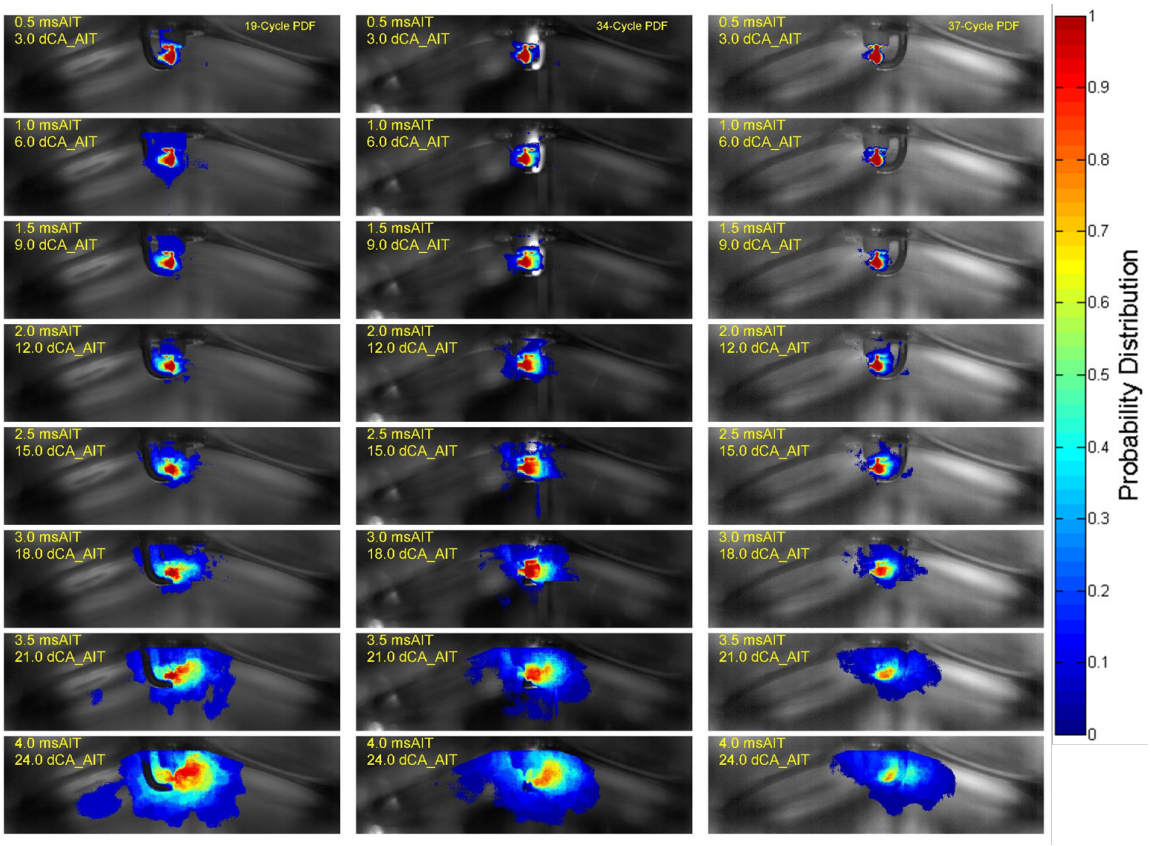

Figure 8-21: 2D-PDF of group B for oval-J spark plug. left: 0° index; middle: 100° index; right: 170° index.

The 1D-PDF in Figure 8-22 shows a clear difference between the three index orientations especially at 4 msAIT. The 0° index orientation exhibits the fasted growing flame kernels (with 42% of cycles whose flame kernel reaching -5 mm at 4 msAIT) than the other two index orientations, and the 170° index results in the slowest growing flame kernels (with only 14% of cycles whose flame kernel reaching -5 mm at 4 msAIT).

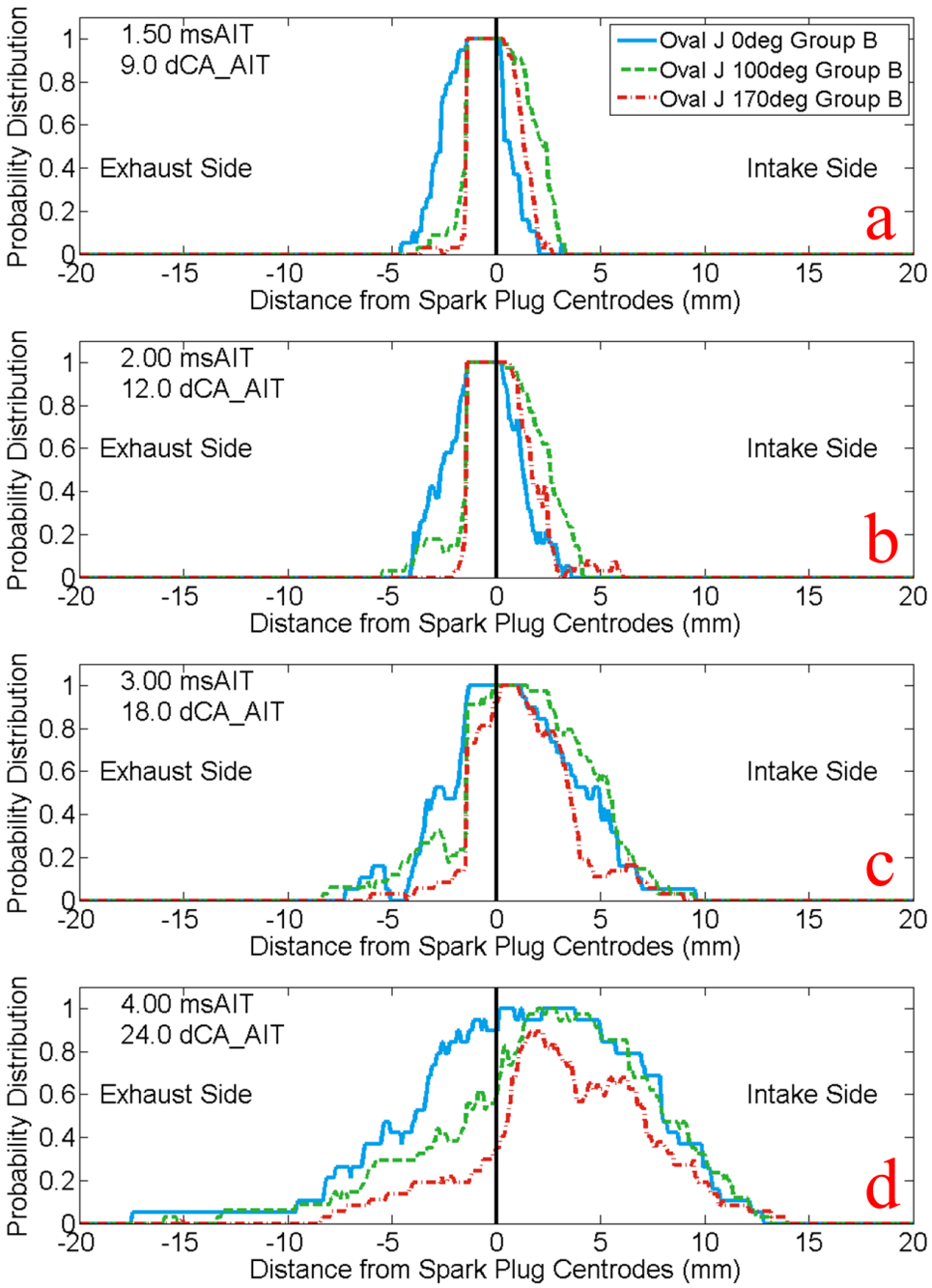

Figure 8-22: 1D-PDF of group B for the oval-J spark plug. (a) 1.5 msAIT; (b) 2 msAIT; (c) 3 msAIT; (d) 4 msAIT.

The difference is clearly exhibited in the MFB and in-cylinder pressure traces in Figure 8-23 and Figure 8-24. The 0° index orientation having the fastest growing mean MFB trace

and mean pressure trace, and the 170° index orientation results in the slowest growing mean MFB trace and mean pressure trace.

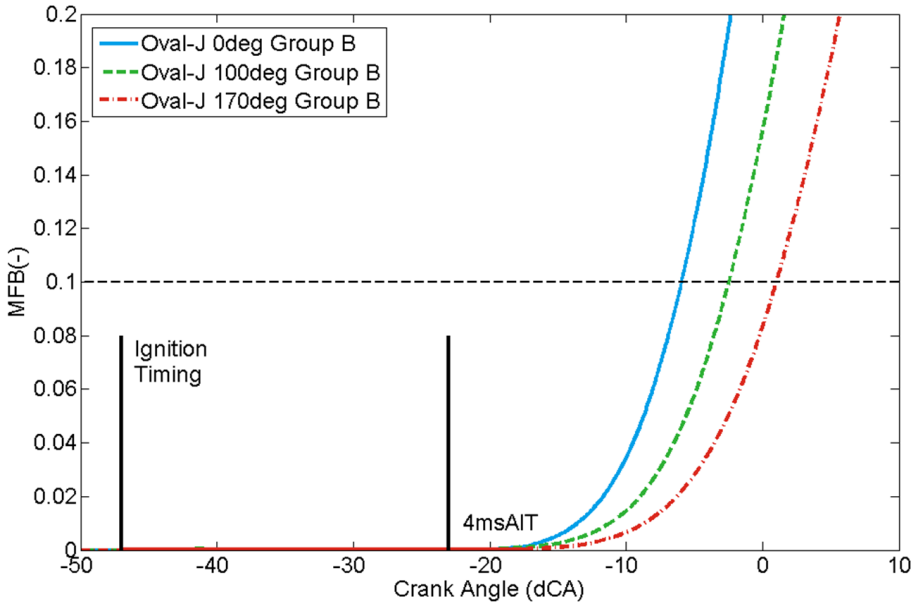

Figure 8-23: Mean MFB for group B for oval-J spark plug.

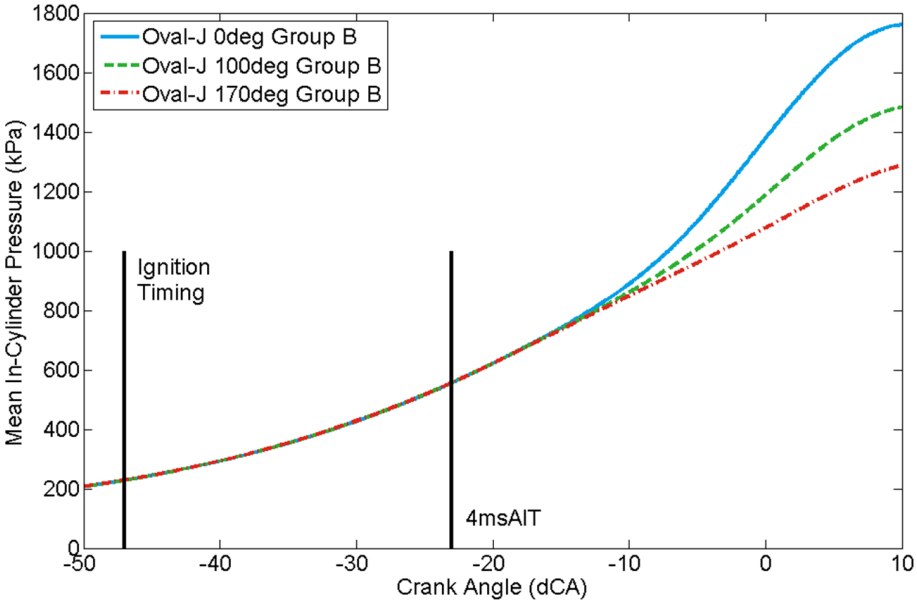

Figure 8-24: Mean in-cylinder pressure for group B for oval-J spark plug.

8.6.2.3 Combustion Metrics Analysis

The mean ignition delay (CA0010) and mean combustion duration (CA1090) of oval-J spark plug tests are shown in Table 8-8 and Table 8-9. For group A where initial flame kernels are convected to the exhaust side in concurrence to the designed tumble direction, 100° index orientation produces the shortest ignition delay (40.8°CA) and shortest combustion duration (21.1°CA). The 0° index orientation produces the longest ignition delay (44.6°CA) and longest combustion duration (28.3°CA). The trend is the same as for DFW shown in Table 8-6 and Table 8-7. Results from both DFW and oval-J spark plug tests demonstrated that for group A where initial flame kernels are convected to the exhaust side in concurrence to the designed tumble direction, the cross-flow index orientations (90° for DFW and 100° for oval-J) result in fastest propagating flame kernels and produce shortest ignition delay and combustion duration, due to the initial flame kernels are properly stretched and have minimum contact with the spark plug among the three studied index orientations. The index orientation where the initial flame kernels are convected to the ground strap (0° for both DFW and oval-J) results in the slowest propagating flame kernels and produces the longest ignition delay and combustion duration.

For group B where initial flame kernels are convected to the intake side counter to the designed tumble direction, the 0° index orientation produces the shortest ignition delay (42.1°CA) and shortest combustion duration (23.8°CA), and the 170° index orientation produces the longest ignition delay (51.1°CA) and combustion duration (38.6°CA). However, we cannot draw definitive conclusions on how the spark plug index orientations impact the initial flame kernel development and the resulted combustion metrics for group B, since there is generally low tumble motion for these cycles, and the interaction between the charge motion and the spark plug is not as certain and definitive as in group A where initial flame kernels are convected to the exhaust side in concurrence to the designed tumble direction.

Table 8-8: Ignition delay CA0010 of oval-J.

Spark Plug	Gap Orient. (degs)	Overall Mean CA0010 (°CA)	Mean CA0010 for Group A (°CA)	Mean CA0010 for Group B (°CA)
oval-J	0	43.7	44.6	42.1
	100	45.1	40.8	47.1
	170	49.0	43.2	51.1

Table 8-9: Combustion duration CA1090 of oval-J.

Spark Plug	Gap Orient. (degs)	Overall Mean CA1090 (°CA)	Mean CA1090 for Group A (°CA)	Mean CA1090 for Group B (°CA)
oval-J	0	26.6	28.3	23.8
	100	27.6	21.1	30.7
	170	34.8	24.1	38.6

In Figure 8-25, CA1090 is plotted against CA0010 for group A. It is observed that 90° orientation results less variations in both CA0010 and CA1090 with std of CA0010 being 2.6°CA and std of CA1090 being 4.6°CA.

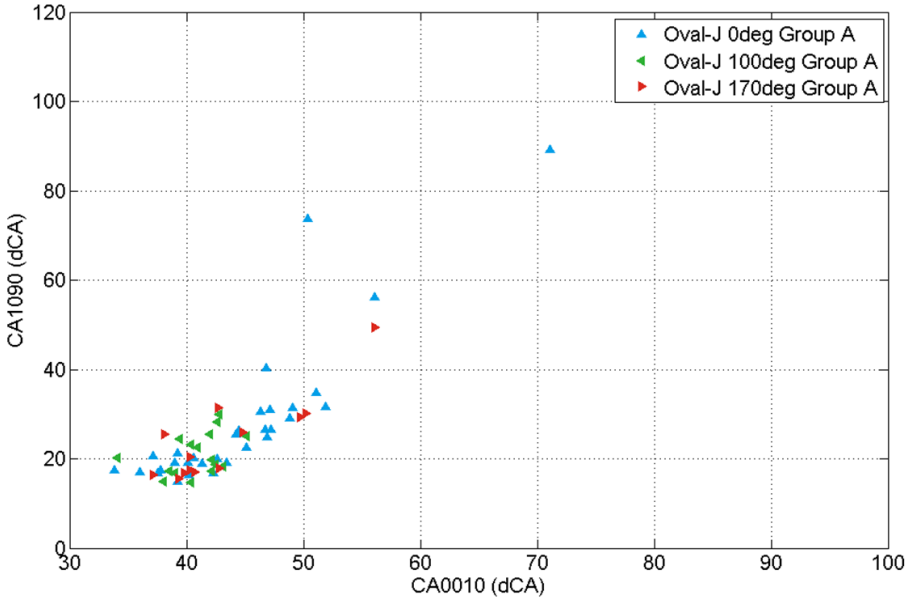

Figure 8-25: CA0190 vs CA0010 of group A for oval-J spark plug.

Before proceeding to the next section of cross-comparison between double fine wire spark plug results and oval-J spark plug results, a few points should be summarized.

The same trend is observed for group A for both double fine wire spark plug and oval-J spark plug. The cross-flow index orientations (90° for DFW and 100° for oval-J) produce the fastest growing flame kernels, shortest ignition delay and shortest combustion duration, while the 0° results in the slowest growing flame kernels, longest ignition delay and longest combustion duration.

The trend is also consistent for group B for both spark plugs. However, contrary to expectation, 0° index orientation results in the fastest growing flame kernels for both spark plugs, instead of 90° index. Notice again that these cycles generally have low tumble motion, which is indirectly reflected by the smaller and less stretched flame kernels, so the detailed information of what direction the charge flow interacts with the spark plug is unknown.

8.6.3 Comparison between Double Fine Wire and Oval-J Spark Plugs

The cross-comparison between double fine wire spark plug and oval-J spark plug for group A are illustrated in Figure 8-26 through Figure 8-28. In all three studied index orientations, the double fine wire spark plug always produces the faster growing flame kernels than the oval-J spark plug.

For 0° index orientation as shown in Figure 8-26, 30% of cycles produced flame kernels that reached -15 mm at 4 msAIT for the double fine wire spark plug; while the oval-J spark plug only has 10% of cycles whose flame kernels reach the same point. For cross-flow index orientation (90° for DFW and 100° for oval-J) as shown in Figure 8-27, 40% of cycles produced flame kernels that reached -15 mm at 4 msAIT for the double fine wire spark plug; while the oval-J spark plug only has 25% of cycles whose flame kernels reach the same point. For 180° index orientation for DFW and 170° for oval-J as shown in Figure 8-28, 39% of cycles produced flame kernels that reached -15 mm at 4 msAIT for the double fine wire spark plug; while the oval-J spark plug only has 23% of cycles whose flame kernels reach the same point.

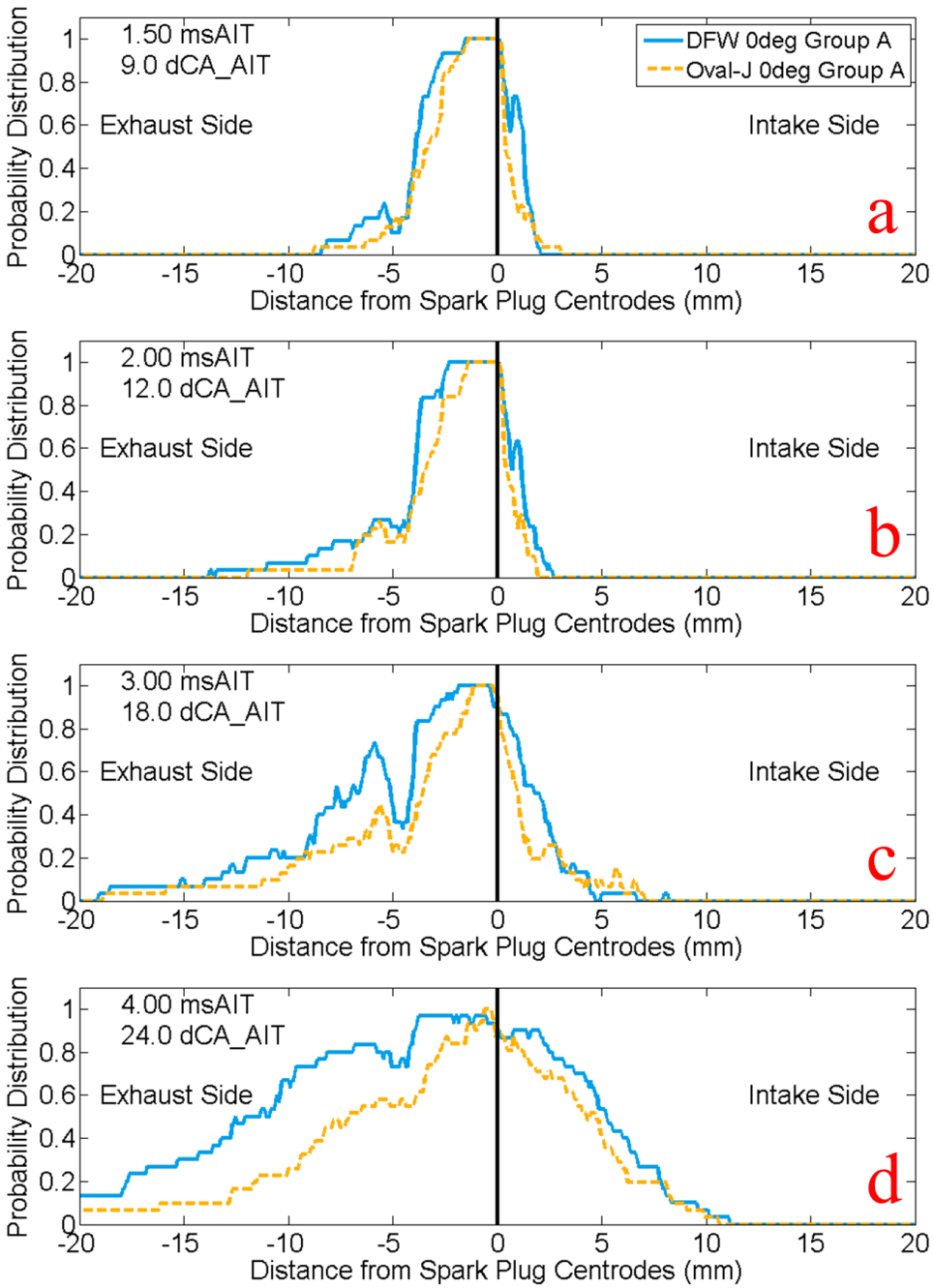

Figure 8-26: Comparison between DFW spark plug and oval-J spark plug for 0° index orientation for group A.

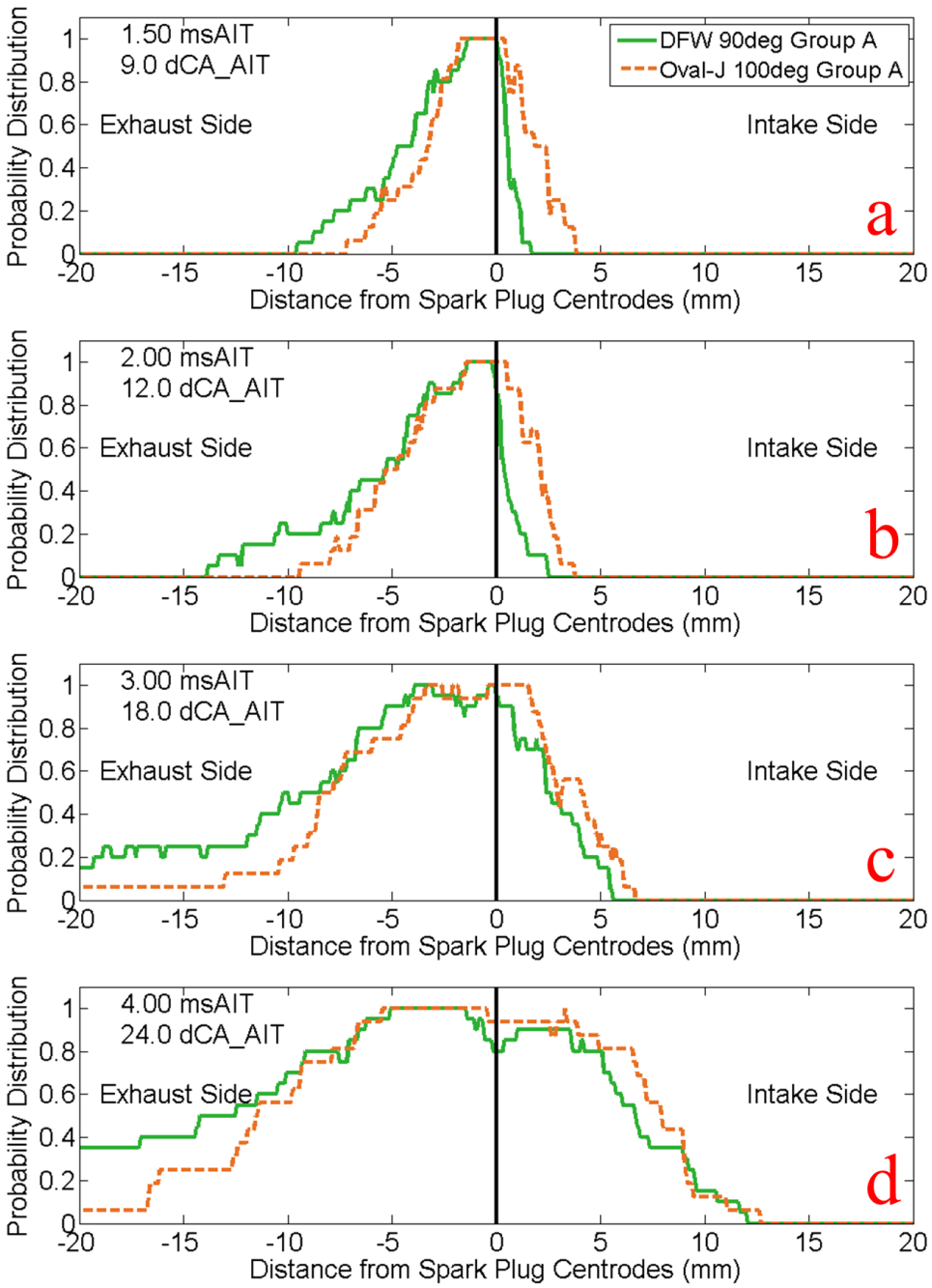

Figure 8-27: Comparison between DFW spark plug at 90° index orientation and oval-J spark plug at 100° index orientation for group A.

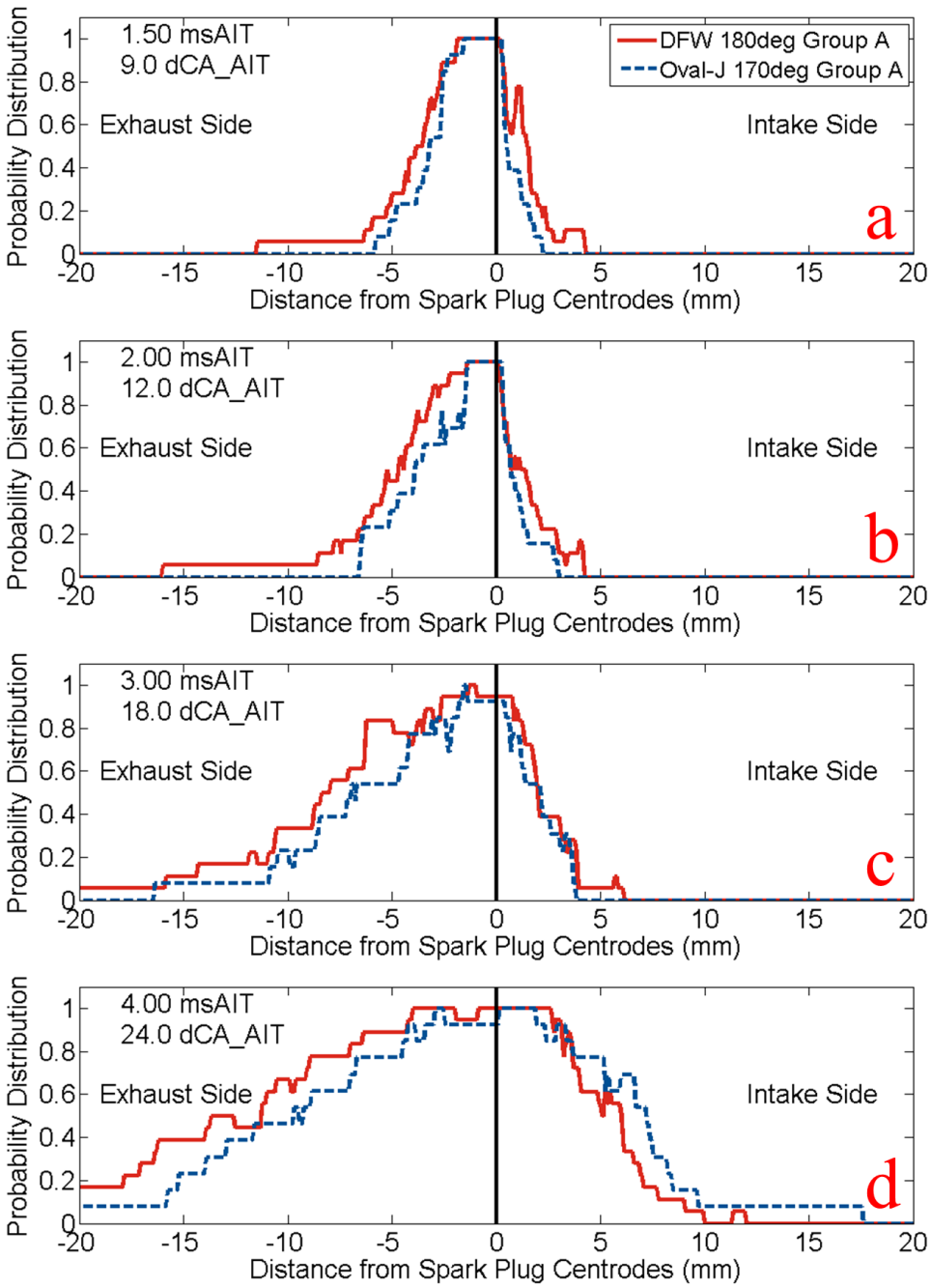

Figure 8-28: Comparison between DFW spark plug at 180° index orientation and oval-J spark plug at 170° index orientation for group A.

The cross-comparison between double fine wire spark plug and oval-J spark plug for group B are illustrated in Figure 8-29 through Figure 8-31. For these cycles, the double fine wire

spark plug only has limited advantage over the oval-J spark plug, except for the 180° index case.

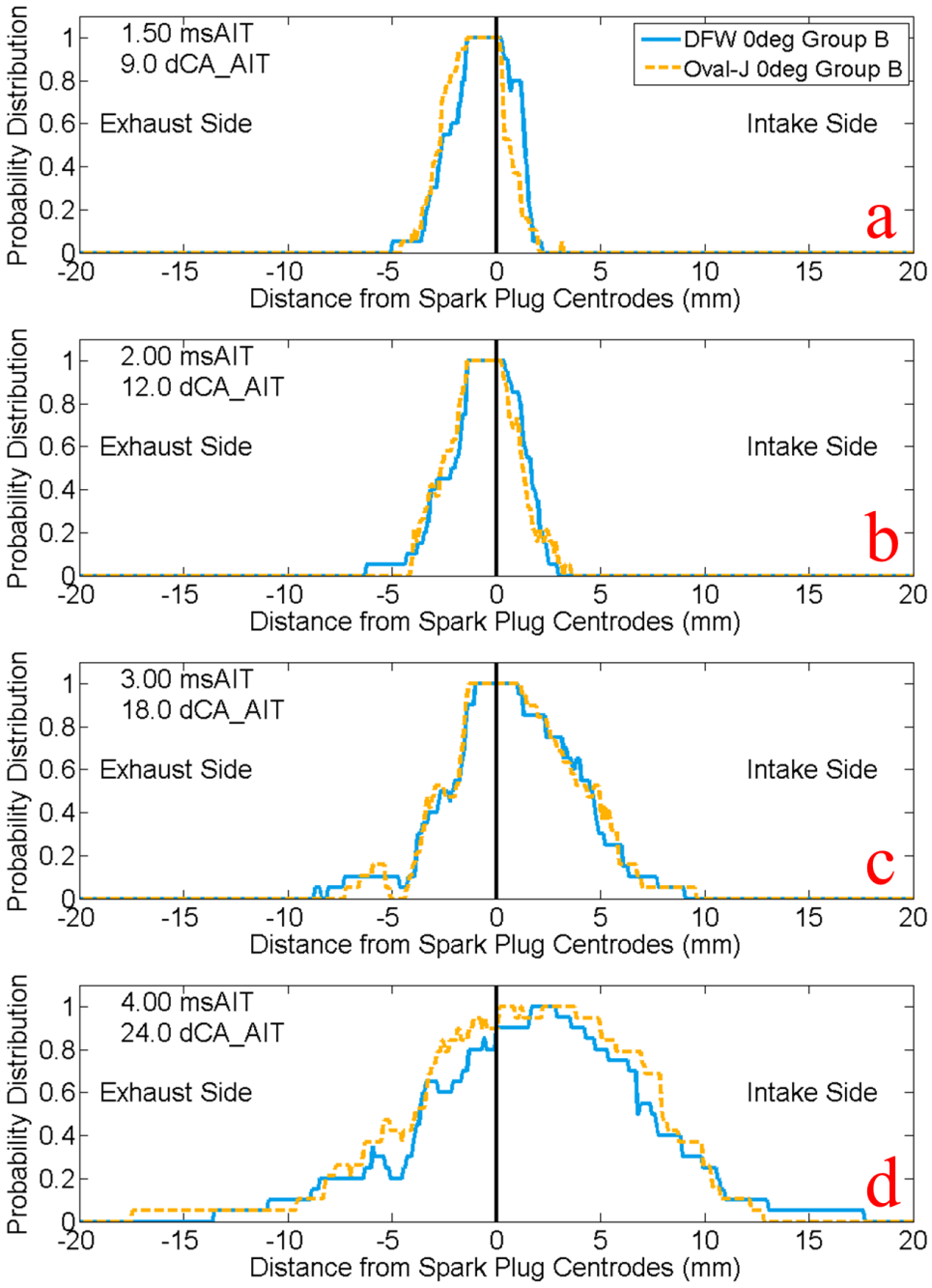

Figure 8-29: Comparison between DFW spark plug and oval-J spark plug for 0° index orientation for group B.

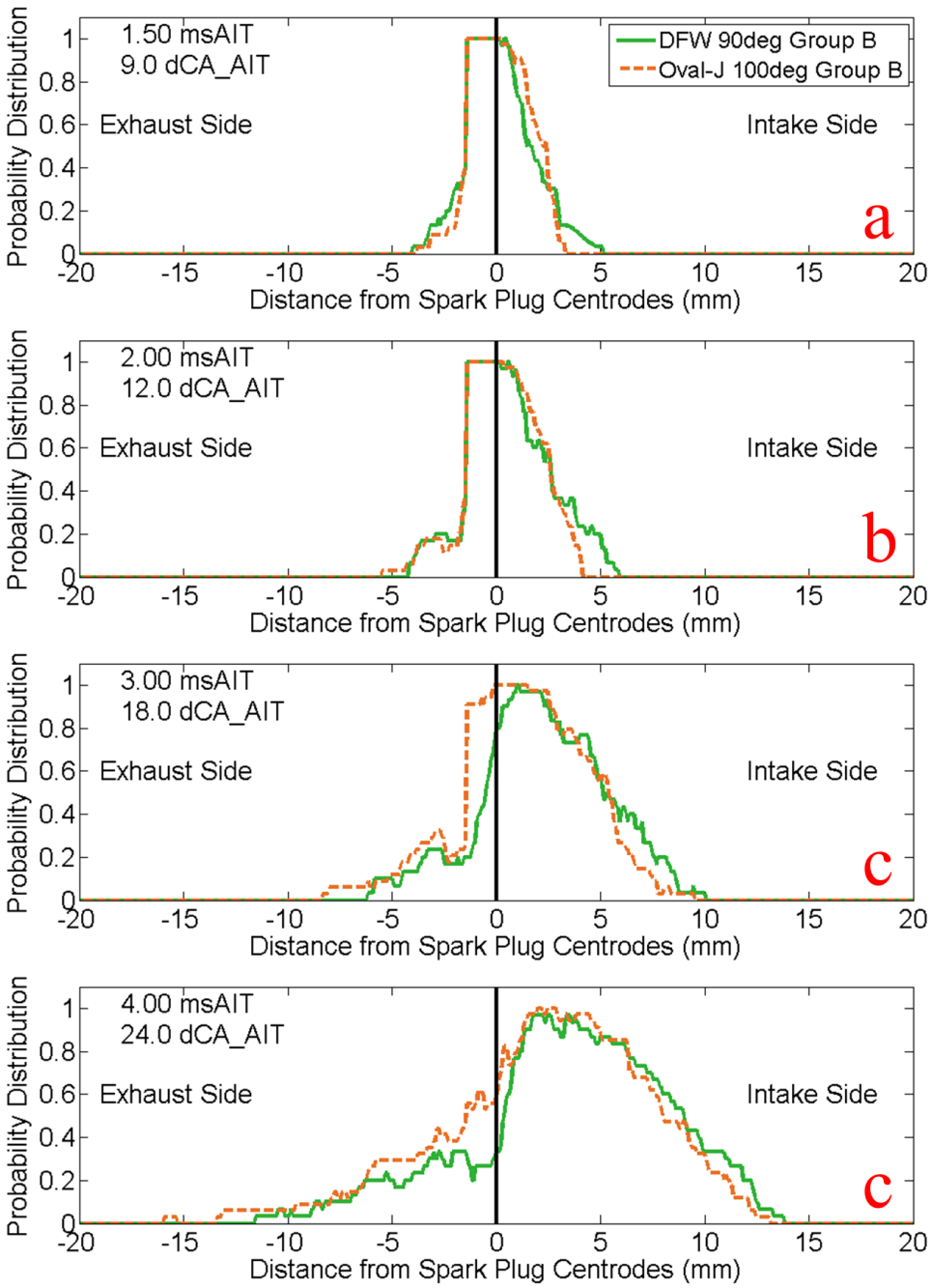

Figure 8-30: Comparison between DFW spark plug at 90° index orientation and oval-J spark plug at 100° index orientation for group B.

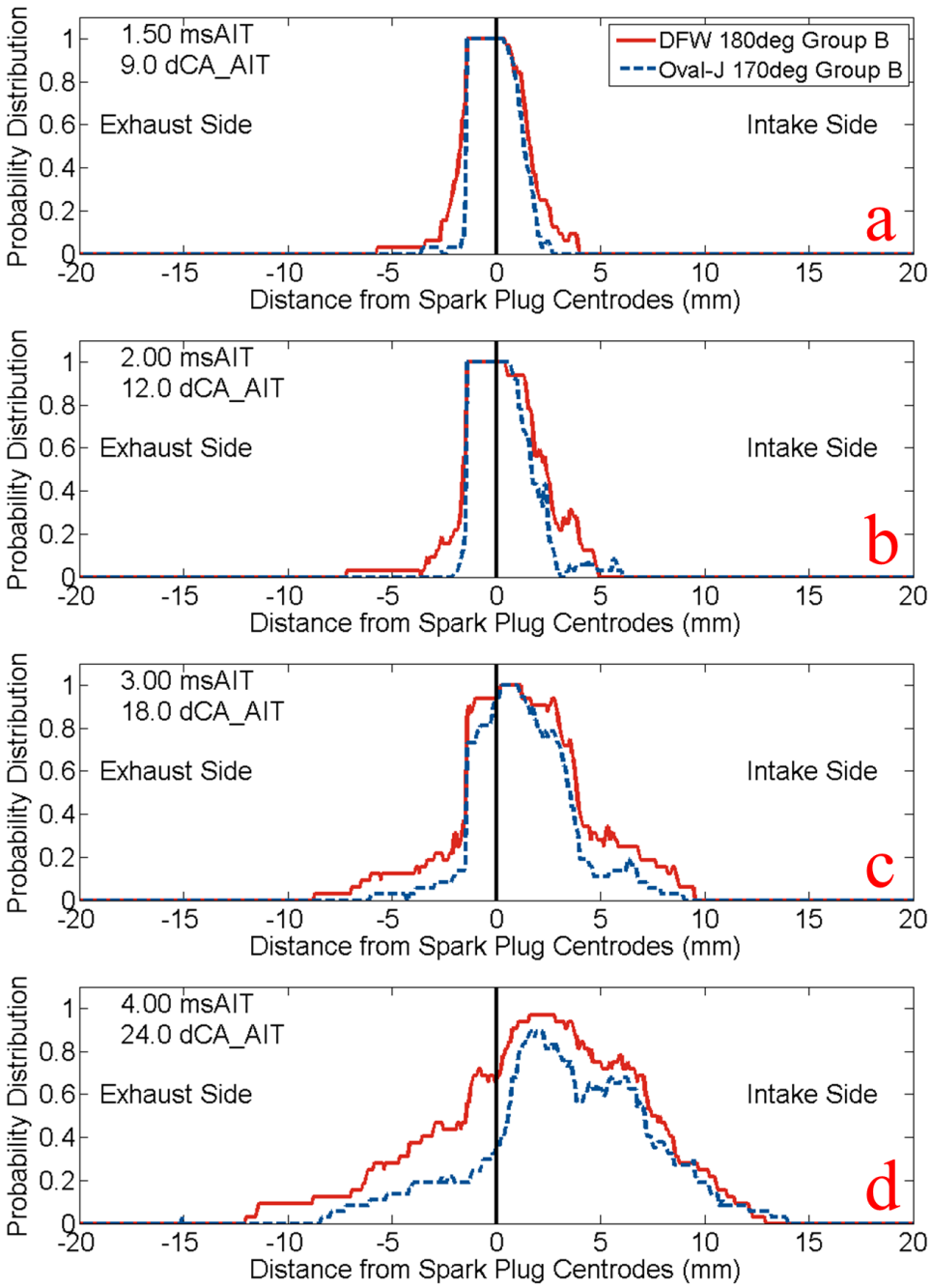

Figure 8-31: Comparison between DFW spark plug at 180° index orientation and oval-J spark plug at 170° index orientation for group B.

8.7 Summary and Conclusions

The influences of the spark plug orientation and plug electrode design on the initial flame kernel development were investigated on a single cylinder optically accessible engine for two types of spark plug electrodes, including a double fine wire spark plug and an oval-J spark plug. The early flame development was captured by a high-speed camera at 10,000 fps and the in-cylinder pressure was measured by a piezo-electric pressure transducer. The images were analyzed using 2D-PDF and 1D-PDF methods and combustion metrics were calculated from the in-cylinder pressure data and crank position signal. The results of the initial flame kernel development were compared for the different index orientations and between the two spark plugs.

Though the base engine was designed to have a tumble motion counterclockwise viewing from the front of the engine (exhaust valves on the left and intake valves on the right), cycles with initial flame kernel being convected counter to the designated direction were observed. The results were categorized into two groups based on the convection direction of the initial flame kernel, either to the exhaust side of the cylinder in concurrence to the designed tumble direction (group A) or to the intake side counter to the designed tumble direction (group B).

For group A where initial flame kernels are convected to the exhaust side in concurrence to the designed tumble direction, the following observations were made:

- The cross-flow index orientations (90° for DFW and 100° for oval-J) always produce the fastest propagating flame kernels with minimum contact with the spark plug. In the case of DFW, 90° index orientation produces 50% of cycles whose flame kernels reaching -10mm (exhaust side) at 3 msAIT. In the case of the oval-J spark plug, 100° index orientation produces 56% of cycles for which the flame kernels reach -10mm (exhaust side) at 4 msAIT. The fast propagating flame kernels with minimum contact with the spark plug result in the shortest ignition delay and combustion duration among the three studied index orientations. For DFW, the 90° index orientation has a mean

ignition delay of 40.2°CA and combustion duration of 20.5°CA; for oval-J, the 100° index orientation has mean ignition delay of 40.8°CA and combustion duration of 21.1°CA.

- The 0° index orientation always produces the slowest propagating flame kernels due to that the initial flame kernels are convected to the ground strap, which not only constrains the flame kernel from fast propagating to the exhaust side, but also leads to high heat loss to the spark plug. As a result, the 0° index orientation has the longest ignition delay and combustion duration for both DFW and oval-J spark plugs.

For group B where initial flame kernels are convected to the intake side counter to the designed tumble direction:

- For the DFW spark plug, none of the three studied index orientations exhibits significant advantages over the other two based on the 1D-PDF analysis. The combustion analysis shows that the 0° index orientation resulted in the shortest ignition delay (43.8°CA); however, the 180° index orientation resulted in the shortest combustion duration (25.9°CA);

- For the oval-J spark plug, the 0° index orientation produces fastest propagating flame kernels with 42% of cycles whose flame kernel reaching -5 mm (exhaust side) at 4msAIT. It also results in the shortest ignition delay (42.1°CA) and shortest combustion duration (23.8°CA). The 180° index orientation produces the slowest propagating flame kernels with only 14% of cycles whose flame kernel reaching -5 mm (exhaust side) at 4 msAIT.

- There is generally a low tumble motion in group B where initial flame kernels are convected to the intake side counter to the designed tumble direction. The interaction between the charge motion and the spark plug is not as definitive and certain as in group A where initial flame kernels are convected to the exhaust in concurrence to the designed tumble direction. We cannot draw definitive conclusions on how the spark

plug index orientations impact the initial flame kernel development and the resulted combustion metrics.

Comparison between DFW and oval-J results shows that for both group A and group B, DFW produces faster propagating flame kernels at all three studied index orientations.

8.8 Further Thoughts

The findings in this study revealed that initial flame kernels could be convected to either direction in an engine that is aimed to have a consistent flow direction at the spark gap; this variation could put an originally upstream spark plug in a downstream position, and vice versa. This could be the cause why Aleiferis [33] and Anderson [54] observed inconsistent results regarding whether upstream or downstream spark plug orientation has the worst results with respect to COVimep.

For current study, the engine was run at a relatively low speed (1000 rpm), and this could lead to a generally low and unstable tumble motion. Further studies with higher tumble and at higher engine speed are planned. Additionally the impact of direct injection on this flow should be studied through comparing PFI and DI in the same engine and through quantifying the flow field velocity with PIV.

8.9 Acknowledgements

Special thanks to Ford Motor Company for the financial and technical support and guidance on this project. Additional thanks go to Mike Bunce and Eric Smith from Mahle Powertrain for their guidance on assembling and instrumentation of the Mahle optical engine, and supplying parts for the project. Finally Ford and Michigan Tech would like to acknowledge NGK for supplying the spark plugs used in this study.

Thanks also go to Owen Marttila, Carl Jolma, Jesse Hill and Joel Duncan from Michigan Technological University for their excellent technical support that greatly facilitated the progress of this project.

8.10 Abbreviations

2D-PDF	2-dimensional probability distribution function
1D-PDF	1-dimenstional probability distribution function
AIT	after ignition timing
ATDC	after top dead center
BTDC	before top dead center
COV	coefficient of variation
°CA	degrees in crank angle
GDI	gasoline direct injection
IMEP	indicated mean effective pressure
PIV	particle imaging velocimetry

9 Investigation of Flow Motion near the Spark Plug

This paper has been approved for publication in 2018 SAE world congress. It corresponds to the third stage of research described in the chapter of main research contributions.

In this study, the flow motion in the vicinity of the spark plug was studied using three methods: the high-speed imaging of the spark arc discharge channel, flow field quantification via PIV and high-speed imaging of the flame kernel under stoichiometric conditions. Two different levels of tumble motions were studied, and it was concluded the flow motion near the spark plug region changes direction from pointing to the exhaust side at early ignition timing to pointing to the intake side at late ignition timing at low tumble. At high tumble, the flow motion direction is well maintained pointing to the exhaust side until late in the compression stroke.

Investigation of Flow Conditions and Tumble near the Spark Plug in a DI Optical Engine at Ignition

Wang, Y., Zhang, J., Wang, X., Yang, Z., Dice, P., Shahbakhti, M., and Naber, J.

Michigan Technological University

Czekala, M., Qu, Q., and Huberts, G.

Ford Motor Company

Michigan Technological University

Department of Mechanical Engineering – Engineering Mechanics

1400 Townsend Drive, Houghton, Michigan, USA 49931

Phone: (906)370-2612

Email: yanyuw@mtu.edu, jnaber@mtu.edu

9.1 Abstract

Tumble motion plays a significant role in modern spark-ignition engines in that it promotes mixing of air/fuel for homogeneous combustion and increases the flame propagation speed for higher thermal efficiency and lower combustion variability. Cycle-by-cycle variations in the flow near the spark plug introduce variability to the initial flame kernel development, stretching, and convection, and this variability is carried over to the entire combustion process. The design of current direct-injection spark-ignition engines aims to have a tumble flow in the vicinity of the spark plug at the time of ignition. This work investigates how the flow condition changes in the vicinity of the spark plug throughout the late compression stroke via high-speed imaging of a long ignition discharge arc channel and its stretching, and via flow field measurement by particle imaging velocimetry. It is observed that the flow motion near the spark plug varies significantly cycle to cycle and can change direction from the bulk tumble flow near the time of ignition, especially when the ignition timing is late in the cycle at low tumble conditions. At a higher tumble, the bulk flow motion is maintained past the early ignition timing; and at late ignition timing, only few cycles show changed flow direction near the spark plug with much lower probability than low tumble conditions. Analysis indicates that at low tumble conditions, the mean horizontal velocity near the spark plug changes from 3.9 m/s pointing to the exhaust side at 60°BTDC to 3.1 m/s pointing to the intake side at 20°BTDC at 1000 rpm; however it is well maintained at 10.6 m/s in average from 60°BTDC to 30°BTDC pointing to the exhaust side and the mean value decreases to 7.3 m/s at 20°BTDC with the maintained flow direction at high tumble conditions. Initial flame kernel convection and propagation were also investigated at the two studied tumble levels.

9.2 Introduction

Spark-ignited (SI) engines fueled with gasoline are currently powering a large portion of light-duty vehicles in the United States (over 95% in 2016) [2]. The light-duty greenhouse gas (LD GHG) regulations require the carbon dioxide emission to be limited to 163 g/mile

in 2025, which converts to 54.5 mpg if the efficiency is solely achieved through fuel economy technologies [5]. This dictates an urgent need to increase the thermal efficiency of SI engines. Diluted combustion has great potentials to increase the thermal efficiency of SI engines from the perspective of reducing throttling and heat losses. Research indicates that by diluting the charge, the brake thermal efficiency of SI engines can be increased well above 45% [18, 19]. However, one major challenge facing SI engines achieving highly diluted combustion is the plummet of the combustion stability. Studies from Ayala and Heywood [30] showed that when the laminar flame speed decreases below a critical value at diluted conditions, misfire and partial burns start occurring which quickly increases the coefficient of variation (COV) of the indicated mean effective pressure (IMEP) such that the engine is no longer drivable.

There are many causes that lead to the increased combustion instability at highly diluted conditions. Previous studies [40] revealed that any factor that causes the flame speed to decrease eventually results in increased combustion instability. For highly diluted charge, the laminar flame speed drops, the physical conditions of the charge experienced by the flame kernel in the later stage are subjected to more variations than fast propagating flames; thus the combustion variability increases [30]. Multiple techniques have been investigated to re-stabilize the combustion at lean limits. Nakai et al. [25] demonstrated by lengthening the ignition discharge duration, the size of the initial flame kernel increases; the increased flame propagation speed re-stabilizes the combustion and extends the lean limit. Tanoue et al. [26] reported that a repetitively-discharging ignition is highly effective in extending the lean limit. Chen et al. [55] and Zhang et al. [53] discovered that the increased ignition energy deposit into the initial flame kernel from a dual-coil ignition system is not the only factor that improves the lean limit. There exists an optimum time interval between the two events of energy deposits from the dual-coil system that the initial kernel size can be effectively enlarged and the lean limit can be extended. At extremely diluted conditions (λ>=1.9), the increased ignition energy alone cannot re-stabilize the combustion further; however, with the addition of high tumble motion, the combustion can again be re-stabilized [21]. Ayala and Heywood [30] also suggested that one main factor that causes

combustion variability is the variation of flow conditions in the initial stage of flame kernel development. Variations in the early stage of flame kernel development will be carried over and magnified to the entire history of combustion, thus increasing the combustion variation and instability. Also suggested by Pischinger and Heywood [34], the convection direction of the flame kernel has impacts on the contact area between of the flame kernel and the spark plug, the cylinder wall, which would introduce variability to heat losses and eventually the combustion instability would increase. Zhao et al. [32] concluded through large-eddy simulation that it is the velocity field that dominates the cycle to cycle variations in the flame propagation, by decoupling the effects of velocity field and equivalence ratio. Peterson's study [42, 43, 63] on a spray-guided spark-ignition stratified-injection optical engine with a center located injector revealed that the convection of the initial flame kernel needs to chase the rich fuel cloud to achieve successful burning of the mixture, otherwise partial burns could occur. In addition, previous studies [64-66] also revealed the potential of using secondary ignition voltage waveform to calculate the flow velocity across the gap, since the stretching of the spark discharge channel causes the increase in the secondary voltage. However, the direction of the flow cannot be determined by this method.

Direct-injection spark-ignition (DISI) engines with the intake side mounted injector dominate the market in the US and the gasoline engines still mainly run on homogenously stoichiometric fuel/air mixture due to strict NOx emission regulations. Also side mounting the injector can reduce the spark plug fouling compared with centrally mounted counterparts. The design of such engines aims to have consistent tumble motion near the spark plug at the time of ignition [12, 13]. However, the previous study by the authors [47] found that the convection direction of the initial flame kernel varies cycle by cycle. The cycles with initial flame kernel convecting in the direction of agreement with the bulk tumble direction are larger and more stretched, resulting in faster combustion and shorter mass fraction burned periods. On the other hand, the cycles with initial flame kernel convecting in the direction counter to the bulk tumble direction are smaller and more centered on the spark-plug electrodes, leading to slower combustion. The authors' previous work [46] also demonstrated that the change in flow direction with respect to the

orientation of the spark plug changes the ignition energy output and discharge duration, which is a factor that influences the size of the initial flame kernel.

The work described in this paper furthers previous studies by investigating the flow conditions near the spark plug from 60° before top dead center (BTDC) to 20°BTDC covering the range of spark timing for highly diluted to stoichiometric conditions in a single cylinder optically accessible gasoline DISI engine with a side-mounted gasoline direct injection (GDI) injector. High-speed imaging of the spark arc channel stretching was used to reflect the flow conditions near the spark plug. Note the "arc" in this context means the arc shape of the spark plasma channel, not the arc phase of the discharge. These results are supported by the flow field measurement through particle imaging velocimetry (PIV) under motored conditions in the region near the spark-plug electrodes. The tumble intensity was varied by installing tumble planks (TP) in the intake ports. Lastly, high-speed imaging of the early flame kernel was conducted by skip-firing the optical engine.

The following sections of this paper will describe the setup of the optical engine, the high-speed camera, and the PIV system. The data analysis methods will be introduced and discussed afterwards, followed by detailed discussions of the results. In conclusion, plans of future research will be described to further gain the understanding of the high variability of the flow motion in DISI engines.

9.3 Experimental Setup

The experiment consists three sections: the high-speed imaging of spark arc stretching, the PIV flow field measurement and the high-speed imaging of the flame kernel during combustion. The experimental procedures will be described in detail in the section of experimental methods. In the current section, experimental setup will be introduced, and the experiment setup varies with each part of the experiment.

9.3.1 Optical Engine

The DISI optical engine at MTU APS LABS in this study was modified from a Ford 4-cylinder gasoline direct injection engine by Mahle Powertrain (Figure 9-1). The engine specifications are summarized in Table 9-1. Cylinder two is the working cylinder and the other three cylinders are deactivated. The cylinder head is elevated to accommodate a Bowditch piston extension, whose bottom is bolted on the original piston; and on the top of the Bowditch extension is threaded a flat top aluminum piston with a 58 mm-diameter Sapphire (single-crystal aluminum oxide Al2O3) window insert. A 45° mirror is secured below the optical piston on the engine block, which reflects the PIV laser sheet up into the cylinder through the optical piston. The elevated cylinder head is separated from the engine block so the optical piston on top of the Bowditch extension cannot be lubricated in the same way as in production engines. Instead, piston rings are made from self-lubricating material torlon. The torlon rings would melt if being exposed under high temperature continuously so skip-firing strategy must be used when firing the optical engine. The quartz liner is held against the cylinder head by a hydraulic clamping plate, which is raised by a hydraulic system during operation of the optical engine. The optical liner can be easily removed for maintenance by releasing the hydraulic pressure.

The original production intake manifold is installed on the optical engine in order to maintain the original in-cylinder flow motion, which features counterclockwise bulk tumble viewing from the front of the engine (Figure 9-1). A custom exhaust pipe is used since the original exhaust pipe leads to a turbocharger, which is removed from the optical engine.

Table 9-1: Optical engine specifications.

Displacement (Liter)	0.6
Bore (mm)	87.5
Stroke (mm)	100
Compression Ratio	10.01 : 1
Fuel	AKI 87
Injector	side-mounted Bosch multi-hole GDI injector
Injection Pressure	4.5 MPa
Piston	flat top piston
Intake	Ford 2L Ecoboost intake manifold
Exhaust	custom exhaust manifold
Intake Valve Opening (°BTDC)	19
Intake Valve Closing (°ABDC)	37
Exhaust Valve Opening (°BBDC)	36
Exhaust Valve Closing (°ATDC)	8
Overlap (°CA)	27

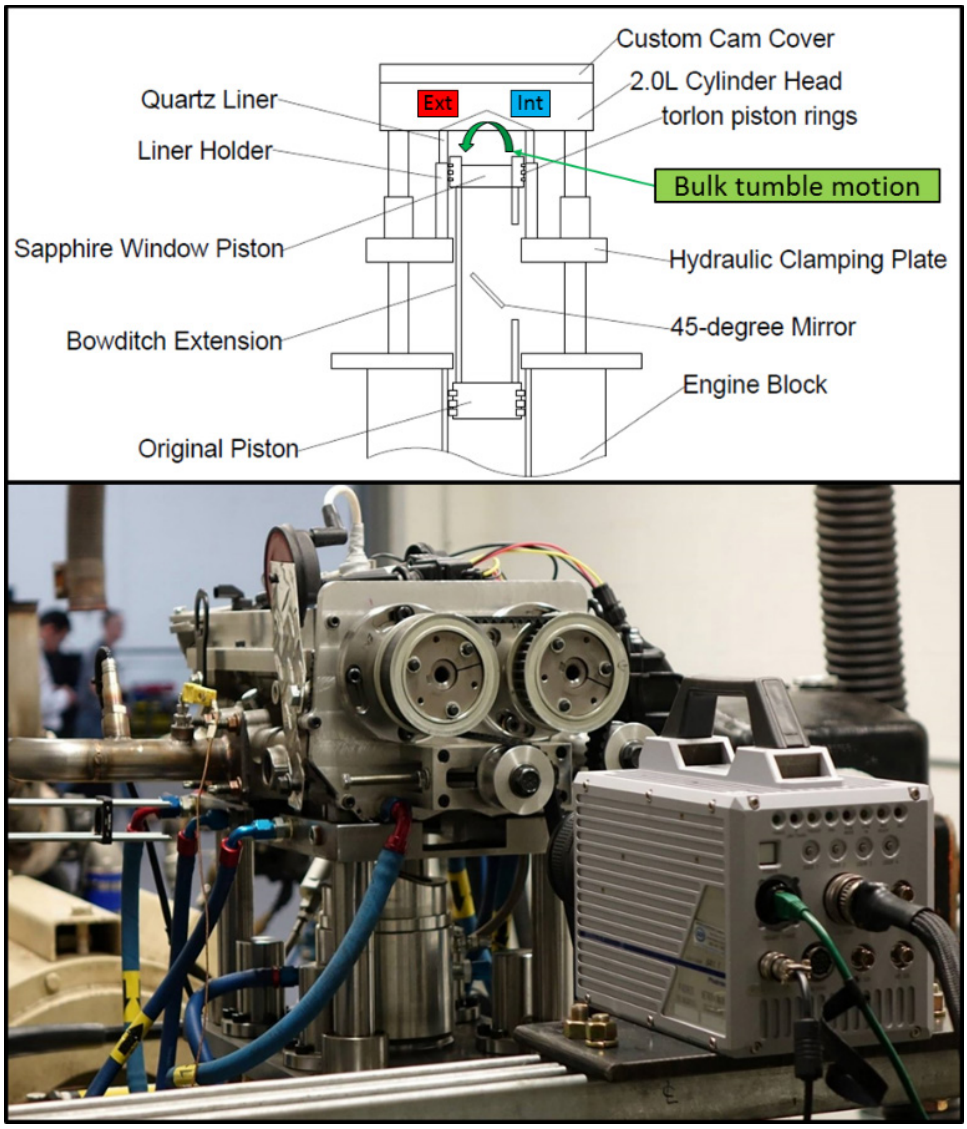

Figure 9-1: MTU Single Cylinder Optical Engine.

9.3.2 Tumble Planks

To achieve two different levels of tumble motion, tumble planks were designed and fabricated to fit into the intake ports. The tumble planks restrict the intake flow to the upper portion of the intake ports, thus increase the entry velocity of the air into the cylinder and guide the flow entry direction to achieve higher tumble. The cases without the tumble

planks installed will be referred to as low tumble and the cases with the tumble planks will be referred to as high tumble in this paper.

9.3.3 Long-Discharge Ignition System

For the high-speed imaging of the arc stretching, the ignition system was composed of two long-discharge high-energy (110 mJ) coils connected through a diode pack as illustrated in Figure 9-2. Both coils were dwelled for 6 ms when the engine was motored at 1000 rpm and for 5.5 ms at 1500 rpm with 2 ms interval between the two coils. Under these conditions the glow discharge lasts for approximately 5 ms to produce a discharge arc channel that exists long enough to be stretched in order to reflect the flow motion at the spark timing. For arc stretching tests, a double-fine-wire spark plug (featuring two fine tips on both center and ground electrodes) of 90° indexing (crossflow) with 0.65 mm gap size was used.

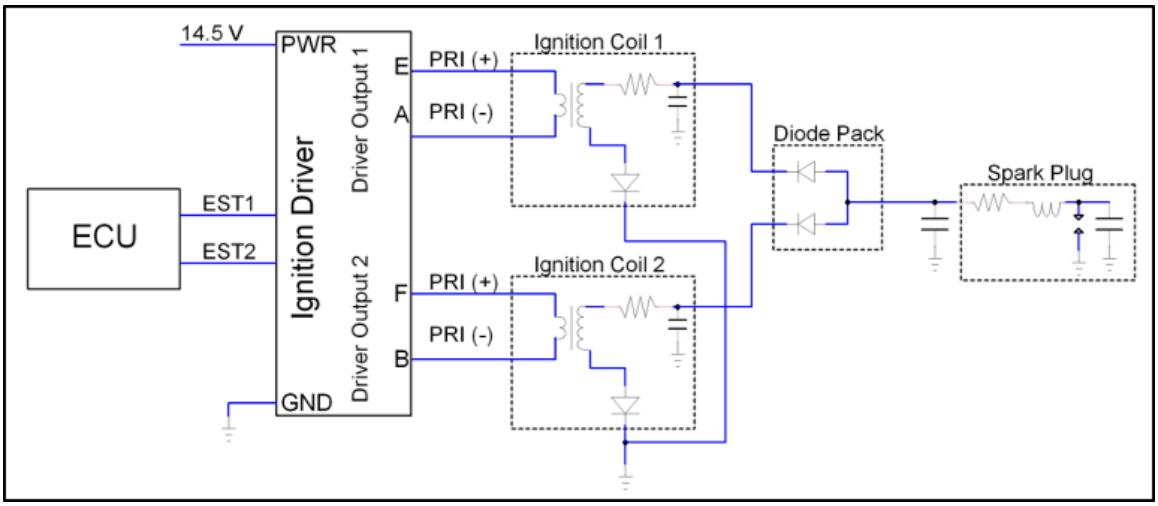

Figure 9-2: Schematic of the dual-coil ignition system to enable long spark discharge.

For the PIV flow field measurement tests, a single-fine-wire spark plug with ground strap removed was used in order to allow the laser sheet to access the vicinity of the spark plug and to reduce glare. The ignition was not triggered for the PIV flow field measurement tests.

For the high-speed imaging of the flame kernel, the single long-discharge ignition system was used. The setup was the similar as the dual-coil ignition system described above

(Figure 9-2) with the exception that only one coil was dwelled and triggered. The same double-fine-wire spark plug was used for the high-speed flame kernel imaging tests.

9.3.4 High-Speed Camera

A Photron SA1.1 high-speed camera was used for the arc stretching imaging tests and also for the flame kernel imaging tests. The detailed description of the high-speed camera configurations for this test is summarized in Table 9-2. The high-speed images were captured starting from 2° crank angle (°CA) before ignition timing (also referred to as spark-advance or breakdown in this paper) at 10,000 frames per second (fps). The camera was pointing to the tumble plane through the quartz liner from the front of the engine.

Table 9-2: High-speed camera specifications.

Camera Model	Photron SA 1.1
ISO	10,000
Frame Rate (fps)	10,000
Resolution	768 × 512
Lens	Nikon 85 mm + 12 mm extension
F/stop	4 for arc stretching tests, 2.8 for flame kernel imaging tests
Trigger	2°CA before ignition

9.3.5 PIV system

A Quantel TSI CFR200 Nd:YAG laser PIV (Figure 9-3) system was used for the PIV flow field measurement tests. The laser head was calibrated to emit pulses of 532 nm wavelength laser with 116 mJ/pulse energy at 5 us pulse interval. The laser beam was expanded vertically by a 50 mm cylindrical lens and then focused by a 1000 mm convex lens to form a laser sheet of approximately 1 mm width near the spark plug. The laser was reflected through the 45° mirror upwards into the cylinder though the optical piston. The resolution of the PIV camera is 1600 × 1192 pixels imaging the vicinity of the spark plug through a 200 mm lens. The scale factor is 11.2 μm/pixel.

Silicone oil of 50 cst. viscosity was atomized by compressed air through a Laskin nozzle particle generator [67]. The silicone seeding was fed into the intake manifold 24 cm

upstream of the intake ports so it had sufficient time to distribute evenly in the intake charge.

The captured image pairs were segregated into 32 × 32 pixel interrogation windows and cross-correlated to obtain the velocity vectors. The velocity field was then validated and the spurious vectors were replaced by the local mean values.

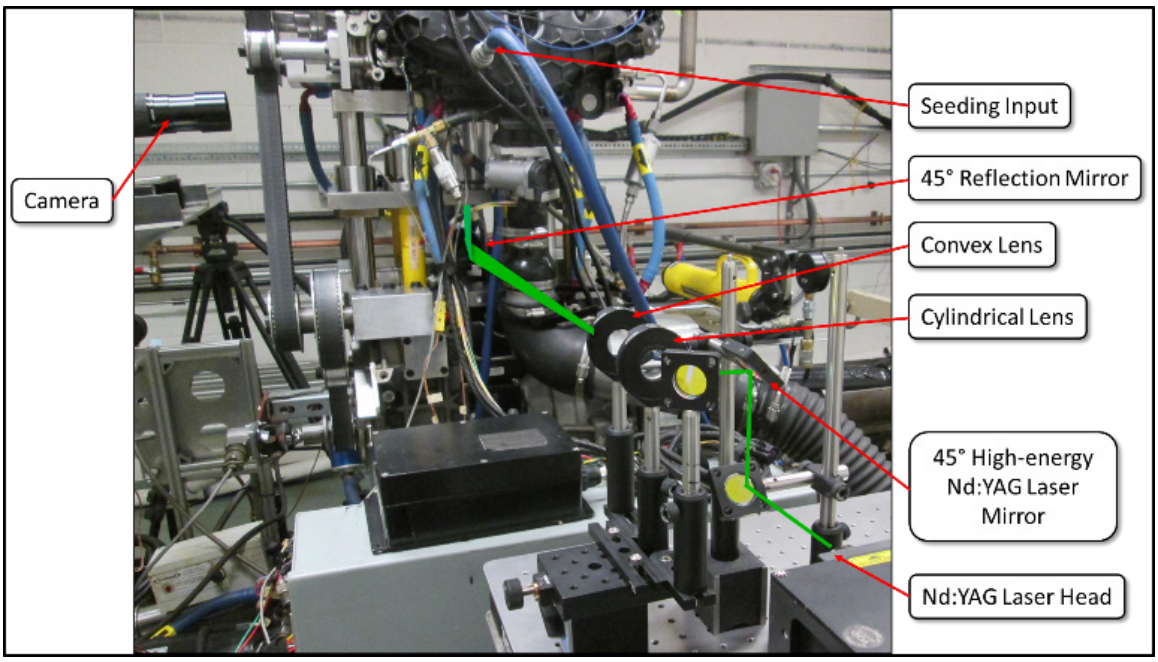

Figure 9-3: PIV system.

For the high-speed imaging studies, the PIV camera was removed and replaced by the Photron SA1.1 camera coupled with an 85 mm lens plus a 12 mm extension tube as stated in the last section.

9.4 Experimental Methods

The experiment of this study was composed of three sections: the high-speed imaging of the spark arc stretching, the PIV flow field measurement and the high-speed imaging of the flame kernel during combustion. For the arc stretching imaging and PIV sections, the optical engine was only motored. However, the triggering of the ignition and the PIV laser

pulse/imaging was controlled by the ECU with skip-fire strategy of 10 firing groups composed of 10 fired (triggered) cycles followed by 15 motored (non-triggered) cycles in each firing group, the same as when engine was fired for the flame kernel imaging tests, which is the last section of the experiment.

9.4.1 High-Speed Arc Stretching Imaging

As introduced in the experimental setup section, the double-fine-wire spark plug with 0.65 mm gap size was installed on the optical engine, and the dual long-discharge-coil ignition system released the ignition energy with 2 ms breakdown phasing to form a long-lasting discharge arc at motored conditions at different engine speeds, manifold absolute pressure (MAP) and tumble levels. The detailed test matrix of the high-speed arc stretching imaging is provided in Table 9-3. The ignition discharge was triggered at predetermined crank angle positions (70°BTDC to 20°BTDC with 10°CA interval) once per cycle for 50 cycles in total at each test point. The stretching of the arc channel was imaged by the Photron SA1.1 camera at 10,000 fps.

Table 9-3: Test matrix of arc stretching high-speed imaging tests.

Test Number	Tumble Level	Engine Speed (rpm)	MAP (kPa)	Ignition Trigger Angle (°BTDC)
Arc-Test 1	Low	1000	46.5	70 - 20
Arc-Test 2	High			
Arc-Test 5	Low	1500		
Arc-Test 6	High			
Arc-Test 3	Low	1000	66.5	
Arc-Test 4	High			
Arc-Test 7	Low	1500		
Arc-Test 8	High			

9.4.2 PIV Flow Field Measurement

For the PIV flow field measurement, the Photron high-speed camera was removed and the PIV system was set up as described in the experimental setup section. The detailed test matrix of the PIV flow field measurement is provided in Table 9-4. The pulse triggering

angle was swept from 60°BTDC to 20°BTDC with 10°CA increment at motored conditions. At each test point, one image pair was taken per cycle at the predetermined trigger angle for total 50 cycles.

Table 9-4: Test matrix of flow field measurement tests via PIV.

Test Number	Tumble Level	Engine Speed (rpm)	MAP (kPa)	PIV Trigger Angle (°BTDC)
PIV-Test 1	Low	1000	48.6	60 - 20
PIV-Test 2	High	1000	47.5	60 - 20
PIV-Test 3	Low	1500	46.2	60 - 20
PIV-Test 4	High	1500	47.2	60 - 20

9.4.3 Optical Engine Combustion Test

Next, the optical engine was skip-fired with the target load at 250 kPa IMEP at 1000 rpm at both low and high tumble and the flame kernel propagation was imaged at 10,000 fps. The test matrix is shown in Table 9-5. To insure homogeneous combustion, AKI 87 gasoline was injected at 360°BTDC at 4.5 MPa rail pressure. The spark-advance was set at 12°BTDC with the single long-discharge coil releasing ignition energy to the double-fine-wire spark plug (0.65 mm gap, crossflow orientation). The optical engine was skip-fired for 5 firing groups of 10 fired/15 motored cycles in each firing group, which is illustrated by a sample IMEP plot in Figure 9-4.

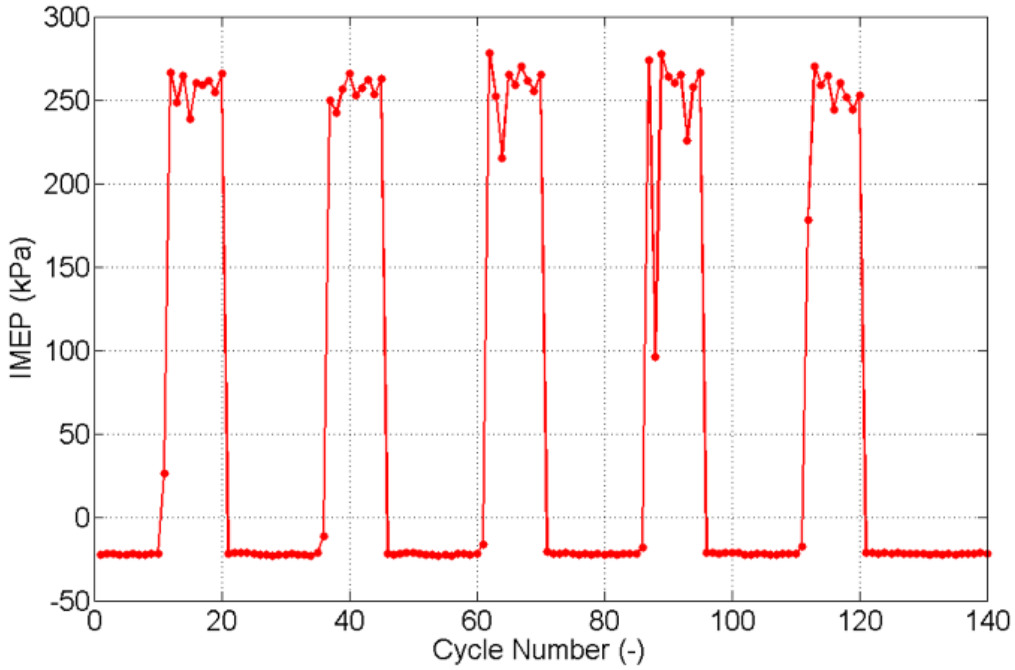

Figure 9-4: Illustration of skip-fire strategy.

The transition following the motored cycles usually occurs within the first four fired cycles in each firing group, thus the first five cycles following the motored cycles were eliminated and statistical analysis was only performed starting from the 6th cycle in each firing group. This made total 25 cycles for each test case.

Table 9-5: Test matrix of combustion test for high-speed flame kernel imaging.

Test Number	Tumble Level	Target IMEP (kPa)	Engine Speed (rpm)	Target Lambda (-)
Combustion-Test 1	Low	250	1000	1
Combustion-Test 2	High	250	1000	1

9.5 Data Analysis and Results Discussion

9.5.1 High-Speed Imaging of Arc Stretching

9.5.1.1 Traces of Spark Arc Centroids in Horizontal Direction

As introduced previously in Table 9-3, at motored conditions, the spark-advance was swept from 70° to 20°BTDC with a 10°CA interval at 46.5 kPa mean MAP and 66.6 kPa mean MAP with low and high tumble conditions for two engine speeds: 1000 rpm and 1500 rpm. The centroid location of the spark arc channel from the spark-plug axis in horizontal direction was calculated and used as a metric to investigate the flow conditions at different piston positions around the top dead center. The arc centroid traces for 1000 rpm at 46.5 kPa MAP are shown in Figure 9-5. The x-axis is the crank angle range in which the ignition discharge occurs and the y-axis is the horizontal distance from the arc centroid to the spark-plug axis. A negative value indicates the arc is stretching to the exhaust side in agreement with the bulk tumble motion, and a positive value means the arc is stretching to the intake side, counter to the bulk tumble motion. In each subplot, traces of all 50 triggered cycles are shown from the breakdown to the end of discharge corresponding to 5.5 ms of duration in average. It is clearly shown in Figure 9-5 on the left that, with low tumble, when the ignition occurs early (70 and 60°BTDC), the arc channel primarily stretches to the exhaust side. In the medium spark-advance range (50 and 40°BTDC), which is the normal spark-advance range for diluted combustion), there exists a transition stage where the arc channel is switching from the exhaust side to the intake side. Cycle to cycle variability exists such that the arc / flow direction maybe in either direction or that there may be very little stretch. Later, as the spark-advance approaches TDC (30 and 20°BTDC), the arc channel stretching has completed the directional change and is to the intake side.

Comparing to the case with the same engine speed and MAP but with high tumble in Figure 9-5 on the right, the difference is noticeable in that the flow motion is well maintained until the spark-advance approaches 40°BTDC. Even for later spark-advance at 30 and 20°BTDC, a few of the cycles (less than 10%) have arc stretching to the intake side.

Figure 9-6 shows the results at a higher engine speed of 1500 rpm. As can be seen, the two events of the dual-coil ignition discharge become more distinguishable, due to the faster energy deposition under high flow motion. Similar to the 1000 rpm case, the high tumble (right) maintains the arc stretching direction to the exhaust side until late in the compression stroke (20°BTDC) and even then the majority of the events are still stretched to the exhaust side.

At 66.5 kPa MAP (Figure 9-19 and Figure 9-20 in the appendix), the arc centroid traces exhibit the same trend as in 46.5 kPa MAP cases. However, at the higher MAP, more cycles result in changed arc stretching direction even with high tumble (right in Figure 9-19 and Figure 9-20 in the appendix). The detailed analysis is discussed in the form of histograms in later sections.

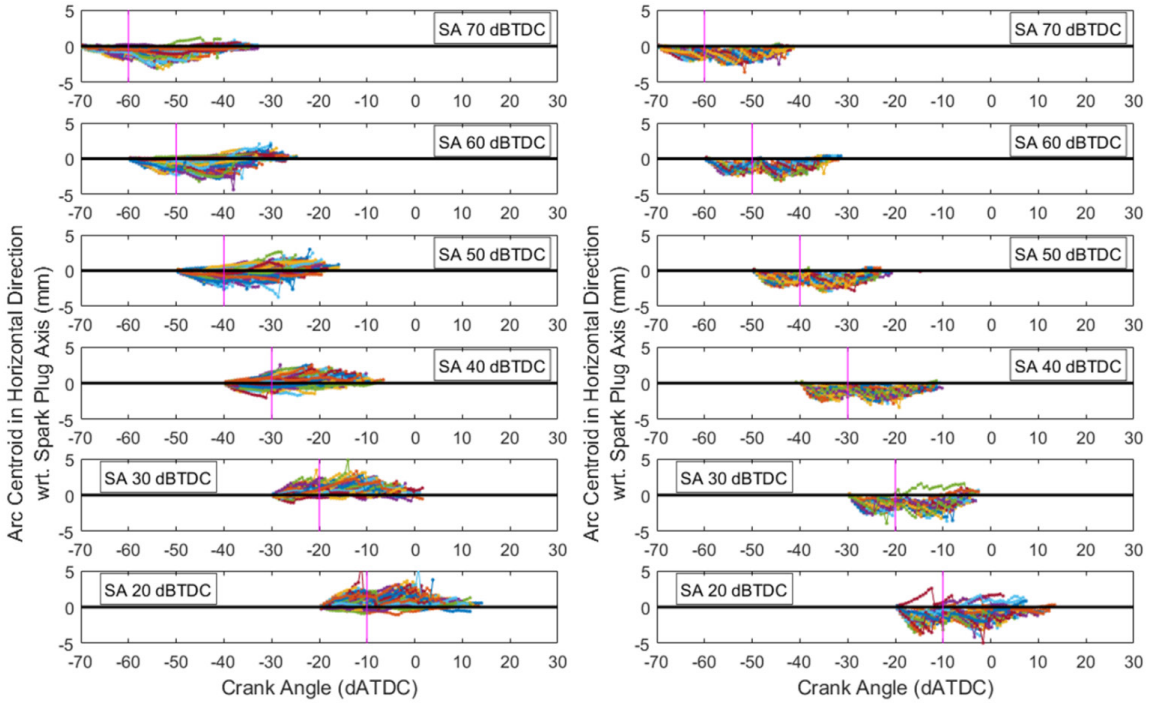

Figure 9-5: Traces of spark arc centroid locations in horizontal direction from spark-plug axis, 1000 rpm, 46.5 kPa (left: low tumble, right: high tumble).

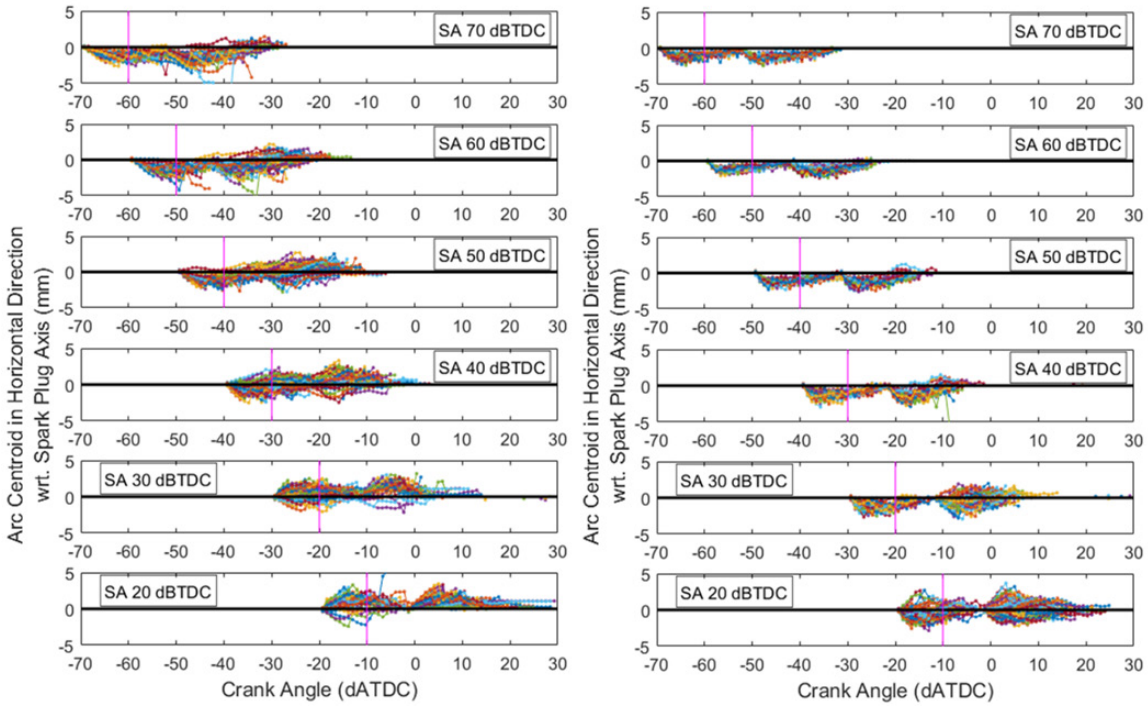

Figure 9-6: Traces of spark arc centroid locations in horizontal direction from spark-plug axis, 1500 rpm, 46.5 kPa (left: low tumble, right: high tumble).

9.5.1.2 Sample High-Speed Spark Arc Images

In this section individual images will be examined in support of the arc stretching figures presented above. In Figure 9-5 and Figure 9-6, x-axis locations at 10°CA after breakdown are marked by vertical magenta lines. This timing will be used as it is between the first and second discharge and the arc is well established. The arc stretch at this moment is more representative of the flow motion near the spark-plug gap.

In Figure 9-7 are sample images of the arc channel at 10°CA after breakdown for spark-advance 40°BTDC cases corresponding to the moment marked by the magenta lines in subplot 4 in Figure 9-5 and Figure 9-6. Note when high-speed imaging the spark arc, the exposure of the camera was very short (100 μs) such that the spark plug cannot be seen. The spark arc channel is overlaid on the pre-captured background images and false-colored. The background of the 1000 rpm, 46.5 kPa MAP cases (a and b in Figure 9-7) is brighter

than other images because it was taken with a flashlight shining into the cylinder while the background of other cases was taken without the flashlight illuminating the cylinder.

On the left side of the images in Figure 9-7 is the exhaust side of the cylinder and on the right is the intake side. In each column are images of 6th, 50th and 94th percentile arc channels based on the ranking of the numerical values of the arc centroid locations from the spark-plug axis. The different stretching directions are clearly illustrated. For the cases with low tumble (a,c), the arc stretches to the exhaust side for the 6th percentile cycles and it tends to stand between the electrodes for 50th percentile cycles. The arc is prone to stretching to the intake side counter to the bulk tumble motion in 94 percentile cycles. For cases with high tumble (b,d), the arc stretches to the exhaust side in all shown images.

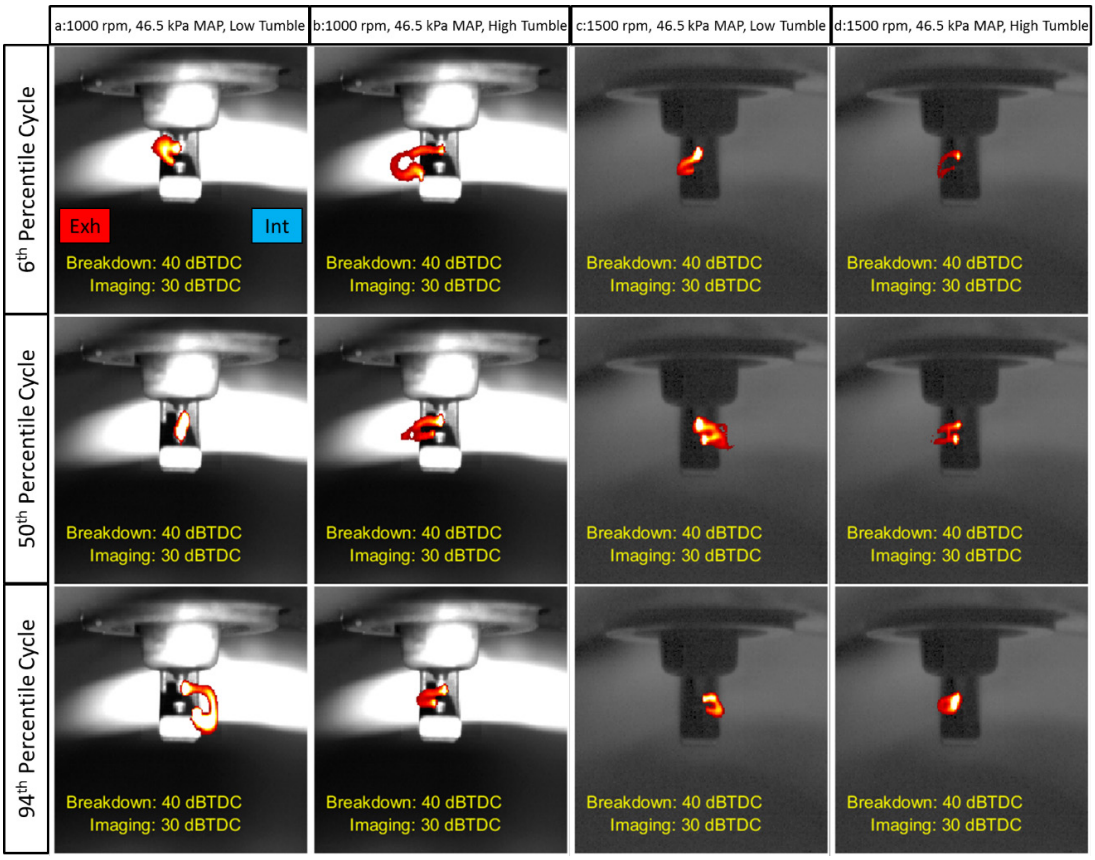

Figure 9-7: Three randomly selected cycles in four cases at 46.5 kPa MAP: (a)1000 rpm, low tumble; (b)1000 rpm, high tumble; (c)1500 rpm, low tumble; (d) 1500 rpm, high tumble.

9.5.1.3 Analysis of the Spark Arc Centroid Locations

To further characterize how different levels of tumble motion influence the arc stretching at different engine speeds and MAP, the arc centroid locations in horizontal direction from the spark-plug axis at 10°CA after breakdown marked by the vertical magenta lines in Figure 9-5 and Figure 9-6 (and in Figure 9-19 and Figure 9-20 in the appendix) are plotted in histogram in Figure 9-8 for 46.5 kPa MAP cases and in Figure 9-9 for 66.5 kPa MAP cases. For cases with the same MAP and engine speed, the histograms are overlaid on each other for low and high tumble cases. For the 1000 rpm case (left in Figure 9-8 and Figure 9-9), as the piston approaches TDC, the distribution of low tumble cases (blue) shifts to the intake side while that of the high tumble cases (red) remains quite consistent on the exhaust side. The trend is the same with the 1500 rpm cases (right in Figure 9-8 and Figure 9-9).

Comparing histograms of the cases at 46.5 kPa MAP (Figure 9-8) and 66.5 kPa MAP (Figure 9-9), one can observe that the high tumble motion is not as effective in maintaining the arc stretching direction to the exhaust side for higher MAP as for lower MAP. At 1000 rpm, 15.1% of cycles still have arc stretching to the intake side at 10°BTDC with high tumble at 66.5 kPa MAP (left in Figure 9-9) where only 4% of cycles have arc stretching to the intake side with high tumble at 46.5 kPa MAP (left in Figure 9-8). At 1500 rpm, 33.3% of cycles have arc stretching to the intake side at 10°BTDC with high tumble at 66.5 kPa MAP (right in Figure 9-9), but only 7.8% of cycles have arc stretching to the intake side with high tumble at 46.5 kPa MAP (right in Figure 9-8).

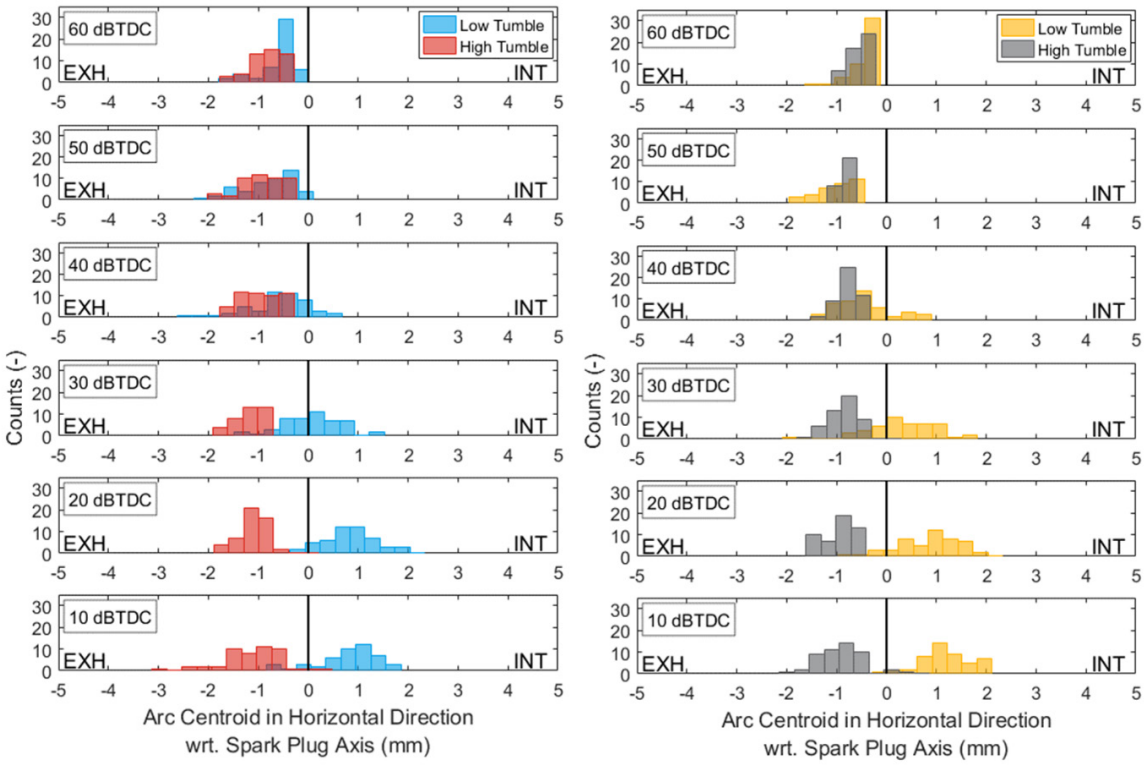

Figure 9-8: Histogram of the spark arc centroids in horizontal direction from spark-plug axis at different crank angles (measured at 10°CA after breakdown in each spark-advance swept point) for 46.5 kPa MAP (left: 1000 rpm, right: 1500 rpm).

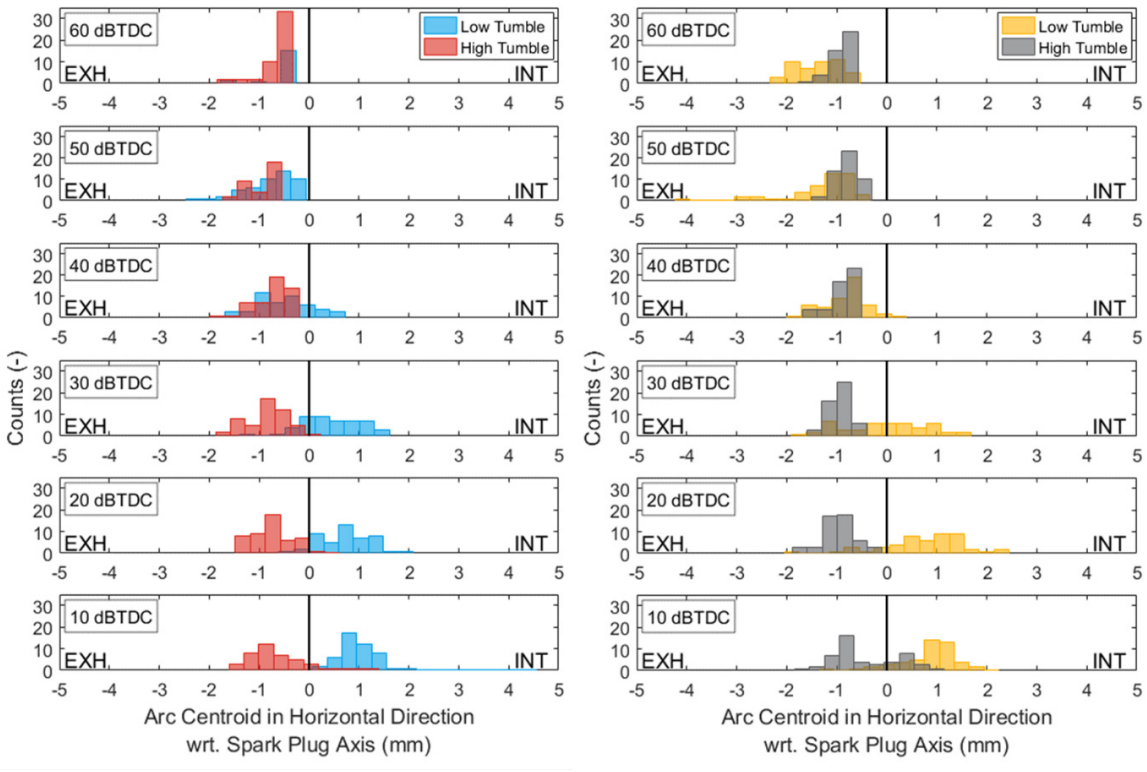

Figure 9-9: Histogram of the spark arc centroids in horizontal direction from spark-plug axis at different crank angles (measured at 10°CA after breakdown in each spark-advance swept point) for 66.5 kPa MAP (left: 1000 rpm, right: 1500 rpm).

In Figure 9-10 and Figure 9-11, the statistical analysis of all cases is summarized in form of mean and standard deviations (std) of the arc centroid locations in horizontal direction from the spark-plug axis. Note each curve is slightly offset horizontally for better visualization of the data points.

At 46.5 kPa MAP (Figure 9-10), as the piston approaches the TDC, the mean value of the 1000 rpm case with low tumble (blue) starts from 0.60 mm on the exhaust side of the spark-plug axis at 60°BTDC but shifts to 0.87 mm on the intake side as piston moves to 10°BTDC. At the same engine speed and MAP with high tumble (red), the mean value is at 0.79 mm on the exhaust side and it stretches even further to 1.1 mm on the exhaust side at 10°BTDC. For the 1500 rpm cases, the mean values follow the same trend. One

interesting observation is that, compared with the 1000 rpm case with high tumble (red), the mean values of the 1500 rpm case (gray) with high tumble are 0.2 mm shorter in average.

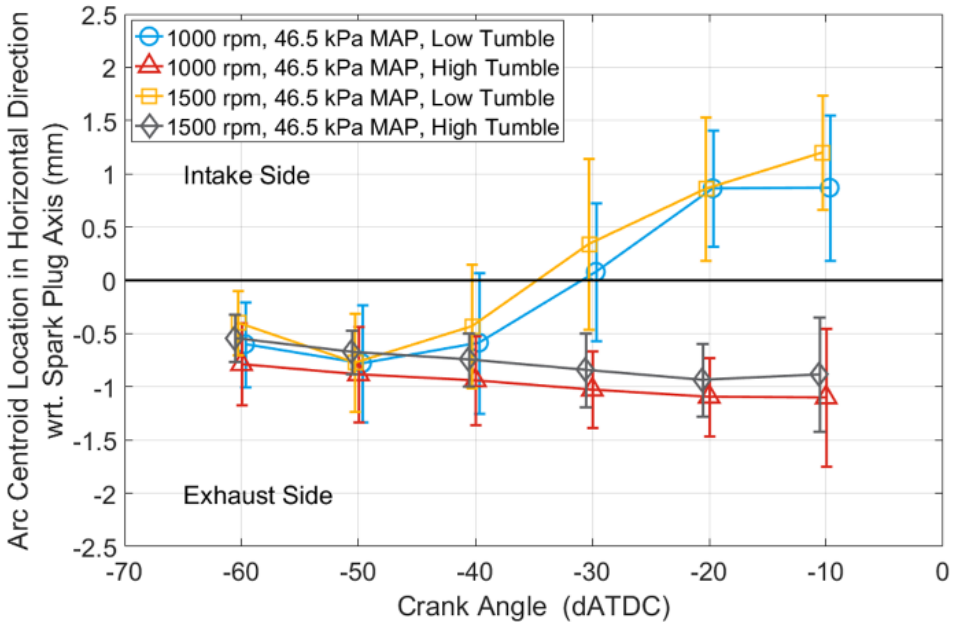

Figure 9-10: Mean and standard deviation of the spark arc centroid locations (measured at 10°CA after breakdown in each spark-advance swept point) in horizontal direction from spark-plug axis for 46.5 kPa MAP cases.

At higher MAP of 66.5 kPa (Figure 9-11), the 1500 rpm case with low tumble (yellow) exhibits longest mean arc stretch on the exhaust side (1.3 mm) compared with other three cases at 60°BTDC. As the piston moves to 10°BTDC, mean value shifts to 0.88 mm on the intake side. The two cases with high tumble (red and gray) have the mean values consistent on the exhaust side. At 20°BTDC, the mean arc centroid location of the 1000 rpm case with high tumble (red) remains at 0.73 mm on the exhaust side in horizontal direction, and it remains at 0.94 mm on the exhaust side for the 1500 rpm case with high tumble (gray). Compared with Figure 9-10, the 1500 rpm case with high tumble (gray) has 0.12 mm in average longer mean stretch than 1000 rpm case (red) from 60 to 10°BTDC.

Observing Figure 9-10 and Figure 9-11, one can see that from 50° to 20°BTDC, the spark arc experiences the directional transition stage from the exhaust side to the intake side with low tumble (blue and yellow).

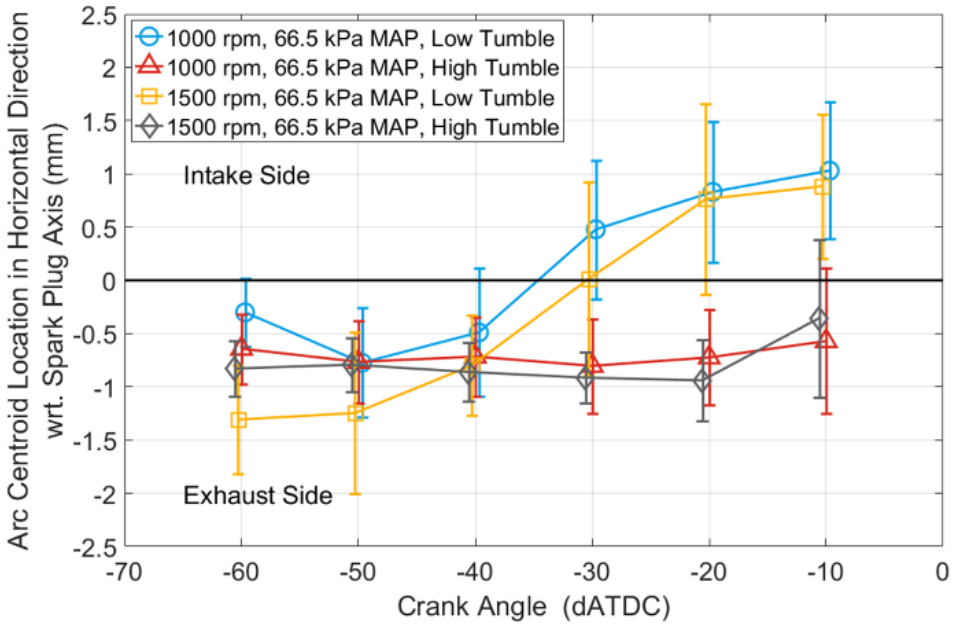

Figure 9-11: Mean and standard deviation of the spark arc centroid locations (measured at 10°CA after breakdown in each spark-advance swept point) in horizontal direction from spark-plug axis for 66.5 kPa MAP cases.

9.5.2 Flow Field Quantification near the Spark Plug

9.5.2.1 Sample Images of Flow Velocity Vectors

Sample flow field calculated from the PIV results are illustrated in Figure 9-12 for the 1000 rpm case with low tumble and in Figure 9-13 for the same engine speed with high tumble. The image covers 8 mm horizontally centered at the spark-plug axis and 6 mm vertically with the spark-plug center electrode tip positioned at 2 mm from the top of the image. On the left side of the image is the exhaust side and on the right is the intake. In both Figure 9-12 and Figure 9-13, from top row to the bottom are 60°BTDC, 40°BTDC and 20°BTDC crank angle positions; and at each timing, three consecutive cycles starting from a random cycle are illustrated. The flow motion can be seen from the sample images that for the cases

with low tumble (Figure 9-12), at 60°BTDC (row 1), the flow direction is pointing to exhaust side in all three cycles. At 40°BTDC (row 2), the first and third cycles have flow motion pointing to the exhaust side, while the second cycle exhibits a flow motion of opposition direction. At the later crank position of 20°BTDC (row 3), all three shown cycles have flow motion from the exhaust side to the intake side.

In Figure 9-13 is shown the 1000 rpm case with high tumble. One can easily observe that with high tumble, the flow motion is stronger and the flow direction is consistently pointing to the exhaust side in all shown cycles.

The sample images of 1500 rpm can be found in Figure 9-21 and Figure 9-22 in the appendix.

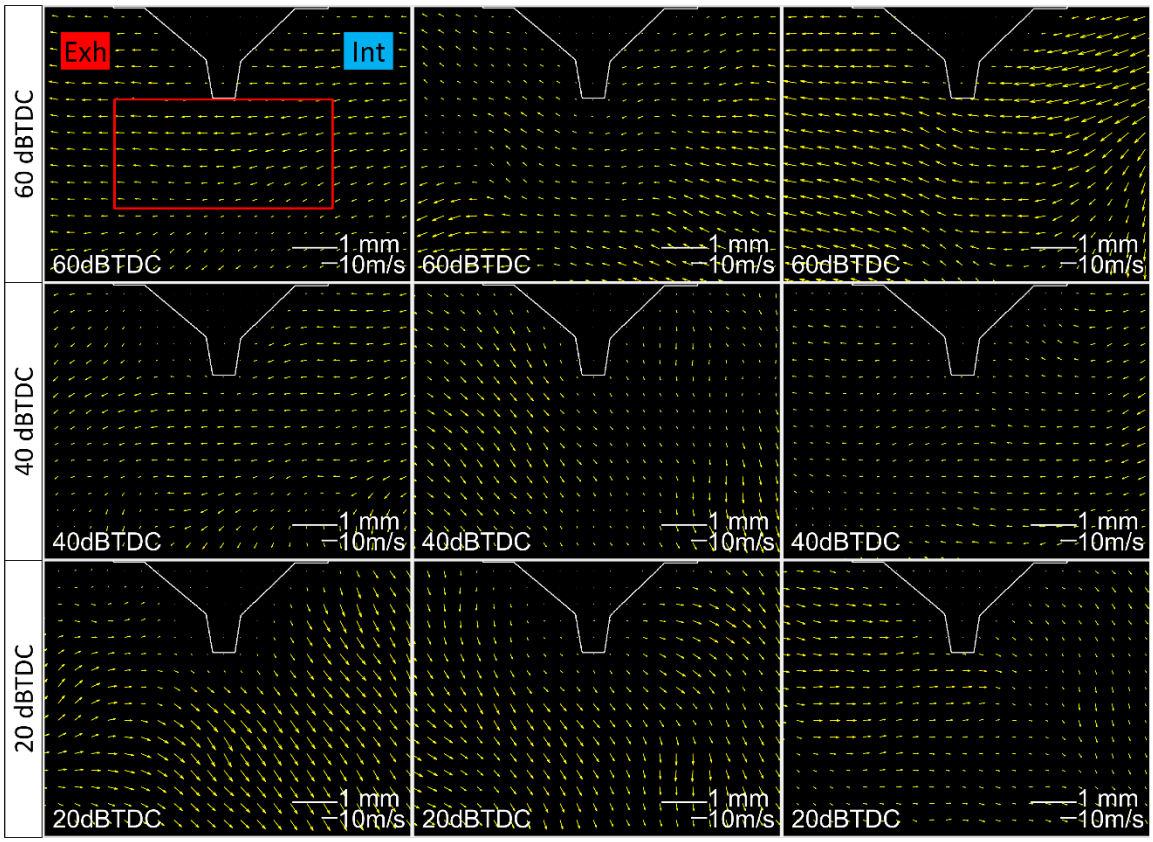

Figure 9-12: Three randomly selected cycles for 60°BTDC, 40°BTDC and 20°BTDC each at 1000 rpm, low tumble.

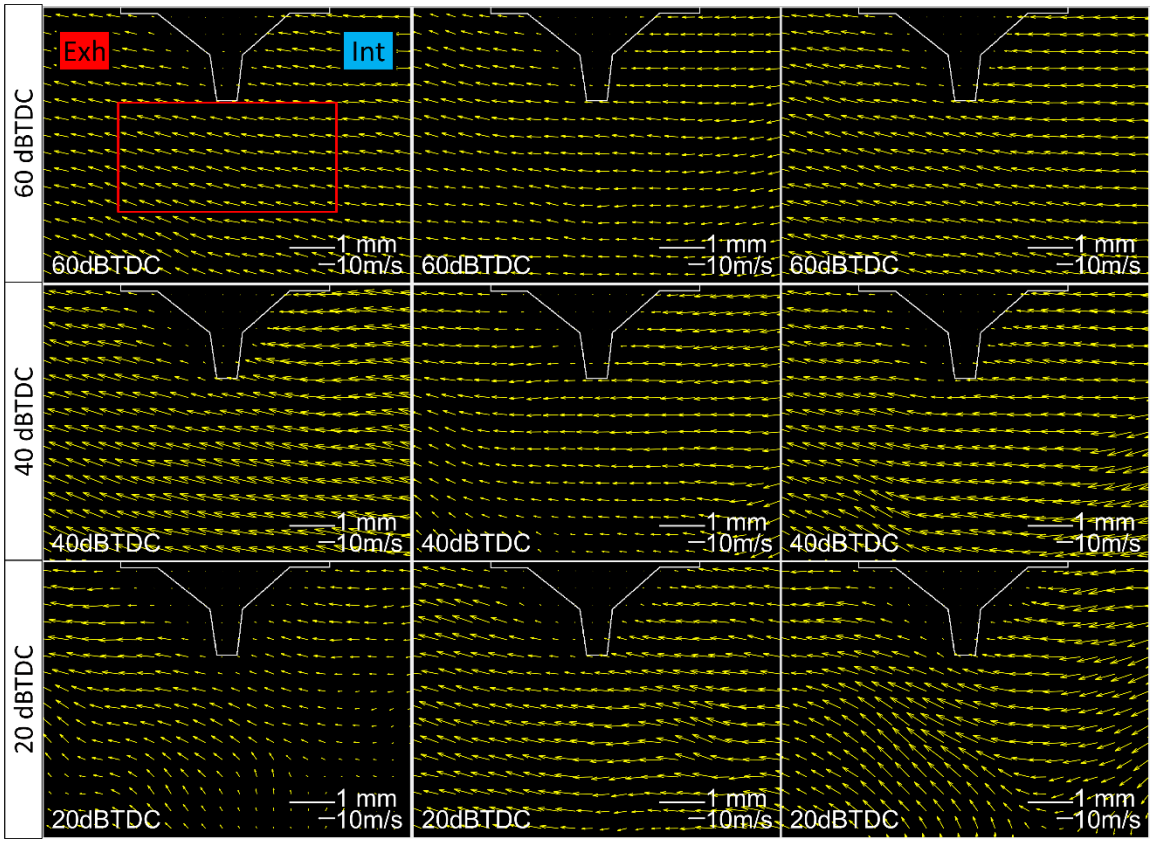

Figure 9-13: Three randomly selected cycles for 60°BTDC, 40°BTDC and 20°BTDC each at 1000 rpm, high tumble.

9.5.2.2 Analysis of Velocity Vectors

To better understand how the flow condition changes near the spark plug, the horizontal component of all velocity vectors from all measured cycles in the 5 mm × 2.5 mm rectangular region upper edged at the spark-plug center tip (marked by the red box in the first sample image in Figure 9-12 and Figure 9-13) are plotted in histograms for different cases (Figure 9-14).

The 1000 rpm cases are shown on the left in Figure 9-14. From top to bottom are 60°BTDC to 20°BTDC with 10°CA interval. The histogram clearly shows the flow direction changes as the piston approaches TDC with low tumble (blue); and the distribution with high tumble (red) remains quite constant around 10 m/s on the left side, which means the flow direction is pointing to the exhaust side in agreement with the bulk tumble motion. Furthermore, as

the piston moves closer to TDC, the distribution becomes wider and flatter, indicating the variation in the horizontal velocity increases as the large-scale flow motion breaks into small-scale eddies.

Comparing the 1500 rpm cases (right in Figure 9-14) with the 1000 rpm cases (left in Figure 9-14), the distributions of both low and high tumble cases become wider. This should be expected since higher engine speed results in stronger flow motion and higher turbulence. The 1500 rpm case (right in Figure 9-14) also illustrates that the horizontal velocity near the spark plug changes direction close to TDC with low tumble (yellow), while the cases with high tumble (gray) produce a well maintained horizontal velocity near the spark plug. In both speeds, 40°BTDC is in the center of the flow directional transition stage for low tumble cases (blue and yellow) where the center of the distribution lies close to 0 m/s velocity.

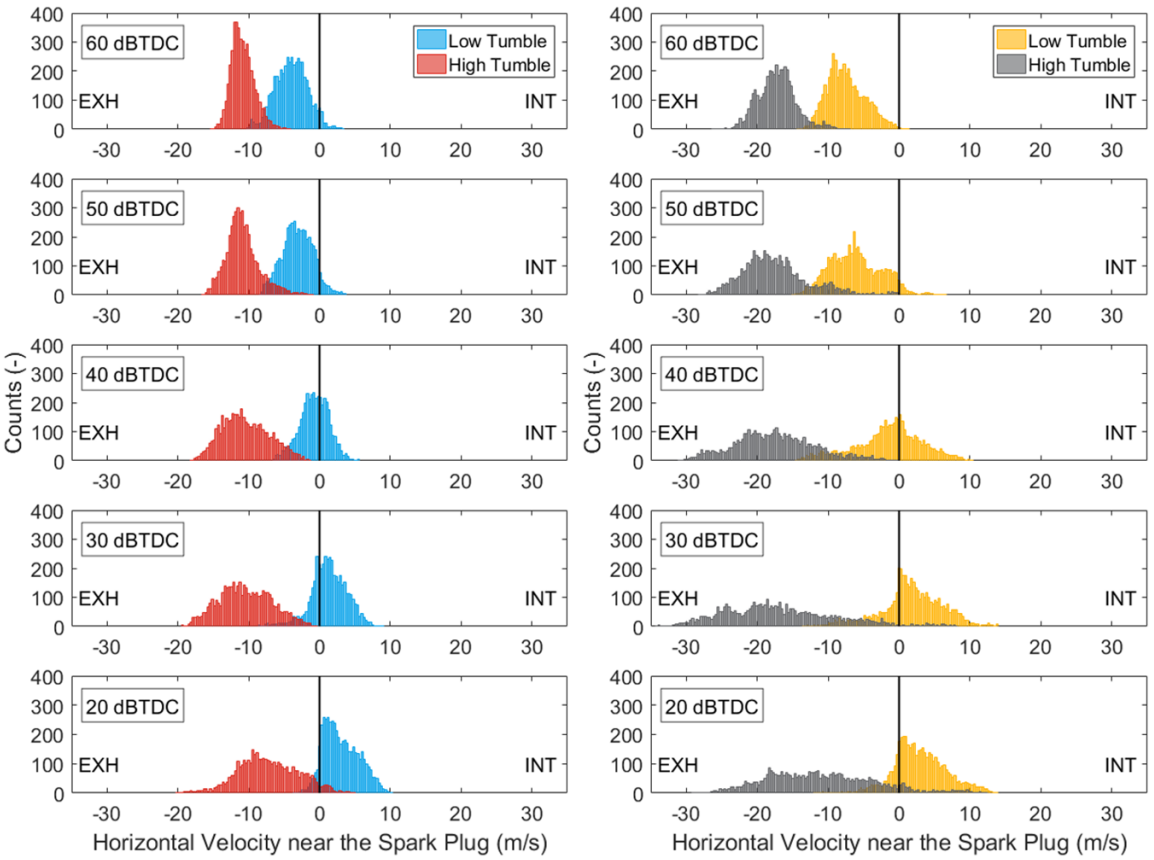

Figure 9-14: Histogram of horizontal velocity components in the 5 mm × 2.5 mm rectangular region upper edged on the spark-plug center electrode (left: 1000 rpm, right: 1500 rpm).

The mean values of the horizontal velocity in the studied near-spark-plug region and standard deviations are plotted in Figure 9-15. Again, each curve is slightly offset horizontally for better visualization. It can be conveniently observed that the flow direction in the vicinity of the spark plug experiences a transition stage from pointing to the exhaust side to pointing to the intake side between 50°BTDC to 20°BTDC for low tumble cases (blue and yellow), and the high tumble cases (red and gray) maintain the flow motion direction pointing to the exhaust side throughout the studied crank angle range. For 1000 rpm cases, at 60°BTDC, the mean horizontal velocity increases from 3.9 m/s ± 2.3 m/s std with low tumble (blue) to 10.8 m/s ± 1.6 m/s std with high tumble (red). At 20°BTDC, mean horizontal velocity with low tumble (blue) reverses direction with the magnitude of 3.1 m/s ± 2.5 m/s std, while the high tumble motion (red) maintains the mean horizontal

velocity direction at 7.3 m/s ± 4.2 m/s std. Further investigation of 1000 rpm with high tumble (red) reveals that as the piston moves closer to TDC, the standard deviation of the horizontal velocity gradually increases though the mean value is well retained at 10.6 m/s in average from 60°BTDC to 30°BTDC, and it decreases to 7.3 m/s at 20°BTDC. With low tumble (blue), the standard deviation is kept at the same level but the mean value changes sign. This is also true for 1500 rpm cases where mean velocity changes from 7.5 m/s ± 2.7 m/s std pointing to the exhaust side at 60°BTDC to 2.9 m/s ± 3.7 m/s std pointing to the intake side at 20°BTDC with low tumble (yellow); and with high tumble (gray), the mean velocity is maintained at 17.3 m/s in average from 60°BTDC to 30°BTDC, and decreases to 11.0 m/s at 20°BTDC with gradually increasing variability.

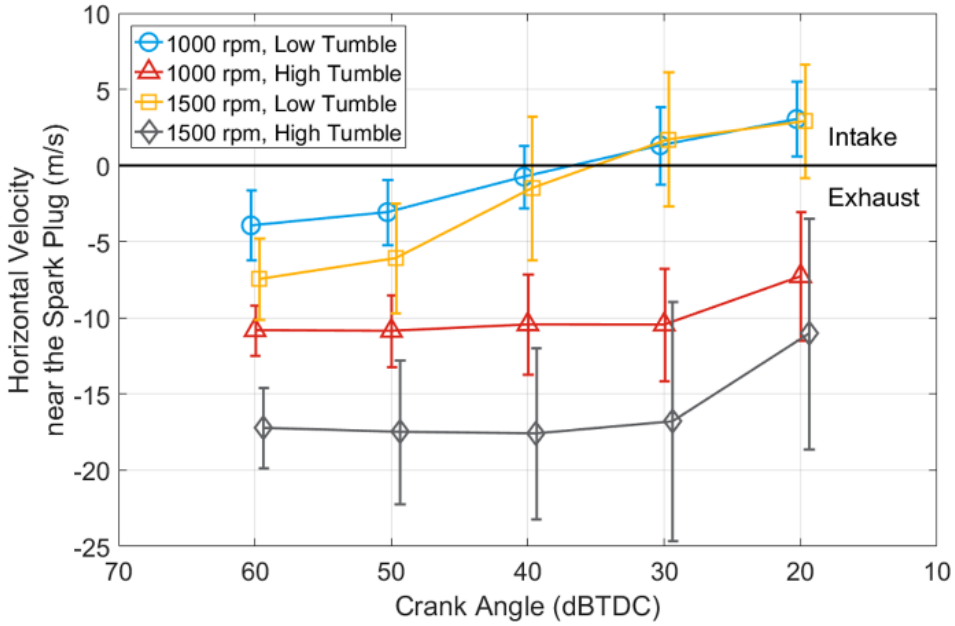

Figure 9-15: Mean and standard deviation of the horizontal velocity components near the spark plug.

This indicates that, for stoichiometric mixture with low tumble, for which the spark timing is commonly between 30 to 10°BTDC, the flow near the spark plug has shifted direction pointing to the intake side counter to the bulk tumble motion. The variability introduced to the flame kernel convection in horizontal direction by flow motion could be smaller; however, the unburned mixture is pushed towards the exhaust side and being compressed

and combusted the last, which might lead to higher probability of knock due to the hot zone on the exhaust side. Moreover, for diluted mixture where the spark timing frequently advanced well beyond 30°BTDC, the flow near the spark plug experiences the directional transition stage such that the initial flame kernel could convect to either side of the spark plug. From the authors' previous study [47], the early flame kernels convecting to the intake side are usually less stretched, smaller and centered at the spark-plug electrodes, resulting in slowly growing flame kernels. As a brief summary, the high tumble motion is desired in order to maintain the flow direction in the vicinity of the spark plug so the early flame kernels are consistently convecting to the exhaust side to form more stretched and larger flame kernels at diluted conditions, and also to prevent the unburned mixture to be compressed and combusted last on the hot exhaust side at stoichiometric conditions.

9.5.3 Engine Firing Tests

9.5.3.1 Combustion Metrics

The test matrix and important combustion metrics of the engine skip-firing tests are summarized in Table 9-6. For the case with high tumble, the ignition delay CA0010 is 1.9°CA shorter, CA50 is 2.9°CA earlier and bulk burn CA1090 is 4.9°CA shorter, compared with the case with low tumble.

Table 9-6: Operation conditions and combustion metrics.

Tumble Level	Mean IMEP (kPa)	Engine Speed (rpm)	Mean Lambda (-)	Mean CA0010 (°CA)	Mean CA50 (°ATDC)	Mean CA1090 (°CA)
Low	260	1000	1.05	16.0	12.9	17.4
High	240	1000	1.04	14.1	9.0	12.5

9.5.3.2 2D Probability Distribution Function (2D-PDF)

The 2D-PDF images of the flame kernels are illustrated in Figure 9-16. The detailed calculation method of 2D-PDF can be found in the authors' paper [47]. As can be seen in Figure 9-16, with low tumble (left), the flame kernels starts propagating to the intake side counter to the bulk tumble motion at 0.5 ms after ignition timing (msAIT). With high tumble (right), flame kernels consistently propagate to the exhaust side. At 2 msAIT, about

20% of cycles result in flame kernels filling the cylinder where no cycles with low tumble have flame kernels filling the cylinder.

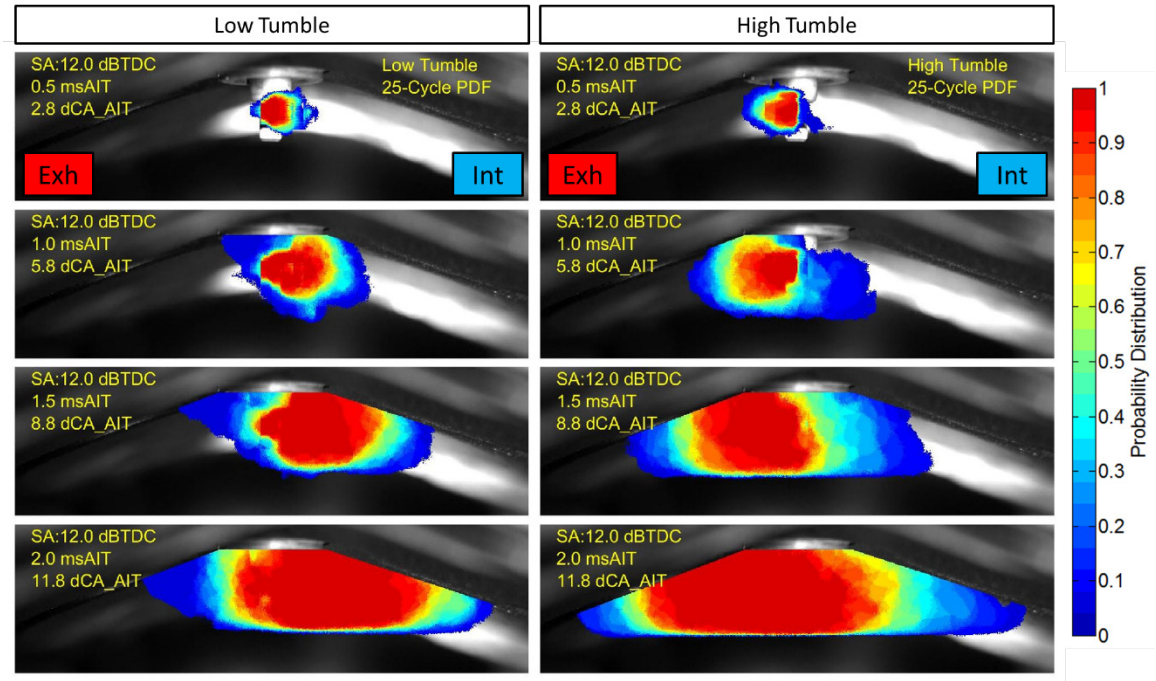

Figure 9-16: 2D-PDF of the flame kernel propagation: (left) low tumble; (right) high tumble.

The mean values and standard deviations of the flame kernel centroid locations in horizontal direction from the spark-plug axis and the projected flame area are plotted in Figure 9-17 and Figure 9-18. From Figure 9-17, just as what has been discussed in the last section, at late ignition timing as 12°BTDC in this case, the flow direction has already completed shifting to pointing to the intake side with low tumble (Figure 9-10 and Figure 9-15); as a result, the flame kernels with low tumble (blue) consistently convect to the intake side with less fluctuation compared with the case with high tumble. Also in agreement with flow field measurement results, the convection direction is well maintained on the exhaust side but the flame centroid location has higher variability with high tumble (red) than the case with low tumble. At TDC, the mean horizontal convection location is 2.0 mm with 2.4 mm std on the exhaust side from the spark-plug axis for the case with high tumble (red); with low tumble (blue), the mean value reaches to 5.9 mm on the intake side

with 1.28 mm std. Please note the seemingly shorter convection distance at TDC with high tumble is caused by the faster burning flame that the centroid location of the flame is converging faster to the geometric center of the cylinder.

In Figure 9-18, flame kernels with high tumble (red) grow faster in average compared with the case with low tumble (blue). At TDC, which is 12°CA after ignition, the mean value of the projected flame area reaches to 249 mm^2 with 35.3 mm^2 std with high tumble (red); while it only reaches to 184.9 mm^2 with 23.0 mm^2 std with low tumble (blue).

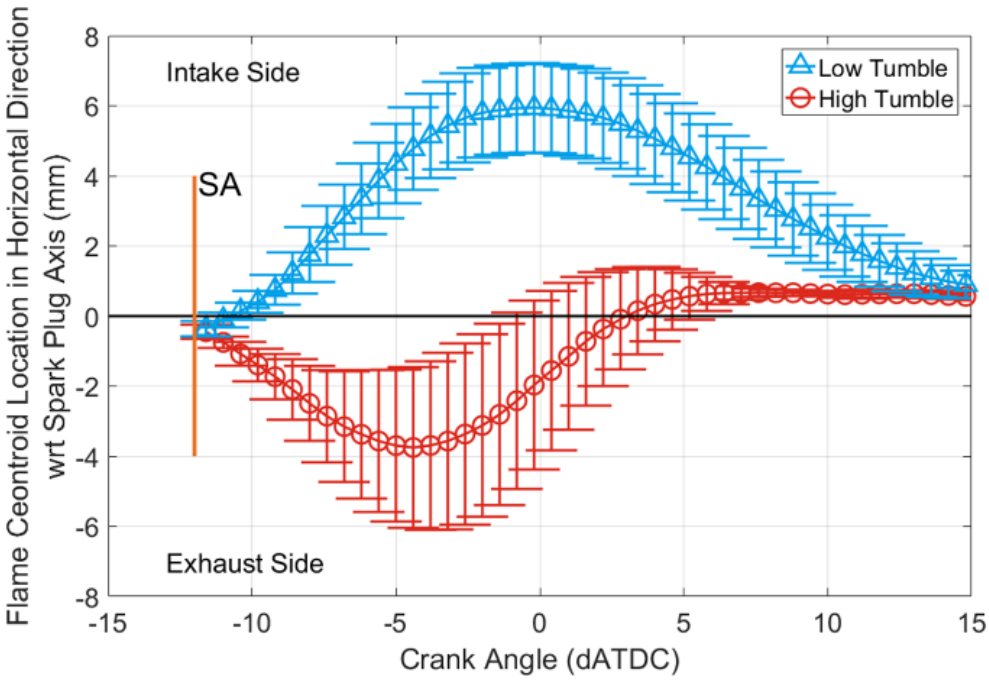

Figure 9-17: Mean and standard deviation of the flame kernel centroids.

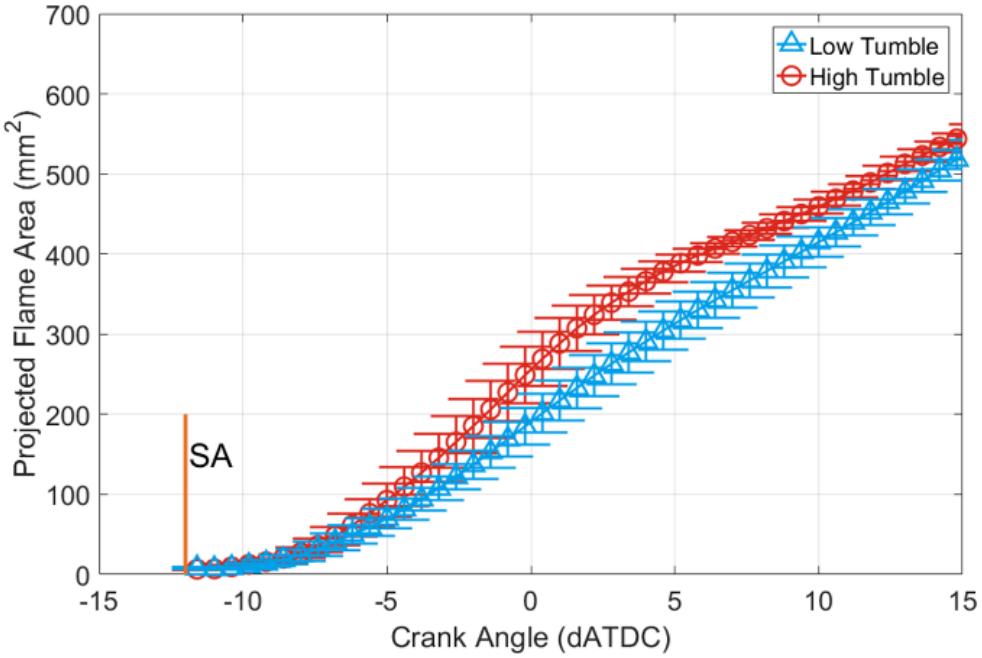

Figure 9-18: Mean and standard deviation of the projected flame area.

9.6 Summary and Conclusions

Though the design of modern DISI engines aims have a consistent tumble motion at the timing of ignition, the authors' previous work [47] revealed that the early flame kernel could convect to the intake side counter to the bulk tumble motion, and it tends to be centered at the spark-plug electrodes and have small projected flame area. The current study furthers the understanding of the variation in early flame kernel convection direction by investigating the flow motion near the spark plug at ignition timing ranging from 70°BTDC to 20° BTDC by means of high-speed imaging of the spark arc stretching and PIV flow field measurement at both low and high tumble levels. Lastly, the results are supported by high-speed imaging of the early flame kernel at the stoichiometric condition at both low and high tumble levels.

At low tumble, the flow can change direction from the bulk motion at the time of ignition. For the studied cases with low tumble, 84% of cycles have arc stretching to the intake side

counter to the bulk tumble motion at 10°BTDC. The transition of flow direction from pointing to the exhaust side to pointing to the intake side introduces variability to the initial flame kernel convection and development.

By increasing the tumble level by means of tumble planks, the flow motion can be well maintained until late in the compression stroke. Increasing the tumble level does not completely eliminate the direction shifting of the flow motion near the spark plug, however, compared with cases with low tumble, the shift occurs much later in the compression stroke (10°BTDC).

At higher MAP (66.5 kPa), the high tumble motion is less effective in maintaining the flow direction near the spark plug at late stages of compression stroke compared with low MAP (46.5 kPa).

At low tumble, the mean value of the horizontal flow velocity near the spark plug changes direction from pointing to the exhaust side with magnitude of 3.9 m/s at 60°BTDC to 3.1 m/s pointing to the intake side at 20°BTDC at 1000 rpm. The trend is similar at 1500 rpm with low tumble.

At high tumble, the mean value of the horizontal flow velocity near the spark plug is well maintained at 10.6 m/s pointing to the exhaust side in agreement with the bulk tumble motion from 60°BTDC to 20°BTDC for 1000 rpm, and at 17.3 m/s pointing to the exhaust side at the same crank angle range for 1500 rpm.

The variation of horizontal flow velocity increases as the piston moves closer to TDC.

The early flame kernels tend to convect to the intake side with lower variability with low tumble for a spark-advance of 12°BTDC due to at this late ignition timing, the flow direction has completely changed direction from the bulk tumble motion.

The early flame kernels are convecting to the exhaust side with high tumble for spark-advance 12°BTDC with higher variability in flame kernel centroid locations in horizontal direction from the spark-plug axis compared with low tumble cases; however, the mean

projected flame area is larger with high tumble and the variability of the projected flame area is on the same level compared with low tumble cases.

The high tumble motion is desired in order to maintain the flow direction in the vicinity of the spark plug so the early flame kernels are consistently convecting to the exhaust side to form more stretched and larger flame kernels at diluted conditions, and also to prevent the unburned mixture to be compressed and combusted last on the hot exhaust side at stoichiometric conditions.

9.7 Future Work

The early flame kernel convection will be investigated through high-speed imaging at a wider range of spark timings at different dilution levels with low and high tumble with simultaneous PIV flow field measurement near the spark plug. Different spark-plug electrode designs will be tested to study the interaction between the initial flame kernel and the electrodes with different tumble levels and its impacts on combustion at both lean and stoichiometric conditions.

9.8 Acknowledgments

We would like to thank Ford Motor Company for funding this project, and providing technical support and guidance.

We also give our thanks to Mahle Powertrain for providing the optical engine, especially thanks to Mike Bunce and Eric Smith for their guidance on instrumentation of the optical engine.

Last but not least, thanks to Joel Duncan and Jesse Hill from Advanced Power Systems Labs at Michigan Technological University for their technical assistance on this project.

9.9 Abbreviations

AIT	after ignition timing
AKI	Anti-knock index
ATDC	After top dead center
BTDC	Before top dead center
CA	Crank angle
COV	Coefficient of variation
DISI	Direction injection spark ignition
Fps	Frame per second
GHG	Greenhouse gas
GDI	Gasoline direct injection
IMEP	Indicated mean effective pressure
LD	Light duty
MAP	Manifold absolute pressure
MFB	Mass fraction burned
PIV	Particle imaging velocimetry
RPM	Revolutions per minute
SA	Spark advance
SI	Spark ignition

Std	Standard deviation
TDC	Top dead center
TP	Tumble plank
TDC	Top dead center

9.10 Appendix

9.10.1 Traces of Arc Centroids for 66.5 kPa MAP Cases

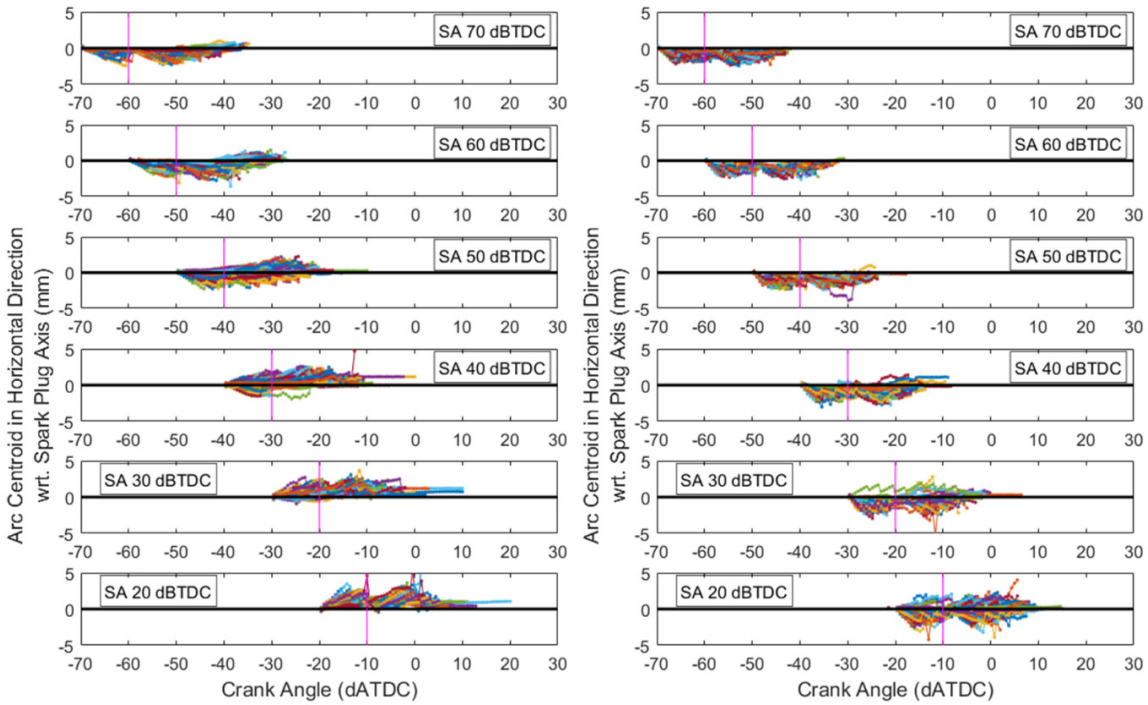

Figure 9-19: Traces of spark arc centroid locations in horizontal direction from spark plug axis, 1000 rpm, 66.5 kPa (left: low tumble, right: high tumble).

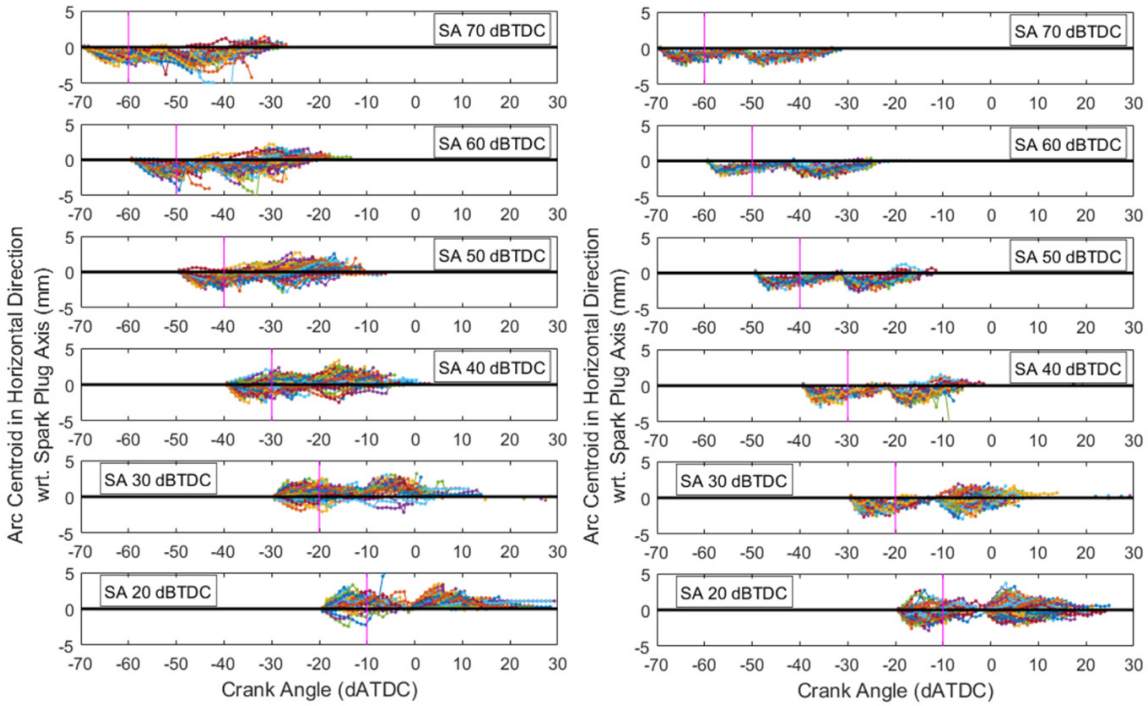

Figure 9-20: Traces of spark arc centroid locations in horizontal direction from spark plug axis, 1500 rpm, 66.5 kPa(left: low tumble, right: high tumble).

9.10.2 Sample Flow Field Velocity Vector Images for 1500 rpm Cases

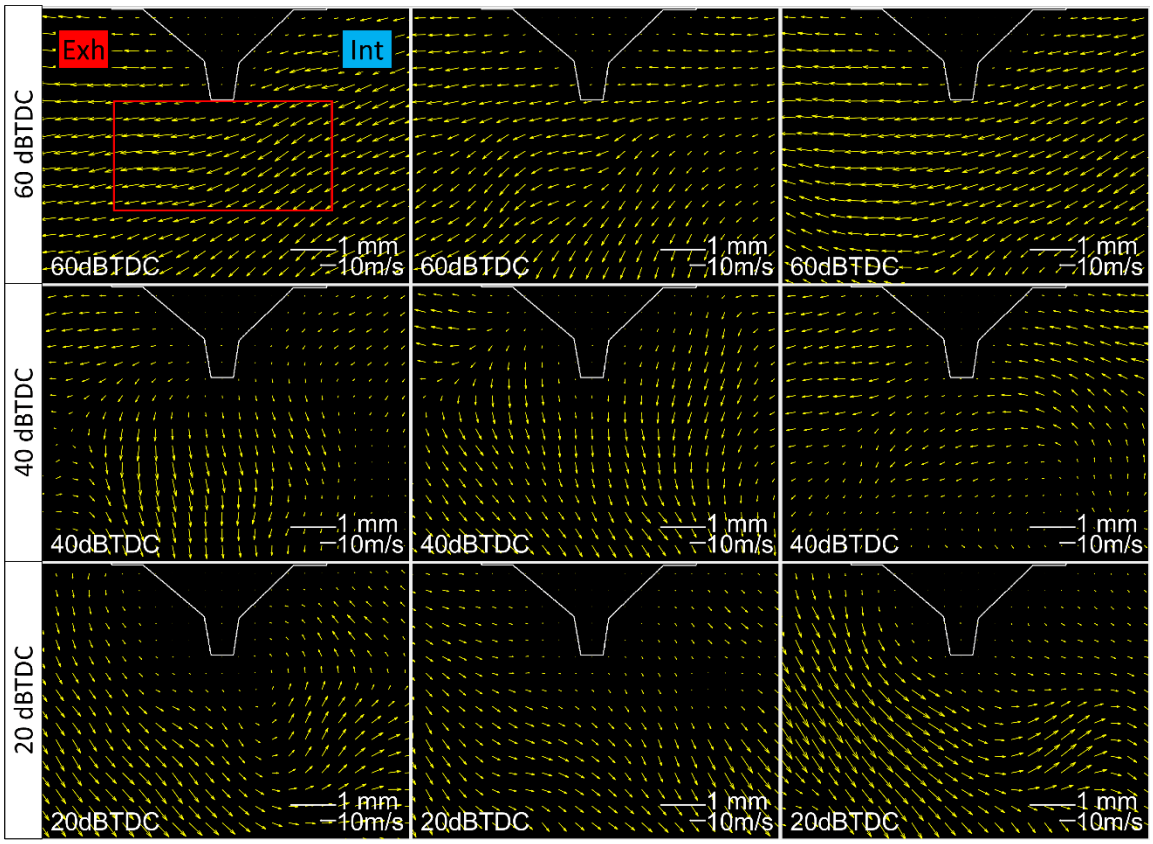

Figure 9-21: Three randomly selected cycles for 60°BTDC, 40°BTDC and 20°BTDC each at 1500 rpm, low tumble.

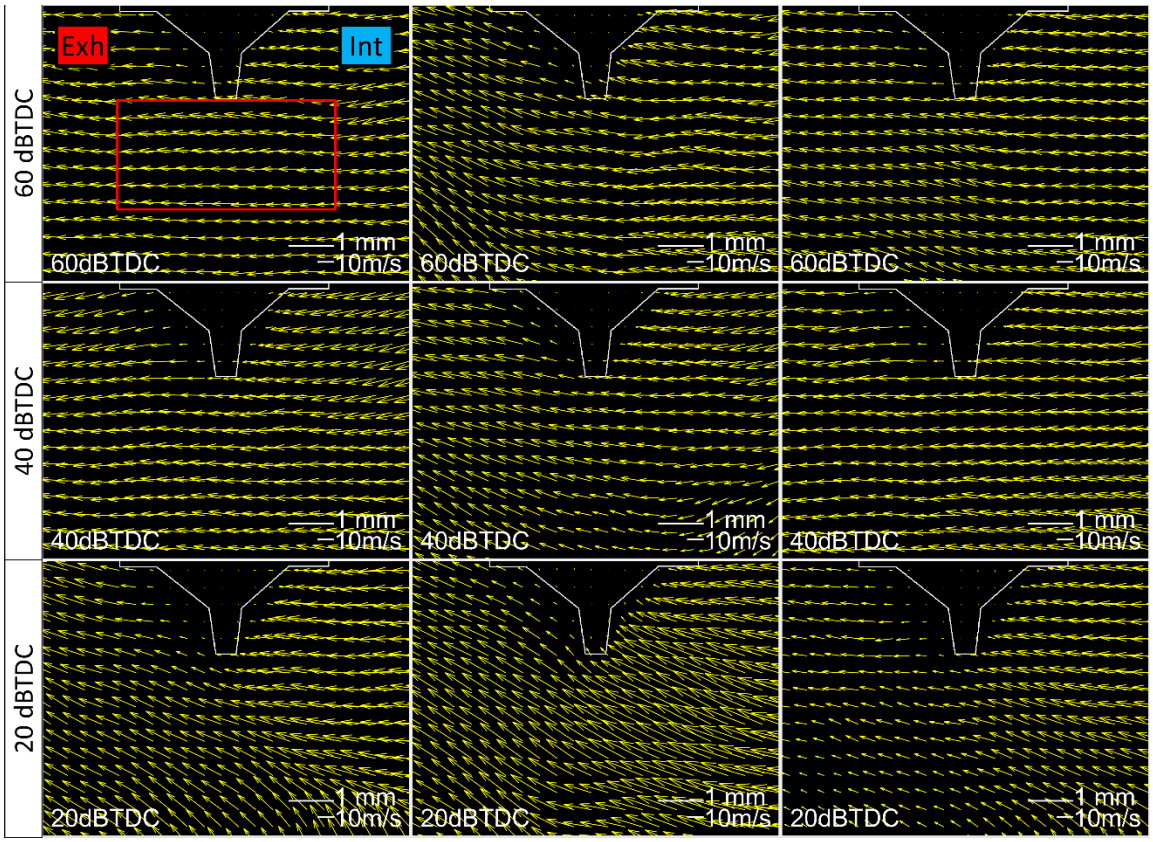

Figure 9-22: Three randomly selected cycles for 60°BTDC, 40°BTDC and 20°BTDC each at 1500 rpm, high tumble.

10 Summary and Future Work

As one of the key enablers of achieving higher SI engine efficiency, diluted combustion faces the major challenge of increased combustion instability as the dilution level increases. The factors that affect the combustion stability have been identified as the cyclic variations in flow motion, cyclic variations in mixture composition, and also the mixture inhomogeneity within each cycle [40]. Previous research have demonstrated that the variation in flow motion is the dominant factor that causes the cycle by cycle variability of combustion [32, 33, 37], however the understanding of detailed mechanism of how the variation in flow influences the cyclic combustion variability is still incomplete.

The research described in this dissertation shed more light on the relationship between the variations in flow motion and the combustion variability by investigating the flow motion near the spark plug and analyzing the flame kernel propagation and combustion.

The flow motion near the spark plug with low tumble was studies via three methods: high-speed imaging of the spark arc channel stretching, flow field quantification using PIV, and high-speed imaging of the flame kernel. The flow motion near the spark plug starts from pointing to the exhaust side at early spark timing (before 50°BTDC) to eventually pointing to the intake side at late spark timing (later than 20°BTDC) with low tumble, as shown by the arc stretching results in Figure 9-8 and by the flow field results in Figure 9-14. In the range between 50°BTDC and 20°BTDC, the flow experiences a directional transition stage where it can point to either direction near the spark plug, which is marked by the pinky box in Figure 10-1.

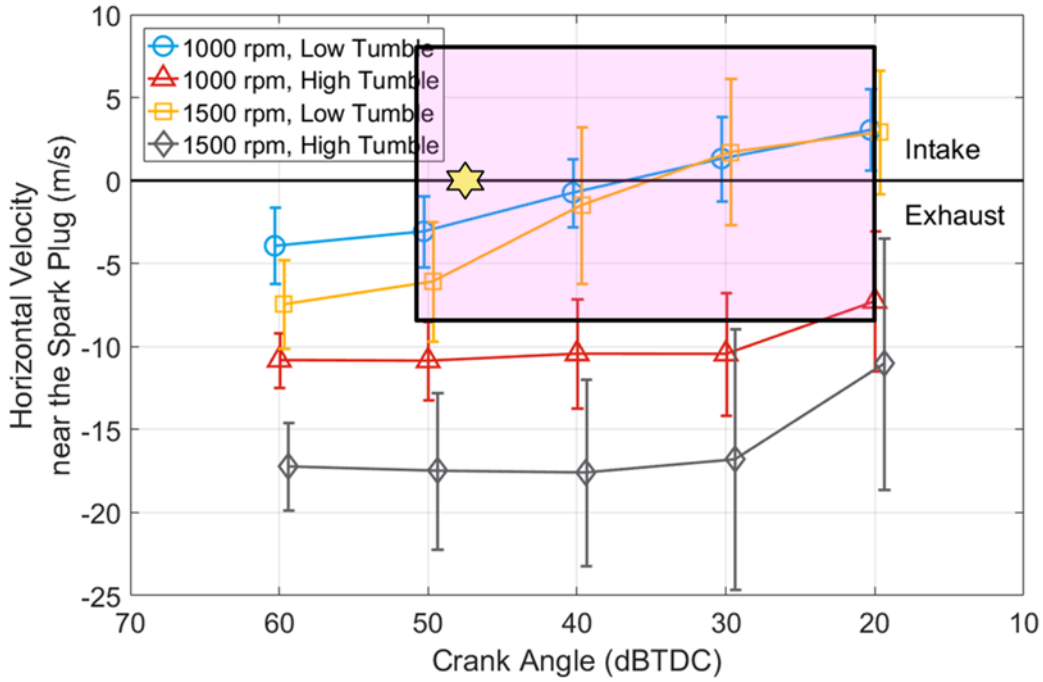

Figure 10-1: Illustration of the flow directional transition window.

The flow motion with low tumble at 40°BTDC (blue distribution in subplot 3 in Figure 9-8 and Figure 9-14) is singled out for illustration here in Figure 10-2, as this moment marks the center of the flow directional transition stage, where cycles have flow pointing to either exhaust side or intake side near the spark plug with a 50:50 ratio.

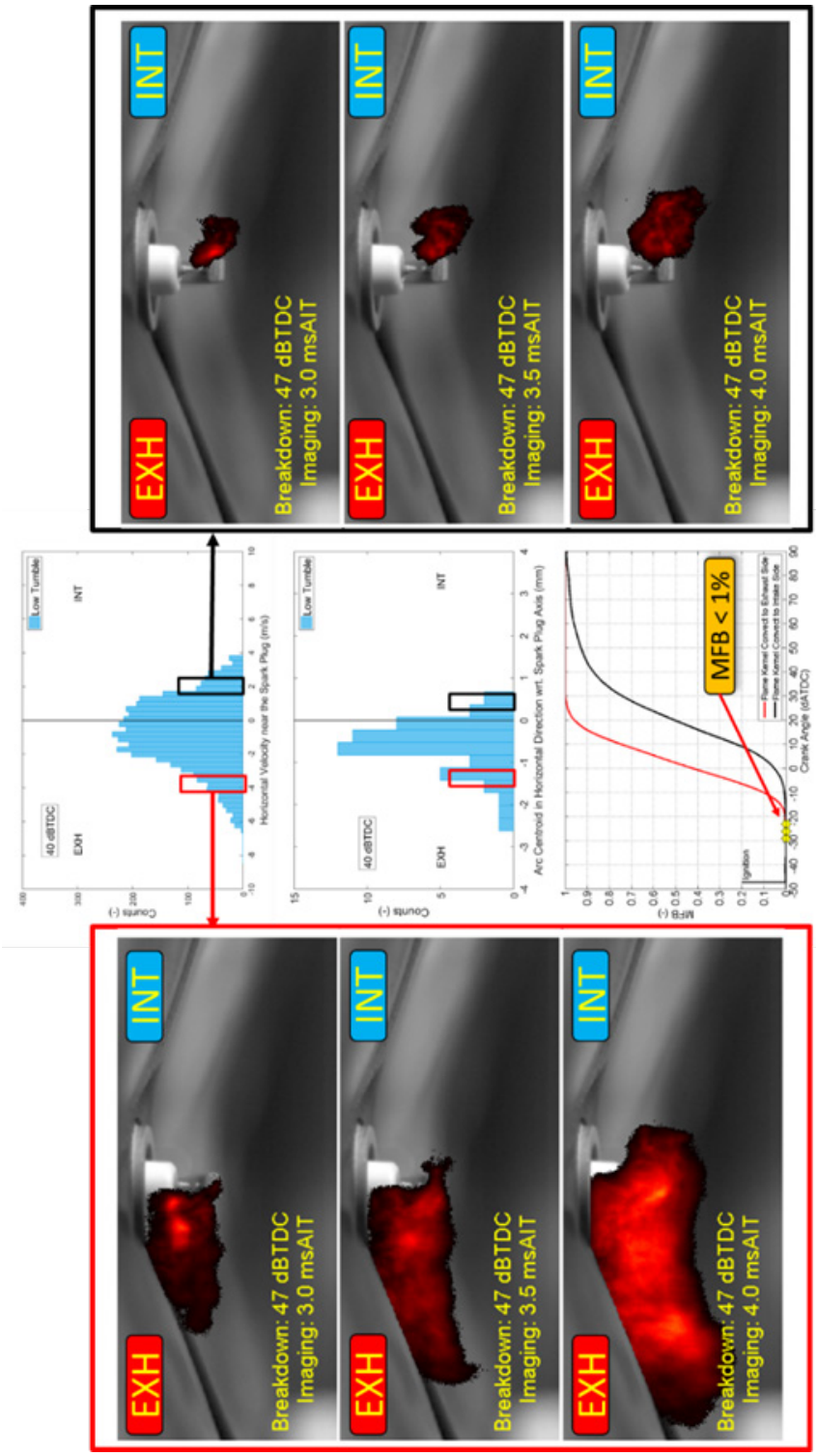

Figure 10-2: Illustration of variations in flow motion and resulting flame kernel and combustion.

With lean combustion (lambda = 1.38) at IMEP 250 kPa and 1000 rpm engine speed, the spark advance was set at 47°BTDC to maintain MBT (marked with the yellow star in Figure 10-1), which falls within the flow directional transition window with low tumble as can be seen in Figure 10-1. Two cycles representing the two different flow conditions are selected based on the early flame convection direction (Figure 10-2). On the left is the cycle where the flow points to the exhaust side near the spark plug, and on the right is the cycle where the flow points to the intake side. It can be easily observed that the flame kernel propagating towards the exhaust side is larger in size, more stretched and growing faster than the flame kernel propagating towards the intake side. The resulting MFB curves are also shown in Figure 10-2. As a result of the different flame developing rate, the MFB curves of these two cycles also exhibit significant difference, where the MFB of the cycle with early flame propagating to the exhaust side rises earlier and the charge is burned faster than the cycle with early flame propagating to the intake side.

The crank positions of the three shown snapshots of the flame are marked with yellow stars on the MFB plot. It is worth noting that at these moments, MFB is still below 1%, indicating that the flame characteristics before MFB reaching 1% is already crucial enough to influence the later stages of combustion.

This research explored the relationship between the variations in flow motion and the combustion variability. The results showed that there exists a flow directional transition stage near the spark plug with low tumble conditions. However, the root cause for this flow transition has not been revealed in this research. The intake-charge-induced tumble is mainly counterclockwise viewing from the front of the engine, namely the main tumble flow points to the exhaust side near the spark plug. The main tumble motion must be overcome by certain processes or mechanisms to lead to the reversed flow direction near the spark plug. To understand what processes and mechanism that could cause the reversed flow near the spark plug, flow velocity field should be investigated in a larger region including near-intake-valve area since the momentum of the charge is generated by the intake stroke through the intake valves. It is also recommended to investigate the flow field on the swirl plane to determine if there is any significant swirl motion occurring in the

cylinder which could also result in reversed flow direction near the spark plug, if the swirl vortex center is not aligned with the cylinder axis.

11 Reference List

1. EIA, "*Annual Energy Outlook 2016 with projections to 2040"*. 2016, Department of Energy. p. 256.

2. "*Light-Duty Automotive Technology, Carbon Dioxide Emissions, and Fuel Economy Trends: 1975 Through 2016"*. 2016, Environmental Protection Agency.

3. "*LEV III and Tier 3 Exhaust Emission Control Technologies for Light-Duty Gasoline Vehicles"*. 2013, Manufacturers of Emission Controls Association.

4. EPA, "*EPA Sets Tier 3 Tailpipe and Evaporative Emission and Vehicle Fuel Standards"*, 2014, Environmental Protection Agency

5. EPA, "*EPA and NHTSA Set Standards to Reduce Greenhouse Gases and Improve Fuel Economy for Model Years 2017-2025 Cars and Light Trucks"*, 2012, Environmental Protection Agency

6. "*2017|2018 Worldwide Emissions Standards | Passenger Cars and Light Duty Vehicles"*. 2017, Delphi.

7. Zhao, H., *Advanced Direct Injection Combustion Engine Technologies and Development Volume 1: Gasoline and Gas Engines*. 2009: Woodhead Publishing. 312.

8. Lake, T., Stokes, J., Murphy, R., Osborne, R., et al. "*Turbocharging Concepts for Downsized DI Gasoline Engines"*, SAE International 2004-01-0036, 2004, doi:10.4271/2004-01-0036.

9. Fraser, N., Blaxill, H., Lumsden, G. and Bassett, M., "*Challenges for Increased Efficiency through Gasoline Engine Downsizing".* SAE Int. J. Engines, 2009. **2**(1): p. 991-1008, doi: 10.4271/2009-01-1053.

10. Zaccardi, J.-M., Pagot, A., Vangraefschepe, F., Dognin, C., et al. "*Optimal Design for a Highly Downsized Gasoline Engine"*, SAE International 2009-01-1794, 2009, doi:10.4271/2009-01-1794.

11. Lecointe, B. and Monnier, G. "*Downsizing a Gasoline Engine Using Turbocharging with Direct Injection"*, SAE International 2003-01-0542, 2003, doi:10.4271/2003-01-0542.

12. Davis, R.S., Mandrusiak, G.D. and Landenfeld, T., "*Development of the Combustion System for General Motors' 3.6L DOHC 4V V6 Engine with Direct Injection".* SAE Int. J. Engines, 2008. **1**(1): p. 85-100, doi: 10.4271/2008-01-0132.

13. Yi, J., Wooldridge, S., Coulson, G., Hilditch, J., et al., "*Development and Optimization of the Ford 3.5L V6 EcoBoost Combustion System*". SAE Int. J. Engines, 2009. **2**(1): p. 1388-1407, doi: 10.4271/2009-01-1494.

14. Jocsak, J., White, D., Armand, C. and Davis, R.S., "*Development of the Combustion System for General Motors' High-Efficiency Range Extender Ecotec Small Gas Engine*". SAE International Journal of Engines, 2015. **8**(4): p. 1587-1601, doi: 10.4271/2015-01-1272.

15. Abraham, P., Reuss, D. and Sick, V. "*High-Speed Particle Image Velocimetry Study of In-Cylinder Flows with Improved Dynamic Range*", SAE International 2013-01-0542, 2013, doi:10.4271/2013-01-0542.

16. Reif, K., *Gasoline Engine Management*. 2015: Springer.

17. Kleeberg, H., Tomazic, D., Lang, O. and Habermann, K. "*Future Potential and Development Methods for High Output Turbocharged Direct Injected Gasoline Engines*", SAE International 2006, doi:10.4271/2006-01-0046.

18. Caton, J.A. "*A Comparison of Lean Operation and Exhaust Gas Recirculation: Thermodynamic Reasons for the Increases of Efficiency*", SAE International 2013-01-0266, 2013, doi:10.4271/2013-01-0266.

19. Lavoie, G., Ortiz-Soto, E., Babajimopoulos, A., Martz, J.B., et al., "*Thermodynamic sweet spot for high-efficiency, dilute, boosted gasoline engines*". International Journal of Engine Research, 2012: p. 1468087412455372, doi: 10.1177/1468087412455372.

20. Attard, W.P. and Parsons, P., "*Flame Kernel Development for a Spark Initiated Pre-Chamber Combustion System Capable of High Load, High Efficiency and Near Zero NOx Emissions*". SAE Int. J. Engines, 2010. **3**(2): p. 408-427, doi: 10.4271/2010-01-2260.

21. Jung, D., Sasaki, K., Sugata, K., Matsuda, M., et al., "*Combined Effects of Spark Discharge Pattern and Tumble Level on Cycle-to-Cycle Variations of Combustion at Lean Limits of SI Engine Operation*". 2017, SAE Technical Paper, doi: 10.4271/2017-01-0677.

22. Attard, W.P. and Parsons, P., "*A Normally Aspirated Spark Initiated Combustion System Capable of High Load, High Efficiency and Near Zero NOx Emissions in a Modern Vehicle Powertrain*". SAE Int. J. Engines, 2010. **3**(2): p. 269-287, doi: 10.4271/2010-01-2196.

23. Bunce, M., Blaxill, H., Kulatilaka, W. and Jiang, N. "*The Effects of Turbulent Jet Characteristics on Engine Performance Using a Pre-Chamber Combustor*", SAE International 2014-01-1195, 2014, doi:10.4271/2014-01-1195.

24. Kuboyama, T., Moriyoshi, Y., Tanoue, K., Hotta, E., et al., "*Very Lean and Diluted SI Combustion Using a Novel Ignition System with Repetitive Pulse Discharges".* SAE Int. J. Engines, 2009. **2**(2): p. 749-755.

25. Nakai, M., Nakagawa, Y., Hamai, K. and Sone, M. "*Stabilized Combustion in a Spark Ignited Engine through a Long Spark Duration"*, SAE International 850075, 1985, doi:10.4271/850075.

26. Tanoue, K., Hotta, E. and Moriyoshi, Y., "*Enhancement of ignition characteristics of lean premixed hydrocarbon–air mixtures by repetitive pulse discharges".* International Journal of Engine Research, 2009. **10**(6): p. 399-407.

27. Van Basshuysen, R. and Spicher, U., *Gasoline engine with direct injection: processes, systems, development, potential*. 2009: Vieweg+ Teubner.

28. Chan, T.W., Meloche, E., Kubsh, J., Rosenblatt, D., et al., "*Evaluation of a Gasoline Particulate Filter to Reduce Particle Emissions from a Gasoline Direct Injection Vehicle".* SAE International Journal of Fuels and Lubricants, 2012. **5**(3): p. 1277-1290, doi: 10.4271/2012-01-1727.

29. Ogata, T., Makino, M., Aoki, T., Shimoda, T., et al. "*Particle Number Emission Reduction for GDI Engines with Gasoline Particulate Filters"*, SAE International 2017-01-2378, 2017, doi:10.4271/2017-01-2378.

30. Ayala, F.A. and Heywood, J.B. "*Lean SI engines: the role of combustion variability in defining lean limits"*, SAE Technical Paper 2007-24-0030, 2007, doi:10.4271/2007-24-0030.

31. Johansson, B. "*Influence of the Velocity Near the Spark Plug on Early Flame Development"*, SAE International 930481, 1993, doi:10.4271/930481.

32. Zhao, L., Moiz, A.A., Som, S., Fogla, N., et al., "*Examining the role of flame topologies and in-cylinder flow fields on cyclic variability in spark-ignited engines using large-eddy simulation".* International Journal of Engine Research, 2017: p. 1468087417732447, doi: 10.1177/1468087417732447.

33. Aleiferis, P.G., Taylor, A.M.K.P., Whitelaw, J.H., Ishii, K., et al. "*Cyclic Variations of Initial Flame Kernel Growth in a Honda VTEC-E Lean-Burn Spark-Ignition Engine"*, SAE International 2000-01-1207, 2000, doi:10.4271/2000-01-1207.

34. Pischinger, S. and Heywood, J.B. "*How Heat Losses to the Spark Plug Electrodes Affect Flame Kernel Development in an SI-Engine"*, SAE International 900021, 1990, doi:10.4271/900021.

35. Bates, S.C. "*Flame imaging studies of cycle-by-cycle combustion variation in a SI four-stroke engine*", SAE Technical Paper 892086, 1989, doi:10.4271/892086.

36. Johansson, B. "*The Influence of Different Frequencies in the Turbulence on Early Flame Development in a Spark Ignition Engine*", SAE International 940990, 1994, doi:10.4271/940990.

37. Johansson, B. "*Cycle to Cycle Variations in S.I. Engines - The Effects of Fluid Flow and Gas Composition in the Vicinity of the Spark Plug on Early Combustion*", SAE International 962084, 1996, doi:10.4271/962084.

38. Aleiferis, P., Taylor, A., Ishii, K. and Urata, Y., "*The nature of early flame development in a lean-burn stratified-charge spark-ignition engine*". Combustion and Flame, 2004. **136**(3): p. 283-302.

39. Sjöberg, M., Zeng, W. and Reuss, D., "*Role of Engine Speed and In-Cylinder Flow Field for Stratified and Well-Mixed DISI Engine Combustion Using E70*". SAE Int. J. Engines, 2014. **7**(2), doi: 10.4271/2014-01-1241.

40. Heywood, J.B., *Internal Combustion Engine Fundamentals, Chapter 9—Combustion in Spark-Ignition Engines, Apr. 1988*. 1988, McGraw-Hill, Inc.

41. B Peterson, V.S., "*High-Speed Flow and Fuel Imaging Study of Available Spark Energy in a Spray-Guided Direct-Injection Engine and Implications on Misfires*". International Journal of Engine Research, 2010(11), doi: 10.1243/14680874JER587.

42. Peterson, B., Reuss, D.L. and Sick, V., "*High-speed imaging analysis of misfires in a spray-guided direct injection engine*". Proceedings of the Combustion Institute, 2011. **33**(2): p. 3089-3096, doi: 10.1016/j.proci.2010.07.079.

43. Peterson, B., Reuss, D.L. and Sick, V., "*On the ignition and flame development in a spray-guided direct-injection spark-ignition engine*". Combustion and Flame, 2014. **161**(1): p. 240-255, doi: 10.1016/j.combustflame.2013.08.019.

44. Maly, R., *Spark Ignition: Its Physics and Effect on the Internal Combustion Engine*, in *Fuel Economy*, J. Hilliard and G. Springer, Editors. 1984, Springer US. p. 91-148.

45. Raffel, M., Willert, C.E., Wereley, S. and Kompenhans, J., *Particle image velocimetry: a practical guide*. 2013: Springer.

46. Wang, Y., Zhang, J., Dice, P., Wang, X., et al. "*An Experimental Study on the Interaction between Flow and Spark Plug Orientation on Ignition Energy and Duration for Different Electrode Designs*", SAE International 2017-01-0672, 2017, doi:10.4271/2017-01-0672.

47. Wang, Y., Zhang, J., Wang, X., Dice, P., et al., "*Investigation of Impacts of Spark Plug Orientation on Early Flame Development and Combustion in a DI Optical Engine".* SAE International Journal of Engines, 2017. **10**(3): p. 995-1010, doi: 10.4271/2017-01-0680.

48. Wang, Y., Zhang, J., Yang, Z., Wang, X., et al. "*Investigation of Flow Conditions and Tumble near the Spark Plug in a DI Optical Engine at Ignition"*, SAE International 2018-01-0208, 2018,

49. Ozdor, N., Dulger, M. and Sher, E. "*Cyclic variability in spark ignition engines a literature survey"*, SAE Technical Paper 940987, 1994, doi:10.4271/940987.

50. Fansler, T.D., Reuss, D.L., Sick, V. and Dahms, R.N., "*Invited Review: Combustion instability in spray-guided stratified-charge engines: A review".* International Journal of Engine Research, 2015. **16**(3): p. 260-305, doi: 10.1177/1468087414565675.

51. Zeng, W., Sjöberg, M. and Reuss, D., "*Using PIV Measurements to Determine the Role of the In-Cylinder Flow Field for Stratified DISI Engine Combustion".* SAE Int. J. Engines, 2014. **7**(2), doi: 10.4271/2014-01-1237.

52. Dulger, M. and Sher, E. "*Experimental study on spark ignition of flowing combustible mixtures"*, SAE Technical Paper 951004, 1995, doi:10.4271/951004.

53. Zhang, A., Cung, K., Lee, S.-Y., Naber, J., et al., "*The Impact of Spark Discharge Pattern on Flame Initiation in a Turbulent Lean and Dilute Mixture in a Pressurized Combustion Vessel".* SAE Int. J. Engines, 2013. **6**(1): p. 435-446, doi: 10.4271/2013-01-1627.

54. Anderson, R.W. and Asik, J.R. "*Ignitability Experiments in a Fast Burn, Lean Burn Engine"*, SAE International 830477, 1983, doi:10.4271/830477.

55. Chen, W., Madison, D., Dice, P., Naber, J., et al. "*Impact of Ignition Energy Phasing and Spark Gap on Combustion in a Homogenous Direct Injection Gasoline SI Engine Near the EGR Limit"*, SAE International 2013-01-1630, 2013, doi:10.4271/2013-01-1630.

56. Abidin, Z., Hoag, K., Mckee, D. and Badain, N. "*Port Design for Charge Motion Improvement within the Cylinder"*, SAE Technical Paper 2016-01-0600, 2016, doi:10.4271/2016-01-0600.

57. Paschen, F., "*On the potential difference required for spark initiation in air, hydrogen, and carbon dioxide at different pressures".* Annalen der Physik, 1889. **273**.

58. "*Advanced Combustion Engine Research and Development 2012 Annual Progress Report*", 2012, Vehicle Technologies Office, Department of Energy

59. Kale, V., Yeliana, Y., Worm, J. and Naber, J. "*Development of an improved residuals estimation model for dual independent cam phasing spark-ignition engines*", SAE Technical Paper 2013-01-0312, 2013, doi: 10.4271/2013-01-0312.

60. Bresler, M., Attard, W. and Reese, R., "*Investigation of Alternative Ignition System Impact on External EGR Dilution Tolerance in a Turbocharged Homogeneous Direct Injected Spark Ignited Engine*". SAE International Journal of Engines, 2015. **8**(4): p. 1967-1976, doi: 10.4271/2015-01-9043.

61. Alger, T., Gingrich, J., Mangold, B. and Roberts, C., "*A Continuous Discharge Ignition System for EGR Limit Extension in SI Engines*". SAE Int. J. Engines, 2011. **4**(1): p. 677-692, doi: 10.4271/2011-01-0661.

62. Alger, T., Gingrich, J., Roberts, C., Mangold, B., et al. "*A High-Energy Continuous Discharge Ignition System for Dilute Engine Applications*", SAE International 2013-01-1628, 2013, doi:10.4271/2013-01-1628.

63. Peterson, B. and Sick, V., "*High-speed flow and fuel imaging study of available spark energy in a spray-guided direct-injection engine and implications on misfires*". International Journal of Engine Research, 2010. **11**(5): p. 313-329, doi: 10.1243/14680874JER587.

64. Maly, R. and Meinel, H. "*Determination of Flow Velocity, Turbulence Intensity and Length and Time Scales from Gas Discharge Parameters*". in *5th International Symposium on Plasma Chemistry*. 1981.

65. Kim, J. and Anderson, R.W., "*Spark anemometry of bulk gas velocity at the plug gap of a firing engine*". 1995, SAE Technical Paper, doi: 10.4271/952459.

66. Pashley, N., Stone, R. and Roberts, G. "*Ignition System Measurement Techniques and Correlations for Breakdown and Arc Voltages and Currents*", SAE International 2000-01-0245, 2000, doi:10.4271/2000-01-0245.

67. Sabroske, K.R., Hoying, D.A. and Rabe, D.C. "*Laskin nozzle particle generator*", U.S. Patent No.5498374, Mar 12, 1996.

12 Appendix

12.1 Additional Work on Ion Sensing

12.1.1 Introduction

Currently the combustion controls on SI engines are mainly open loop based on calibration maps. Research has been conducted to explore the potential of close-loop combustion control. The close-loop combustion control requires some forms of combustion feedback. An ideal scenery involves instrumentation of in-cylinder pressure transducers, from which important combustion metrics (ignition delay, CA50 and etc.) can be directly calculated. However the cost of instrumenting in-cylinder pressure transducers is too high to be worthwhile. Alternatively, ion probes can detect the flame propagation speed, which has the potential as a combustion indicator if it can be proven to highly correlate with combustion metrics. Four locations on the periphery of the optical liner were mounted with the ion probes and preliminary research has been done to investigate the correlation between flame speed calculate from the ion signals and combustion metrics. In this chapter, a brief overview of this work is described.

12.1.2 Experimental Setup

Four ion probes were mounted on the periphery of the optical liner sandwiched between the gasket and the quartz material as in Figure 12-1. The ion current signals were converted and amplified to voltage signal, and recorded in the combustion analyzer ACAP at 0.5°CA resolution. The schematic of the ion probe instrumentation circuit is illustrated in Figure 12-2.

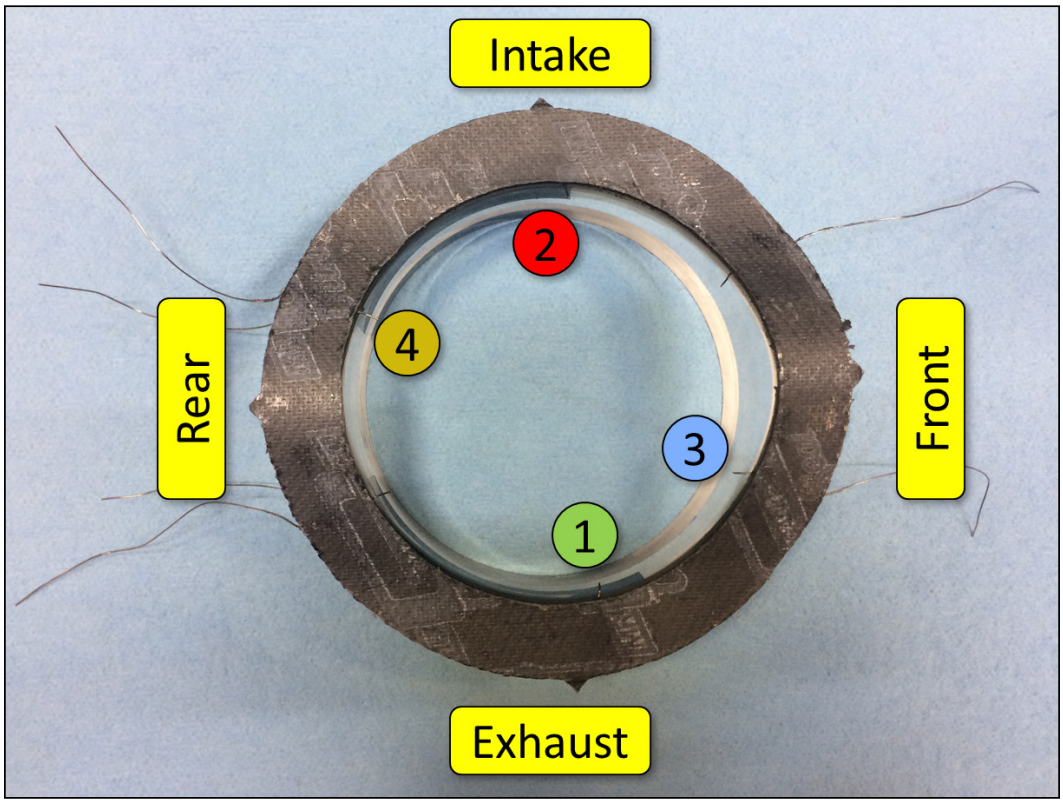

Figure 12-1: Ion probe instrumentation on the optical liner.

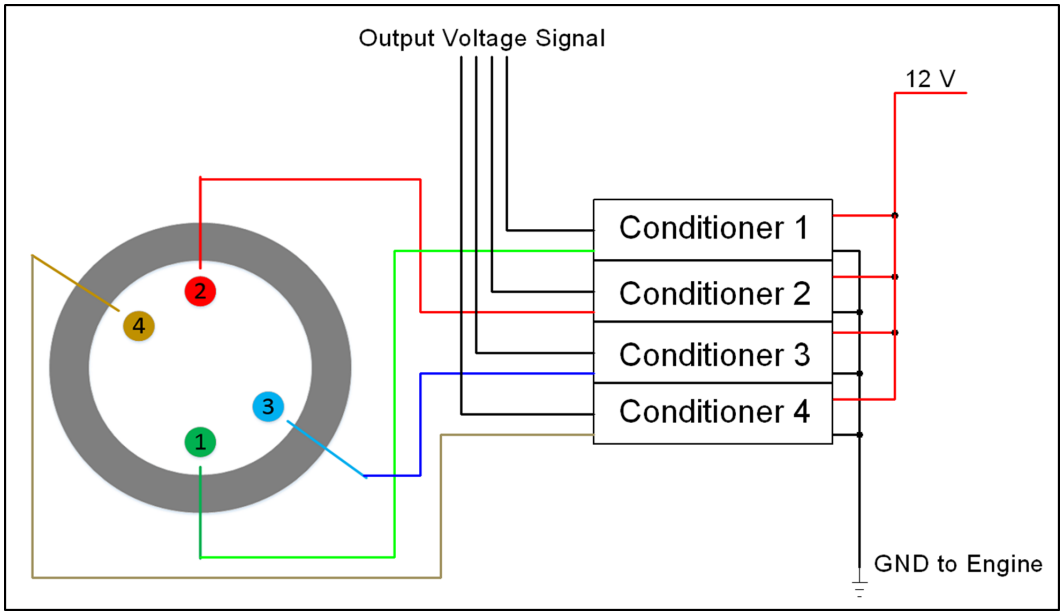

Figure 12-2: Wiring schematic of the ion probes.

The test matrix for ion sensing is summarized in Table 12-1. The experiment was done at two tumble levels to achieve different levels of flow motion. At high tumble, the spark advance was set at 12°BTDC; while at low tumble, two spark advance timing was tested at 12°BTDC and 18°BTDC. The spark timing was set at 18°BTDC at low tumble to bring the CA50 close to MBT.

Table 12-1: Ion sensing test matrix.

Tumble Level	SOI (°BTDC)	SA (°BTDC)	Engine Speed (rpm)	Target IMEP (kPa)
High	360	12	1000	250
	330			
	300			
	270			
Low	360	12		
	330			
	300			
	270			
Low	360	18		
	330			
	300			
	270			

12.1.3 Methodology

The sample ion signals collected from the four probes versus crank angle are illustrated in Figure 12-3. The flame speed towards each probe is calculated by dividing the radius of the cylinder by the crank angle duration between the ignition and the point where ion signal starts rising, as in equation 12-1.

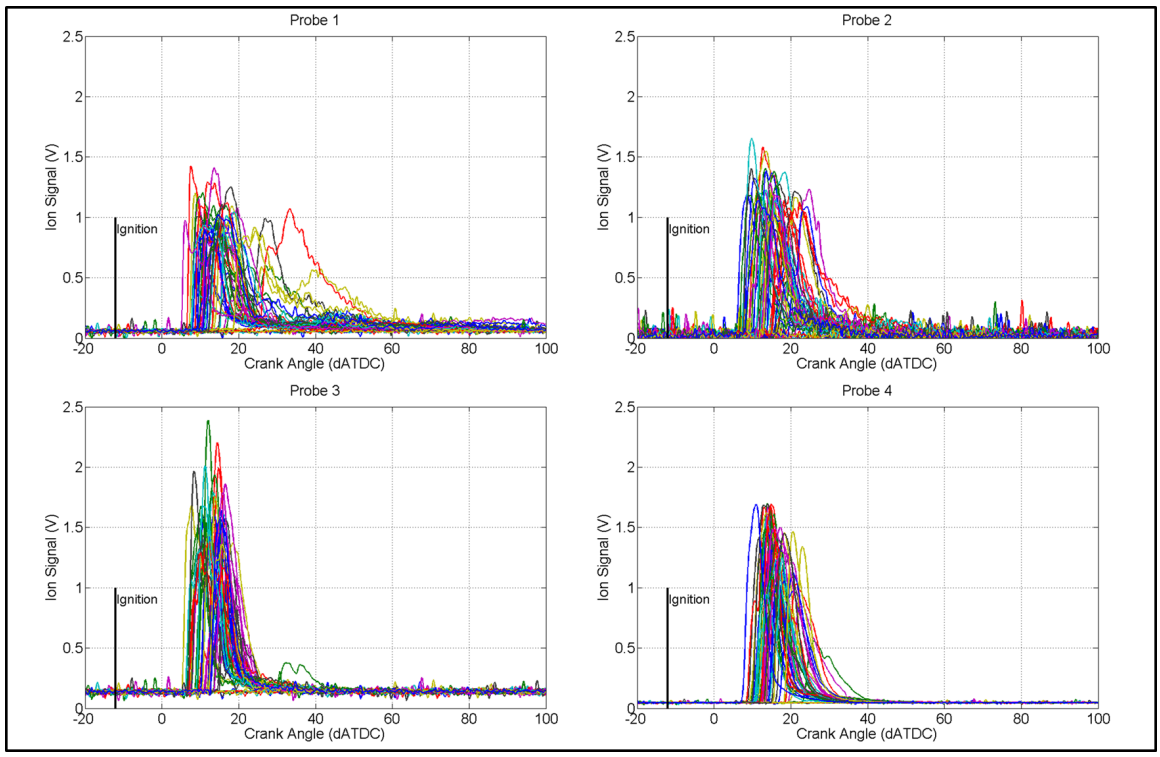

Figure 12-3: Sample ion signals from the four ion probes.

$$V_{flame,probe} = \frac{Bore/2}{CA_{flame\_arrival} - SA} \qquad 12\text{-}1$$

In equation 12-1, $V_{flame,probe}$ is the flame speed toward a particular ion probe. $CA_{flame\_arrival}$ is the crank angle when the ion signal starts rising, and SA is the spark advance.

12.1.4 Results

12.1.4.1 Flame Speed

The cycle-averaged flame speeds calculated from the four probes are illustrated in Figure 12-4 through Figure 12-6. It is expected that the flame propagates faster in all four direction at high tumble (Figure 12-4). With the same spark timing (12°BTDC) at low tumble (Figure 12-5), the flame speed is significantly lower than high tumble cases, and the spark timing needs to be advanced to 18°BTDC (Figure 12-6) to bring up the flame speed to the comparable level with high tumble.

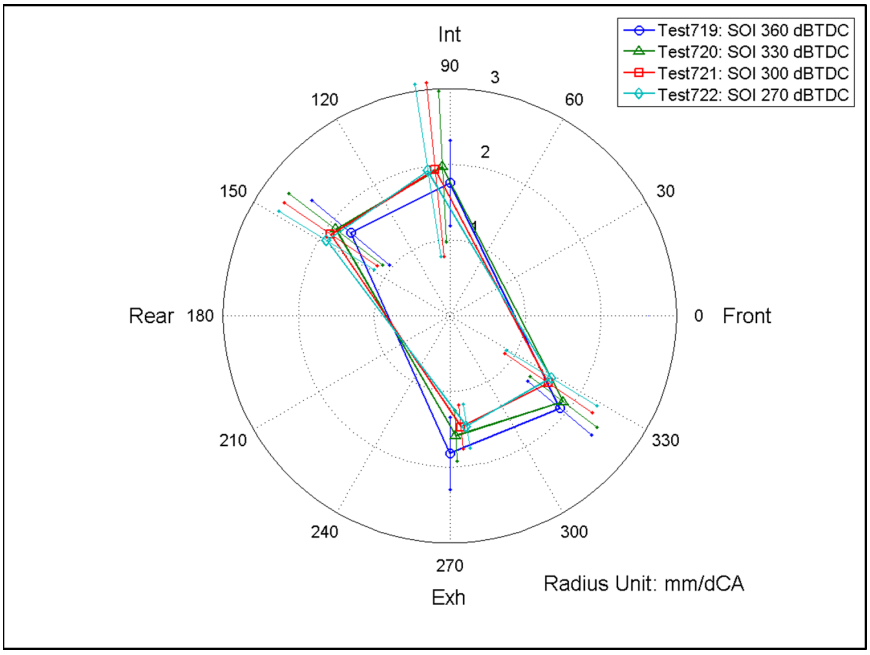

Figure 12-4: Cycle-averaged flame speed towards the four probes, high tumble, spark timing 12°BTDC.

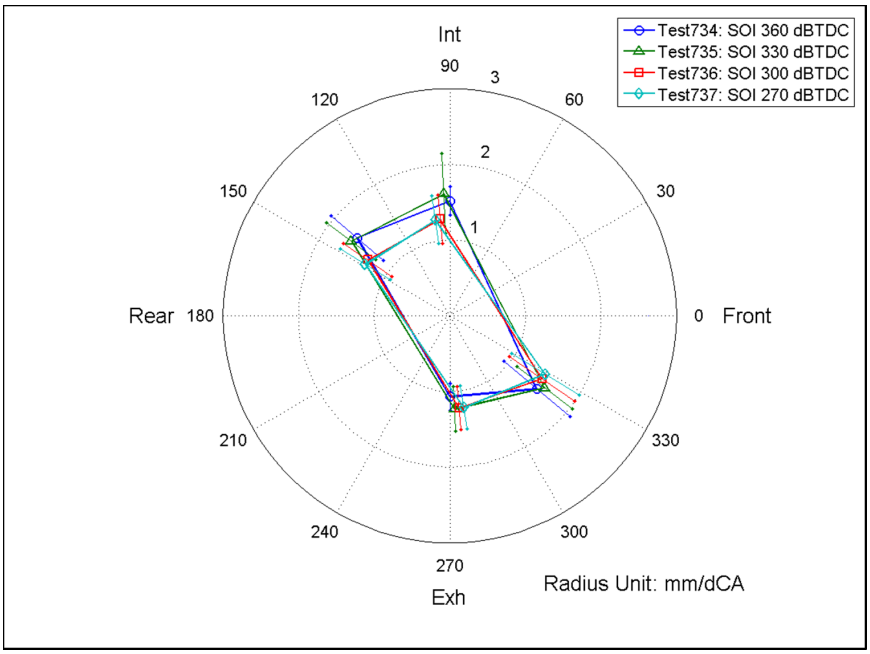

Figure 12-5: Cycle-averaged flame speed towards the four probes, low tumble, spark timing 12°BTDC.

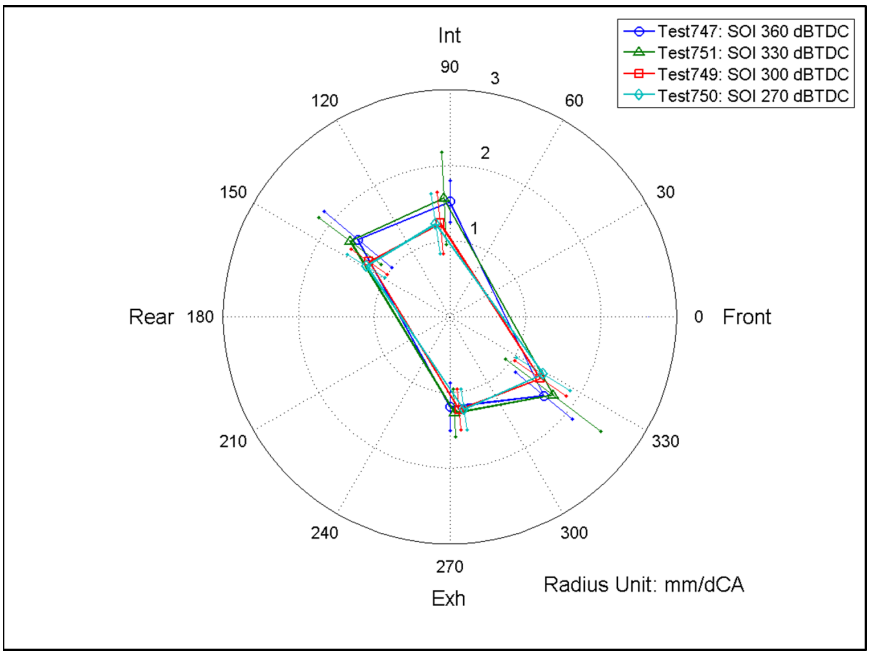

Figure 12-6: Cycle-averaged flame speed towards the four probes, low tumble, spark timing 18°BTDC.

12.1.4.2 Correlation with Combustion Metrics

The mean flame speed averaged among the four probes for each cycle is correlated with the combustion metrics including the ignition delay (CA0010) and burn duration (CA0050). The result shows strong exponential correlation in Figure 12-7 and Figure 12-8. The R^2 value of the correlation between the mean flame speed and ignition delay CA0010 is 0.86 and the RMSE is 1.2°CA. The R^2 value of the correlation between the mean flame speed and CA0050 is as high as 0.90 and the RMSE is 1.6°CA.

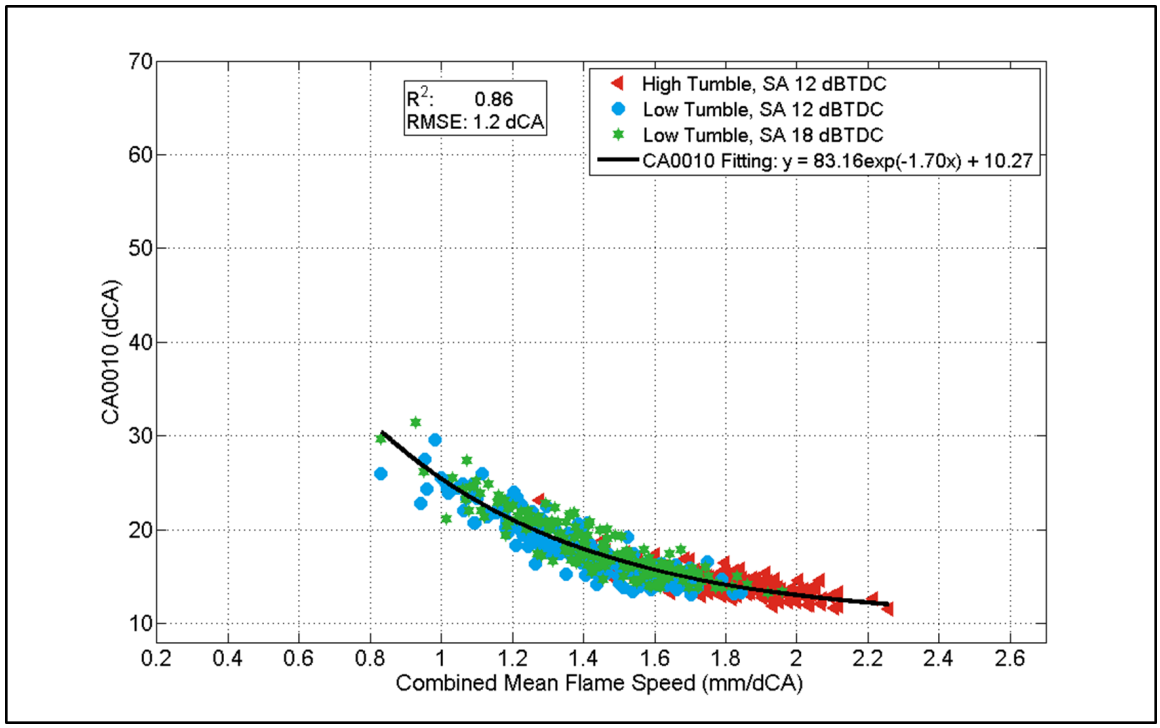

Figure 12-7: Correlation between cyclic mean flame speed and ignition delay CA0010.

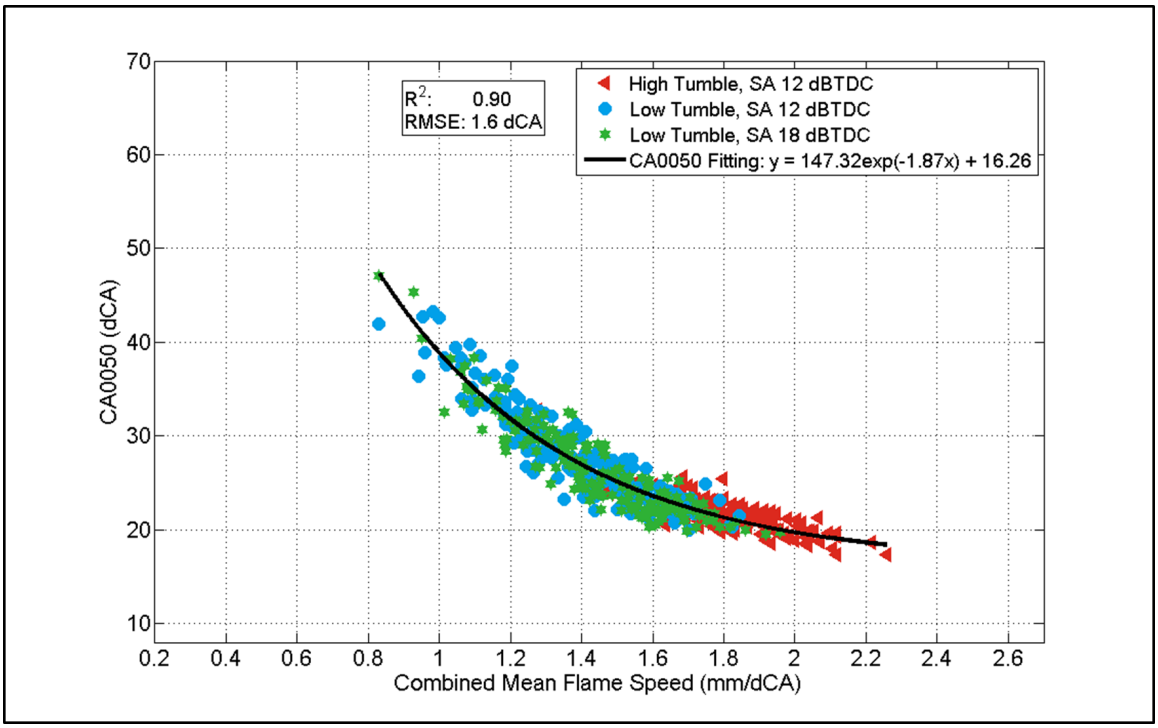

Figure 12-8: Correlation between cyclic mean flame speed and ignition delay CA0050.

12.1.5 Conclusion

The high exponential correlation between the mean flame speed and combustion metrics (CA0010 and CA0050) indicates great potential for the mean flame speed calculated from the ion signals to be used as combustion feedback. However, instrumenting four ion probes in production engines is as challenging and costly as instrumenting in-cylinder pressure transducers. Future work would study the correlation between the flame speed calculated from reduced number of ion probes at various locations in the cylinder and combustion metrics. The potential of ion sensing application as combustion feedback can be enhanced if strong correlation exists with only instrumenting one or two probes at the optimum locations.

12.2 Optical Piston Assembly

The optical piston assembly consists of an aluminum piston frame, the Sapphire piston window, two isolating washers and the inner collar (Figure 12-9). The Sapphire window is seated on the inner collar, and the inner collar is threaded on the inside of the aluminum piston holding the Sapphire window against the aluminum frame such that the upper surface of the window is flush with the aluminum frame top surface. The sealing is provided by two copper isolating washers on both top and bottom of the Sapphire window.

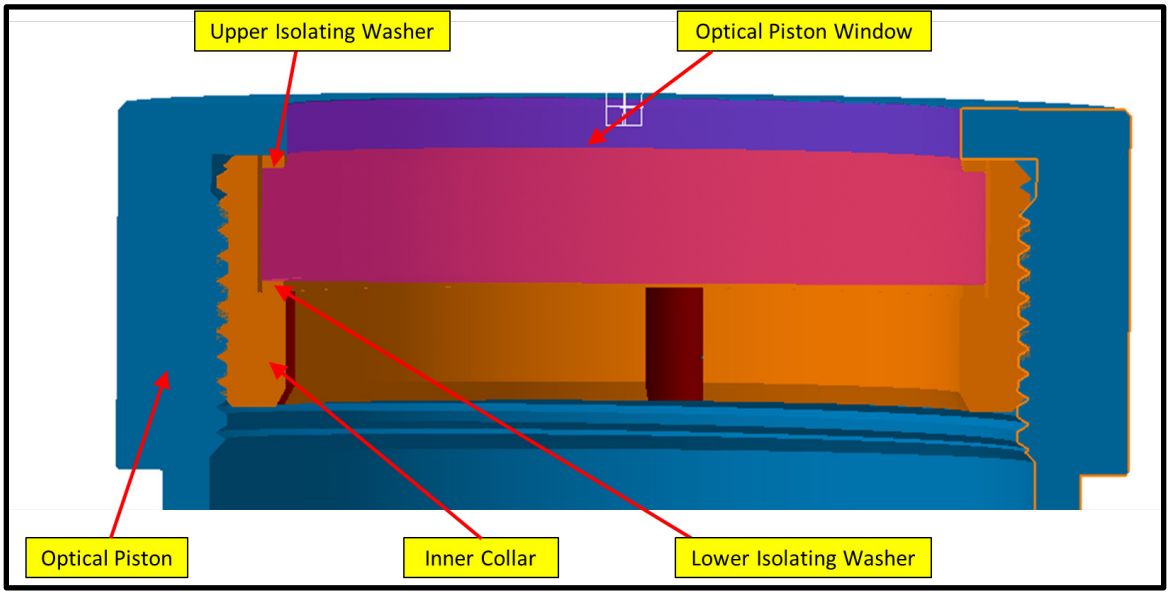

Figure 12-9: Illustration of the optical piston assembly. (Source: Mahle Powertrain).

12.3 Optical Liner Gasket Material

Table 12-2: Optical liner gasket material.

Optical Liner Gasker Material	Dealer	Brand	Part No.	Advantage	Disadvantage
High-Temperature Extreme-Pressure Graphite Gasket Material	McMaster Carr	Unknown	95675K76	soft and flexible, easy to install	can be damaged under high in-cylinder pressure
Ultra Seal Exhaust Gasket Material	Jegs	Mr Gasket	5961	strong, can be non-conductive	hard to install

12.4 Gasket Fabrication

The drawing of the gasket is provided by Mahle Powertrain as in Figure 12-10, and modified by Joel Duncan to mark out the four orientation markers. Material purchased from chapter 12.3 in the appendix can be sent to a third party fabrication shop to be water-jet cut to the desired shape based on the drawing. The current batch of gaskets was cut by Cardinal Rubber & Seal Inc. Their website is http://www.cardinalrubber.com/.

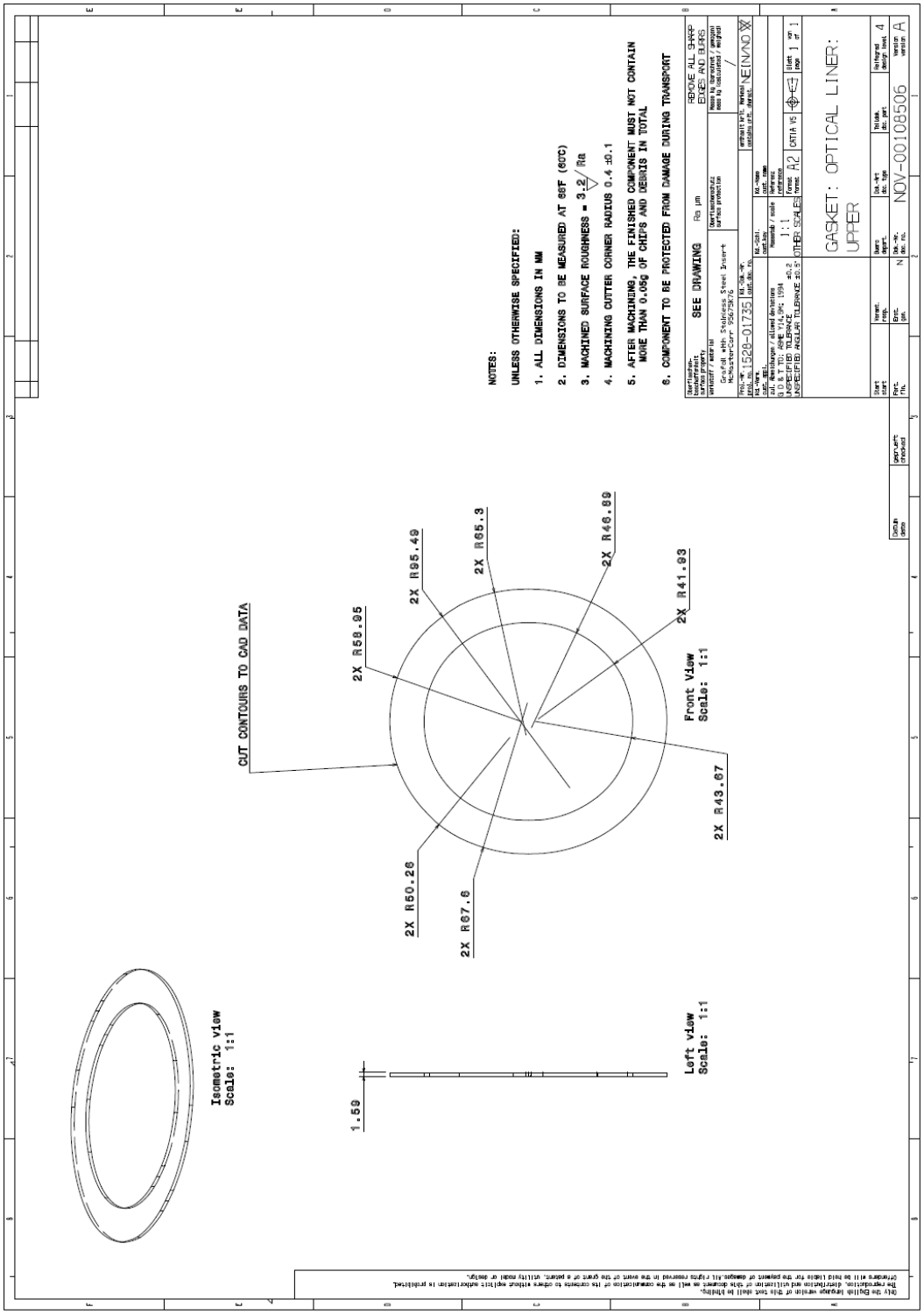

Figure 12-10: Drawing of the optical liner gasket.

12.5 Optical Liner Cleaning, Painting and Gasket Application Procedure

12.5.1 Optical Liner Cleaning

The optical liner needs to be thoroughly cleaned if the gasket fails or moves out of place at high pressure.

Items needed:

1. Basin
2. warm water
3. dish cleaning solution
4. plastic scraper
5. acetone
6. shop towel.

Procedures:

1. Fill the basin with warm water and mix some dish cleaning solution in it.
2. Submerge the optical liner in the basin for 4 hours with the gasket material fully submerged in the soapy water.
3. Peel off the old gasket, and scrape off the remaining adhesive.
4. Use some acetone if the remaining adhesive cannot be scraped off thoroughly.
5. Wipe the optical liner clean and dry with shop towel.

12.5.2 Optical Liner Painting

The optical liner is preferred to be painted in black on the sides on both inside and outside to reduce the random glare from the optical cylinder wall during tests. Please use safety goggles and facial masks when painting the optical liner. Please talk to the lab manager about the necessary procedures to get permission to use a facial mask.

Items needed:

1. compressed air
2. low pressure gauge (set at 15 psig)
3. air hose
4. air brush (Badger Air Brush 360-7 Universal Complete Set)
5. masking tape
6. razor blade
7. flat black engine enamel paint (VHT ESP130007 Enamel Flat Black (288°C))

Procedures:

1. Thoroughly clean the optical liner and dry the surface.
2. Apply the masking tape on the side surface section that is desired to leave transparent. For current research purposes, a window section on the front side of the liner between the tumble plane and the camera is left transparent and thus covered by the masking tape for painting.
3. Cut the extra mask tape along the upper and lower edge of the optical liner with the razor blade.
4. Apply the masking tape on the upper surface of the optical liner. Since the upper surface has a curvature, it is recommended to apply multiple small masking tape pieces covering the entire top curvature seamlessly.
5. Cut the extra masking tape along the upper edge of the top surface.
6. Apply masking tape to the lower surface of the optical liner, and it is not necessary to cut the extra masking tape since it does not get in the way of painting.
7. Set the optical liner on a large piece of cardboard.
8. Connect the Badger air brusher according to the user's manual.
9. Half fill the bottle of the air brush with the black VHT enamel paint.
10. Set the pressure at about 15 psig.
11. Apply three layers of thin film of paint on the inside and outside of the optical liner.
12. Set the painted liner in a safe ventilated place overnight.
13. Immediately clean the air brush and the bottle with acetone thoroughly.

The optical liner with masking tape applied is illustrated in Figure 12-11.

The optical liner immediately after being painted can be seen in Figure 12-12.

The painted optical liner with the masking tape removed can be seen in Figure 3-2.

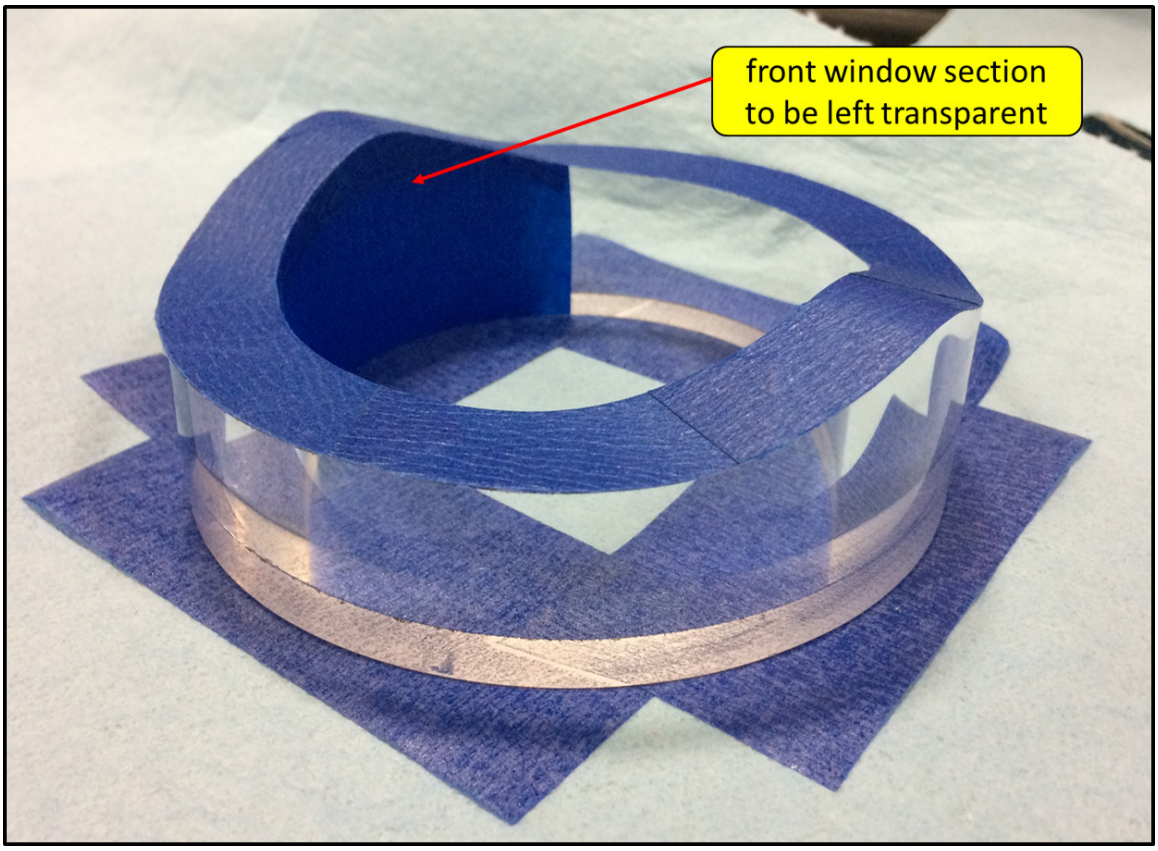

Figure 12-11: Optical liner with masking tape applied before being painted.

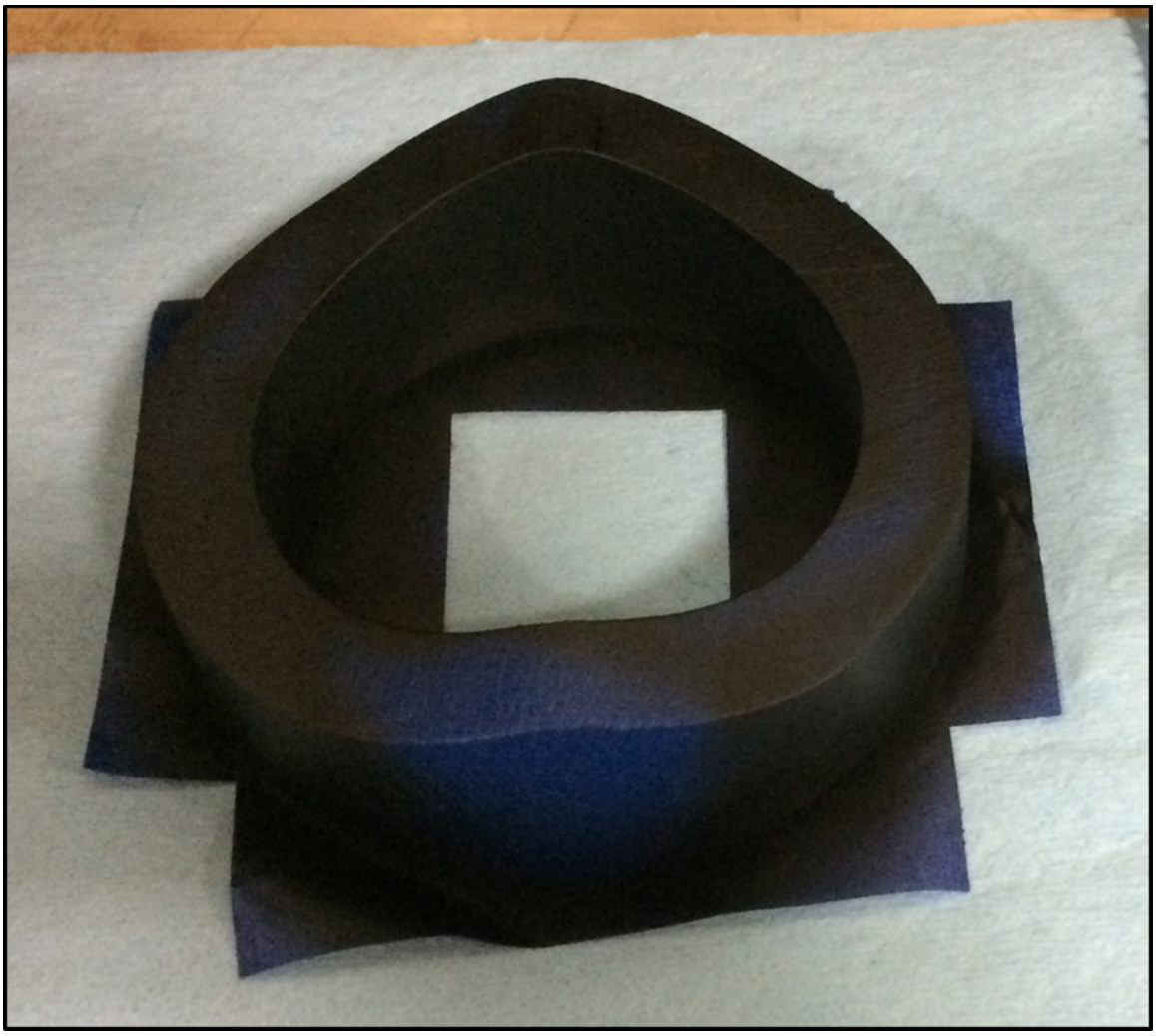

Figure 12-12: Optical liner after being painted and in the drying stage.

12.5.3 Optical Liner Gasket Application

The following procedures of applying the optical liner gasket are summarized from multiple trials and errors and have been proven to be most effective if followed correctly.

1. Make sure the dynamometer is turned off.
2. Connect the engine shaft to the dynamometer.
3. Rotate the optical engine shaft so the piston rests at BDC.
4. Start the oil pump and heater to warm up the optical engine for at least 15 minutes. This is especially important in winter, since the optical liner holder shrinks at low

temperature. The optical liner can only be put in or taken out of the liner holder after it expands at higher temperature.

5. Set the optical liner on a piece of shop towel on the bench.
6. Orient the gasket on the optical liner and press the gasket against the top curvature of the optical liner for a few seconds.
7. Now the gasket has a general shape of the top curvature of the liner.
8. Shake the 3M adhesive bottle before applying the adhesive to the gasket.
9. Set the gasket top side down on a piece of shop towel on the ground.
10. Evenly spray a layer of adhesive on the bottom surface of the gasket.
11. Hold the gasket carefully by edge and align it on top of the optical liner. The alignment is facilitated by the pre-pressed curvature to the gasket.
12. Apply pressure with fingers to press the gasket on the optical liner for 90 to 120 seconds. Two people are preferred since more points can be pressed down on the gasket. Make sure the gasket does not move and is well aligned with the liner in the process.

The following involves operation on the optical engine, and movement of the optical liner needs to be visually watched by the operator. Operation by feel only is not reliable and can result in liner misalignment.

13. Release the hydraulic pressure to lower the clamping deck, and put the optical liner on the liner holder immediately. In this process, the gasket may pop up from the liner upper surface. This does not matter as long as the gasket does not move out of place.
14. Generally align the liner top curvature with the pentroof of the cylinder head and start pumping the clamping deck up quickly. Large strokes of the hydraulic pump are preferred.
15. Slow down pumping when the optical liner is about 20 mm away from the roof, make some adjustment to make sure the optical liner is still in general alignment with the pentroof.
16. When the optical liner is less than 10 mm from the pentroof, start using small strokes to pump the clamping deck. In the meantime, shake the liner holder angularly as the

clamping deck continues to push up the liner holder. In this way, the optical liner is 'self-aligning' with the pentroof.

17. Finally the gasket conforms to the pentroof shape and the optical liner meets the cylinder head tightly. Now pump the hydraulic pressure to 350 psi. Let it set for about 30 minutes.
18. Turn the engine shaft by hand in the engine running direction to feel if pressure can be built in the cylinder.
19. If pressure can be built, the gasket has been successfully glued on the optical liner.
20. Turn the piston back to BDC and release the clamping pressure.
21. Remove the optical liner from the liner holder, and clean the liner as seen fit.

The optical liner with the gasket glued on top can be seen in Figure 3-3.

12.6 Camshaft Phasing Adjustment

The optical engine camshafts are connected with the timing belt through the camshaft end adapters and the timing pulleys (Figure 12-13). The timing pulleys are bolted onto the camshaft end adapters with four head socket screws which are seated in four angular slots. By loosening these screws, the camshaft positions can be adjusted. The length of the slots only allows 30° total cam angle adjustment without adjusting the belt position with respect to timing pulleys. If a larger range of cam angle adjustment is required, the belt needs to be loosened and re-positioned with respect to the timing pulleys.

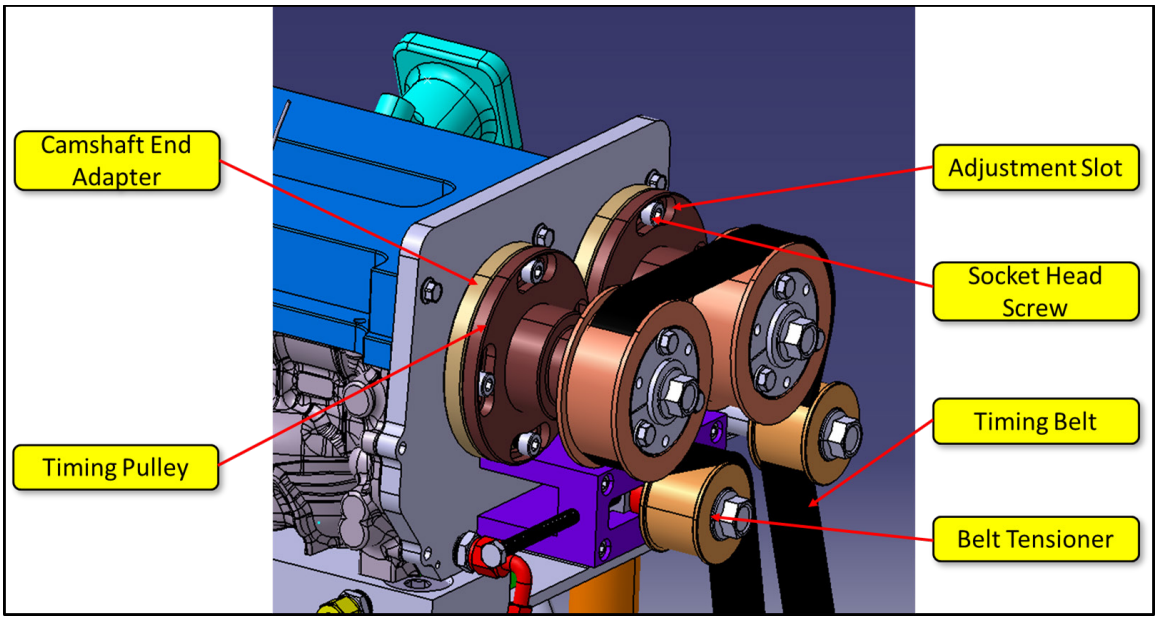

Figure 12-13: Optical engine camshaft assembly. (Source: Mahle Powertrain)

The following procedure should be followed if only small cam angle adjustment is needed.

1. The circumference of the camshaft end adapter is 363 mm. Calculate the circumference length based on required valve timing angle and camshaft end adapter circumference; for example : if the intake valve is to be advanced by 30°CA (15° cam angle), the circumference length = 15°/360°×363 mm = 15 mm.
2. Mark the current relative position between the cam timing pulley and camshaft end adapter; mark the target position of camshaft relative to default position based on calculated circumferential distance (Figure 12-14).
3. Remove the cam cover.

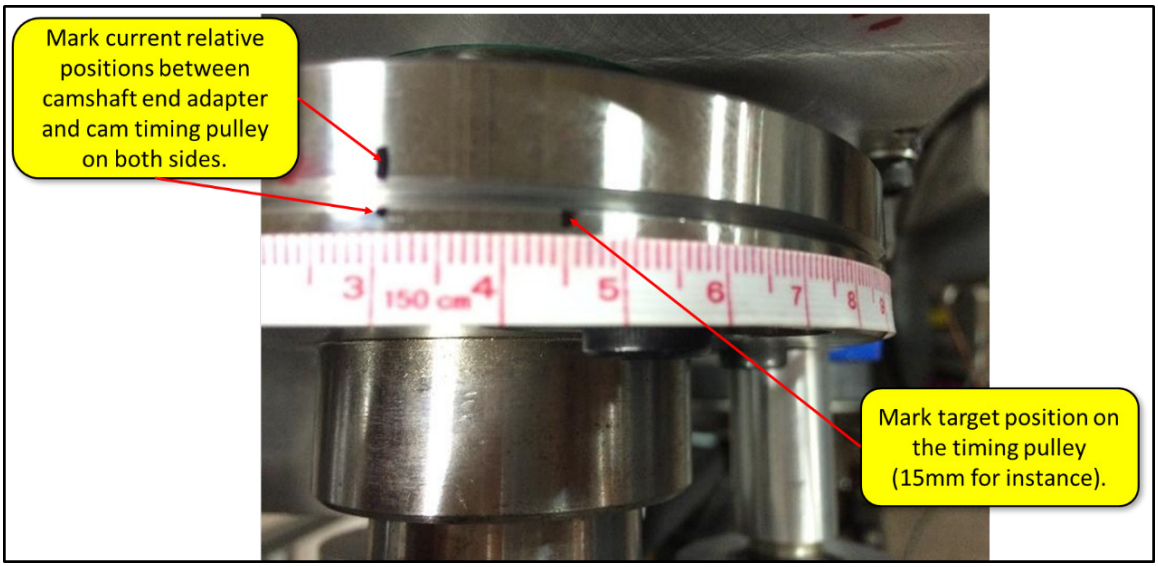

Figure 12-14: Marking the current relative position between the camshaft end adapter and the timing pulley and the target position.

4. Slightly loosen the socket head screws connecting the cam timing pulley and camshaft end adapter.
5. Turn the camshaft with adjustable wrench until the mark on the cam end adapter aligns with the target mark on the cam timing pulley (Figure 12-15).
6. Tighten the socket head screws.
7. Slowly rotate the crankshaft for a complete engine cycle to verify that the valves do not touch the piston.

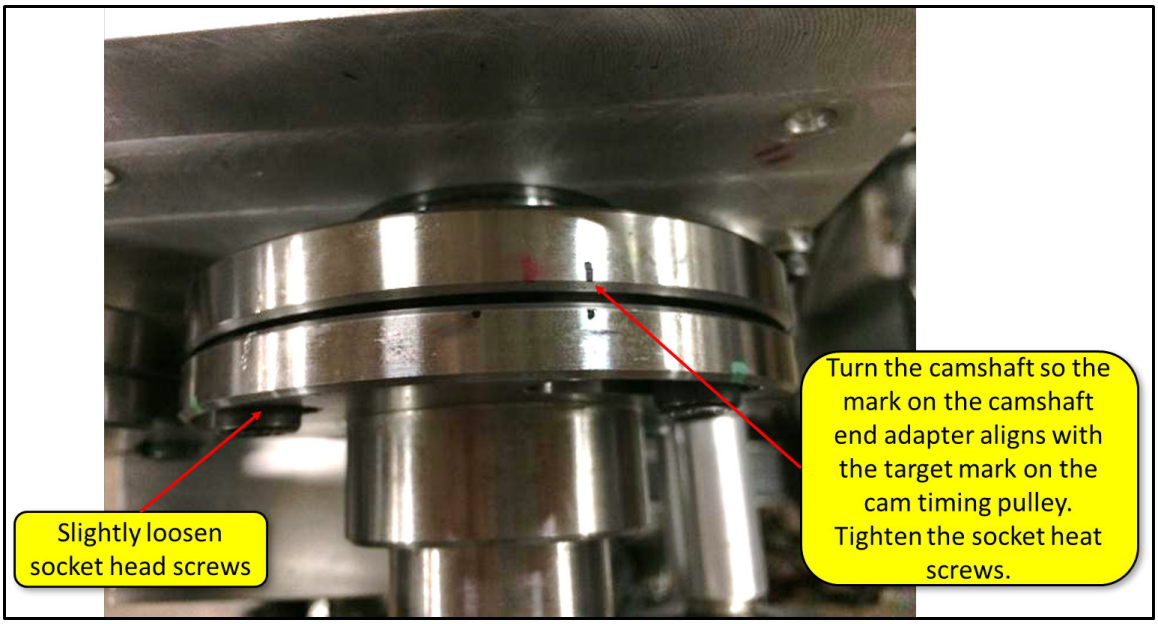

Figure 12-15: Turn the camshaft to the target position.

If a larger range of cam angle adjustment is needed, it is recommended to first resume both camshafts to default parking positions based on the procedure provided in the 2.0 L Ford Ecoboost service manual. In the meantime, pre-set the slot position to leave a large room towards the direction of required adjustment. Tighten everything including the head socket screws and the belt tensioner. During tightening, the timing pulleys may move causing the slot position to change; this may result in insufficient room of the slot for later adjustment. It takes some trial and error to leave enough slot room as well as tightening the screws and the belt tensioner. From here on, follow the procedures given above to adjust the camshafts to the desired positions.

Following the above procedure results in precise adjustment of the camshafts, provided the starting positions of both camshafts are well set to the parking positions.

12.7 Specifications of the In-cylinder Pressure Transducer

Optical Engine In-Cylinder Pressure Transducer

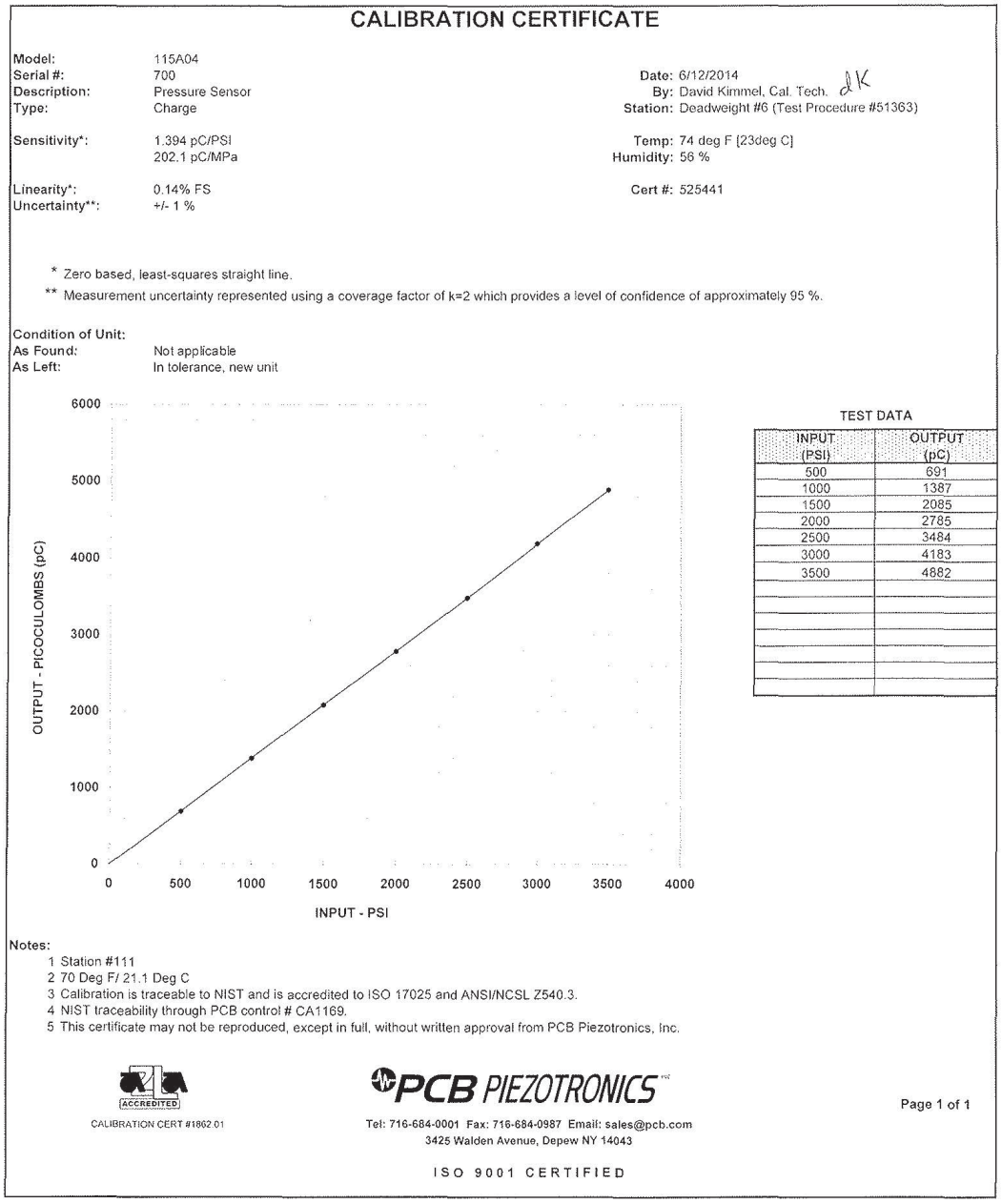

CALIBRATION CERTIFICATE

Model: 115A04
Serial #: 700
Description: Pressure Sensor
Type: Charge

Sensitivity*: 1.394 pC/PSI
202.1 pC/MPa

Linearity*: 0.14% FS
Uncertainty**: +/- 1 %

Date: 6/12/2014
By: David Kimmel, Cal. Tech.
Station: Deadweight #6 (Test Procedure #51363)

Temp: 74 deg F [23deg C]
Humidity: 56 %

Cert #: 525441

* Zero based, least-squares straight line.
** Measurement uncertainty represented using a coverage factor of k=2 which provides a level of confidence of approximately 95 %.

Condition of Unit:
As Found: Not applicable
As Left: In tolerance, new unit

TEST DATA

INPUT (PSI)	OUTPUT (pC)
500	691
1000	1387
1500	2085
2000	2785
2500	3484
3000	4183
3500	4882

Notes:
1 Station #111
2 70 Deg F/ 21.1 Deg C
3 Calibration is traceable to NIST and is accredited to ISO 17025 and ANSI/NCSL Z540.3.
4 NIST traceability through PCB control # CA1169.
5 This certificate may not be reproduced, except in full, without written approval from PCB Piezotronics, Inc.

ACCREDITED
CALIBRATION CERT #1862.01

PCB PIEZOTRONICS
Tel: 716-684-0001 Fax: 716-684-0987 Email: sales@pcb.com
3425 Walden Avenue, Depew NY 14043

ISO 9001 CERTIFIED

Page 1 of 1

Figure 12-16: PCB115A04-700 Calibration 1.

Optical Engine In-Cylinder Pressure Transducer

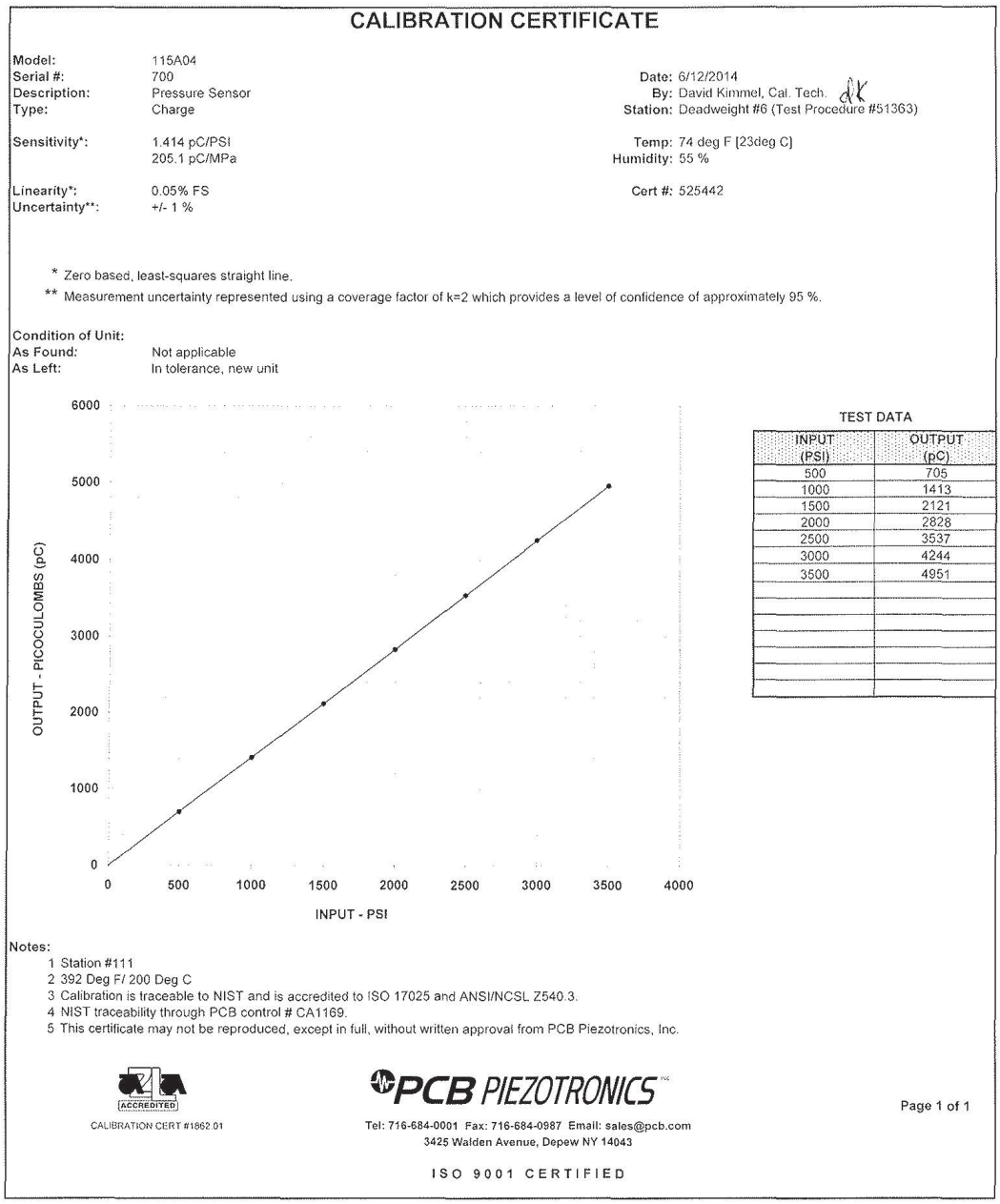

CALIBRATION CERTIFICATE

Model: 115A04
Serial #: 700
Description: Pressure Sensor
Type: Charge

Sensitivity*: 1.414 pC/PSI
205.1 pC/MPa

Linearity*: 0.05% FS
Uncertainty**: +/- 1 %

Date: 6/12/2014
By: David Kimmel, Cal. Tech.
Station: Deadweight #6 (Test Procedure #51363)

Temp: 74 deg F [23deg C]
Humidity: 55 %

Cert #: 525442

* Zero based, least-squares straight line.
** Measurement uncertainty represented using a coverage factor of k=2 which provides a level of confidence of approximately 95 %.

Condition of Unit:
As Found: Not applicable
As Left: In tolerance, new unit

TEST DATA

INPUT (PSI)	OUTPUT (pC)
500	705
1000	1413
1500	2121
2000	2828
2500	3537
3000	4244
3500	4951

Notes:
1 Station #111
2 392 Deg F/ 200 Deg C
3 Calibration is traceable to NIST and is accredited to ISO 17025 and ANSI/NCSL Z540.3.
4 NIST traceability through PCB control # CA1169.
5 This certificate may not be reproduced, except in full, without written approval from PCB Piezotronics, Inc.

ACCREDITED
CALIBRATION CERT #1862.01

PCB PIEZOTRONICS
Tel: 716-684-0001 Fax: 716-684-0987 Email: sales@pcb.com
3425 Walden Avenue, Depew NY 14043

ISO 9001 CERTIFIED

Page 1 of 1

Figure 12-17: PCB115A04-700 Calibration 2.

13 Copyright Documents

13.1 Copyright Permission 1

November 12, 2017

Yanyu Wang (Simon)
Ph.D. Candidate
Advanced Power Systems Labs
Department of Mechanical Engineering-Engineering Mechanics
Michigan Technological University
1400 Townsend Drive
Houghton, MI 49931

Dear Yanyu,

Thank you for your email. Permission is granted for you to include your previously published technical paper 2017-01-0672, "An Experimental Study on the Interaction between Flow and Spark Plug Orientation on Ignition Energy and Duration for Different Electrode Designs," and previously published journal article 2017-01-0680, "Investigation of Impacts of Spark Plug Orientation on Early Flame Development and Combustion in a DI Optical Engine," in your thesis. It is my understanding that the thesis will not be available commercially.

The following conditions apply:

-A new copyright permission request is required for any further use of this material, other than that specified within your original request.

-The SAE material must be clearly identified and include the following statement *"Reprinted with permission Copyright © 2017 SAE International. Further distribution of this material is not permitted without prior permission from SAE."*

-Any language use, other than specified within your email, requires a new copyright request and additional fee.

Best regards,

Mandy L. May
Manager, Digital Publishing
Content Management

SAE INTERNATIONAL
400 Commonwealth Drive
Warrendale, PA 15096

o +1.724.772.8564
e mandy.may@sae.org
www.sae.org

13.2 Copyright Permission 2

SAE INTERNATIONAL

REQUEST FOR PERMISSION TO REPRINT MATERIAL

From: SAE International
Intellectual Property and Contract Licensing
400 Commonwealth Drive
Warrendale, PA 15096
724-772-7000
copyright@sae.org

Text Material:

Author(s) and/or editor(s) Yanyu Wang

Title of selection and source (if different) Investigation of Flow Conditions and Tumble near the Spark Plug in a DI Optical Engine at Ignition

From Page 1, line 1, beginning with the words investigation

To page last page, line last line, ending with the words tumble

Artwork:

Figure number. all figures on page(s) all pages

Table number. all tables on page(s) all pages

Agreed to and accepted by:

Yanyu Wang — Name (please print or type)

Signature

03/15/2018 — Date

Ph.D candidate — Title (please print or type)

Credit or Copyright:
Please supply the proper format for the accreditation. If no accreditation format is provided, SAE will create an accreditation in for the following simplified form: © XYZ Widget Company

Author and Publisher use only:

When submitting approved copyright authorizations to SAE International Intellectual Property and Content Licensing, please include a copy of the licensed material clearly indicating the intended location, including new figure/ table number and caption title, in the new product published by SAE International.

SAE INTERNATIONAL

REQUEST FOR PERMISSION TO REPRINT MATERIAL

From: SAE International
Intellectual Property and Contract Licensing
400 Commonwealth Drive
Warrendale, PA 15096
724-772-7000
copyright@sae.org

To: (please print or type)

Person (if known) Yanyu Wang
Title (if known) Ph.D Candidate
Company Michigan Technological University
Address 815 RL. Smith Bldg, MTU
Address 1400 Townsend Dr. , Houghton, MI-49931
Telephone (906)370-2612
email yanyuw@mtu.edu

Dear Copyright Holder:

SAE International is currently developing a manuscript for publication with Yanyu Wang that is tentatively entitled: Investigation of Flow Conditions and Tumble near the Spark Plug in a DI Optical Engine at Ignition (SAE 2018-01-0208).

The estimated publication date is April 10, 2018.

As the identified copyright holder of record, we are requesting permission to include the material, as listed on page two of this request, in this and all subsequent editions of the above referenced work, in all media expression now known or later developed, including use within learning management systems, foreign language translations, digital database delivery, other derivative works, and in any customization prepared and published by SAE International or its licensees for print and/or distribution throughout the world. We request special permission for use by nonprofit organizations to support the aid by blind or physically handicapped individuals and to adapt the format of the material to fit the technical requirements of any digital delivery system now known or later developed. We also request permission to use the material in conjunction with the marketing and promotion of the work. Appropriate accreditation will be given as provided here within.

Please indicate that you agree with the terms as requested by signing and returning this letter. In signing, you warrant that you/your organization are/is the sole copyright owner(s) of this material, have the authority to grant republication permissions on the behalf of the copyright owner, and/or that said copyright does not infringe on the copyright or other rights of any other parties. If you do not control these rights, we would appreciate a written response indicating as such, and if possible, assistance in identifying with whom we should apply.

Thank you in advance for your assistance.

Sincerely,

SAE International
(For printed versions, please turnover to complete)